NORTHWESTERN UNIVERSITY

System Design and Verification of the Precession Electron Diffraction Technique

A DISSERTATION

SUBMITTED TO THE GRADUATE SCHOOL
IN PARTIAL FULFILLMENT OF THE REQUIREMENTS

for the degree

DOCTOR OF PHILOSOPHY

Field of Materials Science and Engineering

By

Christopher Su-Yan Own

EVANSTON, ILLINOIS

First published on the WWW 01, August 2005
Build 05.12.07. PDF available for download at:
http://www.numis.northwestern.edu/Research/Current/precession.shtml

ABSTRACT

System Design and Verification of the Precession Electron Diffraction Technique

Christopher Su-Yan Own

Bulk structural crystallography is generally a two-part process wherein a rough starting structure model is first derived, then later refined to give an accurate model of the structure. The critical step is the determination of the initial model. As materials problems decrease in length scale, the electron microscope has proven to be a versatile and effective tool for studying many problems. However, study of complex bulk structures by electron diffraction has been hindered by the problem of dynamical diffraction. This phenomenon makes bulk electron diffraction very sensitive to specimen thickness, and expensive equipment such as aberration-corrected scanning transmission microscopes or elaborate methodology such as high resolution imaging combined with diffraction and simulation are often required to generate good starting structures.

The precession electron diffraction technique (PED), which has the ability to significantly reduce dynamical effects in diffraction patterns, has shown promise as being a "philosopher's stone" for bulk electron diffraction. However, a comprehensive understanding of its abilities and limitations is necessary before it can be put into widespread use as a standalone technique. This thesis aims to bridge the gaps in understanding and utilizing precession so that practical application might be realized.

Two new PED systems have been built, and optimal operating parameters have been elucidated. The role of lens aberrations is described in detail, and an alignment procedure is given that shows how to circumvent aberration in order to obtain high-quality patterns. Multislice simulation is used for investigating the errors inherent in precession, and is also used as a reference for comparison to simple models and to experimental PED data. General trends over a large sampling of parameter space are determined. In particular, we show that the primary reflection intensity errors occur near the transmitted beam and decay with increasing angle and decreasing specimen thickness. These errors, occurring at the lowest spatial frequencies, fortuitously coincide with reflections for which phases are easiest to determine via imaging methods. A general two-beam dynamical model based upon an existing approximate model is found to be fairly accurate across most experimental conditions, particularly where it is needed for providing a correction to distorted data. Finally, the practical structure solution procedure using PED is demonstrated for several model material systems.

Of the experiment parameters investigated, the cone semi-angle is found to be the most important (it should be as large as possible), followed closely by specimen thickness (thinner is better). Assuming

good structure projection characteristics in the specimen, the thickness tractable by PED is extended to 40-50 nm without correction, demonstrated for complex oxides. With a forward calculation based upon the two-beam dynamical model (using known structure factors), usable specimen thickness can be extended past 150 nm. For *a priori* correction, using the squared amplitudes approximates the two-beam model for most thicknesses if the scattering from the structure adheres to psuedo-kinematical behavior. Practically, crystals up to 60 nm in thickness can now be processed by the precession methods developed in this thesis.

To my wife Lindsey, for enriching my life throughout my years at Northwestern and for many more to come.
You have our gratitude.

Acknowledgements

First and foremost, I would like to thank my thesis adviser, Prof. L.D. Marks for the opportunity to work with him and for his guidance throughout my training. I am also indebted to Dr. Wharton Sinkler for his mentorship and for his willingness to work with me and share his resources throughout the duration of this work. He has acted quite like a second adviser and I thank him for his many suggestions, excellent feedback, and for his understanding.

Many other people have made this work possible. Thanks go to the members of the Marks research group, especially Arun Subramanian, who has always made himself available as a friend and teacher; my father, Dr. Shi-Hau Own for his continual encouragement; and Vasant Ramasubramanian, who taught me some fundamental electronics that I have found useful in many areas of my life. Winfried Hill of Rochester Polytechnic deserves special thanks for analysis of the electronics and circuit redesign suggestions for the first precession instrument I built. Wharton Sinkler from UOP LLC provided the GITO and MOR specimens and did considerable preliminary work with MOR that supported the results in section 5.4. Jim Ciston, from our group, contributed the background work on Andalusite in section 5.3. I also thank JEOL and Hitachi technical support, especially Ken Eberly and Jim Poulous at Hitachi, for constructive discussions, and Hitachi High Technologies for permission to publish microscope schematics included in this dissertation.

Funding for this project was provided by UOP LLC, STCS, the US Department of Energy (Grant no. DE-FG02-03ER 15457), and the Fannie and John Hertz Foundation. I am deeply indebted to the Fannie and John Hertz Foundation for funding my graduate studies; without the Foundation's singular vision and immense generosity, this work would not have been possible.

Contents

ABSTRACT iii

Acknowledgements vi

List of Tables ix

List of Figures x

Chapter 1. Introduction and Methods 1
1.1. The Electron Microscope in Crystallography 2
1.2. Direct Methods 3
1.3. The Problem of Multiple Scattering 11
1.4. Approaches for Pseudo-Kinematical Electron Diffraction 17

Chapter 2. Precession Instrumentation 27
2.1. Precession Geometry 27
2.2. Retrofit Requirements 34
2.3. Aberration Analysis 35
2.4. Review of Previous Instruments 41
2.5. Design Approach 42

Chapter 3. The GITO Model System 52
3.1. Rapid *a priori* Solution of a Metal Oxide 53
3.2. Precession Simulation 63
3.3. R-factor analysis 69
3.4. Summary 71

Chapter 4. Lorentz Correction Factors 74
4.1. Derivation of Correction Factors 75
4.2. Comparison between models 82
4.3. Discussion: Approach for Solving Novel Structures 96

Chapter 5. Precession Examples 100
5.1. $(Ga,In)_2SnO_4$ 100
5.2. $La_4Cu_3MoO_{12}$ 102
5.3. Al_2SiO_5 108

5.4. Mordenite 109
5.5. Conclusion 114

Chapter 6. Conclusions and Future Work 115
6.1. Future Work 117

References 119

Appendices 123

Appendix A. Electronics Background 124
A.1. Limited-bandwidth systems 124
A.2. Amplifier design 126
A.3. Simple Linear Power Supply Design 130

Appendix B. Implementation 1 133
B.1. Hitachi H-9000 retrofit 133
B.2. Performance and limitations 136

Appendix C. Implementation 2 140
C.1. JEOL 2000FX Retrofit 140
C.2. Performance and limitations 143

Appendix D. Implementation 3 146
D.1. JEOL 2100F 146

Appendix E. Alignment Procedure 150

Appendix F. Intensity Measurement 154

Appendix G. $(Ga,In)_2SnO_4$ Dataset 158

List of Tables

3.1 GITO atom positions from HREM, neutron diffraction (refined), and unrefined positions from precession. Atom positions from PED match very closely with the neutron-refined positions. 62

3.2 Terminology for thickness ranges. 65

4.1 Correction factors for correcting PED intensities. Note $C_{Blackman}$ has corrected integrand. The pre-factor $\frac{1}{\xi_{\mathbf{g}}^2}$ in corrections 1-2 can be approximated by $F_{\mathbf{g}}^2$ in the case of swift electrons. 84

4.2 R_1 for the structure factors with noise added using equation 4.18. 94

4.3 R_1 for C_{2beam}-corrected intensities using noisy structure factors. Table values in percent. 96

G.1 Kinematical amplitudes and experimental amplitudes for the GITO precession experiment (normalized to strongest reflection). See figure 3.2 for experimental errors. Reflections excluded in direct methods are starred (*). 158

List of Figures

1.1 Demonstration of amplitude and phase errors in perbromo-phthalocyanine. 5

1.2 Argand diagram illustrating Sayre's triplet relationship (equation 1.9). 7

1.3 Graphical representation of iterative projection onto sets described by equation 1.10. 8

1.4 Three possible outcomes of the solution search between sets S_1 and S_2 using iterative projection. 9

1.5 Flowchart of the feasible sets '98 (fs98) direct methods algorithm. 10

1.6 Rediffraction of beams that meet the Bragg condition. 12

1.7 Probability histograms of the product $F_{\mathbf{g}}F_{-\mathbf{g}}$ and $F_{\mathbf{g}}F_{\mathbf{h}}F_{-\mathbf{g}-\mathbf{h}}$ for centrosymmetric and noncentrosymmetric (random) models of $C_{32}Cl_{16}CuN_8$ crystal. 16

1.8 Normalized dynamical moduli of $F_{\mathbf{g}}$ plotted against $F_{-\mathbf{g}}$ for the noncentrosymmetric structure in figure 1.7(b) and (d). 17

1.9 Plot of the $J_0(2A)$ and its integral. 19

1.10 The schematic diagram of precession electron diffraction (PED). 21

1.11 Comparison of precessed and conventional DPs of magnesium orthovanadate. 22

2.1 Reciprocal space geometry of P.E.D. 30

2.2 Demonstration of integration of tilted DPs to form a precession patterns, and comparison with a conventional DP. 31

2.3 Precession geometry schematics showing the relationship between ZOLZ and FOLZ excitations and usable diffraction radius γ. 33

2.4 Precession geometry in a modern condenser-objective TEM with double deflection coil system showing the path of the precessed transmitted beam. 36

2.5 Star of merced, formed by the unoptimized precession probe prior to full alignment. 37

2.6 The origin of probe deviation in real space during precession. 39

2.7 Primary aberrations that require compensation in conventional TEMs. 39

2.8 An aberration function containing a mixture of C_{10}, C_{12a}, C_{30}, and C_{45a} yielding flat phase at a high tilt angle. 41

2.9 Overview diagram of the precession system. 43

2.10 Generic amplifier for driving an electromagnetic coil. 43

2.11 Crossover distortion in push-pull amplifiers and its effect on precession patterns. 45
2.12 Mixer-buffer circuit used to add precession capabilities to a deflector amplifier. 46
2.13 Precession software interface. 49
2.14 Precession patterns for 60 mrad cone semiangle (a) and 40 mrad cone semiangle (b). 50

3.1 Structure of $(Ga,In)_2SnO_4$ (GITO). 52
3.2 Friedel errors in the precession pattern (amplitudes). 54
3.3 Comparison of kinematical amplitude and experimental PED intensity patterns for GITO. 56
3.4 Experimental precession amplitudes and dynamical amplitudes plotted against kinematical amplitudes calculated from the known GITO structure. 57
3.5 DM solutions generated from precession amplitudes. 58
3.6 DM solution of GITO from precession intensities (all reflections included). 61
3.7 Precession amplitudes (normalized) plotted against amplitudes calculated by precession multislice. 64
3.8 Montage of amplitude reference plots for GITO. 66
3.9 3-D surface plots of absolute amplitude error ($F_{\mathbf{g}}^{exp} - F_{\mathbf{g}}^{kin}$) against $|\mathbf{g}|$ and thickness. 68
3.10 R_1 for the GITO experimental datasets. 71
3.11 3-D surface plots of absolute amplitude error ($F_{\mathbf{g}}^{exp} - F_{\mathbf{g}}^{kin}$) against $|\mathbf{g}|$ for experimental conditions. 72

4.1 Reciprocal space geometry in (a) $x - y$ plane and (b) $x - z$ plane. 77
4.2 Intensity collected ($I_{\mathbf{g}}$) and excitation error ($s_{\mathbf{g}}$) during the integration in the kinematical model, plotted against azimuthal angle for a low-index reflection. 79
4.3 Scattered intensity ($I_{\mathbf{g}}$) v. excitation error ($s_{\mathbf{g}}$) in the two-beam model. 80
4.4 Equation 4.17 plotted for the three strongest reflections in GITO. 82
4.5 The squared sinc function (a) and the integral of the sinc function (b) plotted against excitation error for a crystal thickness of 500 Å. 85
4.6 Integration limits and scattered intensity for a reflection $\mathbf{g}$ located at $x = R_0$. 86
4.7 The kinematical correction factor C_{kin} for crystal thicknesses between 100 Åand 600Å, for ϕ = 24 mrad. 87
4.8 Comparison of the full correction factors C_{2beam} and $C_{Blackman}$ from table 4.1 plotted against $\mathbf{g}$. 89
4.9 Tableau of correction factor plots for the GITO system calculated for various cone semi-angles and specimen thickness. 90
4.10 Multislice amplitudes with correction factor C_{kin} applied. 91
4.11 Plots of corrected amplitude v. kinematical amplitudes. 93

4.12 Detail plot of simulated intensities for t = 1268 Å corrected using C_{2beam}. 94
4.13 Multislice datasets corrected with C_{2beam} using structure factors with 40% noise added. 95
4.14 Flowchart for generating a starting structure model from a PED data set. 99

5.1 C_{2beam} correction factors, C_{2beam}-corrected experimental amplitudes, and experimental intensities v. true structure factor for the GITO system. 101
5.2 Direct methods potential map generated from C_{2beam}-corrected amplitudes. 102
5.3 001 projection of the $La_4Cu_3MoO_{12}$ structure model. 103
5.4 Experimental conditions for the $La_4Cu_3MoO_{12}$ precession diffraction experiment. 104
5.5 $La_4Cu_3MoO_{12}$ intensity diffraction patterns. 106
5.6 Direct methods solutions from PED on $La_4Cu_3MoO_{12}$. 107
5.7 Amplitude diffraction patterns from (Al_2SiO_5. 109
5.8 Potential maps from direct methods on Andalusite. 110
5.9 Kinematical and precession diffraction pattern from Mordenite. 112
5.10 Structure map from direct methods on Mordenite using kinematical amplitudes to 1 $Å^{-1}$ with no additional phases. 113
5.11 Direct methods potential map of Mordenite generated using high-pass filtered intensities. 113

A.1 Frequency response of an inductive coil system. 125
A.2 Frequency response of a coil system with feedback. 126
A.3 The ideal op-amp. 127
A.4 Basic operational amplifier circuit configurations. 128
A.5 Voltage divider. 129
A.6 Full-wave 48V LC unregulated supply and characteristics. 131

B.1 BD STB circuit, Hitachi H-9000. 134
B.2 Image S. circuit, Hitachi H-9000. 135
B.3 Revised coil driver circuit, based around the OPA544T power operational amplifier. 137
B.4 The hardware for the first-generation precession instrument installed on the Hitachi UHV H-9000. 138

C.1 The hardware for the second-generation precession instrument. 141
C.2 DEF UNIT block diagram for the JEOL 2000FX. 142
C.3 Schematics for the second generation precession system. 143
C.4 Montage of probe images during a precession revolution (close to aligned). Comparison with a well-aligned precessed probe. 144

D.1 Power supply schematics for the new PED system. 147
D.2 BT signal board schematics for the new PED system. 148
D.3 DS signal board schematics for the new PED system. 149

E.1 Alignment procedure for the PED systems described in appendices B-C. 151
E.2 Reciprocal space alignment on the JEOL 3000F systems described in appendix C. 152

F.1 Demonstration of the background subtraction technique for measuring peak intensity. 154
F.2 Measurement of an irregular peak shape. 156
F.3 Comparison of Semper and EDM intensity measurements. 157

CHAPTER 1

Introduction and Methods

With the renewed interest over the past decade in problems concerning atomic-scale structure due to the nanotechnology revolution, transmission electron microscopy (TEM) has become an increasingly important materials characterization tool. Its strengths lie in its inherent versatility combined with relatively small size and cost, and widespread availability. The standard operating mode in the electron microscope is direct imaging, widely used in morphological studies, defect studies, and certain types of atomic scale investigations. By changing lens excitations in the imaging system, the diffraction pattern of the illuminated region is displayed, providing detailed structure and symmetry information with excellent signal to noise ratio.

Attachments are available to augment the spatial information with chemical information through the use of X-ray detectors and electron energy loss spectrometers (EELS), and equipment is also available for specialized studies, for example *in-situ* attachments for studying environmental reactions, electron holography for investigating magnetic materials, and through-focal series reconstruction and tomography which yield structure information to high spatial resolution (Spence 2003). The simultaneous availability of different types of information has made EM very important in many areas of chemistry, biology, and materials science. Elucidation of several important structures such as carbon nanotubes, several superconducting materials, quasicrystals, and many proteins were possible because of the instrument's inherent versatility. As the length scale of materials problems steadily decreases, atomic-scale structural electron crystallography will be seeing more demand.

Catalysis is a particularly important area of application. Refinement of hydrocarbons is a multi-billion dollar industry that ranges from the initial processing of crude oil to the green catalysis of spent fuels. Not only does structural knowledge enable detailed understanding of reaction characteristics, it opens the door for improvement of catalytic mechanisms at the atomic scale, and later facilitates industrial protection of new catalyst structures by way of patents. The latter is a very strong incentive to shift structure studies from large shared facilities into the industrial laboratory, where characterization can occur rapidly and behind closed doors, and ideally at reduced cost.

This Ph.D. thesis concerns the implementation and development of precession electron diffraction (PED), a modification of the transmission electron diffraction mode (TED) intended for atomic-scale characterization of bulk materials. PED has demonstrated great promise for overcoming significant data quality limitations and represents a major step toward the realization of rapid atomic structure characterization in the TEM. This work is divided into two parts: 1) general implementation of a high-performance precession system, and 2) application of the PED system to model materials systems for the purpose of understanding the technique's limitations and to refine its capabilities. Three practical

precession systems are provided in the appendices to provide a guide for constructing and evaluating future PED systems. The goal of this work is to demonstrate that this method can make bulk structural electron crystallography reliable and fast, with the vision that PED may in the near future become a reliable, versatile and ultimately routine tool for determining atomic structures.

1.1. The Electron Microscope in Crystallography

Historically, X-ray techniques have been at the forefront of structural crystallography owing to the development of probabilistic phasing algorithms in the 1950s, collectively called direct methods (DM), that overcame the crystallographic phase problem (Hauptman 1991). These techniques enabled recovery of the critical phase portion of the Fourier components that describe the structure, enabling straightforward determination of structure models from diffraction intensity measurements. While highly suitable for many types of materials studies, evidenced by the vast number of atomic structures elucidated using X-ray radiation over the past 50 years, high-resolution X-ray techniques have some disadvantages from the perspective of nanomaterials characterization:

- Laboratory X-ray sources are not bright enough for studying very thin crystals, surfaces, and interfaces. To obtain scattered intensities with large dynamic range, a bright source such as a synchrotron is necessary.
- The beam diameter from high brightness sources are on the order of 1 μm, and on the order of 0.5 μm in specialized fine-probe laboratory instruments (an exception is the use of Fresnel zone plates that can obtain 100 nm probes in synchrotrons (Suzuki et al. 2005), however they are extremely rare due to cost). In particular:
  - Single crystal dimensions generally must be on the order of the probe size. Heterogeneous materials cannot be studied unless crystallites are larger in size or can be isolated.
  - Nanocrystal studies require powder specimens or homogeneous polycrystals, which generate ring patterns from simultaneous sampling of all orientations of the crystal. Symmetry information is lost in ring patterns and must be acquired using other techniques such as transmission electron diffraction (TED). Additionally, because reflection number scales roughly with the cube of spatial frequency, large cell structures will have overwhelming peak overlap.
  - Peak resolution (line width) is limited by the width of the probe. Decreasing the probe size can cause ring overlap in dense diffraction patterns from large cell materials or superstructures.
- X-ray imaging optics with adequate resolution are not available; the only information from experiments are diffraction intensities. Morphological and defect information is thus not simultaneously available.
- Being a shared resource, synchrotron-based research projects have strict time constraints and shared maintenance costs.

TEM has traditionally played a complementary role to X-ray methods in crystallography, partly because image resolution was insufficient except in specialized high-energy instruments and also because data quality from TED was limited by multiple scattering. Nevertheless, the ability to form a fine probe

and to simultaneously collect diffraction patterns are distinct advantages. In recent years, the field has seen a huge leap in the imaging capabilities of high-resolution imaging (HREM) and scanning modes (STEM) due to the introduction of aberration-corrective optics allowing point resolutions of less than 1 Ångstrøm (Haider et al. 1998; Batson et al. 2002; Haider et al. 1999; Nellist et al. 2004). Unfortunately, atomic resolution images are beyond the reach of most researchers because aberration correctors are still extremely expensive; the vast majority of TEMs are still limited by the resolution of the image-forming optics.

Electron diffraction is a complementary technique that is capable of extracting structural information — albeit incomplete because phase is lost — to much higher resolution (sub-picometer regime) than imaging techniques because it is virtually immune to the resolution-limiting aberrations of the objective lens. It can often be combined with imaging to enhance the resolution of HREM images through the phase extension technique. A probe size of under 25 nm is readily achieved on modern instruments, enabling precise study of very small particles, individual crystallites within a heterogeneous matrix, and fine structures such as interfaces and surfaces in the TEM. This resolves a major constraint posed by X-ray methods.

While the combination of imaging and diffraction tools is very powerful, a central theme in this thesis will be rapid structural characterization. For raw speed, diffraction alone is an ideal technique. Immunity to aberrations in the image-forming optics allows information transfer to extremely high resolution (≈ 0.01 Å), circumventing the need for careful alignments or in the extreme case aberration-corrective optics. Because it is an averaging technique, it is insensitive to instabilities such as instrument vibration, and the effect of non-periodic features such as defects are diminished (this can be a disadvantage depending on the information sought). Additionally, structural information is collected within highly localized features in the form of diffraction spots or Kikuchi lines; consequently, low dose is possible because the signal to noise ratio is high, minimizing radiation damage to the specimen. This is especially critical for structures that damage easily such as open-framework structures and biological molecules.

Electron diffraction has seen limited use as a standalone structural crystallography technique due to problems of data quality arising from multiple scattering, discussed later in section 1.3. This is rapidly changing, as methods are now available (section 1.4) to improve the quality of the data or take advantage of cases where data are kinematical or near-kinematical for effective use with DM. As will be seen in the next section, DM is very robust provided that data quality is sufficient.

1.2. Direct Methods

A structure projection in two dimensions can be represented by a two-dimensional function $f(\mathbf{r})$, where $\mathbf{r} = x\mathbf{a} + y\mathbf{b}$. Diffraction experiments yield information about this function through the Fourier transform relationships:

$$f(\mathbf{r}) = \int_{-\infty}^{\infty} F(\mathbf{k}) e^{2\pi i \mathbf{k}.\mathbf{r}} dk \tag{1.1}$$

$$F(\mathbf{k}) = \int_{-\infty}^{\infty} f(\mathbf{r}) e^{-2\pi i \mathbf{k}.\mathbf{r}} dr, \tag{1.2}$$

where $\mathbf{k} = h\mathbf{a}^* + k\mathbf{b}^*$ and $\mathbf{a}^*$ and $\mathbf{b}^*$ are unit vectors in reciprocal space. It should be noted that this is a crystallographic structure projection so $\mathbf{a}$ and $\mathbf{b}$ are direct lattice vectors, and additionally $f(\mathbf{r})$ is a potential since in electron diffraction the incident beam interacts with the electrostatic potential. The Fourier transform of a periodic structure, $F(\mathbf{k})$, comprises discrete harmonic components (*structure factors*) that are described by an amplitude term $|F(\mathbf{g})|$ and complex phase term $e^{i\phi_g}$, where $\mathbf{g}$ is a reflection vector in reciprocal space. Assuming for the moment that dynamical multiple scattering can be ignored, the intensities measured in a diffraction pattern are related to the structure factor amplitude by $I(\mathbf{g}) = |F(\mathbf{g})|^2$, and the phases are lost. If phases were available, Fourier inversion via equation 1.1 would generate the structure $f(\mathbf{r})$. This is known as the phase problem of crystallography, and recovery of the phases is the central concept of direct methods.

Refinement procedures are very successful at pinpointing the structure to high accuracy given that the model structure from which the refinement is based is already close to the true structure (e.g. deviating by less than ≈ 0.2 Å) (Marks et al. 1998). The difficulty lies in the fact that, unless the set of initial models considered for refinement contains a close approximation to the true structure, the true structure will (almost without exception) never be found. The primary challenge in structure determination is therefore the generation of a small set of potential structures from which a refinement can be based, and which includes the true structure. It is of relevance to note that the phases are more important than the absolute values of the moduli that are measured. That is, the component providing the key spatial information in a structure is the phase. This is advantageous since the problem is rather forgiving from a probabilistic standpoint: the intensities can vary by a large amount but as long as the recovered phases are close to true values the structure is still inherently recognizable, and even the phases can deviate by a small amount without losing interpretability (figure 1.1).

In simple terms, direct methods make use of *a priori* information to constrain the phases of measured reflections. DM codes exploit this information to converge rapidly to a small set of possible solutions, which usually contains the true solution provided that the intensity data are of sufficient quality. Some of the common constraints used are:

(1) Atomicity: Scattering originates from atoms and hence the solution should have atomic features; regions of peak-like charge densities correspond approximately to isolated atom charge densities.
(2) Cell density: Assuming the data has ample resolution (≈ 1 Å), most of the charge density in the unit cell is zero, representing the space between the atoms.
(3) Positivity: Charge density in a real crystal is always positive.
(4) Localization: If solving a structure in three dimensions, atoms will only be displaced from bulk positions in a narrow region at the surface.

Two major families of algorithms are currently used: 1) approaches based upon probability relationships existing between amplitude and phase, and 2) approaches using iterative mathematical projections. Probabilistic approaches were pioneered in the 1950s and have been very popular in X-ray crystallography, while projection methods are a more general case that have proven to be versatile and robust.

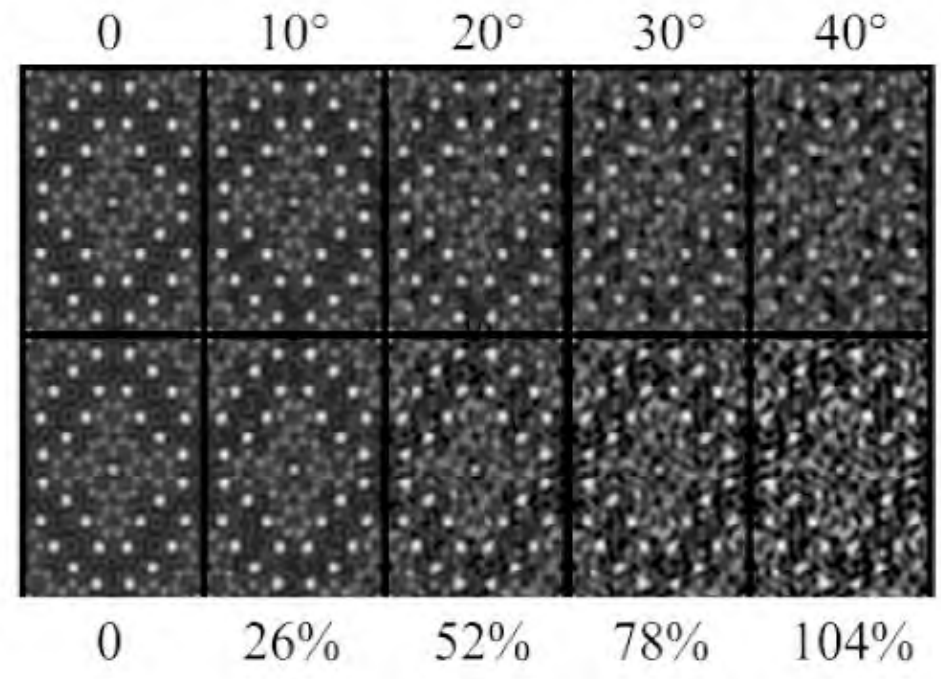

Figure 1.1. Demonstration of amplitude and phase errors in perbromo-phthalocyanine. The bottom row shows amplitude errors (a modified R_1 - see eqn 1.17) and the top shows phase errors (standard deviations, columns give comparable R-factor), both increasing to the right. Amplitude errors were generated using noise in steps of 8% of the strongest beam amplitude. Reproduced from Marks and Sinkler (2003).

1.2.1. Probabilistic Direct Methods

The structure factor is defined in terms of the unit cell contents as:

$$F(\mathbf{g}) = \sum_{i=1}^{N} f_i e^{2\pi i \mathbf{g}.r_i}, \tag{1.3}$$

where N is the number of atoms in the unit cell and f_i is the scattering factor for the i^{th} atom in the unit cell. It is convenient in direct methods to normalize the structure factors to the largest value the amplitude can take on as defined by the unit cell contents, resulting in *unitary structure factors* defined by,

$$U(\mathbf{g}) = \sum_{i=1}^{N} \left(f_i / \sum_{j=1}^{N} f_j \right) e^{2\pi i \mathbf{g}.r_i} = \sum_{i=1}^{N} n_i e^{2\pi i \mathbf{g}.r_i}, \tag{1.4}$$

where n_i is the unitary scattering factor. Many direct methods flavors make use of a more complicated normalization, denoted $E_{\mathbf{g}}$, that generates similar results to the relationships derived below. To obtain E's, the structure factor is simply divided by the sum of the scattering factors.

Harker and Kasper were the first to show that structure factor amplitudes could give information about structure factor phases (Harker and Kasper 1948). Using Cauchy's inequality, they proved that for a centrosymmetric crystal (one with an inversion center), all structure factors are forced to be real and phase determination becomes a sign determination problem according to the relationship:

$$U^2(\mathbf{g}) \leq \frac{1}{2}\left[1 + U(2\mathbf{g})\right]. \tag{1.5}$$

If $U^2(\mathbf{g}) > \frac{1}{2}$ then $U(2\mathbf{g}) \geq 0$, or in other words the sign of reflection $U(2\mathbf{g})$ is positive regardless of the value of $|U(2\mathbf{g})|$. This inequality opened the field of direct methods.

The primary breakthrough in direct methods was the development of the triplet formulation which allows phase determination of a given reflection by two others that are related statistically. This is used in the majority of direct methods algorithms. The earliest form of this is the Sayre equation, derived from Fourier theory using a simple convolution:

$$F_{\mathbf{g}} = \frac{\theta_{\mathbf{g}}}{V} \sum_{\mathbf{h}} F_{\mathbf{h}} F_{\mathbf{g}-\mathbf{h}}, \tag{1.6}$$

where $\theta_{\mathbf{g}}$ is the ratio of the atomic form factor to the squared atomic form factor and V is the unit cell volume (Sayre 1952) (subscripts will be used as a shorthand to indicate the quantity corresponds to the given reflection denoted by the subscript). This relationship takes advantage of atomicity: if $f(\mathbf{r})$ is squared then atomic features become more sharply defined but the positions remain the same and accordingly the phases for the structure factors are the same. Rewriting this we get,

$$|F_{\mathbf{g}}| e^{i\phi_{\mathbf{g}}} = \frac{\theta_{\mathbf{g}}}{V} \sum_{\mathbf{h}} |F_{\mathbf{h}} F_{\mathbf{g}-\mathbf{h}}| e^{i(\phi_{\mathbf{h}} + \phi_{\mathbf{g}-\mathbf{h}})}, \tag{1.7}$$

hence,

$$\phi_{\mathbf{g}} \approx \phi_{\mathbf{h}} + \phi_{\mathbf{g}-\mathbf{h}}. \tag{1.8}$$

Rearranging gives the triplet relation for the phases:

$$\phi_{-\mathbf{g}} + \phi_{\mathbf{h}} + \phi_{\mathbf{g}-\mathbf{h}} \approx 2n\pi, \tag{1.9}$$

where n is an integer. The relationship is illustrated by the Argand diagram in figure 1.2 for a five-term summation for the right hand side of equation 1.7. If the magnitude $|F_{\mathbf{g}}|$ of reflection $\mathbf{g}$ is large and $|F_{\mathbf{h}}|$ and $|F_{\mathbf{g}-\mathbf{h}}|$ are also large for a particular value $\mathbf{h} = \mathbf{h}'$, the sum becomes dominated by the $\mathbf{h}'$ term. The vector sums must match, and even though the phases for smaller terms may deviate, the phase of the component $F_{\mathbf{h}'} F_{(\mathbf{g}-\mathbf{h}')}$ approximates that of reflection $\mathbf{h}$. The probability distribution was derived

by Cochran (Cochran 1955) demonstrating that equation 1.9 is statistically sound and that for strong reflections — which contribute strongly to structural features — it becomes distinctly peaked at $2n\pi$ phase difference.

Practical application of the triplet relation within direct methods begins by defining the phases for a small subset of the reflections in the intensity data set (called the basis set). These are preferably strong reflections for which the true phases may or may not be known; if unknown, random phases are usually given. By propagating triplet relationships in a process called phase extension, estimates of the phases of the remaining reflections can be determined. The phases are probabilistic, hence even if the starting phases are correct, the extended phases may not be correct though usually they are indeed correct or close. Additionally, the phase-extended solution must necessarily be self-consistent, e.g. for a given reflection of unknown phase, multiple reflection vector pairs can define its phase so it may receive conflicting phase assignments. In such a case it is necessary to eliminate discrepancies by modifying some of the starting phases. The key to finding probable starting structures is to rapidly search through solutions to find the ones that are self-consistent for all the measured reflections. A figure of merit (FOM) is calculated to measure the correctness of the potential solutions, and the solutions can be ranked based according to their FOMs. The solution with the lowest FOM is not necessarily the true solution, however the correct solution will necessarily have a low FOM.

1.2.2. Feasible Sets

Alternate methods based upon iterative projection methods were developed for analogous problems concerning information recovery in mathematics and signal processing. The fundamental idea is to

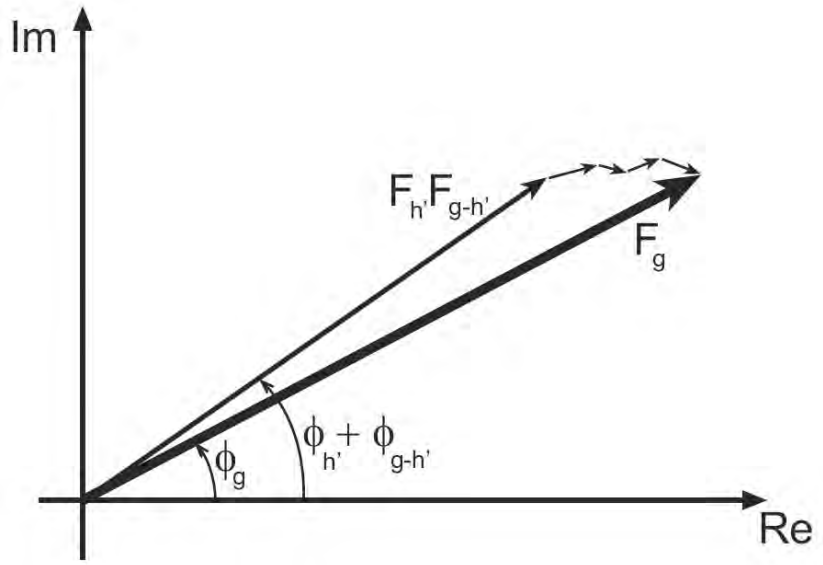

Figure 1.2. Argand diagram illustrating Sayre's triplet relationship (equation 1.9). For strong amplitudes $|F_{\mathbf{g}}|$, $|F_{\mathbf{h}'}|$, and $|F_{\mathbf{g}-\mathbf{h}'}|$, the phase sum is approximately $2n\pi$.

group possible solutions into a *feasible set* and rapidly determine their overlap (potential solutions) through the use of projection operators. A set is a general term describing a group of entities that satisfies certain conditions and constraints. In the context of structural crystallography, two sets are of relevance: 1) the set S_1 of structure factors $|U_g^{exp}|e^{i\phi\mathbf{g}}$ that have been constrained by the experiment; and 2) the set S_2 that satisfies atomistic constraints, itself comprising the overlap of independent sets defined by the *a priori* constraints listed in the previous section. These sets are depicted graphically in fig 1.3. The projection operator is employed within an iterative sequence, and is described by the projection direction, for example,

$$(U_{\mathbf{g}})_{n+1} = P_2 P_1 (U_{\mathbf{g}})_n. \tag{1.10}$$

In relation 1.10, P_1 is the projection from set S_1 to S_2 and P_2 is the projection from set S_2 back to S_1.

An important property of a set is convexity: a set is convex if it contains all points on a line connecting any two of its members. A strong convergence is observed if both sets are convex (Youla 1987). Unfortunately, the set S_1 constrained by experimental amplitudes exclusively is not convex (whereas the related set where phases are known, excluding moduli, is convex), so a strong convergence is not guaranteed. However, for the general case of non-convex sets it was shown that the iteration can at worst only stagnate (Levi and Stark 1984).

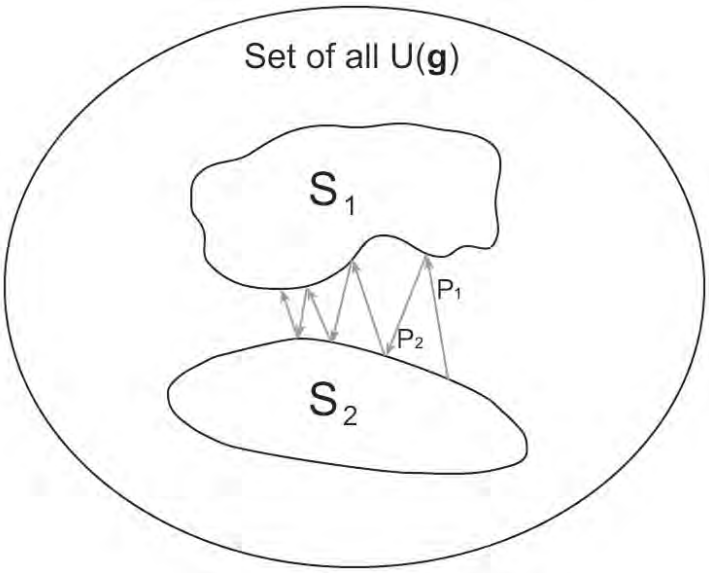

Figure 1.3. Graphical representation of iterative projection onto sets described by equation 1.10. S_1 is the set of structure factors constrained by the observed experimental intensities $|U_g^{exp}|e^{i\phi\mathbf{g}}$ and S_2 is the set of structure factors that satisfies the *a priori* constraints. The magnitude of P_n represents the calculated figure of merit (FOM); rapid convergence toward a feasible solution accompanies minimization of the FOM.

The problem space is uniquely defined by the constraints imposed upon the sets being explored. Depending upon the way these constraints are defined, three possible outcomes are possible (see figure 1.4). In an ideal case, a uniquely defined solution (figure 1.4(a)) is recovered that satisfies all constraints within the sets. This is almost never the case, and typically there is an intersection of sets or no intersection (figures 1.4(b) and (c), respectively). In the case where there is overlap, there may be a large number of potential solutions (Combettes 1996) and additional constraints can be imposed — for example a uniqueness constraint to filter out redundant "like" solutions — to reduce the number of feasible solutions. In the third case, where constraints are too strict, no overlap occurs and the projection algorithm attempts to decrease the distance between sets, in other words it will minimize the figure of merit as best it can. An example is the case where measured amplitudes deviate from kinematical too strongly, giving solutions that do not make chemical sense (e.g. the potential map indicates atoms that are too close). In defining the problem, the constraints are ideally balanced to minimize the number of potential solutions without overly constraining the feasible sets. A consequence of having a non-convex set is that all three cases can be simultaneously satisfied. More than one local minimum is available, and a feasible set of discontinuous solutions can be generated, i.e. multiple solution families with different defining features.

The various flavors of direct methods can be interpreted from the projection standpoint through the identification of their projection operators and constraints. Classical direct methods can be interpreted as the iterative procedure incorporating 1) projection of the phases using probabilistic relationships (triplets, quartets, etc.), and 2) correction of the moduli. The iterative procedure used in the feasible sets '98 (fs98) code written at Northwestern University is shown in figure 1.5, and uses the projection operators:

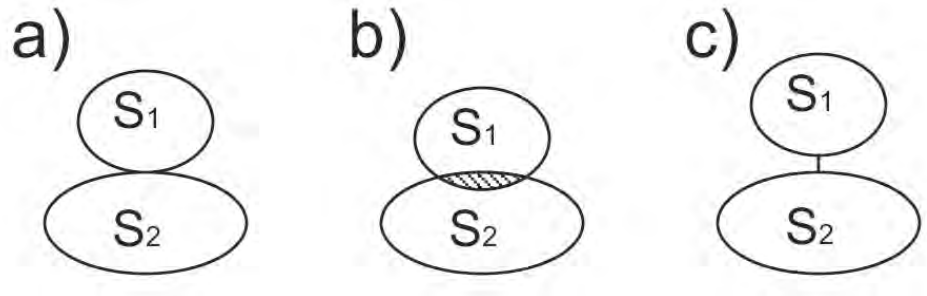

Figure 1.4. Three possible outcomes of the solution search between sets S_1 and S_2 using iterative projection. Case a), where a single unique solution is clearly defined, is rare. Case b) demonstrates considerable overlap of sets, a consequence of loose constraints where many solutions satisfy both constraint sets. c) shows a case where there is no overlap between sets. The algorithm will seek the solutions that minimize the distance between the sets.

$$P_1 u_{\mathbf{r}} = \begin{cases} 0 & \text{if } u_{\mathbf{r}} < 0 \\ u_{\mathbf{r}} \ln \frac{u_{\mathbf{r}}}{\langle u_{\mathbf{r}} \rangle} & \text{if } u_{\mathbf{r}} > 0 \end{cases} \tag{1.11}$$

$$P_2 U_{\mathbf{g}} = |U_{\mathbf{g}}^{exp}| e^{2\pi i \phi_{\mathbf{g}}}. \tag{1.12}$$

P_1 is a peak-sharpening projector similar to Sayre's squaring operation which ensures atom-like features and only positive charge density. P_2 re-constrains the solution in reciprocal space by correcting the moduli to known (experimental) values.

The projection cycle is monitored by a recovery criterion, the figure of merit (FOM), which serves as a metric for the algorithm's effectiveness and can optionally be used to determine when the algorithm should cease. Several types of FOMs are available with varying characteristics designed to minimize certain types of error; the one used in fs98 is as follows:

$$FOM = \sum_{g \neq 0} \frac{|(U_{\mathbf{g}})_{n+1} - \alpha (U_{\mathbf{g}})_n|}{(U_{\mathbf{g}})_{n+1}}, \tag{1.13}$$

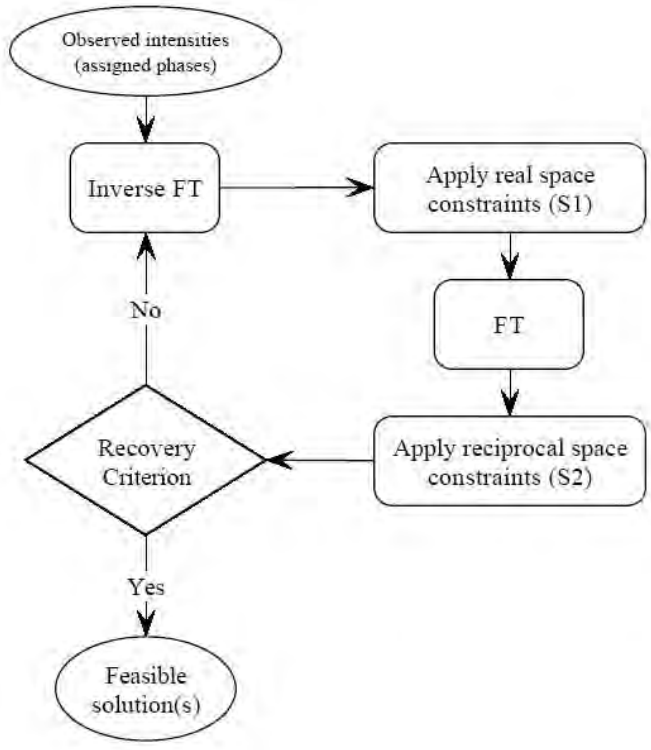

Figure 1.5. Flowchart of the feasible sets '98 (fs98) direct methods algorithm.

where α is chosen to minimize equation 1.13. In the case of a true solution with no measurement error, equation 1.13 will be zero.

1.2.3. Genetic Algorithms

Due to the non-convexity of the amplitude constraint, the intersection of the crystallographic constraints could exist at any number of local minima. It is therefore important to probe all of these minima, as the true solution could be contained within any one of these intersections. Genetic algorithms are a powerful method to perform global search of the possible sets with low information overhead (Landree et al. 1997). They act similarly to the population growth of biological systems with environmental pressures, where offspring with enhanced adaptations are propagated with each successive generation.

In genetic algorithms, the starting phases of a basis set are defined as randomly chosen binary strings. The basis set is chosen based upon statistical relationships within the data set; in simple terms, strong reflections that define other beams are chosen with regard to potential phase relationships. This is done to avoid redundant solutions and to ensure convergence. About 10-20% of the total number of beams in the data set is included in the basis set. The binary string describing phases of the basis set is referred to as a chromosome. For example, each beam's phase — which in the centrosymmetric case can either be 0° or 180° — is represented by a single bit: 1 or 0. For each iterative projection the population is evaluated according to equation 1.13. After the individuals in an entire generation have been subjected to iterative projection and evaluated by equation 1.13, a new generation is born through a process called cross-sharing. Here, the chromosome is broken up into schemata (short contiguous binary segments) which are randomly re-combined with schemata from other populations that have favorable FOM to generate new chromosomes to be used in the next iteration. The children generated with each iteration will generally have improved collective FOM due to natural selection.

To enhance the search capabilities, random mutations are introduced where a single bit or multiple bits within a chromosome are flipped. This causes new areas of solution space to be probed that would otherwise be missed due to non-convexity. Another enhancement, intended to prevent too rapid of convergence, is to sort schemata according to their similarity. This encourages parallel evolution of different 'species', effectively probing multiple niche solutions within the solution space. The algorithm with these enhancements tends to converge rapidly; in fs98 the algorithm is set to terminate by default after 36 populations.

In practical application, direct methods are very successful provided that the quality of intensities is sufficient. In the next section, it will be seen that in electron diffraction they usually are not (except in special cases) due to multiple scattering.

1.3. The Problem of Multiple Scattering

In the simplest interpretation, the radiation incident upon the specimen is scattered by the atomic planes of the crystal when the Bragg condition,

$$\lambda = 2d \sin \theta_B, \tag{1.14}$$

is satisfied (d is the distance between scattering planes and θ_B is the Bragg angle). The ideal case for DM is when intensity in a diffracted beam is a result of single scattering events from the scattering planes (kinematical diffraction). For X-rays, the probability of scattering is already low, therefore the probability for multiple scattering is vanishingly small. The measured intensity is then related to structure factor according to the relationship,

$$I_g^{exp} = |F_g|^2. \tag{1.15}$$

Electrons, however, interact more strongly with matter than X-rays by 3-4 orders of magnitude. The intensities of scattered beams deviate from kinematical and equation 1.15 no longer holds. This phenomenon, termed dynamical diffraction, is demonstrated in figure 1.6 for two beams. The probability for rediffraction is a function of specimen thickness, therefore as the electrons propagate through the specimen, intensity is continually exchanged between diffracted and transmitted beams. At the exit surface the diffracted beam intensity no longer represents the scattering strength as indicated by the structure factor.

In the configurations of high symmetry that are of most interest in crystallographic studies, many beams are simultaneously excited. Within a zone axis pattern (ZAP), a large number rediffraction paths are simultaneously available and the intensities in the pattern become distorted — more severely if strong scatterers (heavy elements) are present or if the specimen is thick. Images are likewise affected since the same beams contribute to the image: contrast oscillations of image features with increasing thickness prevent direct interpretation of HREM images except for suitably thin specimens. The quality

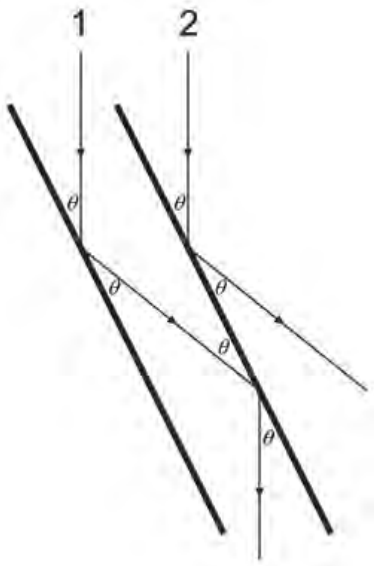

Figure 1.6. Diffracted beams that meet the Bragg condition (equation 1.14) are necessarily in the same condition to be rediffracted back into the incident beam. Demonstrated here for two beams, this is the origin of dynamical diffraction.

of crystallographic information available in TEM is thus limited by the cell contents and their arrangement and by the specimen thickness. It is relevant for PED to note that much less intensity exchange occurs when only a few beams are simultaneously excited. If only two beams are strongly excited at a time, the least distortion of intensities occurs.

1.3.1. Multislice

In structure studies involving high resolution imaging, image simulation is used to account for the effects of multiple scattering. First, an image is simulated based upon a structure model, then it is checked to see how closely it resembles the experimental image, the structure is refined, and the process repeated. Like direct methods, many flavors of image simulation have been developed. The type employed in the analyses in the following chapters is the multislice approach.

Multislice describes the interaction of three components:

- ψ: The electron wave;
- P: The propagator of the electron wave in space;
- Q: A thin slice of the specimen projected onto a plane (phase grating).

The crystal is divided into N thin slices through which the electron wave propagates sequentially, where slice thickness $\times N$ is the specimen thickness. The multislice algorithm is described by the following general formula (Cowley and Moodie 1957):

$$\psi_{n+1} = [\psi_n \cdot Q_n] \otimes P_{n \to n+1}. \tag{1.16}$$

The symbol $\otimes$ is the convolution operator. In a multislice routine, the incident beam is scattered by the phase grating (also called the transmission function, $e^{ik\phi}$) and the intensities of the diffracted beams are tracked. The potential within a slice n is iteratively projected using the propagator onto the next slice $n + 1$ and the process is repeated until N total slices have been processed. The exit wavefunction is then collected and either used to form a diffraction pattern in reciprocal space or is convolved with the microscope function (contrast transfer function, any apertures, and environmental effects) to form a simulated image.

Multislice simulations are employed in some structure refinement procedures such as NUMIS and MSLS (Jansen et al. 1998). The starting structure determined by direct methods is used to calculate simulated patterns that are compared to the experimental intensities. A FOM is used to evaluate the goodness of fit, usually given as some error metric such as χ^2 or an R-factor as follows:

$$R_1 = \frac{\sum_{\mathbf{g}} \left| F_g^{exp} - F_g^{calc} \right|}{\sum_{\mathbf{g}} \left| F_g^{exp} \right|}; \tag{1.17}$$

$$R_2 = \frac{\sum_{\mathbf{g}} \left| I_g^{exp} - I_g^{calc} \right|}{\sum_{\mathbf{g}} \left| I_g^{exp} \right|}. \tag{1.18}$$

During refinement, atom positions are relaxed iteratively and the simulation is repeated to minimize the error metric. The minimum R_1 is usually greater than 20% for electron diffraction data whereas it is usually less than 5-10% for X-ray data (compared to kinematical simulation), and sometimes less than 1% for some inorganics (e.g., Khattak et al. (1975); Newsam (1988); Yu et al. (1995)). The R_2 metric is typically larger than R_1 and can in some cases better describe how well structure factor ratios are preserved within the data set.

Here it is relevant to mention the effect of specimen thickness variation on electron diffraction data. In image-based structure solution techniques, it is likely that the simulated image will match some band of the experimental image if the simulated thickness is within the range of experimental thickness. While diffraction has much better signal-to-noise than HREM, the experimental data does not often match simulation closely regardless of whether average experimental thickness is consistent with simulated thickness. This is because thickness and orientation variation affects all of the beams in the pattern; therefore one cannot readily differentiate the contributions to intensity from different thicknesses.

1.3.2. Dynamical Direct Methods

Simulation always requires an initial model. It is the role of direct methods to provide this. However, dynamical effects will affect the reliability of direct methods, especially for bulk structures, hence *a priori* knowledge about how dynamical data affects direct methods solutions is needed for proper interpretation of direct methods results. The structure map that is restored for moderately thin specimens ($<$ 20 nm) closely resembles the modulus of the Babinet $|1 - \psi(\mathbf{r})|$, where $\psi(\mathbf{r})$ is the complex exit wave (Sinkler et al. 1998a). Electron diffraction data can be expected to give structure maps with atom-like features for specimens up to moderate thickness, however they will be distorted with increasing thickness. It is therefore necessary to be conservative with their interpretation (Marks et al. 1998):

(1) Not all peaks will be in correct places, and often will be off by more than 10 pm;
(2) Charge density will not be correct;
(3) There may be too few or too many peaks.

Here, it is important to mention a special dynamical case of scattering dominated by a single atom type (Sinkler and Marks 1999a; Marks and Sinkler 2003). In the case of structures that project well, a channeling model is applicable that describes the shape of periodic oscillation of the electron wave-function as it propagates down individual atomic columns. Mathematically, the shape of each atom in projection can be described by some two-dimensional complex function $a(\mathbf{r})$. By convolution, this yields the reciprocal space function,

$$\Psi(\mathbf{k}) = A(\mathbf{k}) \sum_i e^{2\pi i \mathbf{k}.r_i}, \tag{1.19}$$

where i represents the set of atom positions in projection and $A(\mathbf{k})$ is the complex atom shape function in reciprocal space. Hence,

$$I(\mathbf{k}) = |A(\mathbf{k})|^2 \left| \sum_l e^{2\pi i \mathbf{k}.r_i} \right|^2 \tag{1.20}$$

The amplitude term $A(\mathbf{k})$ can be replaced by any real function $B(\mathbf{k})$ that generates a real feature in the object plane. For example, one could use a function $B(\mathbf{k}) = S(\mathbf{k})|A(\mathbf{k})|$, where $S(\mathbf{k}) = \pm 1$. In this case, we have an effective atom in real space described by the real symmetric function $b(\mathbf{r})$. The important point is that there need not be a direct relationship between the true complex wavefunction and the recovered pseudoatom; the features simply have to be similar (e.g., satisfying an atomicity constraint). This is the origin of the correspondence between the modulus of the Babinet and direct methods solutions: there needs not be a direct correlation between the two. In the special case where channeling conditions give rise to atom features of the same type (excluding other types), such as for the thickness range of 5-20 nm in GITO crystals, all positions of that type will be recovered by Direct Methods (Sinkler et al. 1998b).

It is clear that kinematical diffraction is a poor model for absolute electron diffraction intensities, yet, as seen above and in other cases, classical direct methods applied to manifestly dynamical data often works, although results are hard to predict (Sinkler et al. 1998a; Weirich 2004; Nicolopoulos et al. 1995; Dorset et al. 1997). For example, a light atom column may be recovered while a column of heavy atoms may be missing from the solutions. This is rather counterintuitive, however, the link between the two can be found by examining the statistics of dynamical scattering within the 1s channeling model (Hu et al. 2000; Chukhovskii et al. 2001). The important points are given below:

(1) Phases of $+\mathbf{g}$ and $-\mathbf{g}$ reflections obey, statistically, the relationship

$$\phi_{\mathbf{g}} + \phi_{-\mathbf{g}} \approx 2n\pi + \alpha, \tag{1.21}$$

where α is a phase deviation constant. It is dependent upon the type of atoms present and the thickness, and not upon $\mathbf{g}$. When relationship 1.21 holds, the data represents an effective kinematical approximation to the true structure. This behavior is shown in figure 1.7(a)-(b) for thin crystals of $C_{32}Cl_{16}CuN_8$, reproduced from Hu et al. (2000).

(2) The triplet sum phases obey a similar relationship:

$$\phi_{-\mathbf{g}} + \phi_{-\mathbf{g}} + \phi_{\mathbf{g}-\mathbf{h}} \approx 2n\pi + \beta, \tag{1.22}$$

where β is a deviation constant similar to α, also dependent upon the cell contents and specimen thickness. Figure 1.7(c)-(d) demonstrates this relationship, reproduced from Chukhovskii et al. (2001).

(3) Friedel's law — that intensity of symmetry equivalents must be equal — is not stricly obeyed in dynamical scattering, however, it is obeyed statistically (figure 1.8).

The key result is that the structure must project well and the thickness must be sufficiently small for direct methods to work on dynamical data. In the case of psuedo-kinematical dynamical data, α in the Friedel pair relationship and β within the triplet sum is close to zero, approximating the kinematical statistics. On the other hand, in dynamical direct methods, α and β can span any value between 0 and $2n\pi$. A caveat is that multiple atom features may cause the value of β to lose statistical significance, e.g., the statistics begin to break down when many types of atom features are present (poor projection) or when thickness is too large for direct methods to recover from the intensities phases that follow equation 1.22.

While dynamical direct methods has been seen to be quite effective in model systems, in addition to small thickness usually some prior knowledge of the unit cell is required to predict favorable conditions (such as emphasis of like atom types due to channeling). Because *ab initio* direct methods on TED data sets generally break down severely with increasing crystal thickness, it is difficult when working with

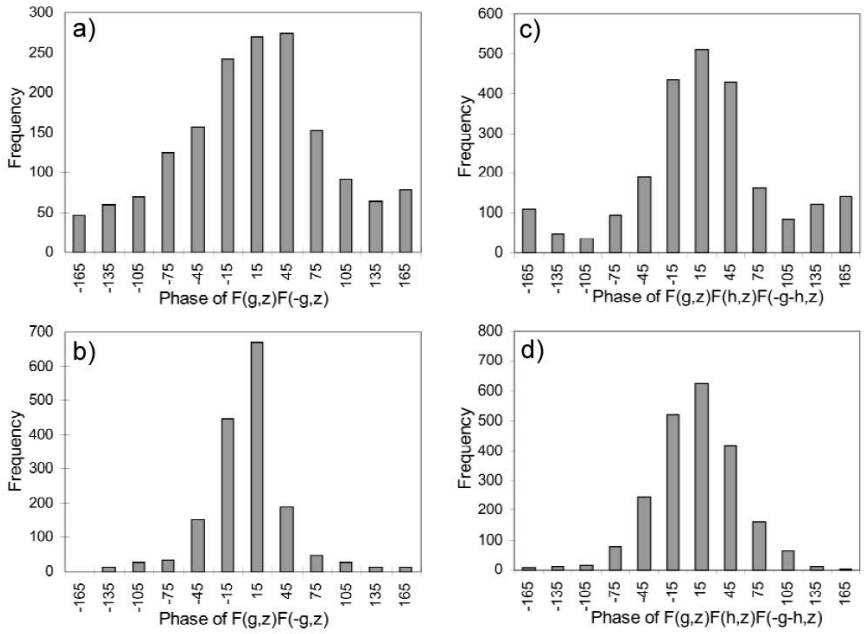

Figure 1.7. Probability histogram of the product $F_{\mathbf{g}}F_{-\mathbf{g}}$ for (a) centrosymmetric and (b) noncentrosymmetric (random) models of $C_{32}Cl_{16}CuN_8$ crystal. (c) and (d) are similar centrosymmetric and noncentrosymmetric histograms for the triple product $F_{\mathbf{g}}F_{\mathbf{h}}F_{-\mathbf{g}-\mathbf{h}}$ for the same crystal. All structure factors calculated by multislice, t = 5.264 nm. Taken from Hu et al. (2000) and Chukhovskii et al. (2001).

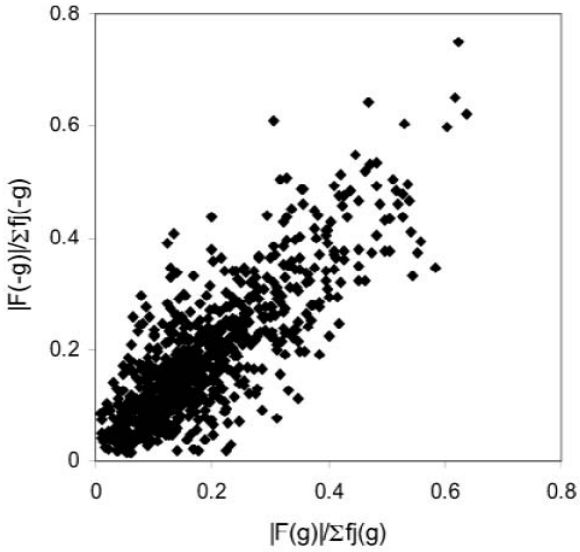

Figure 1.8. Normalized dynamical moduli of $F_{\mathbf{g}}$ plotted against $F_{-\mathbf{g}}$ for the noncentrosymmetric structure in figure 1.7(b) and (d). Friedel's law is obeyed statistically for this thickness (5.264nm).

novel systems to avoid pitfalls where not all atoms are simultaneously expressed, or where atom positions deviate too much to be usable as starting positions. For this reason, direct electron crystallography of novel complex bulk structures using conventional ED is still relatively impractical unless extremely thin and flat specimens are available. In spite of this, a small number of cases exist where data quality can be improved through clever means, of which PED is one form.

1.4. Approaches for Pseudo-Kinematical Electron Diffraction

As seen in section 1.2, if intensities are kinematical the structure factor phases are recoverable and the true structure easily retrieved. The method has been shown to be robust: intensities can vary by 10% or 20% in many situations and the phasing algorithm can still recover enough accurate phases to reconstruct the true structure or something very close. Apart from very simple structures such as silicon or magnesium oxide that are trivially solved by direct methods, there are a number of cases where electron diffraction data can yield starting structures suitable for refinement (Marks and Sinkler 2003). The most obvious case is that of thin specimens, however thickness must generally be on the order of 5-10 nm, or even less if the specimen contains heavy elements. This is difficult to achieve practically for many materials, and is also difficult for crushed (powder) specimens unless a definite cleavage plane for the zone of interest is present.

The logical extension of thin specimens is the case of surfaces, for which the Marks research group has considerable expertise. Special measures must be taken during the experiment, because a) substrate bulk spots are much stronger than surface spots and b) bulk spots necessarily overlap some surface spots in epitaxial superstructures and usually overlap for surface reconstructions, meaning in either case there

are holes in the intensity data. The latter is addressed by an intensity prediction algorithm: rather than forcing unknown intensities to zero, therefore applying an incorrect constraint, an approach is taken that maximizes the entropy of the intensity summed over the real space map, in essence interpolating unknown reflections (Marks et al. 1998). Taking advantage of highly elongated reciprocal lattice rods arising from the Fourier transform along the surface normal, the measurement of surface reflections is made by tilting the substrate off the zone axis to damp multiple scattering by the bulk and to increase signal of surface reflections. The intensities measured by this technique are very close to kinematical and it is fairly straightforward to recover a good structure map.

A different class of approaches *assumes* deviation from kinematical. Instead of seeking kinematical data, it exploits the fact that the statistical relationships contained within the data set that code for phases (e.g., equation 1.6) may be preserved as long as relationships between the intensity values are preserved (Marks and Sinkler 2003). This is called intensity mapping and requires that dynamical intensity relationships be consistent with kinematical:

$$I_{\mathbf{g}} > I_{\mathbf{h}} \quad iff \quad |F_{\mathbf{g}}| > |F_{\mathbf{h}}|. \tag{1.23}$$

This interpretation is applicable to texture and powder patterns which provide an intensity averaging effect. The scattering from powder specimens has been described by Blackman (1939):

$$\frac{I_{\mathbf{g}}^{dyn}}{I_{\mathbf{g}}^{kin}} = \frac{1}{A_{\mathbf{g}}} \int_0^{A_{\mathbf{g}}} J_0(2x)dx, \tag{1.24}$$

where $A_{\mathbf{g}}$ is an integration limit proportional to kinematical structure factor $F_{\mathbf{g}}$ and crystal thickness t. The ratio of any two reflections within a powder data set is thus given by:

$$\frac{I_{\mathbf{g}}^{dyn}}{I_{\mathbf{h}}^{dyn}} = \frac{I_{\mathbf{g}}^{kin} F_{\mathbf{h}} \int_0^{A_{\mathbf{g}}} J_0(2x)dx}{I_{\mathbf{h}}^{kin} F_{\mathbf{g}} \int_0^{A_{\mathbf{h}}} J_0(2x)dx}. \tag{1.25}$$

The limits of equation 1.25 have interesting consequences. In the case of small A_g and A_h, the thickness and/or structure factor are small. The integral scales directly with A_g for small A, and equation 1.25 reduces to:

$$\frac{I_{\mathbf{g}}^{dyn}}{I_{\mathbf{h}}^{dyn}} = \frac{I_{\mathbf{g}}^{kin}}{I_{\mathbf{h}}^{kin}}. \tag{1.26}$$

In the alternate case where A's are large, both integrals go to $1/2$, and

$$\frac{I_{\mathbf{g}}^{dyn}}{I_{\mathbf{h}}^{dyn}} = \frac{F_{\mathbf{g}}^{kin}}{F_{\mathbf{h}}^{kin}}. \tag{1.27}$$

In the worst case corresponding to the first two zeros of the Bessel function where $A_g \approx 1.2$ and $A_h \approx 2.75$ (see figure 1.9),

$$\frac{I_{\mathbf{g}}^{dyn}}{I_{\mathbf{h}}^{dyn}} \approx 0.454 \frac{F_{\mathbf{g}}}{F_{\mathbf{h}}} \approx 1. \tag{1.28}$$

The order is still preserved, consistent with equation 1.23, implying that the statistical relationships generated by this ordering will also be preserved. This has been supported in experimental work by Vainshtein and also by Dorset (Vainshtein 1964; Vainshtein et al. 1992; Dorset 1995). The Blackman formula will be revisited in significant detail in chapter 4.

1.4.1. The Precession Technique

Intensities in lamellar texture patterns and powder patterns demonstrate a clear relationship with structure factor as seen in equation 1.24, and the role of thickness has been characterized relatively simply. These intensities represent a statistical integration of off-axis conditions where dynamical coupling between many beams is minimized. In the case of texture patterns, a limited window of off-axis conditions is sampled whereas for powder patterns, all off-axis conditions are sampled. In large-angle convergent beam electron diffraction (CBED) studies, the same effect has been noted for high order Laue zone (HOLZ) reflections (Vincent et al. 1984; Vincent and Bird 1986). In the condition that the convergence

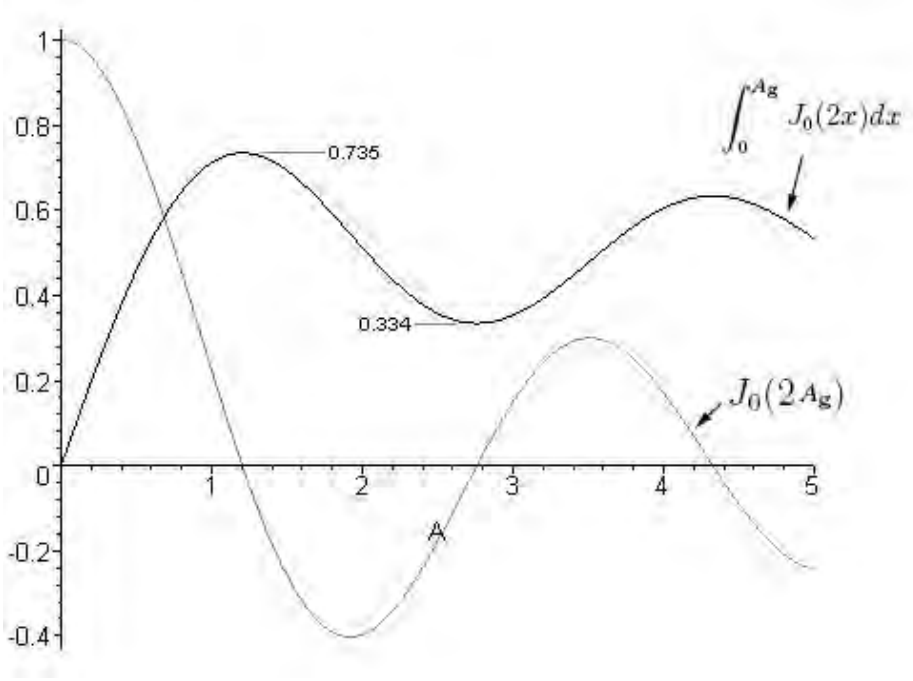

Figure 1.9. Plot of the $J_0(2A)$ and its integral. Values for the first local maximum and minimum are indicated.

angle is increased to the radius of the first order Laue zone (FOLZ), the high order reflections become filled with bright excess lines that map the Bragg condition for those reflections. The intensities of the lines were found to be two-beam in character and became kinematic in small crystals, fitting the Blackman description (equation 1.24).

Integration of k-line segments is difficult from a measurement standpoint. The precession electron diffraction (PED) mode stemmed from this work, devised as a method to facilitate easier measurement of the HOLZ reflections (Vincent and Midgley 1994). The unforeseen advantage, however, was that not only did precession integrate HOLZ reflections, the rest of the zone axis pattern became available for measurement with similar expected improvements in data quality. Because it was devised with both data quality and measurement simplicity in mind, it is especially promising as a method for obtaining psuedo-kinematical datasets.

In the experimental configuration for electron beam precession, the incident illumination (can be convergent or parallel) is tilted off zone to large angle ϕ — typically 25-50 mrad corresponding to a reciprocal resolution on the order of an inverse Ångstrøm at 200 kV — and precessed in a serial manner about the optic axis forming an effective hollow cone of illumination upon the specimen (figure 1.10). The diffracted intensities, which constitute an off-zone diffraction experiment for each individual tilt, are de-scanned in a complementary manner to the tilt scan signal restoring the spots to their default zone axis pattern locations. This results in an effective integration of all tilts within the hollow illumination cone, i.e., around the edge of the cone. The PED pattern is thus an interpretable ZAP containing integrated intensities from off-zone conditions that are by nature less dynamical because fewer beams are simultaneously excited: strongly excited beams have little opportunity to exchange intensity with others (except for the transmitted).

This geometry yields several very interesting features:

- The pattern may be indexed as a conventional diffraction pattern while the intensities have actually been gathered from off-zone reflection conditions.
- Inelastic dynamical effects such as Kikuchi lines and intensity variations in CBED spots are reduced by averaging over incident beam directions.
- Since the beam is entering the sample from an off-axis direction, much of the dynamical scattering that is particularly strong at the exact Bragg condition (or zone axis channeling condition) is avoided.
- Many more FOLZ reflections are excited, under more kinematical conditions, by the Ewald sphere allowing the acquisition of an increased number of intensities for use in structure solution techniques.
- More HOLZ reflections are illuminated, yielding expanded 3-dimensional data sets provided that spots from separate Laue zones do not overlap.

Figures 1.11(a)-(b) demonstrate these characteristics in the diffraction pattern from a thick magnesium orthovanadate ($Mg_3V_2O_8$) crystal. The precession pattern was captured in selected area precession mode on the Hitachi UHV H-9000 modified for precession (Appendix B). A very moderate precession angle ($\approx$ 5 mrad) was used to form the pattern in 1.11(b). The extension by precession of the HOLZ

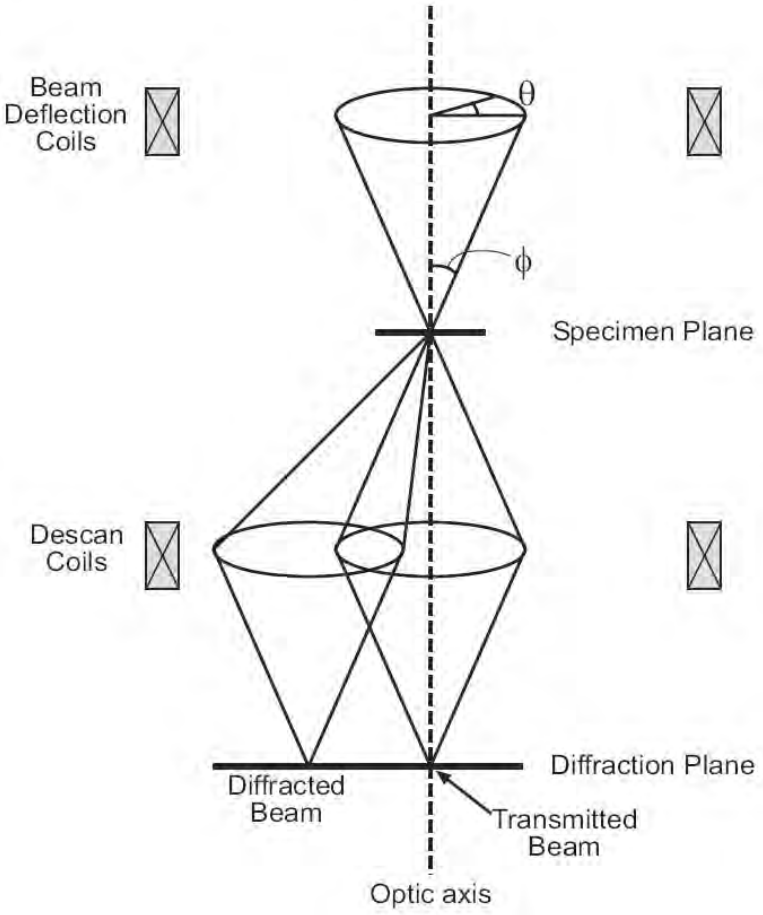

Figure 1.10. The schematic diagram of precession electron diffraction (PED). The beam is tilted off zone by angle ϕ using the beam tilt coils and serially precessed through an angle $\theta = 2\pi$. A complementary de-tilt is provided below the specimen by de-scan coils to restore the zone axis pattern.

ring into an annulus of width $\approx$ 10 mrad is clearly seen, as well as blending of inelastic dynamical effects into a radially diffuse background. This dynamical background suppression can improve intensity measurements by considerably simplifying the problem of background subtraction.

The improved quality of the precession data over that of conventional ED has been demonstrated experimentally (Vincent and Midgley 1994; Own et al. 2004), and a small number of structures have been solved via the technique, some *a priori* (Gjønnes et al. 1998a; Gemmi et al. 2003; Own and Marks 2005b), and others by a combination of simulation and/or correction using forward calculations (Vincent and Midgley 1994; Gjønnes et al. 1998b). Additionally, precession has been used to derive Debye-Waller temperature factors from monatomic specimens using Wilson plots with good accuracy (Midgley et al. 1998). Some of the capabilities demonstrated by the technique are listed below:

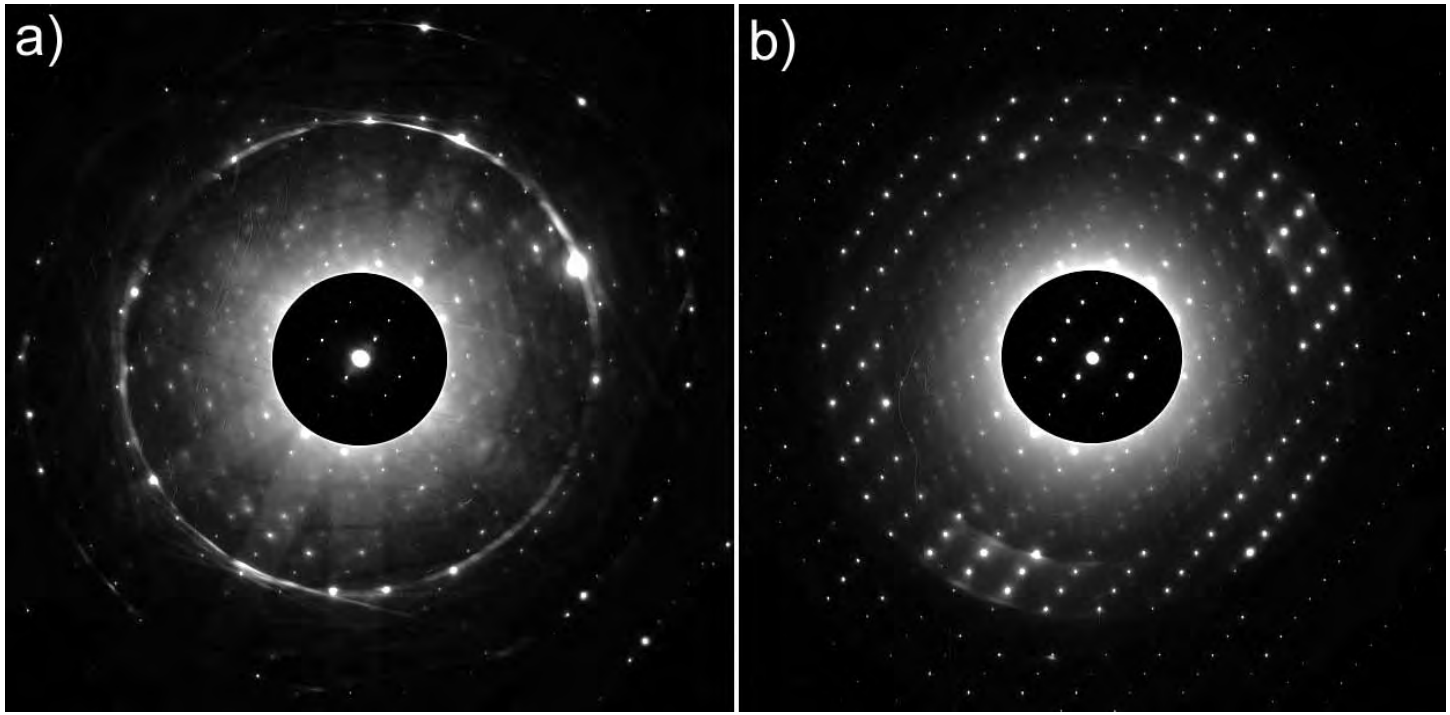

Figure 1.11. (a) Selected area DP of the [532] zone axis of magnesium orthovanadate ($Mg_3V_2O_8$). (b) Precessed SADP of the same orthovanadate using a moderate precession angle of 5.2 mrad to illustrate the effects. Several HOLZ annuli are apparent and non-systematic effects in the ZOLZ are averaged into a radially diminishing background. Note: Images (a) and (b) have identical exposure times, digitizing conditions, and have received the same digital image processing, so they can be directly compared.

(1) Pseudo-kinematical intensities are available under some experimental conditions as will be seen below;
(2) 3-dimensional datasets can be acquired under appropriate conditions from a single zone axis pattern. Low electron energy or large cell dimension in the optic axis are necessary, and Laue zone overlap must be avoided (see section 2.1);
(3) Decreased intensity oscillation with thickness is observed (also occurs with thickness averaging);
(4) Greater tolerance to orientational errors, and specimens do not have to be perfectly on-zone to obtain symmetric patterns;
(5) Consistency of intensity values among different projections allows more accurate merging of multiple 2D projections into 3D datasets;
(6) Enhancement of fine detail in the solution of a large structure over that of conventional TED (Gemmi et al. 2003);
(7) If some structure factors are known, precession can be used to gain crystal thickness information with reasonable accuracy (within 10-15 nm).

1.4.2. Past Studies using PED

While promising, *a priori* structure determination of unknown or partially-known phases using PED has met with varied success, primarily because a rigorous understanding of errors has not been established. The technique was originally devised to complement CBED techniques, augmenting known structure factors measured through other means. From the standpoint of being a standalone technique, it is understood that precession data are distorted by dynamical effects necessitating careful treatment of data (Own et al. 2004), however the approaches toward data treatment have not been fully consistent in structure studies thus far. It has been suggested that thin specimens are preferred in order to circumvent the dynamical effects, though it was not known how thin. Nevertheless, to be a robust technique precession must be able to reliably handle unknown specimens exhibiting a variety of scattering strengths and physical geometries.

A correction factor has been presented in the literature in various forms to treat the nonlinearities at larger crystal thickness (Gjønnes 1997). It comprises two parts, a geometry part that corrects for integration geometry effects (Lorentz portion), and a two-beam part that corrects for thickness-dependent dynamical effects (Blackman portion). Starting from the Lorentz-modified Blackman formula

$$I_g^{exp} \propto \frac{A_{\mathbf{g}}}{\left(1-\left(\frac{\mathbf{g}}{2R_0}\right)\right)} \int_0^{A_{\mathbf{g}}} J_0(x)dx, \tag{1.29}$$

where R_0 is the radius of the zeroth order Laue zone (ZOLZ), the approximate kinematical intensity can be derived from the experimental intensity I_g^{exp} using the correction term:

$$I_g^{kin} \propto I_g^{corr} = \left(\left(1 - \left(\frac{\mathbf{g}}{2R_0} \right) \right) \frac{A_{\mathbf{g}}}{\int_0^{A_{\mathbf{g}}} J_0(x)dx} \right) I_g^{exp}, \tag{1.30}$$

applicable for convergent beam PED. The original form (Vincent and Midgley (1994), not shown) was refined to improve the Lorentz portion, and a new form was also derived to augment the convergent illumination version with a parallel illumination form (Gjønnes 1997). A detailed analysis of correction factors and their validity will be given in chapter 4. Note that the argument of the integrand in equations 1.29 and 1.30 is different from the Blackman formula integrand (equation 1.24). The value of $A_{\mathbf{g}}$ used — critical for calculating accurate correction factors — is not clearly defined in the literature. This discrepancy will also be addressed in chapter 4.

The correction factor refined by Gjønnes for parallel illumination was used in an *a priori* investigation of Ti_2P. The structure was investigated by combining several 2D projections into a 3D dataset and inverting using SIR97 DM software (Gemmi et al. 2003). The assumption was made that intensities were proportional to structure factor in the limit of large thickness, hence intensities were corrected only for precession geometry (not two-beam effects) before merging the projections, and corrected intensities were used with direct methods rather than amplitudes. The three precession datasets were found to merge much better than selected area electron diffraction (SAED) projections ($R_{1,2}$ = 13% and $R_{1,3}$ = 22%; subscripts denote the experimental datasets being compared), facilitated in part because severe streaking effects arising due to disorder were eliminated in the precession data. The precession solution had a higher final R-value (36%) than the solution from SAED (27.3%), however the structure maps from precession localized additional peaks that were suppressed in SAED, helping to explain why the superstructure arises.

The refined correction in equation 1.30 was also used in an elaborate *a priori* investigation of a thick crystal (Al_mFe, with nominal thickness 150 nm) that involved correction of dynamical intensities starting from a small accurate set of starting structure factors (Gjønnes et al. 1998b; Cheng et al. 1996). Careful CBED measurements and simulation were required to extract a starting set of (h00) and (hk0) systematic rows. The thickness of the crystal was evaluated by comparing experimental precession intensities to simulated precession intensities generated using equation 1.29. The specimen was reported to be very thick, at about 150nm.

The raw data was then scaled by the Lorentz-corrected two-beam intensity relationships (equations 1.25 and 1.29) using the known structure factors to acquire new 'effective' structure factors (U_g^{eff}). The two-beam portion of the corrections were simplified based upon the assumption that thickness averaging damps intensity oscillations for large A_g, resulting in an average value centered around the integral (see figure 1.9). This allowed a closed-form calculation using an exponentially-damped sinc function instead of requiring integration of the Bessel function J_0. These effective structure factors represent less accurate but nevertheless quasi-kinematic amplitudes that augment the known (h00) and (hk0) structure factors, completing the dataset.

Phase extension using triplets starting from the high confidence reflections ((h00) and (hh0) rows) revealed inconsistencies in signs for some strong reflections, and Bethe potentials (Bethe 1928) were used to correct for 3-beam interaction effects of 330, 530, and 860 beams that defined phases for many beams in the dataset. This resulted in four structure possibilities that were analyzed individually using dynamical n-beam Bloch wave calculations based upon Bethe-corrected structure factors respective to each possible set. The best match showed a moderately successful correlation of intensities with the uncorrected experimental amplitudes ($R_1 \approx 32\%$), and R_2 was slightly higher at about 38%.

Solution was possible because accurate structure factors were available for strong beams, allowing separate treatment of errant beams in an n-beam refinement (to first order) beyond the expected two-beam case. Bloch wave simulation was required to distinguish which of the corrected structure factors were satisfactory, and confirmed that precession intensities are still subject to strong dynamical multi-beam coupling, at least for very thick specimens. While this study shows promise that structure solution with thick specimens is possible using precession, the fundamental problem is that considerable information must already be known about the structure in order to solve it. The above study represents a classic example of a bootstrap approach to structure solution via electron diffraction, which is both time and resource-consuming — not practically rapid or accurate enough to be competitive with X-ray methods on a wider scale.

A parallel effort on the same material system was undertaken by J. Gjønnes et al. (1998a) using precession intensities corrected only with the Lorentz factor (no two-beam correction). A merged data set was created from eight projections, and intensities with known phases from energy-filtered CBED measurements (Cheng et al. 1996) were added to augment it. Linear scaling of intensities during the merge yielded excessive error, therefore a non-linear least-squares procedure was used. The errors were still quite large, with a standard error of 36% for 13 reflections common to four datasets, therefore the data merge was noted by the authors as the most uncertain step in the study. Multiple 3D codes were used to phase the dataset — a simple Fourier synthesis, MICE, and QTAN — and a chemically reasonable structure model was obtained. Refinement using SHELXL97 showed a poor fit with the corrected experimental intensities (R_1 = 42%), however the shifts to the refined positions were not large ($<$ 25 pm). Large deviations from experimental structure factors were found in the refinement of the $hk0$ reflections, indicating that non-systematic dynamical scattering was indeed present.

Comparing this study to K. Gjønnes et al. (1998b), both studies found similar structure results for the [001] projection. The $hk0$ structure factors with full correction (two-beam and Lorentz) matched the high-confidence CBED structure factors more closely than the structure factors with only Lorentz correction. Seeing as the merged dataset quality was somewhat uncertain, the authors attributed much of the success of the latter study (the 3D study) to the forgiving nature of statistical direct methods. The specimen was estimated to be very thick ($\approx$ 100 nm), and dynamical effects were considered to be the major source of error in the study. It will be seen in chapter 3 that in addition to specimen thickness (and variability), precession cone semi-angle ϕ is a key variable in the reduction of dynamical effects in the data. Unfortunately, neither study reported this experimental parameter in detail (Berg et al. (1998) reported ϕ in the range of 16-43 mrad); it is likely that thickness variability combined with inconsistent precession angle were the source of the inconsistency between projections.

The essential requirement for PED is that its intensities must demonstrate systematic behavior following equation 1.23. Some indication of the errors being systematic and slowly varying has been implied in literature results; for example, Gjønnes et al. (1998b) implies insensitivity of the correction factor to thickness variation, and the present theory indicates that the results should be pseudo-kinematical owing to the many similarities with powder and texture intensities. These postulates require validation. The next chapter concerns development and implementation of a new generation of high performance precession system on which to conduct precession studies, and in the following chapters PED is investigated in detail with the goal of discovering systematic behaviors within measured intensities. It will be seen that the behaviors indeed satisfy the intensity mapping constraint in several cases and are predictable.

CHAPTER 2

Precession Instrumentation

Precession is a tool designed to improve the quality of diffraction data from the TEM. Consequently, developing effective instrumentation and protocols is critical to the quality and reliability of results. In this chapter, the requirements and underlying principles for obtaining high-quality precession patterns are described. The principles and methods described in this chapter are embodied in the real-world implementations presented in appendices B and C; appendix D presents a third-generation precession instrument that is currently being constructed. Appendix A contains background information for understanding the implementation details for readers who are unfamiliar with electronics. Finally, appendix E contains general procedures for aligning the family of precession systems presented here to obtain high-quality precession patterns. The contents of this chapter and some of the referenced appendices are reproduced from Own et al. (2005a) and Own and Marks (2005a). Details are also contained within US patent application number 60/531,641, filed December 2004 (Own and Marks 2004).

Considerable testing and validation is necessary before a new technique can become widely accepted. An obstacle to this is the inherent scarcity of equipment in the field on which to test and understand experimental parameters, and development of a common language to describe them. At the start of this work in 2000, there were two known precession instruments based upon the Philips EM430 and Philips CM30/T microscopes (Vincent and Midgley 1994; Gemmi 2001). The early precession studies using these instruments have described experiments and compared precession to conventional methods (refer to section 1.4.1), but only cursory information has been given about implementation of the precession devices used. Additionally, these investigations have not described experiment parameters in detail. It is now apparent that experiment geometry is critical to the behavior of the resulting dataset (Own and Marks 2005b; Own et al. 2005b), thus a comprehensive set of variables including cone semiangle, convergence, probe size, and specimen image stability should necessarily accompany such studies.

It is convenient to first define some general language for precession. Tilt before the specimen is referred to as BT (beam tilt) and the synchronous de-tilt below the specimen is called DS (de-scan). In this chapter, precession electron diffraction patterns will be referred to as "precessed DP's" while conventional selected-area or focused-probe diffraction patterns will simply be called "DP's".

2.1. Precession Geometry

Precession electron diffraction is in principle equivalent to the X-ray Buerger precession camera. However, instead of precessing the crystal and detector, the beam itself is precessed. The geometry is straightforwardly demonstrated using schematic pictures. Figure 1.10 from chapter 1 describes the

principle most simply: the incident beam is tilted before the specimen and the diffracted beams are synchronously de-tilted after the specimen and measured at the diffraction plane. To understand the experiment parameters, it is necessary to examine this process in detail in reciprocal space.

In the kinematical description, the electron probe, which has wavelength λ much smaller than the atomic spacings, is similarly represented in reciprocal space by the wavevector $\mathbf{k}_0$, where $|\mathbf{k}_0| = 1/\lambda$. The electron probe interacts with the crystal and is scattered by the periodic atoms within the structure with amplitude $\phi_{\mathbf{g}}$, given by

$$\phi_{\mathbf{g}} = \sum_{n=1}^{N} F_n e^{-2\pi i \mathbf{k}.\mathbf{r}_n}, \tag{2.1}$$

where F_n is the scattering factor from unit cell n and N is the number of unit cells. The scattering from a periodic lattice of atoms in real space therefore gives rise to a reciprocal lattice, representing spatial frequencies within the real structure. In other words, possible excitations (where Bragg's law, equation 1.14, is satisfied) are described by the intersection of a sphere of radius $|\mathbf{k}|$ with the reciprocal lattice. This is the well-known Ewald construction, and the sphere describing possible excitations is called the Ewald sphere. Mathematically, the excited reflection vector is defined as $\mathbf{g} = \mathbf{k}_0 - \mathbf{k}_\mathbf{g} - \mathbf{s}_\mathbf{g}$, where $|\mathbf{k}_0| = |\mathbf{k}_\mathbf{g}|$, and $|\mathbf{k}_\mathbf{g}| \gg |\mathbf{g}|$, and $\mathbf{s}_\mathbf{g}$ is a quantity called *excitation error* which will be defined shortly. For 200 kV electrons, $|\mathbf{k}_0| \approx 40$ Å^{-1}.

In electron diffraction, scattering from the crystal can occur when Bragg's law is not perfectly met. The deviation from the point of perfect intersection signifying the Bragg condition is quantified by the *excitation error*, $\mathbf{s}_\mathbf{g}$. The scattering can be approximated by an integral,

$$\phi_{\mathbf{g}} = \frac{F_g}{V_c} \int_{crystal} e^{-2\pi i \mathbf{k}.\mathbf{r}} d\mathbf{r}, \tag{2.2}$$

where V_c is the volume of the unit cell. This is the Fourier transform of the crystal. In TEM, the crystal is thin in the z direction but large in the x and y directions, so by the Fourier transform relationship, the reciprocal lattice points are finite shapes (the shape function) elongated distinctly in the z-axis (relrods):

$$\phi_{\mathbf{g}} = \frac{F_g}{V_c} \int_0^A \int_0^B \int_0^C e^{-2\pi i \mathbf{k}.\mathbf{r}} dx dy dz, \tag{2.3}$$

where A, B, and C are crystal dimensions in the x, y, and z axes, respectively. Excitation of a relrod can thus occur when the Ewald sphere does not intersect the reciprocal lattice point exactly, and in kinematical theory the intensity scattered into reflection $k_\mathbf{g}$ is directly related to the shape of the relrod that represents $\mathbf{g}$. Following from the Fourier inversion of the top hat function that represents, in the z-axis, the flat crystal bounded on both sides by vacuum, the shape function is the sinc function:

$$|\phi_{\mathbf{g}}| \approx \frac{F_g}{V_c} \frac{\sin \pi A u}{\pi u}, \tag{2.4}$$

where u is the component of $\mathbf{s_g}$ along the z direction. The thicker the specimen, the smaller the oscillation periodicity of the shape function and the more peaked about $u = 0$. The set of all excited reflections projected along the z-axis onto the x-y plane forms the diffraction pattern.

The configuration of the Ewald construction relevant to PED is depicted in figure 2.1. The BT operation in precession is equivalent to rocking the Ewald sphere about a pivot point corresponding to the forward-scattered reflection (origin) of the zeroth-order Laue zone (ZOLZ). For the moment, ignore convergence (α) and consider only the dashed lines in the figure. In the snapshot represented by figure 2.1(a) where $\theta = 2n\pi$ and cone semi-angle is at fixed ϕ, reflection $\mathbf{g}$ — whose intensity is shown schematically on the right as a vertically-oriented sinc function — is excited with a moderate positive excitation error $\mathbf{s_g}$. Reflections near $x = R_0$ exhibit maximum $\mathbf{s_g}$, and reflections at $2R_0$ have $\mathbf{s_g} = 0$. Beyond $2R_0$, $\mathbf{s_g}$ becomes negative and decreases monotonically with increasing spatial frequency. In the x-y plane, the intersection of the Ewald sphere with the ZOLZ describes a circle of illuminated reflections tangent to the origin as shown in figure 2.1(b). The reflections with most positive $\mathbf{s_g}$ are at the center of this circle.

In real-world experiments, the beam usually has a finite convergence angle α, and sometimes PED is operated with a convergent beam mode where α is relatively large. When the convergence angle is non-zero, a segment of the shape function describing reflection $\mathbf{g}$ becomes simultaneously excited, where the sampling range along the z-direction depends upon the convergence angle α as shown by the solid lines in figure 2.1(a). In the limit of parallel illumination, $\alpha \rightarrow 0$. The parallel illumination configuration is used for the systems presented in this thesis.

During precession, the tilted beam precesses about the z-axis tracing out a circuit of $\theta = [0, 2\pi]$. The important point is that, at any given θ along the precession, few reflections are simultaneously excited. Typically only one reflection will be strongly excited and the other excitations along the ZOLZ ring are only weakly coupled because systematic re-diffraction paths are not simultaneously active. In terms of the intensity collected, the sphere intersects each reflection in reciprocal space through a range of excitation errors $\mathbf{s}_g$ and spends very little time during the exposure dwelling in any particular multiply-excited condition where dynamical effects may be prominent.

The intensity is integrated at the detector (conjugate with the diffraction plane) by taking a time-resolved measurement over an integral multiple of the revolution period. In practice, the exposure time is not synchronous to the precession, therefore the precession is run very rapidly ($\approx$ 60 Hz) to ensure complete integration. Figure 2.2 demonstrates the integration process using simulated [010] patterns of a $(Ga,In)_2SnO_4$ crystal of 412 Å thickness (the real space analog of figure 2.2 is figure C.4 in the appendix). Amplitude patterns are used to more clearly portray the Laue circle. Figure 2.2(a) shows eight discrete tilts along the precession circuit described by θ, each tilted by ϕ = 24 mrad. In each snapshot, usually only one reflection is strongly excited. The most prominent dynamical effects are systematic rediffraction paths which are excited only along the Laue circle and tangent to the transmitted beam. A given systematic path is excited only momentarily during the precession twice and is limited in extent — the maximum index of multiply-excited systematic reflections — by the curvature of the Laue circle. The center image is the precessed DP, representing a sum of the amplitudes of 1000 discrete tilts. Figure 2.2(b) is the simulated pattern of the conventional DP for the same thickness. The difference

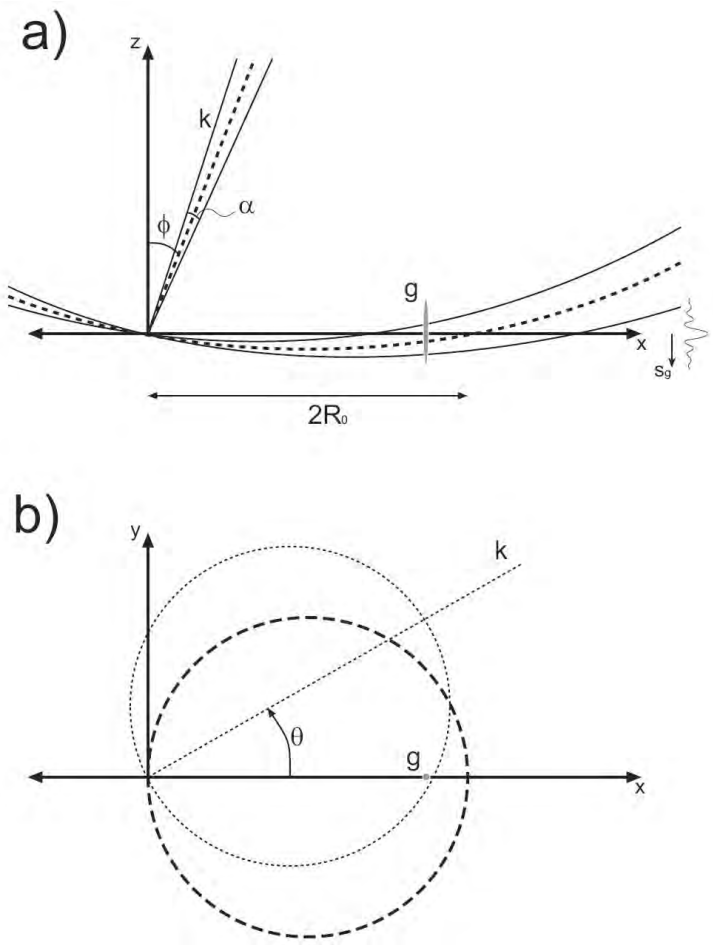

Figure 2.1. Reciprocal space geometry in (a) $x - y$ plane and (b) $x - z$ plane. The beam precesses about the z-axis maintaining constant ϕ. In (b), the ZOLZ (bold dashed circle) precesses about the z-axis.

between the two patterns is readily apparent, and analyses in the next chapter will show the intensities in (a) are much more kinematical than (b).

As pointed out in section 1.4, PED is similar to powder and lamellar texture diffraction, which operate on a similar principle of integration over excitation error by crystal rotation. However, there are some important differences. Powder diffraction integrates the excitation error over all of reciprocal space, and texture patterns integrate excitation error only about a small cone of axes with average axis direction perpendicular to the incident beam. The symmetry is completely lost in powder patterns and is often compromised in texture patterns along one axis, whereas the full symmetry of the ZAP is preserved in PED. Another difference is that the thickness of the crystal is often more controlled in PED than in the polycrystal diffraction methods. This arises because the fine probe in PED illuminates a

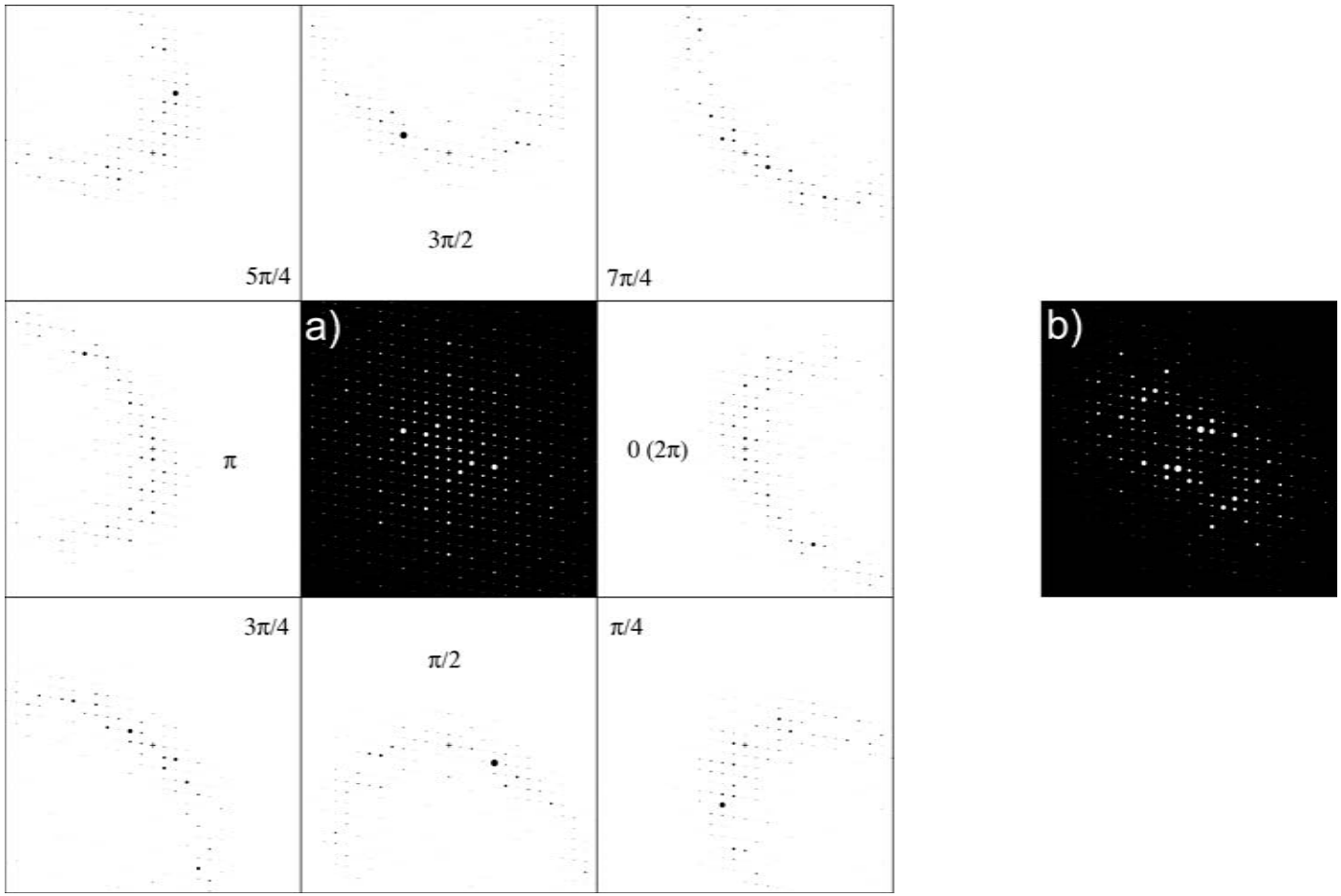

Figure 2.2. Center precession pattern (a) is an integration of the simulated tilt series (contrast inverted) that surrounds it forming an effective cone of illumination. (b) is the non-precessed pattern. $t = 41$nm, $\phi = 24$mrad, patterns represent structure factor amplitudes.

smaller specimen region (reducing the possibility for large thickness variation), and because polycrystal diffraction is subject to crystallite size distribution and morphology within the specimen — experimental variables that are difficult to control.

PED using higher beam tilt angles more closely approximates powder diffraction and, as shall be seen in later chapters, the intensities become more kinematical with increasing ϕ. Electron optical limitations limit the highest angle possible in the instrument, however, the structure itself also affects the maximum targeted semi-angle due to first-order (FOLZ) and zoroth-order Laue zone (ZOLZ) overlap. Figure 2.3(a) demonstrates this limitation: during precession the FOLZ point closest to the precession axis, defined by point F, is revolved to the opposite side of the projection axis during precession (indicated by F'). If F' lies directly above a ZOLZ reflection and has considerable scattering intensity, the zeroth-order reflection intensity will be obfuscated and must be excluded from the dataset. This excludes structures where the HOLZ are easily distinguishable from the ZOLZ, but for unknown structures this analysis applies unequivocally. The usable radius of the diffraction pattern is described by the relationship

$$\gamma = \arccos\left(\frac{k\cos(\phi) - \frac{1}{c}}{k}\right) - \phi, \tag{2.5}$$

where ϕ is the cone semi-angle, c is the projection-axis unit cell dimension or repeat distance along the beam direction, $\mathbf{k}$ is the wavevector, and γ is — by the small-angle approximation — the approximate usable DP radius in radians.

Figure 2.3(b) shows the unit cell dimension c plotted against γ for four different cone semi-angles, showing the rapid decrease in usable DP radius as unit cell dimension increases. For reference, γ = 25 mrad corresponds to $\approx$ 1 Å^{-1} at 200 kV. Increasing ϕ also increases the Laue zone overlap constraint — in the worst case, investigating a large unit cell structure of 25 Å in the projected direction will yield very little trustworthy diffraction information when $\phi > 50$ is used (recall that the number of reflections increases roughly with the square of $|\mathbf{g}|$). While it is desirable to harvest reflections to as high of resolution as possible, the most important spots for Direct Methods are those within an annulus containing key information about interatomic distances (Sinkler et al. 1998b). To generate a good initial starting structure model, Direct Methods should have reflections to roughly 1 Å^{-1}, corresponding to $\gamma \approx$ 25-30 mrad at 200 kV. For this reason, structures or projections for which $c > 15$ Å will be difficult to work with at large ϕ due to FOLZ overlap, while structures with $c < 10$ Å are very amenable. Higher energy is advantageous here because the Ewald sphere is flatter for smaller λ.

PED will be most amenable for certain zones of plate-like structures, where the projection normal to the cleavage plane results in a small repeat distance along the beam direction. The GITO structure is a good example: the projection-axis dimension c = 3.17 Å. According to equation 2.5, GITO yields a usable DP radius (γ) of 100 mrad when ϕ = 24 mrad, and this decreases to about γ = 60 mrad (quite ample) when ϕ = 100 mrad. It should be noted that the ZOLZ reflections can potentially be recovered if a partial scan ($\theta = [0, \pi]$ radians) is used. The logical extension of this is a data mining approach where discrete tilts are acquired independently and the spots integrated in software rather than within

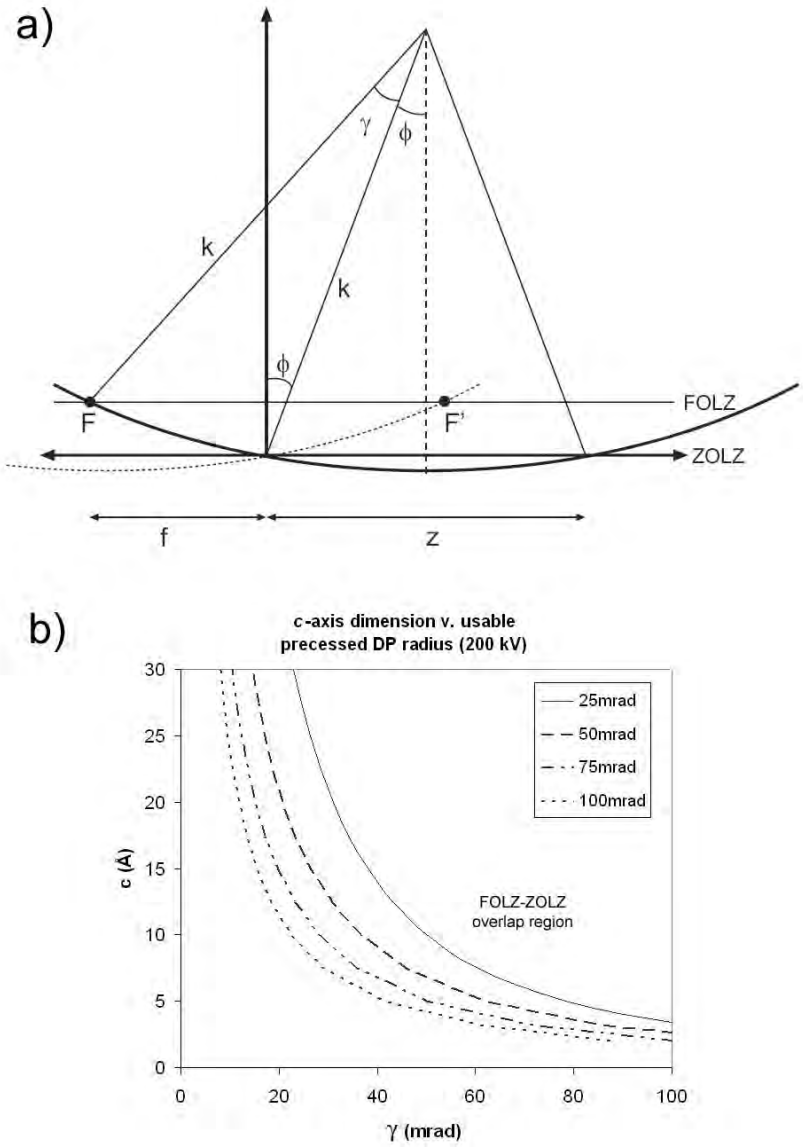

Figure 2.3. a) Precession geometry schematic showing the relationship between ZOLZ and FOLZ excitations. The distance z corresponds to the zero order zone radius; γ corresponds to the usable diffraction radius in mrad. b) Plot of unit cell dimension against usable diffraction radius γ for various cone semi-angles. The lines describe γ, which decreases with ϕ and specimen unit cell thickness.

a single exposure. This approach is rather complex in terms of implementation but very powerful, and some discussion will be reserved in chapter 6 for this topic.

2.2. Retrofit Requirements

Nearly any TEM can be retrofitted for precession diffraction. The electron beam path must be altered at some point in the microscope by a physical deflector system, so a location will always be available at which analog signals from the precession system can be inserted. An exception would be the case of digital power amplifiers, however, it is unlikely that such amplifiers would be used in high current applications like coil drivers due to switching noise. The scheme that will be described in the following sections is therefore applicable to both digitally-controlled microscopes and older analog instruments.

Practically, the microscope must be equipped to acquire both images and diffraction patterns from a specimen. A double-tilt goniometer stage is required, as is mechanical specimen height adjustment. In terms of the optics, the microscope should be able to form a fine probe and spherical aberration should be relatively low to ensure good probe localization. Pre-specimen optics must support a tilt angle of at least 25 mrad. De-scan is best accomplished in immediately-post-specimen deflectors if available, and if not, intermediate lens deflectors with sufficient range are desirable. The least desirable location for de-scan is at the projector deflector since the camera length cannot be changed without losing alignment. Almost all microscopes include the image shift feature, and the image deflectors almost without exception can support large deflection amplitude, so this location would likely be most commonly used for de-scan in older instruments.

An important requirement is a detector with a sufficient dynamic range from which measurements can be acquired. Electron-sensitive film is very common but has a dynamic range of only about 10^2. An exposure scaling system is discussed in appendix F that can be used to obtain intensities with very high dynamic range (4 or 5 orders of magnitude) and good statistical confidence by scaling multiple negatives. Imaging plates are also very effective for quantitation due to very high dynamic range (between 16 and 20 bits, or roughly 10^5) (Zukhlistov et al. 2004).

Recently, charge-coupled devices (CCDs) have been coming to the forefront as the preferred image acquisition tool. The effective dynamic range from CCDs is not particularly large due to shot noise; additionally, they are delicate and expensive, but their convenience hugely outweighs their disadvantages. CCDs typically have 12-14 bit dynamic range, and the low 2-4 bits are obscured by noise — the effective dynamic range is thus $\approx 10^3$ for CCDs. The dynamic range can be increased by broadening the spot profiles slightly (also applicable to the other parallel detection techniques listed above). This can be accomplished by converging the beam or changing diffraction spot focus. This allows longer exposure times by increasing the intensity measurable before pixel saturation. A caveat is that broadening the peaks can cause weak reflections to fall below the noise floor preventing their measurement, so a careful optimization is desired.

The measurement technique that yields the highest dynamic range is the diffractometer method (Bagdik'ianc and Alexeev 1959; Avilov et al. 1999). In this scheme, the diffraction pattern is shifted serially using the image deflectors such that electrons are collected sequentially for each spot into a Faraday cup. The dynamic range is dependent upon how long the intensities are integrated. A drawback is that it is a serial technique, hence the acquisition takes a long time, especially if high dynamic range is needed. Additionally, the Faraday cup aperture is fixed in size, hence care must be taken to avoid quantifying multiple spots simultaneously especially in the case of large cell structures. Often this can

be avoided by increasing camera length, though diffuse background effects cannot be eliminated (in any case, they are reduced by precession).

Ultimately, it may not be possible to install a PED system in many microscopes because of administrative issues. The service warranty is a very important factor: not all manufacturers are supportive of modifications to their instruments so this issue must be handled with care.

To summarize, the key practical requirements for implementation of precession:

- The precessed incident beam must yield a symmetric cone of incident directions about the crystal zone axis;
- The de-scan must bring the diffracted beams together to form uniform points (or non-overlapping discs in the case of beam convergence) for accurate measurement;
- If spatial accuracy is desired in the experiment (e.g., fine-grained polycrystalline specimens), the conical probe fulcrum must intersect the specimen precisely in 3-dimensional space;
- A detector must be able to acquire the integrated intensities at sufficient dynamic range for quantitation;
- The manufacturer must continue to support the microscope with a moderately invasive accessory attached.

2.3. Aberration Analysis

While the precession mode can be readily implemented on a variety of instruments, ultimate performance is limited by the classic problem of objective lens (OL) aberrations. The primary difficulty in implementing electron precession on conventional instruments lies in the objective's inability to accurately focus high angle rays onto a precise region of the specimen, and to release the diffracted beams in trajectories that precisely describe the diffraction vectors with respect to the incident radiation. Aberrations throughout the optical system adversely affect the ray trajectories, resulting in a delocalized hollow cone probe fulcrum at the specimen and poorly converging diffraction points at the diffraction plane.

Figure 2.4 is a cartoon of a modern condenser-objective instrument showing the ray paths traversed by a precessed transmitted beam. It demonstrates in more detail the role of the objective lens in PED. The convergence point at the specimen should ideally be as small as possible to reduce the chance of illuminating a specimen defect and to minimize the variation in sample thickness and orientation. Aberrations are inherent in all cylindrically symmetric round lenses (Scherzer 1936), therefore the ray path of the incident beam will necessarily deviate from ideal as the incident beam precesses azimuthally through the objective lens field. This may cause the probe to wander in the image (specimen) plane during precession. Highest performance is obtained when the alignment is optimized to minimize this wandering effect.

An idea of minimum probe size that can be obtained is available by studying the behavior of convergent probes. In conventional microdiffraction, the diameter d (containing 70% of the intensity) of a filled convergent probe is dominated by the spherical aberration coefficient C_s, and is described by the following relation:

$$d_{70\%} = 0.66\lambda^{3/4}C_s^{1/4}, \tag{2.6}$$

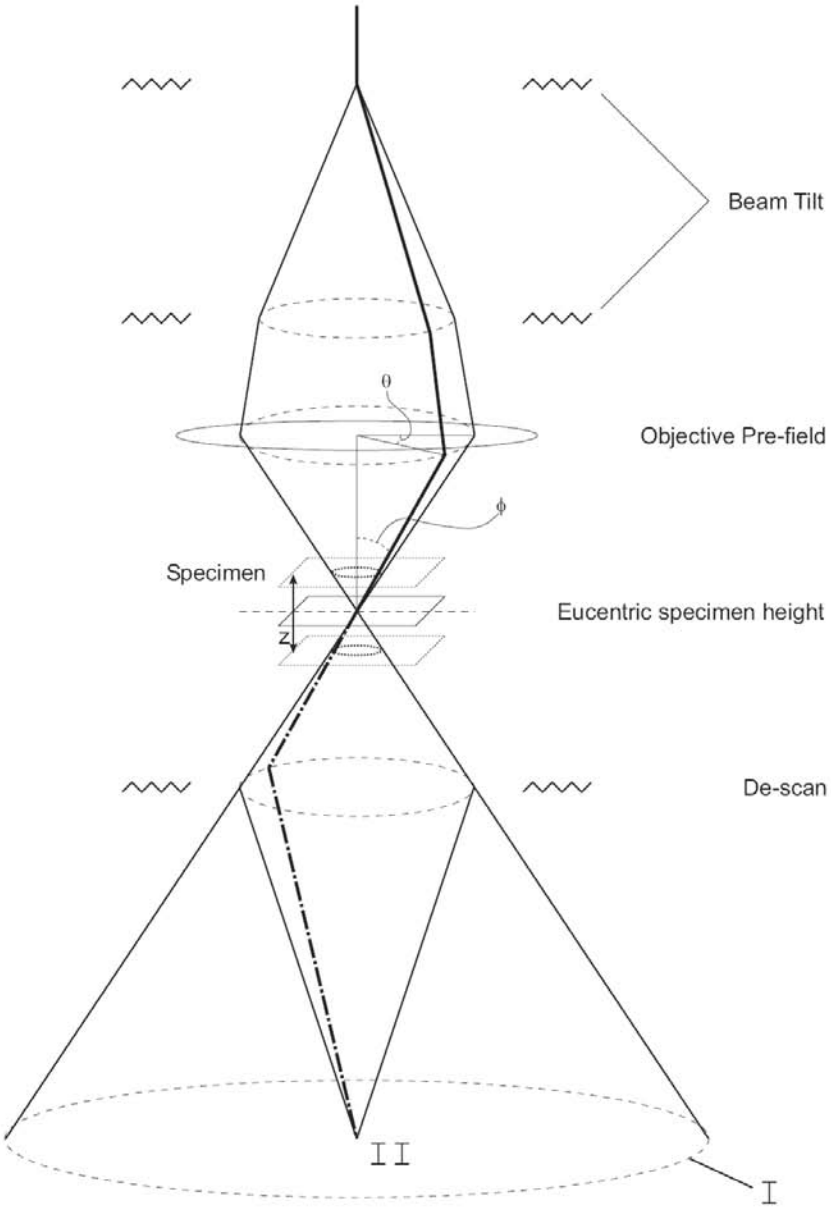

Figure 2.4. Precession geometry in a modern condenser-objective TEM with double deflection coil system showing the path of the precessed transmitted beam. The objective prefield acts as an additional condenser lens. Circle I is generated by the beam tilt scan. De-scan collapses circle I down to point II.

where λ is the electron wavelength (Spence and Zuo 1992). In equation 2.6, the defocus has been optimized to yield the smallest probe. This puts strict constraints upon precession: the smallest probe size is obtained when C_s is minimized and when the defocus term is smaller than the spherical aberration term. Minimum C_s is obtained at a specific known lens excitation (in amperes) that is measured at the factory and is different for every lens. Therefore, to obtain the finest probe, the defocus must be tuned not by the OL excitation, which is fixed, but by the specimen height z (i.e., it must be tuned mechanically). At the start of alignment, the specimen must therefore be at the eucentric height ($\Delta z = 0$) which is usually the expected crossover.[1] The unaligned condition yields a circle only if non-spherical aberration terms are small (as indicated in figure 2.4 and 2.5); ellipses or polygons/stars result if the non-spherical terms are large. Figure 2.5 shows a case where the three-fold aberration is prominent. After alignment, the lobes in the image were brought down to a disc approximately 25 nm in diameter.

Before going into the details of the aberrations, it is relevant to mention field emission electron sources. They have higher brightness than thermionic sources and, additionally, the radiation emitted is extremely coherent (the field emission gun is the electron optic analog of the laser). When a field emission source is used with the Koehler mode of illumination — a mode where the illumination aperture is conjugate with the sample — a highly coherent small probe results with very parallel illumination. This mode, called nano-beam diffraction (NBD), is the mode in which the latest precession system installed in the JEOL 3000F is typically operated.

[1]Eucentric height is formally defined as the height of the specimen at which its image does not move laterally as a function of specimen tilt.

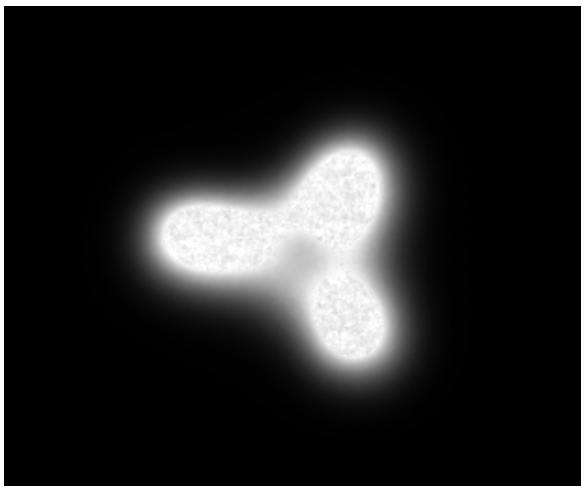

Figure 2.5. Star of merced, formed by the unoptimized precession probe prior to full alignment. The three-fold astigmatism term is dominant. Each lobe is roughly 25 nm. The image was taken on a JEOL 2000FX retrofitted for precession.

PED involves much larger angles than the conventional probe convergence angle of micro- and nano-diffraction, hence higher order aberrations and their effects should be considered.[2] The aberration function is described by radial and axial components in the x-y plane in the Krivanek notation, a convenient form for precession (Krivanek et al. 1999). The following aberration function is expanded to fourth order in this notation:

$$\begin{aligned}\chi(\rho,\theta) &= \rho(C_{01a}\cos(\theta)+C_{01b}\sin(\theta)) \\ &\quad+\frac{\rho^2}{2}(C_{10}+C_{12a}\cos(2\theta)+C_{12b}\sin(2\theta)) \\ &\quad+\frac{\rho^3}{3}(C_{23a}\cos(3\theta)+C_{23b}\sin(3\theta)+C_{21a}\cos(\theta)+C_{21b}\sin(\theta)) \\ &\quad+\frac{\rho^4}{4}(C_{30}+C_{34a}\cos(4\theta)+C_{34b}\sin(4\theta)+C_{32a}\cos(2\theta)+C_{32b}sin(2\theta)) \\ &\quad+\frac{\rho^5}{5}(C_{45a}\cos(5\theta)+C_{45b}\sin(5\theta)+C_{43a}\cos(3\theta)+C_{43b}\sin(3\theta) \\ &\quad+C_{41a}\cos(\theta)+C_{41b}\sin(\theta)). \qquad (2.7)\end{aligned}$$

χ describes the distance between the aberrated wavefront and the Gaussian wavefront along the aberrated ray (see figure 2.6); a ray intersecting the aberration function at a point (ρ,θ) will be subjected to a deviation described by a polynomial radially and a harmonic function azimuthally. For precession, we are interested in illuminating the lens in an annulus whose radius is considerably beyond the limits of conventional TEM imaging. The minimum desired ϕ is on the order of 20 mrad, and benefits continue to occur past 50 mrad. In real space, the aberration function produces a deviation from the Gaussian focal point (wandering probe), and in reciprocal space, a deviation in the ray's incidence angle. In practice either is easy to optimize by itself; however, correcting one without compromising the other is the major challenge in aligning a precession system. Consistency of the cone illumination semi-angle has proven to be a relatively loose constraint ($\pm$1 mrad is sufficient, see section 3.1) so real space localization can be considered the primary optimization constraint.

It has already been mentioned that spherical aberration can be roughly compensated for by a simple defocus adjustment, or more preferably by a shift in specimen height to preserve optimal excitation of the objective. In conventional microscopes, the next limiting aberration after C_s is three-fold astigmatism (Krivanek and Stadelmann 1995). Two-fold is present but can be relatively easily corrected by the objective stigmators. The coefficients of largest concern in the context of equation 2.7 are three-fold astigmatism (C_{23a} and C_{23b}) and two-fold astigmatism (C_{12a} and C_{12b}), illustrated in figure 2.7.

Beam tilt purity and the two-fold OL stigmators can compensate for most of C_{12}, however sometimes C_{23} is left over and must be corrected dynamically during scan alignment. In the precession implementations given in the appendices, additional two-fold and three-fold compensations are made

[2]This discussion excludes diffraction ronchigrams, which are often used for probing and tuning aberrations in aberration-corrective systems. The convergence angle in ronchigrams is often hundreds of mrad.

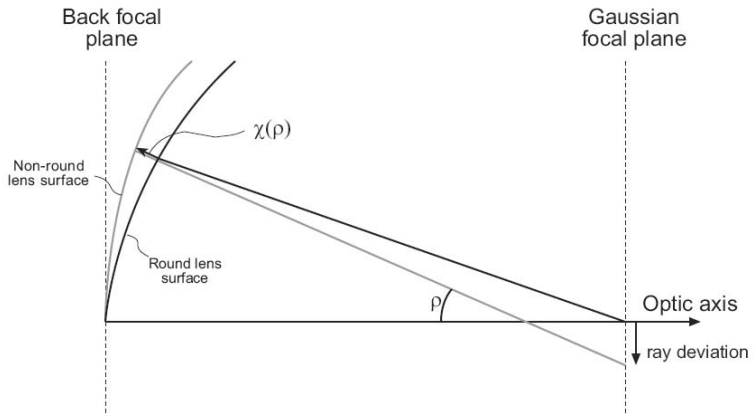

Figure 2.6. The aberration function $\chi(\rho)$ describes the deviation from the ideal round lens along the projected direction of the aberrated ray. The aberrated ray deviates in angle from ideal by ρ; in real space this corresponds to a deviation of probe location (the origin of probe 'wandering').

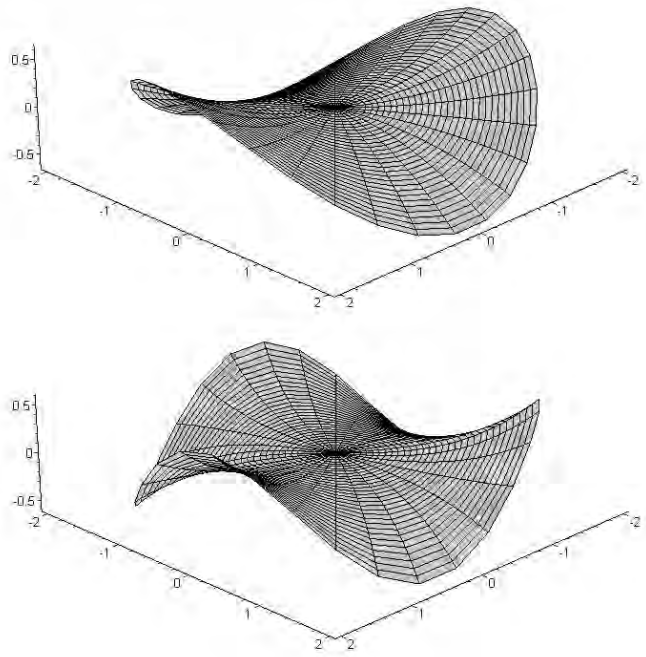

Figure 2.7. a) Two-fold (potato chip) and b) three-fold (monkey's saddle) aberration functions (arbitrary units). These are the primary aberrations that require compensation in conventional instruments.

in the conical scan in conjunction with tilt purity adjustments to achieve a suitable compromise between incident ray direction in reciprocal space and real space convergence. The practical limits have been about 40-50 mrad in the JEOL instrument. Above this threshold we have found a combination of higher-order objective aberrations and projector distortions to dominate.

Aberration-corrected instruments are particularly suitable for the precession mode. Scan systems with several degrees of freedom are by default incorporated into the latest instruments and are well-suited for providing the deflections for conical illumination. The latest generation correctors can provide up to about 70 mrad cone semiangle without geometric compensation in the scan, thus a simple circular deflection path described by the scan system will yield optimal conditions for the experiment. Especially advantageous is the fact that experiments can be executed at various ϕ with single-variable adjustment allowing quick experiment setup and enabling non-conical experimental geometries (potentially useful as alternative modes of precession) that would otherwise be impossible to generate without a comprehensive aberration model of the microscope column.

In such instruments the primary aberrations are higher-order. Beyond the flat phase patch, the aberration function increases rapidly (e.g., correction to C_5 in the latest Nion Co. corrector produces an aberration function increasing to the 6^{th} power with angle). An attempt to extend the precession semi-angle to very high values ($>$ 75 mrad) will yield rapidly diminishing returns. However, geometric compensation similar to that used on the Northwestern implementations utilizing an N-fold function, where $N-1$ is the corrector order, should nevertheless yield beneficial results.

The de-scan section of the precession instrument collects diffracted beams from each tilt condition into discrete integrated spots suitable for quantitation. This collection must happen somewhere between the image plane and back focal plane. The constraints are different from the beam tilt because the symmetry about the specimen is broken (except in the case where immediately post-specimen deflectors are available). Since precession involves angles considerably larger than those in conventional diffraction patterns, and angles become larger as the diffracted beams travel down the column, deflectors must be capable of larger deflections. The high angles involved also subject the diffracted beams to distortion in the intermediary lenses (astigmatism) in addition to projector lens distortion (astigmatism, pincushion/barrel, and spiral).

The de-scan should ideally be executed immediately post-specimen to avoid these effects. The second choice is in the intermediary optics before the diffraction pattern is formed. Sometimes this is not possible because the intermediate alignment deflectors are too feeble. The last resort is the imaging deflector: almost all conventional instruments incorporate a user-accessible deflector located just above the projector lens. Newer instruments are incorporating more post-specimen deflection coils, therefore better de-scan may be achieved in modern instruments.

2.3.1. The Future

The ability to tailor the aberrated wavefront extends naturally to an ultra-high-angle dynamically correcting scheme, suggested by N. Dellby of Nion Co. Since the precession is executed in discrete steps and the incident beam typically has small convergence ($<$5 mRad), the correction system can extend the

hollow probe performance in a given angular direction by compromising the central disc of flat phase and shifting it off of the lens axis. The aberration function of figure 2.8 demonstrates this principle.

The aberration function displayed contains a mixture of C_{10}, C_{12a}, C_{30} (or C_s), and C_{45a} to create an extended flat phase patch that could in practice be scanned around the lens axis by altering the aberration coefficients dynamically. Similarly, a rotationally symmetric ridge function (muffin tin form) could be generated - effectively a combination of defocus, C_s, and C_5 - creating a flat phase annulus that, while not focusing rays to the Gaussian plane, is nevertheless suitable for high-angle conical precession. This would extend the usable convergence angle to beyond 100 mrad while maintaining a static set of aberration coefficients, yielding excellent stability and higher angles than those achievable with an instrument corrected to be aberration-free.

2.4. Review of Previous Instruments

The earliest precession instrument was reported by Vincent and Midgley in 1994 and was based on a Philips EM430 operating at 300 kV. A Wien bridge oscillator provided the precession scan signals; frequency was capped at 30 Hz to prevent distortions due to deflector bandwidth limitations. The stock instrument included inputs for beam tilt, however the de-scan circuitry did not support external control. Therefore, the de-scan controls were completely replaced by the analog oscillator.

This early instrument was reported to theoretically yield better than a 10 nm diameter probe in convergent illumination mode, however in practice it gave a 100 nm probe due to probe-wandering caused

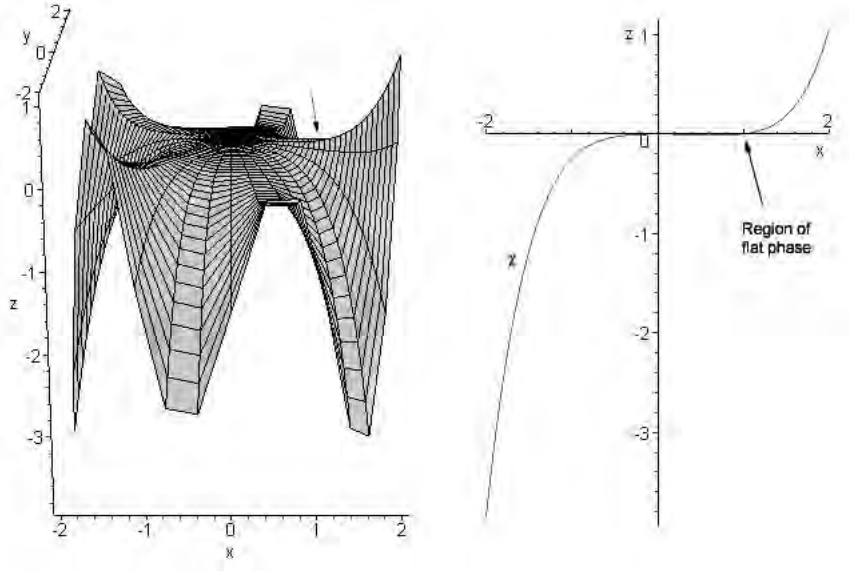

Figure 2.8. An aberration function containing coefficients C_{10}, C_{12a}, C_{30}, and C_{45a} (mixed in a respective ratio of 1:2:3:3). The effective aberration surface has rough 5-fold symmetry. In the x-z section on the right, an odd-order function describes a region of flat phase extended in the $+x$ direction indicated by the arrows.

by aberrations. The feasible tilt range was reported at 8° (≈ 140 mRad), however the earliest experiments were conducted below 25mRad and later experiments on Al_mFe using more parallel illumination had 16-40 mrad semiangle. Both of these figures are more consistent with the < 50 mrad figure we have found typical for this type of optical distortion-limited system. Projector lens distortion was the primary limiting factor causing errors in the de-scan at moderate angles that complicated automated measurement.

Gemmi has developed a precession instrument on a 300 kV Philips CM30T chassis that operates at 35 Hz (Gemmi 2001). The sinusoidal signals were generated in an outboard analog oscillator and fed into the external interface. The signals were digitized by the interface and outputted to the scan coils in analog form by the microscope CPU. This A-D-A process is active only in the selected-area channeling-pattern operating mode (part of STEM mode on the CM30T). Nanobeam illumination mode was used, which is the Koehler equivalent on this instrument (parallel illumination). One of the limitations of this type of system is that signal quality at the coils is limited by sampling rate and A-to-D converter precision at the input, and at the output by the D-to-A's (DACs) supplying the coil drivers. Due to this uncertainty, some difficulty with de-scan precision in early revisions was reported that appears to have later been resolved (Gemmi et al. 2003).

The study by Gemmi et al. (2003) on Ti_2P generated a three-dimensional dataset merged from several zone axis patterns collected on the CM30T. In this study, the device was operated with parallel illumination, forming sharp spots. A moderate tilt angle of 17 mRad was reported, limited by distortions in the optics, and the probe size on the specimen was approximately 100 nm.

The early studies demonstrated PED's potential as a crystallography tool, however, optical distortions clearly limited both instruments' performance and affected the results. The next section demonstrates an approach using simple geometric distortion compensations that enhance PED data quality and improve the alignment speed and reproducibility of precession experiments.

2.5. Design Approach

The design approach described in this chapter has been applied to two different microscope systems. The first embodiment was based upon the Hitachi UHV H-9000 microscope (see appendix B for details). On that instrument, the aberration compensations were essential but proved to be insufficient for high-precision precession due to the fact that manual specimen z-height adjustment was not available on this microscope, and the specimen was almost never inserted into the microscope near the eucentric height. Better design and careful refinement of alignment procedure yielded very good performance and high reliability for a second system based upon the JEOL 2000FX (appendix C). The hardware for the second system has since been moved onto a JEOL 3000F field-emission microscope, where minor modifications have been applied to further improve performance. An overview of the system design is presented in figure 2.9.

Beam deflection above the specimen with complementary synchronous de-scan below can be produced in most instruments using the beam tilt coils and the projector image shifts. This can be accomplished by supplying the appropriate scan signals directly to the analog coil driver circuits. We aimed to provide a simple and straightforward human-machine interface to control precession hardware that has

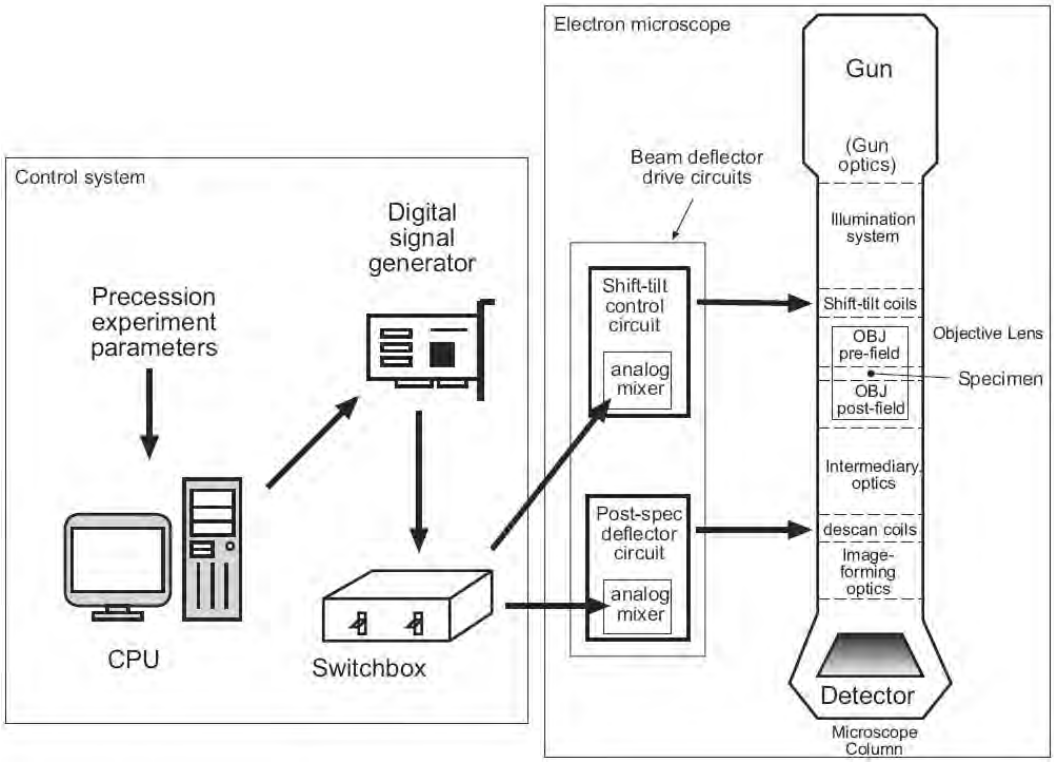

Figure 2.9. Overview diagram of the precession system.

been designed for stability and reliability. It is intended to work within the framework of the existing system without affecting any original functionality.

2.5.1. Stock Instrument Hardware

Deflection systems inside common TEMs follow a general theme wherein a control voltage is supplied to a current amplifier that drives current in a coil (figure 2.10). In such systems, control voltages are typically under 10 volts, and currents in the coils do not exceed one or two amperes. The preamplifier shown in the schematic is often configured to sum several signals (two in figure 2.10), so it will also also be referred to as a summing junction (SJ).

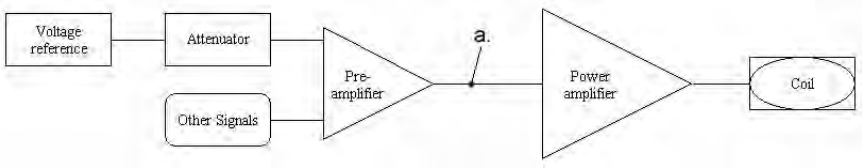

Figure 2.10. Generic amplifier for driving an electromagnetic coil.

Microscopes are used primarily for steady-state operation (scanning microscopes excluded), therefore coil drivers in many microscopes have been designed for DC operation and stability. Consequently, they will not have the bandwidth to support precession in many cases. This generates major problems for a PED retrofit, which needs a slew rate on the order of a 1000 V/s (several hundred Hz at full amplitude) with low distortion. While the coils can usually support operation in the KHz regime, the coil drivers often do not have the necessary bandwidth, especially in older instruments. Coil drivers are typically bipolar, meaning they amplify both negative and positive signals. A typical driver stage is made up of a preamplifier stage followed by voltage-to-current amplifier whose output devices comprise a pair of power transistors operating in push-pull configuration (see appendix B for a sample circuit). When fed a bipolar signal that is too fast for it to track, the output stage will respond too slowly when crossing the zero voltage point of the waveform, generating distortion. This arises because a transistor exhibits a non-zero time delay between the application of signal to the gate and the start of current flow from source to drain. In precession, this will result in a kinked "pinwheel" pattern in the scanned beam. The effect is called crossover distortion or "the class B problem," and the effects on the waveform and scanned beam are shown in figure 2.11.

The solution to crossover distortion is to either bias the output transistors so that they never turn off (e.g., always conducting current) or switch to faster output transistors. A simple coil driver stage based on power operational amplifiers is provided in the Hitachi example to demonstrate a solution to this problem (appendix B).

Most deflection coils are dipoles, meaning two windings are used to deflect the beam in orthogonal directions within a plane perpendicular to the optic axis. Identification of the axes in each coil is key since rotations or opposing field polarities often exist between deflectors throughout the column; this knowledge will prevent mismatch of precession direction between scan and de-scan and give an idea of the phase shift between the coil sets that must be applied when the system is aligned.

2.5.2. Circuit Modifications

The precession signal can be conveniently inserted at any point in the circuit where the signal is in voltage form and low in amplitude (a few volts). An example is between the pre- and power amplifer at point **a** in figure 2.10, where a small amplifier module can be inserted in series to combine the scan signal with microscope console commands. Alternatively, if summing junctions are preferred, the preamplifier can be configured in summing mode and the signal can be added as an extra input to the preamplifier. Simple circuit building blocks based on operational amplifiers (op-amps) are very suitable for this purpose; op-amps are easy to use due to compact and simple physical circuit layout, and have high intrinsic power supply rejection ratio (e.g., a variety of supplies can be used, including unregulated types). A section on operational amplifier use is supplied in appendix A.

The first two precession implementations used add-on mixer modules placed in series on low-level signal lines. Custom modules were used for reasons of versatility, listed here:

- When they were initially designed, it was not certain whether the input impedance of the stock circuit was sufficient for application of external signals. High impedance op-amps could be used.

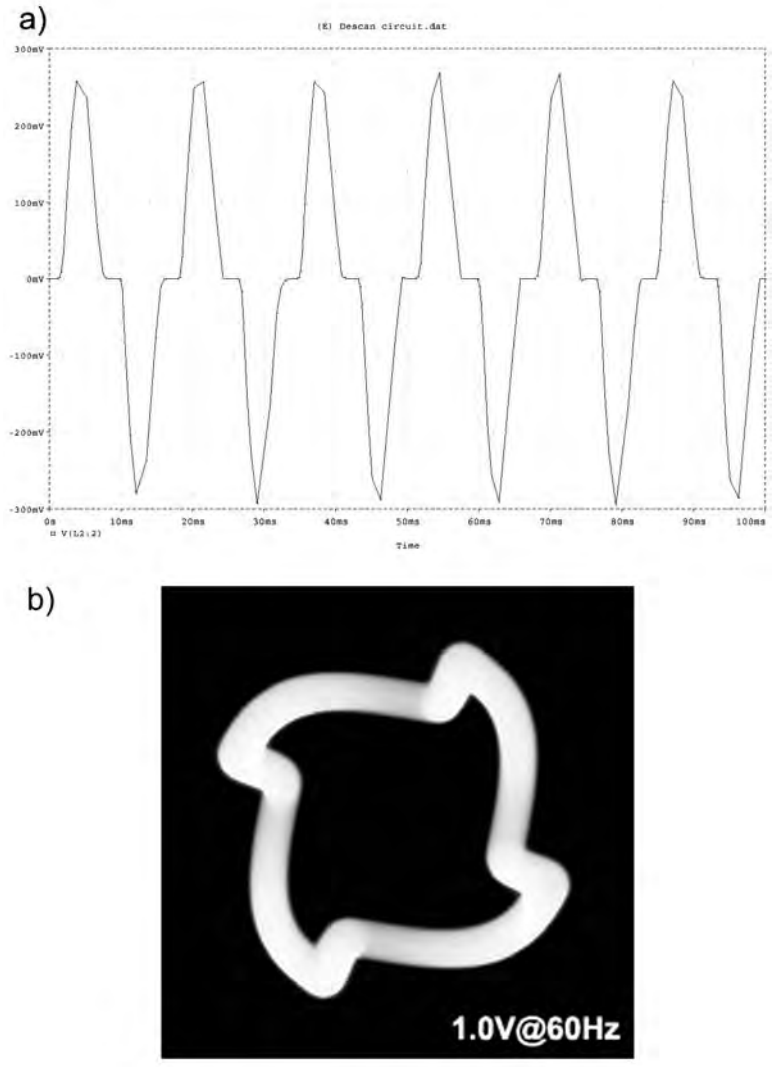

Figure 2.11. a) Simulated waveform for the H-9000 bipolar push-pull DS amplifier demonstrating crossover distortion. At each zero-crossing point, there is a plateau in the waveform. b) A precessed beam tilt pattern demonstrates how this distortion manifests in the pattern: since x and y coils are out of phase by 90° a pinwheel pattern is generated.

- It was thought that several auxiliary signals might be added in the future. A circuit board had several quick-release inputs for future expansion.
- In some cases, the signal may need to be scaled above the output range of the scan signal source, or scaled down to increase the effective resolution of the source. Individual gain settings could be easily set by altering input resistor values.

Figure 2.12 shows the mixer-buffer module used in both implementations described in this paper, comprising a single-ended inverting mixing amplifier (SJ) followed by an inverting buffer stage that corrects polarity and isolates the SJ from downstream electronics. One amplifier circuit is used for each input (four total), and the gain of each external input can be altered by changing the value of the input resistor for V_{prec}. A 15 V split supply was used, and appropriate bypassing was used to enhance amplifier performance. The 3.3 nF feedback capacitor in the mixer stage limits the bandwidth to about 5 KHz in the case that downstream components are sensitive to the high-frequency components from the signal generator's non-oversampling DAC. A low-distortion part (e.g., film-type) is preferred for this application.

It is relevant to note that while beam tilt is controlled by two inputs at the console, 4 or 6 independent windings in a stacked coil pair work in combination to provide the tilts. Many microscopes allow high-level beam tilt control from just two analog signals because shift-tilt alignment has traditionally been executed in analog circuitry; the precession scheme presented here applies to this type of microscope. Modern digital microscopes now more commonly accomplish shift-tilt alignment in the digital domain, hence there may not be a location to insert the two beam tilt signals. The solution would either require using the external interface (A-D-A process) or, more desirably, require low-level modification of individual coil drivers (e.g., extra scan inputs) and additional programming to accomplish shift-tilt alignment and ultimately conical illumination.

2.5.3. PC Hardware

A PCI-671x series data acquisition and control (DAQ) board by National Instruments was chosen for the Northwestern systems. This board employs 12-bit DACs (sufficient resolution for precession) to generate signals in the range of $\pm$ 5 V. Depending on the microscope, the gain on this input signal may need adjustment to match the signal levels inside the microscope. The PCI-671x's main strength is on-board cyclic buffering which allows a fast non-CPU-limited output rate. The standard operation rate is

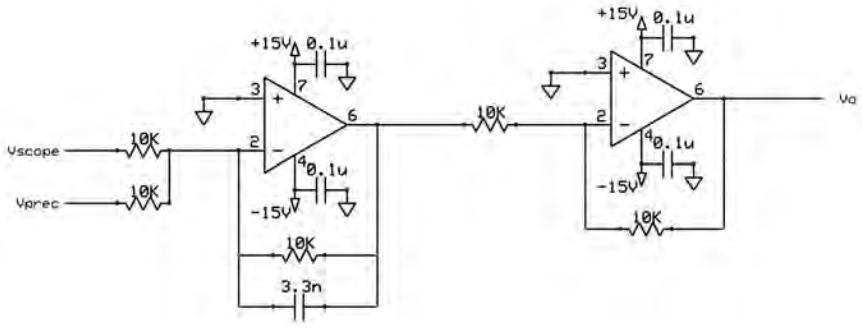

Figure 2.12. Mixer-buffer circuit used to add precession capabilities to a deflector amplifier. The first stage sums the normal microscope signal with the precession scan signal and is followed by an inverting buffer stage that corrects phase and isolates the mixer from downstream components. This circuit can be installed at point a in figure 2.10.

60-120 cycles per second with an angular resolution of better than 1° ($>$ 360 tilts); for four combined channels, this is under 0.1 megasamples per second and is well within the 1 MS/s limit for this board. The rate is chosen to synchronize to the AC mains frequency to prevent beat frequency artifacts from showing up in the scan (an example is given in appendix C). Larger angles require higher resolution and correspondingly higher output rates, so for $\phi > 30$ mrad, 0.5° angular resolution is often used. DAQ boards from other vendors may be equally suitable and can offer higher performance, and if higher resolution is needed, the PCI-673x from NI offers 16 bits of resolution.

A primary concern with PC-based systems is inherently dirty ground due to switching power supplies and digital circuitry. In general, the PC's ground reference should be bridged to the microscope near the relevant signal circuitry but placed at a common point that offers stiff earthing. Additionally, long runs of cable should be shielded to prevent external fields from modulating the signal. To prevent ground loops, the shield should be connected to ground only at one end of the interconnections (preferably at the source). For microscopes that require very high stabilities, differential scan signals should be utilized to prevent noise from entering the microscope.

2.5.4. Software

The scan generator provides four computer-generated sinusoidal signals calculated by a software routine. Deflection coordinates for each point in the conical scan are calculated, sent to the hardware buffer, and the subsequent waveforms are outputted 90° out of phase to describe a circle of deflection points where the phase difference polarity defines the direction of rotation in each deflector plane. Aberrations in the objective lens can be compensated for by adjusting deflection coordinates in the BT scan to counteract the effect of the aberration contours in the lens. The DS coil deflections are applied in the direction opposite to the tilt to bring the circle generated by BT scan down to a point in the diffraction plane (point II vs. circle I in figure 2.4). The DS signal is phase shifted with respect to the BT scan by a fixed value ϕ_{DS} in the azimuthal plane.

The DS controls can be used to circumvent distortions in the projector deflectors and lens, or to remove the effect of small residual aberrations not eliminated by the BT. With care, the integrated intensities can be brought down to measurable spots a fraction of a milliradian in diameter. Small errors in BT can be readily compensated by careful de-scan alignment even when moderate to large ϕ is used ($>$ 25 mRad).

While astigmatism in magnetic lenses is described by hyperbolic functions, approximate two-fold and three-fold functions are sufficient for their compensation. The software algorithms that generate these compensations are based upon the following set of relations:

$$x_1 = A_1 \cos\theta; \tag{2.8}$$

$$y_1 = A_1 \sin\theta; \tag{2.9}$$

$$x_2 = s \cos\theta; \tag{2.10}$$

$$y_2 = -s \sin\theta; \tag{2.11}$$

$$x_3 = [A_3 \cos 3(\theta + \phi_3)] \cos\theta; \tag{2.12}$$

$$y_3 = [A_3 \cos 3(\theta + \phi_3)] \sin\theta; \tag{2.13}$$

$$x_{out} = [(x_1 + x_2) \cos\phi_2 + (y_1 + y_2) \sin\phi_2] + x_3; \tag{2.14}$$

$$y_{out} = [-(x_1 + x_2) \sin\phi_2 + (y_1 + y_2) \sin\phi_2] + y_3. \tag{2.15}$$

The functions x_1 and y_1 represent the basic oscillatory functions that produce the precessed circle as θ traverses 2π radians. Functions x_2, y_2, x_3, and y_3 are used to generate two- and three-fold compensations, where the variable s is a scaling factor for the two-fold elliptical function related to the base deflection amplitude (cone semi-angle ϕ), and ϕ_2 and ϕ_3 are phase shifts that rotate these two- and three-fold compensation functions in the azimuthal plane. These constituents yield the functions x_{out} and y_{out}, which contain various pre-field correction amplitudes in addition to the conical precession scan. In practice, the correction magnitude is on the order of 1% of the base deflection amplitude A_1.

The software interface comprises BT amplitude controls, the two-fold and three-fold compensations described above, and phase shift ϕ_{DS} between BT and DS scans. The amplitude and two-fold functions are mirrored for the descan. Additionally, the software allows control of the precession rate and precise tuning of frequency and angular resolution. The interface, based on LabView visual language, is shown in figure 2.13.

Lens distortions in the lower column can complicate intensity quantification at higher α. If the descan is done at the projector, the quality of precessed diffraction spots is highly dependent upon cone semi-angle. The spot uniformity deteriorates with increasing ϕ and diffraction spot centers become displaced in the diffraction plane due to projector distortions (figure 2.14). This was a limitation on the EM430 on which the first precession instrument was based. For some microscopes, the maximum possible tilt may be restricted by objective lens aberrations before post-specimen distortions become a limiting factor.

A number of modern instruments have incorporated post-specimen deflectors that mirror the scan coils prior to the specimen. This is very advantageous for PED, so we include here some guidelines for implementing shift-tilt alignment in software. The common scan coil arrangement uses two deflector pairs, which usually have their axes relatively aligned in the column. Four inputs are necessary for the scan, and another four are necessary if the de-scan has the same type of configuration. The deflectors will behave linearly with input current throughout most of their range, however for large scan angles, the brightness centering (shift) should be zeroed to avoid hitting nonlinearities asymmetrically as ϕ increases. The shifts can be zeroed via the spot size alignment feature on many microscopes. Shift-tilt purity can be accomplished by applying a simple linear combination of the tilt inputs:

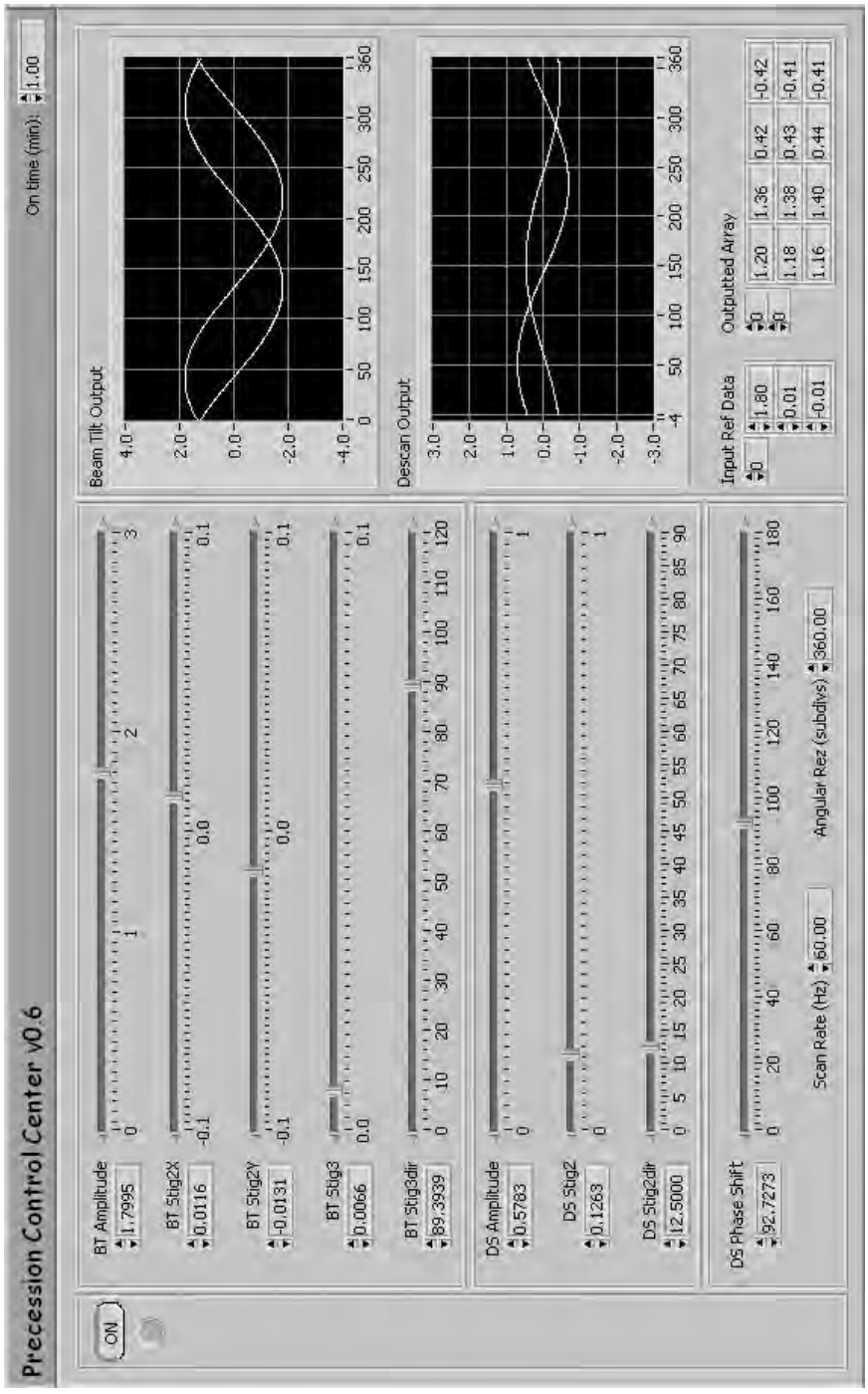

Figure 2.13. Precession software interface.

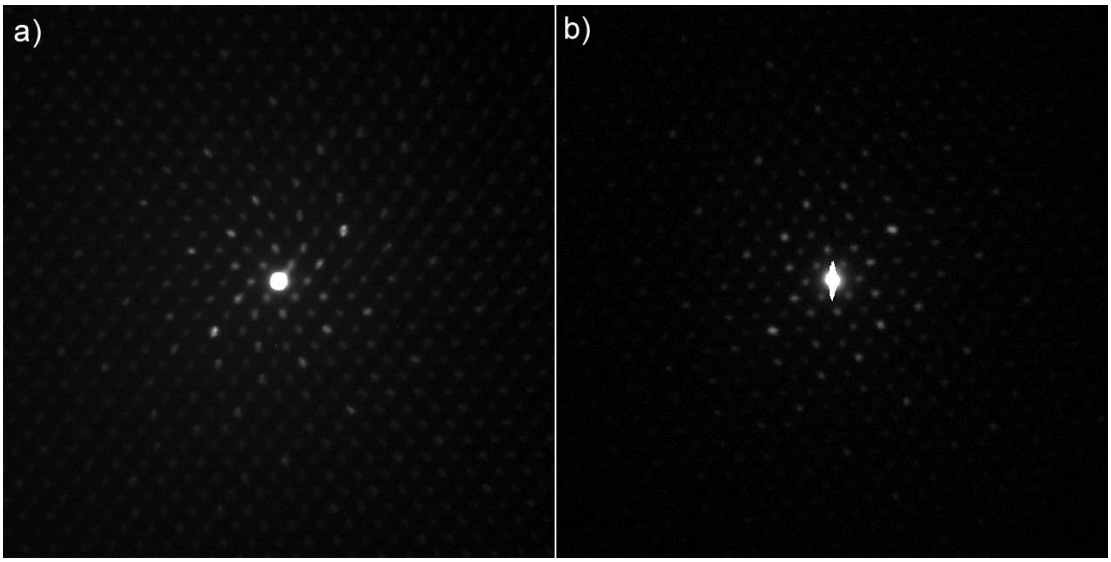

Figure 2.14. Precession patterns for 60 mrad cone semiangle (a) and 40 mrad cone semiangle (b). Spiral distortions in the projector lens alter the shape of the spots and shifts their position, preventing straightforward intensity measurement. Using a smaller cone semi-angle gives an improved and easier to measure spot pattern.

$$x_u = Ax_t; \tag{2.16}$$

$$y_u = By_t; \tag{2.17}$$

$$x_l = x_t + Cy_t; \tag{2.18}$$

$$y_l = y_t + Dx_t. \tag{2.19}$$

The variables x_t and y_t denote the tilt signals sent from the precession system (or microscope), and x_u, y_u, x_l, and y_l correspond to the upper deflector pair and lower deflector pair, respectively. The four coefficients A, B, C, and D correspond to the shift-tilt purity controls available on most microscopes. These are used for the "wobbler" alignment; precession performs a similar operation, but it probes aberration space isotropically so it can provide an even better alignment than the wobbler. Many azimuthal phase shifts are present along the beam path, since at least 4 deflector coils with 8 individual windings will be active, so 16 bits of resolution in the signal generator is recommended to ensure alignment. The recently-released commercial precession system called SpinningStar from NanoMegas Corp. uses this scheme in pre- and post-specimen deflectors. This allows free scaling of the tilt amplitude without compromising the alignment, so in this case the de-scan amplitude would be dependent upon the scan amplitude variable.

2.5.5. Conclusions

The key aim for this design approach has been to balance function, usability, and complexity. By utilizing graphical-tool-based object-oriented software to control the digital electronics, the system preserves the intuitive analog feel of a stock instrument yet is not limited by the inflexibility and inherent design complexity of a fully analog system. With distortion compensation, the precession pattern quality improves dramatically, and images can be digitized readily by automated cross-correlation methods (appendix F).

The example systems in the appendices show that retrofit of precession mode onto conventional instruments is not difficult, and (perhaps more importantly) that a high-performance implementation can be very inexpensive. The systems described each required less than US$2,000 in parts costs. Excellent results can be expected if the most important requirements are met, namely compensation of aberrations, manual z-height correction, and careful user alignment.

Before concluding this chapter, it must be mentioned that in the progress of conducting the work presented here, not only were important instrumentation parameters elucidated, it was also discovered that it is sometimes much easier to install PED capability on older analog instruments. This has extremely important ramifications in the field. While fancy-ass instruments such as aberration corrected microscopes with sophisticated detectors make PED work better, all that is necessary is a microscope that has well-implemented shift-tilt purity controls with sufficient range, a pair of post-specimen deflectors, and an electron film magazine. The resolution extension by a factor of 100 granted by PED promises new life to old instruments. Currently, a huge installed base of thousands of TEMs incapable of atomic-resolution imaging exists that would directly benefit from this type of retrofit. In many cases, the costs for a commercial precession retrofit would prove a factor of 5 or 10 smaller than the cost for full replacement of the instrument.

In the next two chapters, the precession system shall be put to use in an investigation of real materials. The care put into ensuring precise and reproducible measurements by the instrumentation will be readily apparent in the quality of the recovered data and the results they generate.

CHAPTER 3

The GITO Model System

It was seen in chapter 1 that the results from precession electron diffraction were somewhat mixed in the early precession studies. To really understand what is going on, it is of paramount importance to study the precession method using a model system with known characteristics. In this chapter we investigate precession physics using the Ga-In-Sn-O ternary oxide model system (GITO). The aim of these studies is to understand why precession works in some cases and not in others by closely studying the errors that arise due to the precession operation. The results presented here are reproduced from Own and Marks (2005b) and Own et al. (2005b).

The GITO system was previously investigated as a transparent conducting oxide substrate material for potential use in flat panel displays and solar panels (Edwards et al. 2000; Hwang et al. 2000). The phase studied here, denoted m-phase, was first identified using powder X-ray diffraction, solved by a combination of electron diffraction and high-resolution imaging, and later confirmed by neutron diffraction (Sinkler et al. 1998b). Its chemical formula is $(Ga,In)_2SnO_4$. This phase has a monoclinic unit cell with $\mathbf{a}$ = 11.69 Å, $\mathbf{b}$ = 3.17 Å, $\mathbf{c}$ = 10.73 Å, and γ = 99°. The plane group is p2, and the origin can be defined by fixing the phases of two non-collinear reflections with odd parity. The plate-like structure is shown in figure 3.1.

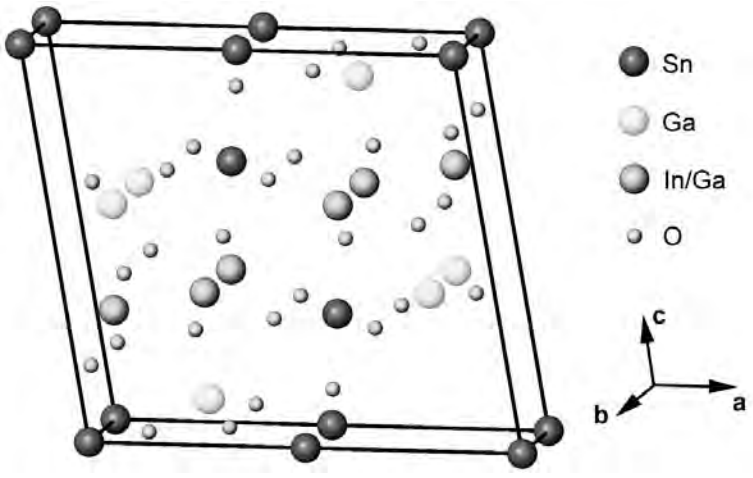

Figure 3.1. Structure of $(Ga,In)_2SnO_4$ (GITO). In/Ga balls represent mixed occupancy sites.

The GITO structure contains relatively heavy elements, making it a strong dynamical scatterer. However, the atomic arrangement projects well in the zone axis investigated here ([010]), so it is a good candidate for probing precession at larger thicknesses. A quick calculation using the relationship

$$R_{overlap} = k \sin \gamma \tag{3.1}$$

where γ is defined by equation 2.5 shows that the FOLZ overlap radius will be 4.14 Å^{-1}. Here, k is the modulus of the electron wavevector (here, 200 kV), $\mathbf{b}^*$ is the reciprocal unit cell distance along the projection axis, and ϕ is the precession semiangle (24 mrad). The small cell distance along the $\mathbf{b}$-axis makes the [010] projection particularly suitable for study because the entire measurable dataset is immune to Laue zone overlap (this can be a disadvantage since HOLZ are unavailable for 3D data collection, though 3D data are not needed for the current study). Since the structure is known, there is high confidence in the comparison between simulated data and experiment.

3.1. Rapid *a priori* Solution of a Metal Oxide

A two-dimensional electron precession dataset from GITO was captured on a precession system based upon the JEOL 2000FX microscope described in Own et al. (2005a) and reproduced in appendix C. Operating conditions were as follows: [010] projection; 200kV accelerating voltage; cone semiangle of 24 mrad (0.96 Å^{-1} in the diffraction plane); parallel illumination; 60 Hz precession scan rate; smallest condenser aperture (10 μm); and $\approx$ 50 nm probe size. The dataset (henceforth referred to in this chapter as "precessed") was captured on a GATAN US1000 CCD. A second dataset was acquired by conventional fine probe diffraction (henceforth referred to as "dynamical") using an identical illuminated region and illumination conditions excepting beam precession, and identical probe size and exposure times within experimental error.

Intensity measurements of the digital images were conducted using the EDM crystallography software package (Kilaas et al. 2005). The intensities collected from the datasets were symmetry averaged and used directly with the fs98 code packaged within EDM. The software uses an accurate cross-correlation algorithm similar to that described by Xu et al. (1994) to collect intensities, wherein a unitary spot motif generated by combining reflection profiles is used to quantify the reflection intensities. Details about measurement accuracy are described in appendix F. The precession system was able to bring the diffracted beams down to uniform spots suitable for measurement by this method, and 121 unique intensities were collected in the range of 0-1.4 Å^{-1}. Their values are given in table G.1 in appendix G.

Precession decreases the error between Friedel symmetry equivalents, hence a slight mistilt of the zone axis with respect to the incident beam is tolerable for quantitative electron crystallography. For instance, a mistilt of less than one milliradian is readily compensated by a precession cone semi-angle of 25 mrad because the effect of shape function geometry is essentially eliminated due to the integration. In more specific terms, the sinc-like functions that describe the excitation are sampled well into their tails where nearly no intensity is contributed (see figure 2.1a), therefore nearly all the available intensity is sampled and the integrated intensities will obey Friedel's law. (A caveat applies if the integration

inadequately samples the intensity contained within the relrod, for example, very low $|\mathbf{g}|$ or ϕ is too small).

This effect is seen in the experimental data. Error between Friedel equivalents was evaluated in both precessed and non-precessed diffraction patterns according to the metric,

$$E_{Friedel} = \frac{|F_{\mathbf{g}} - F_{\overline{\mathbf{g}}}|}{2}. \tag{3.2}$$

The non-precessed ZAP was aligned visually to be as on-zone as possible during the diffraction experiment. Datasets were normalized to the strongest reflection to facilitate a direct comparison, and the errors have been plotted in figure 3.2. The precession data had a higher minimum measurement threshold, indicative of more kinematical behavior since the transmitted beam is stronger in relation to scattered beams (note that both datasets had identical exposure times). Figure 3.2 shows that the Friedel error in the precession pattern is overall quite low, and, excepting the strongest reflection, the percentage error decreases as amplitude increases. In contrast, the dynamical dataset errors have larger scatter, and several error points exceed 10% of the reflection amplitude. This is noteworthy because the Friedel error in the dynamical pattern was larger than precession even though spots in the non-precessed dataset were

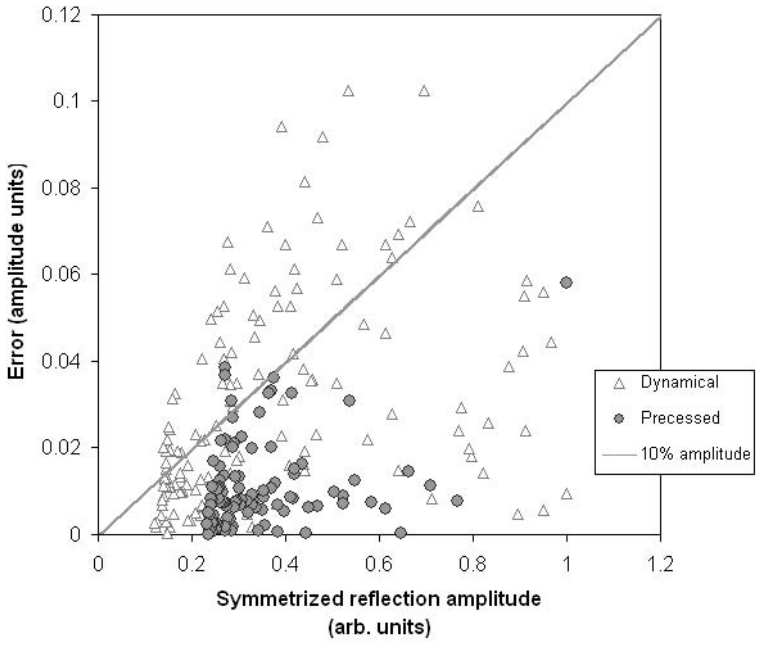

Figure 3.2. Friedel errors (amplitudes). Most precession errors (circles) are less than 10% of the amplitude and decrease with increasing amplitude. Non-precessed Friedel errors have more scatter and often exceed 10% of the measured amplitude due to the asymmetric sampling of relrods.

isotropically-shaped and more peak-like, hence easier to measure than the precession pattern which exhibited residual projector distortions that altered spot profiles asymmetrically.

3.1.1. Direct Methods on GITO: Comparison between Dynamical and Precession Diffraction

The set of kinematical amplitudes computed from the known GITO structure will be used as the benchmark for comparison with experimental data. Diffraction patterns from kinematical and experimental PED datasets are shown in figure 3.3. From a qualitative standpoint, it can be seen that key reflections in the experimental precession data with spacings that define the atomic positions (about 0.25Å^{-1} to 1Å^{-1}) match well in relative intensity. The experimental pattern contains increased intensity near the transmitted beam and the outer reflections are damped (figure 3.3(b)), owing to a combination of a Lorentz-type geometric contribution (section 2.1), Debye-Waller type radial damping, and typical dynamical behavior where reflections near strong beams are overemphasized due to strong multiple scattering. The experimental map is especially promising because stronger structural reflections beyond 0.5 Å^{-1}, even though they are damped, still exhibit qualitatively well-correlated intensity ratios.

To better quantify these effects, the experimental dataset amplitudes were plotted against the kinematical amplitudes from the known structure. Figure 3.4 shows experimental precession and dynamical datasets normalized to the strongest intensity in each set. The reflections have been symmetrized by averaging Friedel complements to remove the effects of tilt. Reflection amplitudes are coded by symbol in ranges of $\mathbf{g}$ = 0.25 Å^{-1} within the plots. In order for a pseudo-kinematical interpretation to be applicable, the amplitudes must be approximately linear and ratios between reflections should be preserved. The precession data contains several outlier reflections, primarily at $F_{norm}^{kin} \approx 0.2$ (note that this value is specific to the GITO [010] zone axis), and exhibits a distinctive positive offset of weak reflections whose values are above the measurement threshold. Regardless of the offset, most reflections follow the targeted linear trend, and the precession dataset is distinctly linear in comparison to the dynamical amplitudes of figure 3.4(b), which are hopelessly mixed.

Raw GITO precession datasets maintain good linearity to $t \approx 20$ nm according to precession multislice simulations that will be shown later in this chapter. As the thickness increases, intensity deviations manifest first in the reflections outside of the structure-defining reflection range and eventually encroach into the range of reflections that have strong bearing on the structure. This will cause direct methods to generate poorer structure maps. Due to the precession geometry, low-index precessed reflections receive considerable coupled intensity from the transmitted beam, thus the reflections of greatest concern are those nearest the transmitted beam that are usually weak for real structures. This behavior suggests that, for unknown structures of moderate thickness, a good starting point is to exclude reflections that fall outside of the structure-defining range of 0.25 $\text{Å}^{-1} < \mathbf{g} < 1.25$ Å^{-1}. This approach is effective with precession data from GITO crystals to about t = 750 Å when a 24 mrad precession semi-angle is used. Higher precession semi-angles can improve this to some extent (extending the range by 5-10 nm) but HOLZ overlap with the ZOLZ is likely. Larger thicknesses will certainly require a forward calculation to correct the intensities for multiple scattering; one such approach is the two-beam correction employed in the earlier study by Gjønnes (Gjønnes et al. 1998b). The conditions for when this is necessary are established in later sections of this chapter.

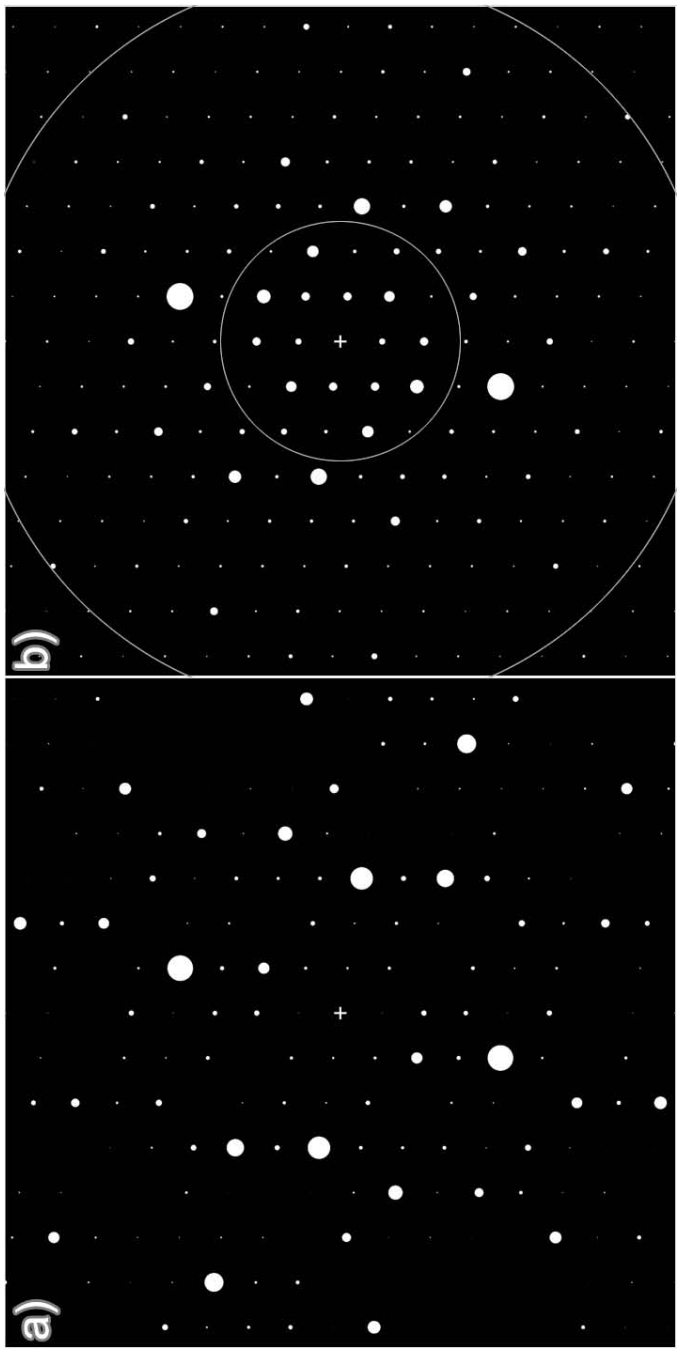

Figure 3.3. (a) Kinematical amplitudes pattern (radius proportional to amplitude) and (b) experimental PED intensity pattern (radius proportional to intensity). The annulus describing the range 0.25-0.75 $\mathrm{\AA}^{-1}$ is bounded by the circles.

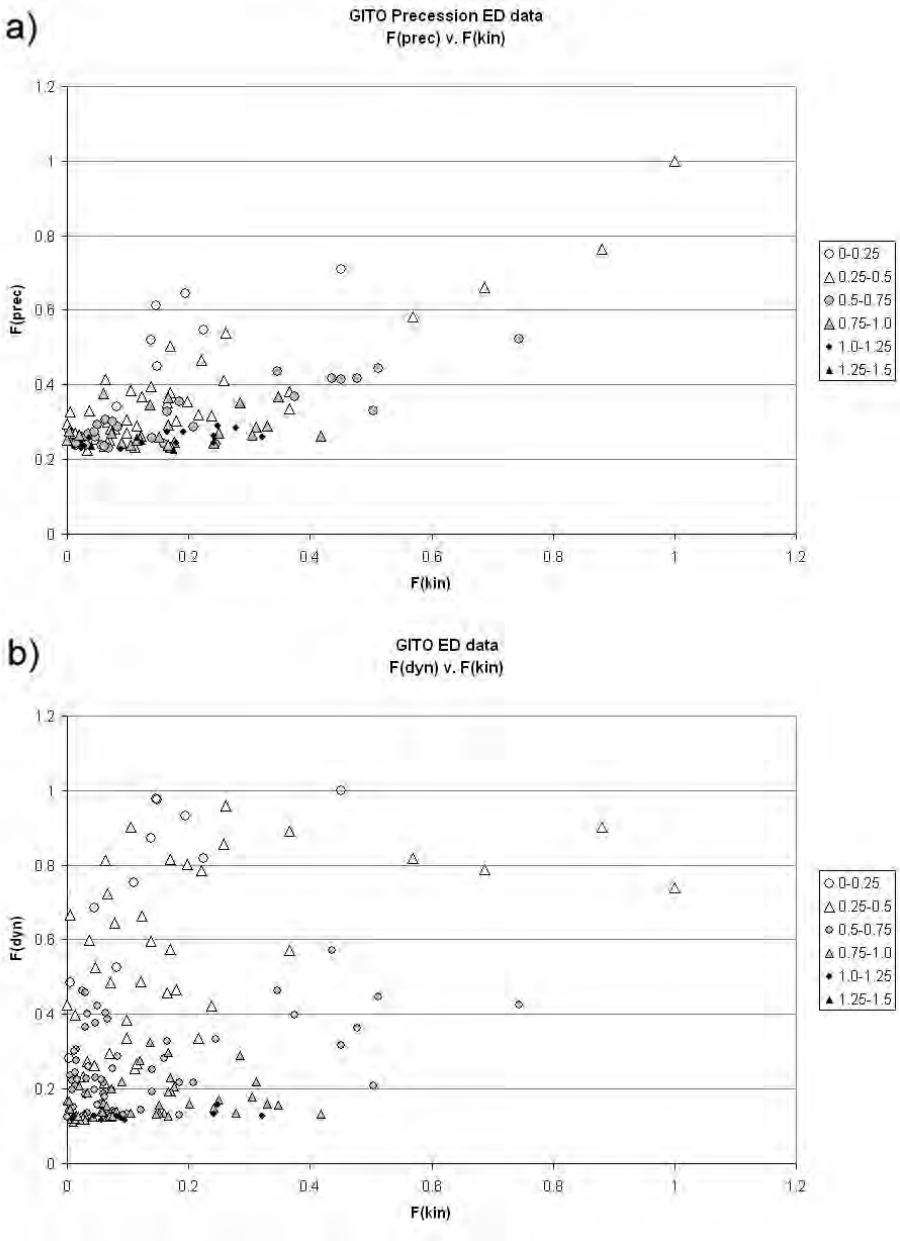

Figure 3.4. (a) Experimental precession amplitudes and (b) dynamical amplitudes plotted against kinematical amplitudes calculated from the known GITO structure. Amplitudes shown are the square root of the measured intensity.

The precession amplitudes with $\mathbf{g} < 0.25$ Å^{-1} excluded were employed in a direct methods calculation and produced four unique solutions (shown in figure 3.5(a)). The solution with the clearest peak-like features from the dynamical dataset is given in figure 3.5(c) for comparison. The precession solutions bear near-identical features to each other and demonstrate well-defined peak locations. Some of the strong scatterers in the structure are weakly emphasized (i.e., the In/Ga columns at $0.35\mathbf{a}$,$0.38\mathbf{c}$, see figure 3.1). However, all expected atom locations contain atom-like features above the noise floor that would be considered as potential atom locations in an *a priori* structure investigation. The quality of these solutions, compared with the solution from the dynamical dataset acquired from the identical specimen region, is unmistakable.

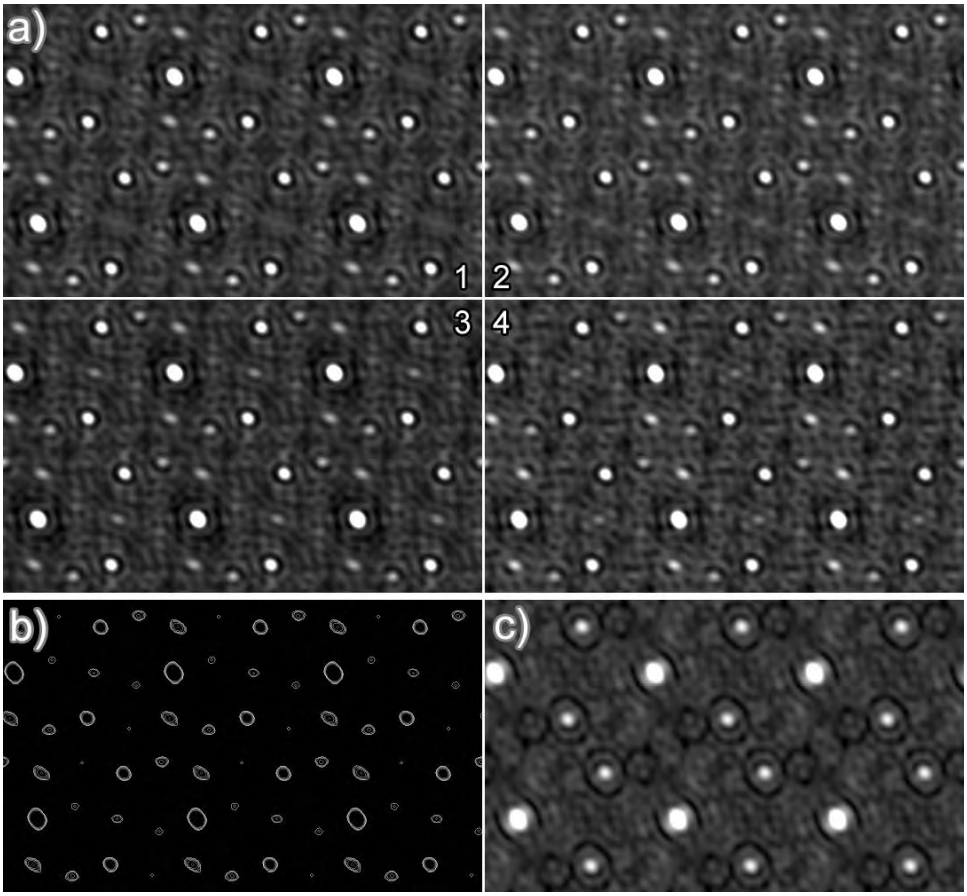

Figure 3.5. a) Four unique DM solutions generated from precession amplitudes. Reflections below $\mathbf{g}$ = 0.25 Å^{-1} were excluded. b) Topographical map of solution 4. Well-defined peaks above the noise floor correspond to atomic positions. c) DM solution from dynamical dataset. No high resolution phases were used to generate these maps.

Figure 3.5(c) is typical of a first-try solution with a complex oxide of unknown thickness. The quality is not as good as the precession solutions; it is well-known that bulk oxide structures are as a rule very difficult to solve from TED data alone. In stark contrast to precession, the best dynamical solution only located Sn atoms at the corners and middle of the unit cell, and the central atoms were placed at incorrect positions. Of seven unique solutions generated from the dynamical data, only two possessed atom-like features. Neither of the solution maps would be trustworthy unless more *a priori* information was available to constrain the calculation such as phases from high resolution images.

In addition to generating excellent starting structures, some favorable effects of thickness insensitivity are also seen in the PED data. Thickness fringes were present in the image of the illuminated region, indicating that the crystal was wedge-shaped. As was described in section 1.4, aspects of the structure such as the oxygen columns or heavy cation columns (manifesting as sharp well-defined features) exchange prominence in the exit wavefunction with increasing crystal thickness. This is due to differing oscillation periodicities with thickness for atomic columns of differing composition. To get projections that faithfully indicate all features of one type (critical for direct interpretability), thin and uniform crystals are required to avoid overlap of oscillations from multiple thicknesses of the same column type.

In the case of GITO, the Babinet solutions generate peak-like features only at anion columns, arising from slow variation of channeled intensity within oxygen 1s states (Sinkler and Marks 1999b). Simulated images show that interpretability of the Babinet rapidly diminishes beyond about 30 nm thickness. The poor quality of the dynamical solution in figure 3.5(c) suggests that the specimen must be thicker than 30 nm and/or contributions from multiple thicknesses are destroying the intensity relationships that generate correct phases. In contrast, not only were realistic solutions extracted by PED from a specimen that was thicker than 30 nm and wedge-shaped, peak-like features were readily recovered at the *cation* locations showing that the solution results from pseudo-kinematical direct methods rather than dynamical direct methods. In other words, intensity relationships are preserved regardless of thickness variation. From this result, it can be concluded that PED of moderately thick crystals ($<$ 50 nm) with good projection characteristics requires no additional phase information to restore structure maps of the kinematical scatterers.

It has been suggested by Dorset and others to increase contrast of the electron diffraction data by using intensities with direct methods rather than structure factor amplitudes (Dorset 1995; Gemmi et al. 2003; Weirich 2004). As discussed in section 1.4, this approach is supported by a two-beam argument applicable to polycrystal diffraction, texture patterns, and possibly also to precession data (effective integrated two-beam). From Blackman theory (Blackman 1939), the measured intensity $I_{\mathbf{g}}$ is related to the kinematical structure factor $F_{\mathbf{g}}$ as

$$I_{\mathbf{g}}^{dyn} \approx F(\mathbf{g})^{\alpha}, \tag{3.3}$$

where the exponent α varies from 2 to 1 as the product of thickness t and $F(\mathbf{g})$ increases (equations 1.26 and 1.27). In the limit of PED on thicker crystals where the structure is unknown, use of intensities approximates a dynamical two-beam correction that can be used to generate starting structure maps.

This is supported by the intensity diffraction pattern of figure 3.3(b), which matches the kinematical amplitude pattern of 3.3(a) well. The practical effect of using intensities is a preferential enhancement of strong beams which, if the strong structure-defining amplitudes are nearly correct with respect to each other, emphasizes key structural features above "noisy" weak reflections that can generate ambiguous oscillation maxima in the Fourier synthesis.

Incorporating this alternate approach with the GITO data, the strong structure-defining reflections in the 0.25 Å - 0.5 Å region become more prominent as the contrast between strong and weak beams is enhanced. The resulting map (figure 3.6(a)-(b), where all measured reflections were included in the direct methods) more clearly shows atom-like features at all expected cation locations due to attenuation of noisy reflections. Peak locations from the intensities-derived map are consistent within a few picometers to those found by using amplitudes with low-$\mathbf{g}$ reflections excluded (figure 3.5).

The question arises as to why both the amplitudes (excluding low-$\mathbf{g}$ outliers) and intensities (all reflections) generate good solutions with atom positions coinciding perfectly. Recalling equations 1.26 and 1.27 that describe the limits of the Blackman equation, the answer lies in the fact that intensity ranking relationships are preserved in both cases so they will likely yield similar phase relationships. In the intensities case, the value of structure-defining reflections are much stronger than weaker reflections, so atom-like features are sharper, however this will only be be applicable in the limit of large thickness ($A_{\mathbf{g}}$ large).

The cation positions measured from the amplitudes-derived map (unrefined) are given in table 3.1. HREM and neutron-refined GITO atom positions from Sinkler et al. (1998b) are reproduced for comparison, showing good correspondence with precession results. Precession-derived maps without subsequent refinement result in column positions located on average within 4 picometers of the neutron-refined positions.

3.1.2. Discussion

In this section, electron precession has demonstrated the ability to linearize the GITO dataset to a kinematical approximation allowing nearly-direct interpretation. The experimental precession data from GITO is linear in the regime where the structurally important reflections are located, and appears to be much less sensitive to the variations in thickness that prove debilitating for conventional electron diffraction datasets. The results also suggest a systematic behavior to the data errors present. Exclusion of overemphasized reflections in precession datasets that have little bearing on the structure is a suitable starting strategy, and a second strategy in the limit of large thickness is to use intensities.

A comprehensive understanding of these errors in relation to thickness and illumination conditions is now necessary to allow use of precession data in a general pseudo-kinematical capacity. It is encouraging that precession data, from experimental conditions that would ordinarily be very difficult for generating useful starting structures, has been directly usable with little to no modification, and without phase information. In the next section, we will use simulation to understand why this is so.

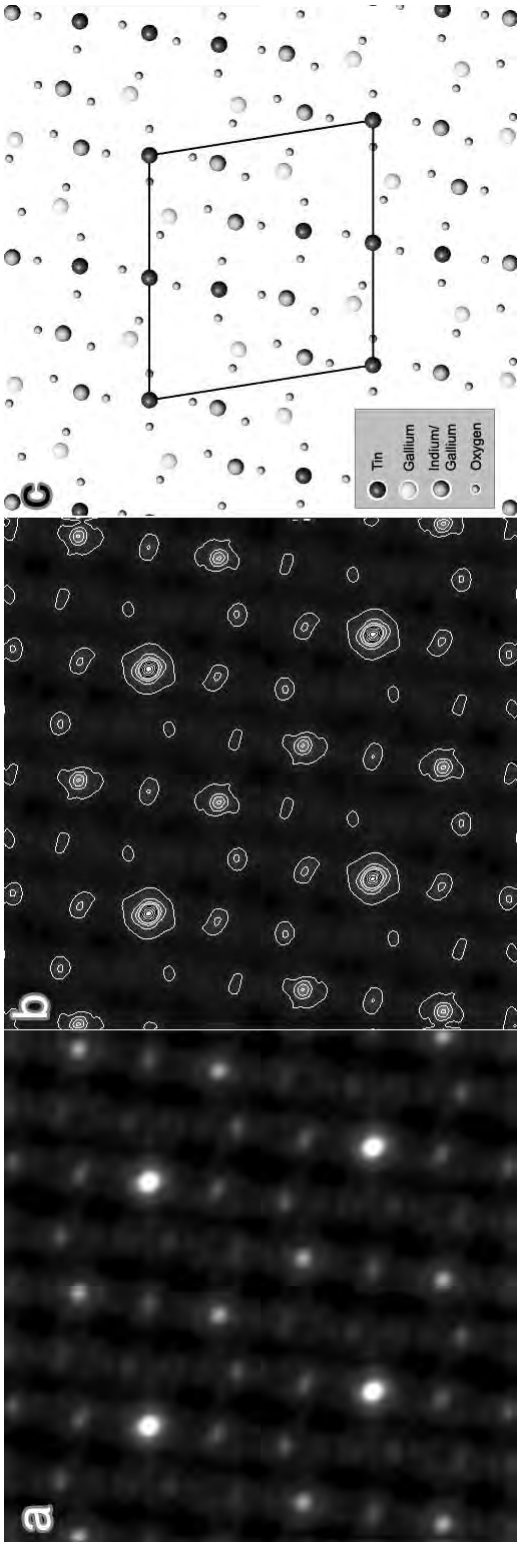

Figure 3.6. DM solution of GITO from precession intensities (all reflections included).

Table 3.1. GITO atom positions from HREM, neutron diffraction (refined), and unrefined positions from precession. Atom positions from PED match very closely with the neutron-refined positions.

	HREM		**Neutron**		**Precession**		Displacement (Å)	
	x	z	x	z	x	z	ΔR_{HREM}	$\Delta R_{neutron}$
Sn1	0.0	0.0	0.0	0.0	0.0	0.0	0.0	0.0
Sn2	0.515	0.062	0.5	0.0	0.5	0.0	0.474615	0.0
Sn3	0.594	0.320	0.5918(6)	0.3112(7)	0.585113	0.312169	0.017950	0.0065(5)
In/Ga1	0.305	0.360	0.3281(6)	0.3859(7)	0.345947	0.379929	0.275989	0.0516(5)
In/Ga2	0.078	0.328	0.0756(8)	0.3053(9)	0.079877	0.305699	0.057683	0.0023(7)
Ga1	0.172	0.672	0.1500(5)	0.6022(6)	0.172498	0.602720	0.552591	0.0684(8)
Ga2	0.234	0.031	0.2624(5)	0.0869(5)	0.232436	0.078043	0.255026	0.1217(5)

3.2. Precession Simulation

The n-beam calculations by Gjønnes et al. (1998b) on Al_mFe were made along the azimuthal precession circuit θ within 0.5° of the Bragg condition for each reflection and were reported to converge using a small number of beams within an aperture radius of 1 $Å^{-1}$ (roughly 20 beams, varying in quantity and selection with Bragg reflection along the circuit). Details of which beams were used, how they were chosen, and the resolution of the calculation were unfortunately never published. No other precession data simulations have been reported thus far, so a comprehensive benchmark of experimental precession results does not yet exist in the literature. While the details are not available, it is nevertheless evident that the problem space in the previous study was sampled somewhat sparsely. Here, full dynamical multislice calculations will be used to establish a robust baseline for comparison with the experimental data from GITO.

Precession datasets for the [010] projection of GITO were simulated using the NUMIS multislice code for a wide range of thicknesses at 200 kV with parallel illumination. The neutron-refined atom positions from table 3.1 were used in the simulations, and Debye-Waller factors of 0.3 Å and 0.5 Å were used for the cations and oxygen atoms, repectively. Individual tilt events were calculated along the azimuthal circuit (increasing ϕ as in figure 1.10) and integrated into a unified dataset. The granularity of the simulation will be referred to as "angular resolution" corresponds to $\frac{360^o}{N_t}$ with units of degrees, where N_t is the number of discrete tilts. Since tilt inherently enhances intensity loss from the edges of the matrix used in the multislice calculation, care was taken to prevent loss of intensity during propagation through the crystal that might skew the exit wave amplitude. First, the phase grating was expanded in dimension such that greater than 99.5% of incident intensity was retained for all simulations to 160 nm (1000 slices). Second, calculations were set to include beams to a very high resolution of about 7.5 $Å^{-1}$ to ensure re-diffraction from high-angle beams back into the central beams was fully accounted for. For comparison, un-precessed datasets using zero tilt ("dynamical" datasets) were also calculated for identical thicknesses using the same simulation settings. The simulation output included reflections to 1.5 $Å^{-1}$ which is just beyond the measurement limit for most experimental datasets.

An analysis of intensity integration convergence was conducted to confirm reliability of the tilt summation approach. Several precession simulations were conducted on the GITO system with integrated intensities normalized to the transmitted beam. Convergence for small thickness was first to be evaluated. Convergence was rapid, occurring with 8 discrete tilt samples for 4 nm specimens, and 32 tilts for 16 nm. At larger thickness, it was found that much higher resolution was necessary for convergence: substantial errors appeared by t = 50 nm for ϕ = 24 mrad and the errors were exacerbated when larger cone semi-angle was used (in the worst case up to 20% error in strong beams is seen). The strong dynamical mixing in thick specimens combined with the rapid integration of higher-index relrods at large precession angle necessitated finer sampling. For this reason 0.36° angular resolution (1000 discrete tilts) was used for all simulations in this study.

Figure 3.7 confirms that precession multislice correctly describes the data. The thickness of 412 Å, to be derived from the experimental data in the last section of this chapter, demonstrates good agreement within experimental error. This is in part due to PED's insensitivity to the thickness variation, further

evident from the regression analysis of un-precessed experimental data (not shown) which yielded a much lower $R^2 \approx 0.45$.

3.2.1. Amplitude Reference Plots

Plotting experimental data against the kinematical reference is a useful metric for gauging how well a dataset will solve, previously demonstrated by the amplitude plots of 3.4. This will now be extended through multislice simulation to efficiently explore a large portion of experiment space.

Since beam intensities often span several orders of magnitude and strong beams are substantially more intense than most beams in the set, the data are easier to interpret if amplitudes (normalized to the strongest beam) are plotted. In the ideal case, the two axes will have a one-to-one correspondence. However, as long as a roughly linear relationship is preserved, favorable solutions will still be generated, even with errors of 10-20% in the strong reflections. Weak intensities that have received extra scattering intensity due to dynamical effects — in effect weak beams converted into strong beams — are the most detrimental to the success of direct methods. They are a frequent feature of dynamical datasets such as the dynamical GITO dataset from figures 3.3(b) and 3.4(b).

A montage of reference plots of multislice precession data is given in figure 3.8 demonstrating trends over thickness t and cone semi-angle ϕ. The montage is divided into three dataset groups:

(1) The top row of plots is the un-precessed case (dynamical).
(2) The left column shows the behavior for a very thin specimen (4 nm).

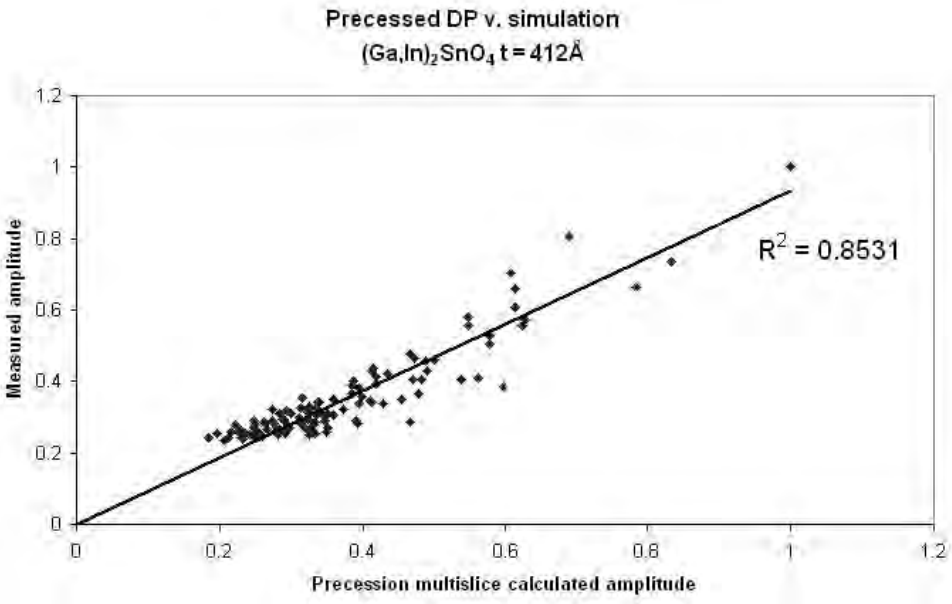

Figure 3.7. Precession amplitudes (normalized) plotted against amplitudes calculated by precession multislice.

(3) The 16 plots in the lower right show the effect of increasing precession angle for a variety of specimen thicknesses.

The precession angle ϕ of 10, 24, 50, and 75 mrad corresponds to reciprocal distances (in Å^{-1}) of 0.398, 0.956, 1.99, and 2.99, respectively, at 200 kV. The following table establishes some simple terminology for describing the relevant thickness regimes:

Table 3.2. Terminology for thickness ranges.

thickness range	descriptor
0-25 nm	small
25-50 nm	moderate
50-100 nm	large
100+ nm	'very large'

A qualitative analysis of the multislice data reveals interesting global behaviors. As would be expected, the data become less kinematical with increasing t regardless of precession angle. A clear improvement can be seen in the small-to-moderate range of thicknesses as ϕ increases.

Looking first at the smallest thickness of 4 nm (at the practical limit of sample preparation methods), ϕ = 0 mrad demonstrates some scatter and already the strongest reflection has over 1000% error (the reflection at $F^{kin}_{norm} \approx 0.25$). Introducing a small precession angle of 10 mrad improves the linearity of datasets and in the plots for small thickness crystals one can readily track the errant reflections migrating toward the kinematical reference line described by $F^{prec}_{norm} = F^{kin}_{norm}$. Moving to 24 mrad, datasets from thin specimens become even more kinematical, and accompanying additional increase of ϕ, the weak reflections improve further.

Unfortunately the improvements break down when t is large, and a marked positive error in the weaker reflections is seen in all datasets for large thickness. This condition will require corrections which will be discussed in chapter 4. Nevertheless, the precession datasets at high angle will indeed be more amenable to Direct Methods than the dynamical dataset; for example the 127 nm PED data behaves quite similarly to the 63 nm PED data, and both would yield better structure maps than most un-precessed diffraction experiments excepting the thinnest geometries. The intensities have similar aggregate behavior over a range of thicknesses, implying a systematic character to the errors.

The plots in figure 3.8 indicate PED data can be used directly with structure solution codes with no modification up to moderate thickness (at least 30 nm). Positive error in the weak reflections primarily occurs in the low index reflections and is due to the sampling geometry; as shown in the previous section, the most errant reflections cluster near the transmitted beam because the excitation error for low index reflections is small (corresponding to slow sampling of the relrods) and in precession, systematic dynamical effects are limited to low g by the Laue circle. These errant reflections can be excluded because they are not structure-defining reflections. In the regime of moderate-to-large specimen thickness (40-70 nm), however, the errors encroach into the structurally important reflections and will require more sophisticated correction measures.

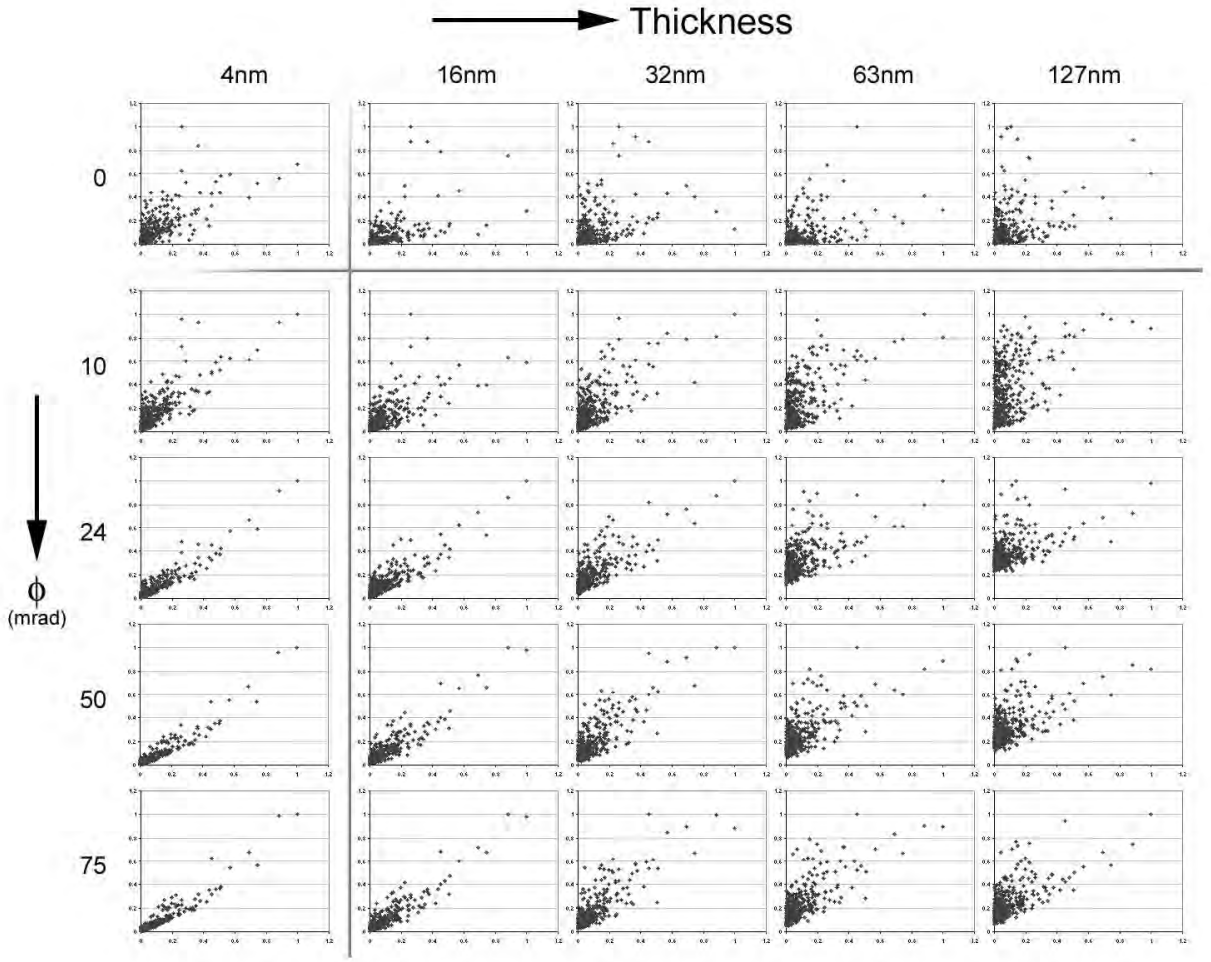

Figure 3.8. Montage of amplitude reference plots for GITO. In each plot, the abscissa represents kinematical amplitudes and calculated amplitudes are plotted along the ordinate. The plots are arranged in order of increasing thickness and angle as indicated.

3.2.2. Amplitude Error Analysis

A more thorough understanding of what is going on is afforded by examining the errors quantitatively. The deterioration of linearity between precession intensities and the kinematical reference as t increases manifests mostly in the low-g reflections. With increasing crystal thickness, the positive error of weak reflections becomes larger from geometry: since in reciprocal space the periodicity of oscillation within the sinc-like relrods is reduced (refer to figure 2.1), reflections near the transmitted beam are sampled less rapidly and therefore more intensity is integrated than higher-g reflections. A second source of error arises from dynamical effects: because dynamical effects are most prevalent near the transmitted beam (both systematic and non-systematic dynamical scattering), low-g reflections receive considerable dynamical scattering intensity. By 63 nm there is already substantial scatter in the datasets due to this phenomenon.

Realistically, to use PED data without modification, small-to-moderate thickness specimens are needed. This is a marked improvement from the conventional dynamical case: in the case of GITO, the range of experimental thicknesses that yield directly-interpretable pseudo-kinematical data (specifically yielding cation positions) is extended by about a factor of ten from a few nanometers to at least several dozen nanometers. The thickness range for which DM would be effective will predictably decrease for structures that project poorly or contain heavier atoms, and increase for materials that contain lighter atoms that project well but scatter less strongly. Examples of this can be seen in chapter 5.

A better understanding of precession in the GITO system is afforded by examining error surfaces plotted with respect to $|\mathbf{g}|$ and thickness t (Figure 3.9). These 'lobster tail' plots represent absolute deviations from kinematical of the normalized precession multislice datasets ($E_{norm} = F_{\mathbf{g}}^{exp} - F_{\mathbf{g}}^{kin}$) and give a wide view of experiment space within a single plot. Absolute errors are employed because the reflections of most interest are the strong ones (the ones that define phase relationships for other beams). Large errors correspond to intensities that should be weak and become strong due to excitation of alternate scattering paths or vice versa. Generally, low error throughout the dataset is desired, but special attention should be given to the structure-defining reflections that lie within the range 0.25-1.0 Å^{-1}. Strong reflections in this range are most important for the success of structure solution codes, and if errors in this regime are circumvented the dataset becomes more tractable.

It is important to recognize that tolerable errors correspond to about 10-20% intensity error for strong reflections ($\approx$ 40% peak amplitude error). Errors in figure 3.9 are differentiated graphically by dividing the error regime into blocks corresponding to 20% amplitude error. The regime of most interest is the band corresponding to error = $\pm$0.4 (blue/dark blue). Note that while neighboring $|\mathbf{g}|$ do not have an intrinsic relationship with each other unless they are related within systematic rows, the data have been presented as continuous surfaces to better illustrate oscillatory behavior in the error map. The bumpiness of the surface, a result of the sharpness of oscillations between neighboring $\mathbf{g}$, is a crude but effective estimator of the amount of dynamical scattering occurring within the system.

Figure 3.9(a) is the error surface for the conventional diffraction dataset plotted with respect to $\mathbf{g}$ and t. The error values reflect the classic damping effect where reflections near the transmitted beam are strong and their amplitudes decay with $\mathbf{g}$ (e.g., when intensities are large, their errors will likely be large

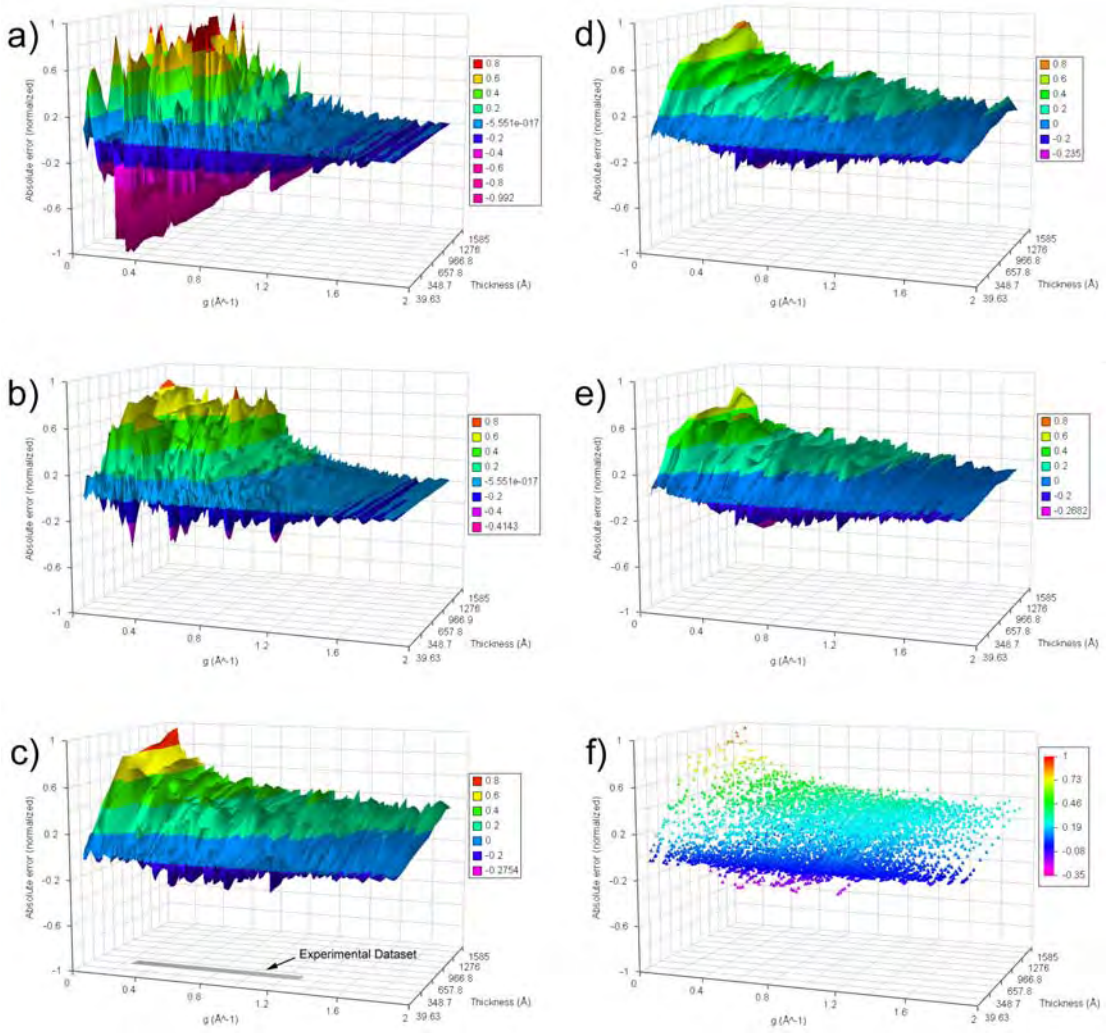

Figure 3.9. 3-D surface plots of absolute amplitude error ($F_{\mathbf{g}}^{exp} - F_{\mathbf{g}}^{kin}$) against $|\mathbf{g}|$ and thickness. (a) Dynamical (non-precessed) dataset errors showing particularly large error spread within structure-defining reflections $g \subset [0.25, 1]$. (b)-(e) Precession dataset errors for ϕ = 10, 24, 50, and 75 mrad respectively. Experimental dataset parameters are indicated in plot (c). (f) Scatter plot for 24 mrad showing that for realistic specimen thicknesses ($<$ 50 nm) almost all errors fall within the range [-0.2, 0.4].

as well). For small t, there is substantial error beyond the $\pm 40\%$ range indicating strong dynamical effects. Oscillations are relatively high in amplitude, though most errors are on the order of about 0.2-0.4. The important structure-defining reflections are the most adversely affected, with amplitude errors as high as ≈ 0.6, and demonstrate rapid oscillatory behavior with t. The thick crystal regime demonstrates

very dynamical characteristics and the largest errors are tens of thousands of percent occurring in the band of critical structural reflections.

PED at 10 mrad reduces positive errors to < 0.8 and the error surface is flattened. More notably most negative errors are eliminated (figure 3.9(b)). Gaussian radial damping is still present for all thicknesses, and 10 mrad is still quite dynamical even for small thickness where dynamical effects should be lowest, in accordance with the 10 mrad plots in figure 3.8. Increasing the angle to 24 mrad enhances the flattening effect considerably, and the error for thin crystals is greatly diminished (figure 3.9(c)). As t increases, the errors grow, especially for low $\mathbf{g}$ due to accentuated systematic dynamical effects occurring near the transmitted beam. The peak error occurs for the largest thickness (160 nm) near the transmitted beam. Large precession semi-angle (3.9(d)-(e)) decreases the overall error, and additionally flattens the low-thickness region quite like a serrated knife-edge such that intensities remain kinematical for larger t ($\approx$ 5 nm more for each 25 mrad step in angle). Figure 3.9(f) is a scatter plot for α = 24 mrad that shows that the error surface is thin (low oscillation) and is sharply tilted up toward small $\mathbf{g}$ and very large t. This is common for all precession datasets above 20 mrad.

The experimental parameter space where directly interpretable data will be available corresponds to reflections that have low aggregate error ($t < 50$ nm). This is an extremely useful range because it is easy to make real specimens (both powder and single crystal) within this dimension. As thickness increases, the positive offset of low-$\mathbf{g}$ reflections creeps into the structure-defining reflections as seen in the experimental data, necessitating corrective measures.

The results from this section are best summarized as a list of features:

(1) Precession flattens the error surface (thickness oscillations are dramatically reduced).
(2) Errors manifest as a positive offset in reflections near the transmitted beam and are exacerbated with increasing thickness.
(3) Higher precession angle further enhances the error-flattening property and reduces the errors near the transmitted beam.
(4) Higher angle can convert intensities at low $\mathbf{g}$ and small-to-moderate thickness into nearly-kinematical intensities.
(5) The above statement is not without limit - increasing angle yields diminishing returns and too high of an angle results in FOLZ overlap.
(6) Dynamical data exhibit Gaussian radial damping on the $\mathbf{g}$ axis whereas precession distributes errors over the band.
(7) PED data, bandlimited to include only structure-defining reflections, are nearly kinematical.
(8) The flattening effect is limited: corrections will be necessary for large thickness.

3.3. R-factor analysis

Until now, the discussion has centered around recovering a starting structure model. Refinements, while very successful for surfaces, may be difficult for bulk structures if the data is confounded by contributions from multiple thicknesses. In simple terms, the success of structure refinements depends upon reliably locating global minima in the error metric. The solution space for bulk structures is enormous because not only are the spatial positions variables, the thickness varies as well and is a

poorly conditioned variable (e.g., a relatively small change in thickness generates large changes in the dataset). In conventional diffraction and imaging studies of bulk structures, rapid intensity oscillation with thickness often increases errors across the dataset that either obscure the global minimum and/or create multiple minima.

It is relevant to mention the case of surface reconstructions in some detail, because refinement is often straightforward. It is known that thickness is very small so kinematical methods can often be employed where thickness is not a variable. If multislice refinement is used, the solution space to be probed is minimal because possible atom positions are usually confined due to planarity. In relation to conditioning of the thickness variable, recall that precession is less sensitive to thickness in general, evidenced qualitatively in the surface plots of figure 3.9. Bulk refinement will benefit considerably if thickness becomes a better-conditioned variable through thickness insensitivity.

In the previous section, application of DM to precession data has recovered the atom locations to within 4 picometers of the known GITO structure on average. This is essentially the correct structure, therefore, precession multislice can be compared directly with the experimental data from GITO to study the effect of thickness in PED.

R-factors (see equations 1.17 and 1.18) have been calculated for the experimental datasets (both precessed and non-precessed) against the simulated crystal thicknesses. The same atom positions and Debye-Waller factors from section 3.2 were used in the simulations, and thickness was the only parameter that was varied. A 24 mrad cone semi-angle was used for the precession simulations. Values for R_1 are plotted in figure 3.10(a), with the region around the expected thickness sampled more finely than elsewhere. The precession R-factor demonstrates a clear global minimum that spans a relatively broad range of thicknesses (30-45 nm) and the lowest value (R_1 = 11.78%, 121 symmetrized reflections measured) corresponds to a thickness of 41.2 nm. A plot of experimental amplitudes v. simulated amplitudes for this case is shown in figure 3.7. The relatively flat minimum supports the observation of thickness insensitivity because a contiguous range of t matches the experimental precession data well.

The precession R_1 values within the vicinity of the minimum are exceedingly low compared to the dynamical experiment, which oscillates with only one clear minimum (best R_1 = 43.98% at 31.7 nm, 172 reflections; note this is not a refined R_1). Additionally, the unrefined precession R_1 is much lower than those found in conventional electron crystallography refinements. For comparison, unweighted R_2 (calculated using intensities, equation 1.18) for precession is 23.6% matching the same thickness of 41.2 nm. R_2 is naturally higher because most intensities are very small in value compared to the strong beams and because it is unweighted all intensities are treated equally (small intensities in the denominator dominate the sum).

Detail plots are shown in figure 3.11 for both experimental datasets illustrating the parameter space they occupy. The critical observation is that with precession, the experimental parameters yield low absolute error and additionally maintain the same character with increasing thickness. With reflections $\mathbf{g} < 0.25$ Å^{-1} excluded, the integrated precession intensities naturally correspond quite well with the kinematical intensities.

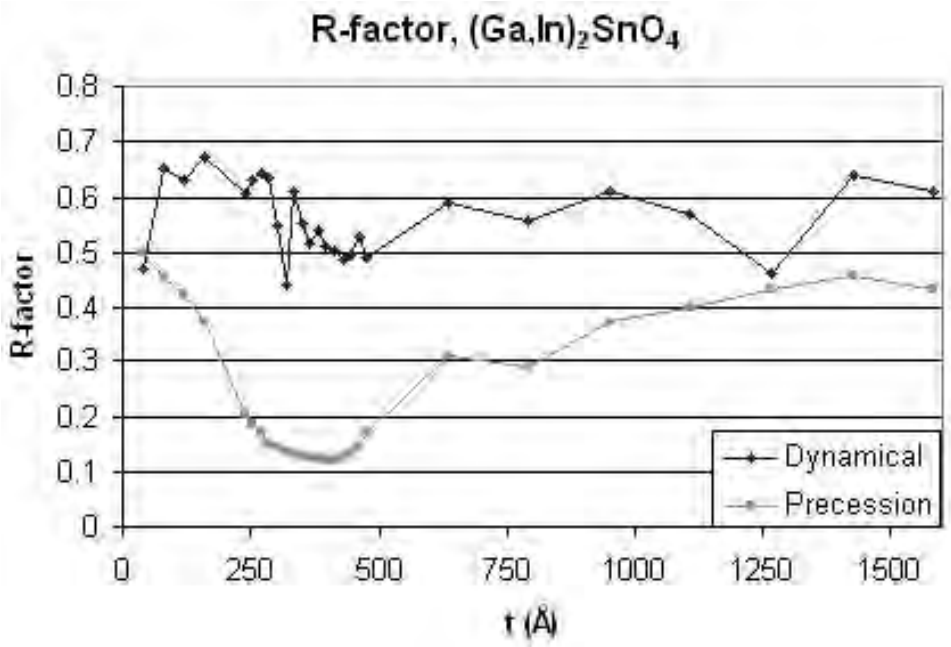

Figure 3.10. R_1 for the GITO experimental datasets. Precession datasets have a clear global minimum and indicating a nominal thickness of ≈ 40 nm.

3.4. Summary

In this chapter PED on the GITO system has been investigated in detail from the perspective of empirical results and also through simulation. An experimental dataset obtained on a high-performance precession system produced the true structure in two different ways: 1) by excluding $g < 0.25$ from the amplitude dataset, and 2) by using the intensities. The two solution methods are complementary, both valid because the thickness of the GITO specimen was within a moderate thickness regime where either method could apply within a pseudo-kinematical interpretation. The experimental results demonstrate that PED has a number of forgiving qualities:

- Zone axis patterns no longer need to be perfectly aligned because the precession angle (large in relation to a mistilt) can compensate for tilt misorientation.
- Pseudo-kinematical interpretation is possible within a large range of thickness.
- Thickness becomes a better-conditioned variable; intensities oscillate more slowly with thickness in general.
- Corrections are not necessary unless the crystal is very thick ('large' thickness).

A wealth of information has been uncovered about the behavior of PED because of multislice's ability to efficiently probe experiment space. First, the validity and robustness of precession multislice was confirmed. Analysis of the error trends over a large range of experimental parameters showed that the behavior of intensities with thickness is predictable. It was seen that errors mostly occur for beams near the transmitted beam and encroach into the structure-defining reflections ($g > 0.25$ Å^{-1})

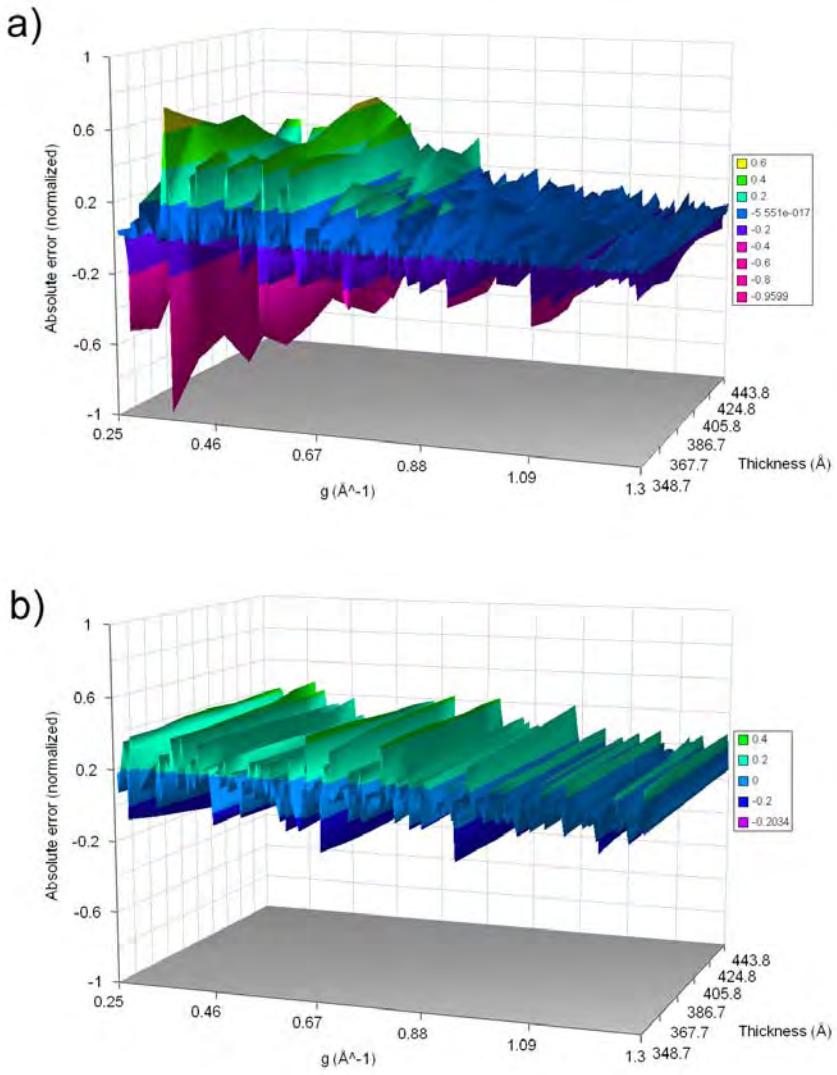

Figure 3.11. 3-D surface plots of absolute amplitude error ($F_{\mathbf{g}}^{exp} - F_{\mathbf{g}}^{kin}$) against $|\mathbf{g}|$ for (a) dynamical and (b) precession data. The ranges of $\mathbf{g}$ and t match experimental parameters from section 3.1. Errors are decreased from (a) to (b) and very little oscillation of intensity occurs with increasing thickness. Granularity of t is 3.17 Å.

for moderate to large thickness. For large thickness, correction factors are necessary to combat the low-$\mathbf{g}$ positive offset. Lastly, the thickness range for successful direct methods using only diffraction intensities has been extended from a few nm to approximately 50 nm for the GITO system.

The systematicity of the errors, in particular the clustering of large errors near the transmitted beam, is highly advantageous because phases for low-index reflections are the easiest ones to extract from

high-resolution images. For direct methods codes that predict unknown reflection intensities (such as fs98) the low-index phases from HREM can be fixed, further enhancing the probability that the direct methods algorithm will find the true structure.

Some other interesting features have been discovered. A critical precession angle exists below which dynamical behavior still dominates. Larger ϕ improves the pseudo-kinematical quality of the dataset, therefore larger cone semi-angles angles (at least 20-25 mrad) are desirable. As long as HOLZ overlap is avoided and the reflections are uniform enough that they can be easily measured, PED data should be acquired using the largest angle possible on the instrument. Additionally, if the structure is known, precession can be used to pinpoint specimen thickness to 5-10 nm accuracy. This final point warrants extra discussion. Some standard methods for determining crystal thickness in the electron microscope are HREM-multislice comparisons, electron energy loss spectroscopy on the zero loss peak, and fringe characterization in convergent beam electron diffraction (O'Keefe and Kilaas 1988; Egerton 1989; Gjønnes and Moodie 1965). These all require structure factors which may not be available when studying novel structures. Precession has an advantage here because it can possibly give the true structure which will serve as the key to unlock the thickness information simultaneously contained within the diffraction data. Keeping in mind the results from this chapter, this is limited to moderate thickness. However, in the next chapter PED's abilities will be extended to include larger thickness.

CHAPTER 4

Lorentz Correction Factors

In the last chapter, it was demonstrated that electron diffraction amplitudes extracted from PED patterns with large precession angle ϕ can be used with direct methods to generate very good starting structure maps. The only processing necessary is high-pass filtering of low-index reflections. Multislice simulations showed that — for a much larger range of experimental thicknesses than conventional diffraction — PED data has low enough error such that it is sufficient for use with direct methods without modification. However, the simulations also showed that this is not the case for large thicknesses ($>$ 50 nm), and a correction of the intensities would be required when the crystal is thick.

Precession electron diffraction is intended for finding initial starting structures from unknown materials, therefore in practice usually very little *a priori* information about the structure will be known when first investigating a novel material. The thickness is another piece of information that is almost always missing. Any practical correction factor must therefore be based upon a simple model that is highly tolerant of error within the input parameters. In other words, what is sought is a *well-conditioned* model.

While the structure of a novel material is not known, useful information is known about the characteristics of the PED experiment. First, the microscopist knows the geometry of the incident intensity, as well as where the major errors in the scattered intensities lie. Additionally, it may be possible to tell during the experiment whether the specimen spans a large range of thicknesses and/or is uniformly very thick using morphological clues (such as edge effects), thickness fringes, or the presence of diffuse scattering and/or Kikuchi lines. Finally, it is known that precession decreases dynamical coupling such that systematic paths are suppressed and, at any given time, usually only one beam is strongly excited. The simplest model that describes this is a model involving only two beams: the incident and a scattered beam.

In this chapter, the correction factors based upon two-beam approximations will be investigated in detail to understand how they work and when it is appropriate to apply them. The results will also give some new insight into how PED itself works. Some of the contents will be a more accurate reworking of the analysis previously done by Gjønnes (1997) and Vincent and Midgley (1994). First, an exact geometrical model will be established that can be evaluated numerically. This will serve as a reference for comparison with the Gjønnes correction factors. It will initially take the form of a simple kinematical correction and then will be expanded to include dynamical two-beam effects. The distinction between the kinematical geometry portion (Lorentz) and the dynamical portion will be discussed, then they will be compared to their analogues within the Gjønnes correction factors. Lastly, a comparison of these

models to multislice simulation will be given, with the goal of finding the limits of where each model is applicable to real data.

The corrections based upon two-beam dynamical theory, while simple, require that the structure factors already be known. The term *forward calculation* will be used to describe this, meaning that correction requires the structure factors be known which — if they are previously known — negates the need for calculating the correction factors in the first place. Nevertheless, the investigations of the particular corrections described in this chapter help to elucidate the nature of PED and represent a much simpler model with which to describe the physics of precession than the calculation-intensive full dynamical multislice. Additionally, the tolerance for input error is investigated.

4.1. Derivation of Correction Factors

The similarities of PED to powder diffraction were recognized early on by Vincent and Midgley (1994), who proposed the first correction factor for PED in the first paper on PED. This was based upon a two-beam dynamical model intended for correcting powder diffraction intensities (Blackman 1939). This correction factor was revised by Gjønnes (1997) to better describe the geometrical effects and a number of variations of this factor have been used in the literature (Vincent and Midgley 1994; Gjønnes et al. 1998b,a; Midgley et al. 1998; Gemmi et al. 2003). The version of the Gjønnes correction factor intended for parallel illumination (analagous to the convergent form of the Gjønnes factor in equation 1.30) is

$$I_g^{kin} \propto I_g^{corr} = \left(\mathbf{g}\sqrt{1-\left(\frac{\mathbf{g}}{2R_0}\right)}\frac{A_{\mathbf{g}}}{\int_0^{A_{\mathbf{g}}} J_0(x)dx} \right) I_g^{exp}, \tag{4.1}$$

where $\mathbf{g}$ is the reflection vector and $A_{\mathbf{g}} = \frac{2\pi t U_{\mathbf{g}}}{k}$ (as defined in Gjønnes et al. (1998a)). In the definition of $A_{\mathbf{g}}$, t is the specimen thickness in Ångströms, $U_{\mathbf{g}}$ is the structure factor, and k is the wavevector magnitude of the incident radiation. Equation 4.1 represents two corrections: 1) a pre-factor to correct for geometry (Lorentz portion) and 2) a two-beam dynamical correction (Blackman portion).

There are two problems with equation 4.1. First note that the value of $A_{\mathbf{g}}$, which must be defined absolutely, is critical for calculating the correct value of the integrated intensity. As pointed out in section 1.4.2, the argument of the integrand in equation 4.1 is different from that used in the Blackman formula (equation 1.24) by a factor of two, altering the periodicity of the Bessel function J_0. The forms of $A_{\mathbf{g}}$ used in Gjønnes (1997) and Gjønnes et al. (1998b) had conflicting definitions and, furthermore, the structure factors ($U_{\mathbf{g}}$) that were used to define $A_{\mathbf{g}}$ had not been clearly defined. Without knowledge of the pre-factor constants, the correctness of $A_{\mathbf{g}}$ in these studies is not certain. The second problem is that an assumption has been made that the geometry effects can be separated from the dynamical scattering effects. The conditions for this approximation to hold were not specified in the derivation of the correction factor (Gjønnes 1997).

In this section, the correction will be re-derived using kinematical and two-beam electron diffraction theory. The re-derivation is more exact than the previous models and will be used to explore the limits

of their approximation. For completeness, the original derivation by Blackman (1939) is included at the end of this section in section 4.1.3. The reader is referred to Gjønnes (1997) for the derivation of the Lorentz portion in equation 4.1.

4.1.1. Kinematical Precession

Recall from section 2.1 that the intensity measured in precession represents a finite integration of the scattered intensity. The relevant geometry, shown previously as figure 2.1, is reproduced here as figure 4.1. The intensity scattered by the crystal is the true intensity ${F_{\mathbf{g}}}^2$ multiplied by some function dependent upon specimen dimensions. Intensity is scattered when this shape function — which manifests in reciprocal space as a rod shape (relrod) — is intercepted by the Ewald sphere. The true intensity can also be recovered by dividing the measured intensity by the value of the shape function at the interception point, described by excitation error $\mathbf{s_g}$. Similarly, the true intensity can be recovered from the measured *integrated* intensity from PED by dividing by the integrated shape function, in other words

$$|F_{\mathbf{g}}|^2 \propto I_{\mathbf{g}}^{corr} = C(\mathbf{g}, t, \phi) I_{\mathbf{g}}^{exp}, \tag{4.2}$$

where $C_{\mathbf{g}}$ is inversely proportional to the precession integral of the shape function of the scattered intensity.

In this derivation, we seek to evaluate the integral of the scattered intensity over excitation error that occurs during the precession:

$$I_{\mathbf{g}}^{prec} = \int I_{\mathbf{g}}(\mathbf{s_g}) d\mathbf{s_g}. \tag{4.3}$$

Equation 4.3 is more conveniently treated as an integration over the precession variable θ representing the circuit traced by the Laue circle, given by

$$I_{\mathbf{g}}^{prec} = \int_0^{2\pi} I(\theta) d\theta. \tag{4.4}$$

The change of variables can be made starting from the equation of the Ewald sphere:

$$(x - \mathbf{k}_x)^2 + y^2 + (z - \mathbf{k}_z)^2 = \mathbf{k}^2, \tag{4.5}$$

where $\mathbf{k} = 1/\lambda$, and $\mathbf{k}_x$ and $\mathbf{k}_z$ represent the deviation of the Ewald sphere origin in x and z, respectively, due to precession. For a reflection $\mathbf{g}$ located at $(x, y) = (|\mathbf{g}| \cos\theta, |\mathbf{g}| \sin\theta)$, the Cartesian variables can be converted to functions of θ starting with the substitution

$$(\mathbf{g} \cos\theta - \mathbf{k}_x)^2 + (\mathbf{g} \sin\theta)^2 + (z - \mathbf{k}_z)^2 = \mathbf{k}^2. \tag{4.6}$$

Simplifying using geometric identities, substituting $\mathbf{s_g}$ for z, and utilizing $|\mathbf{k}_x|^2 + |\mathbf{k}_z|^2 = |\mathbf{k}|^2$, this reduces to

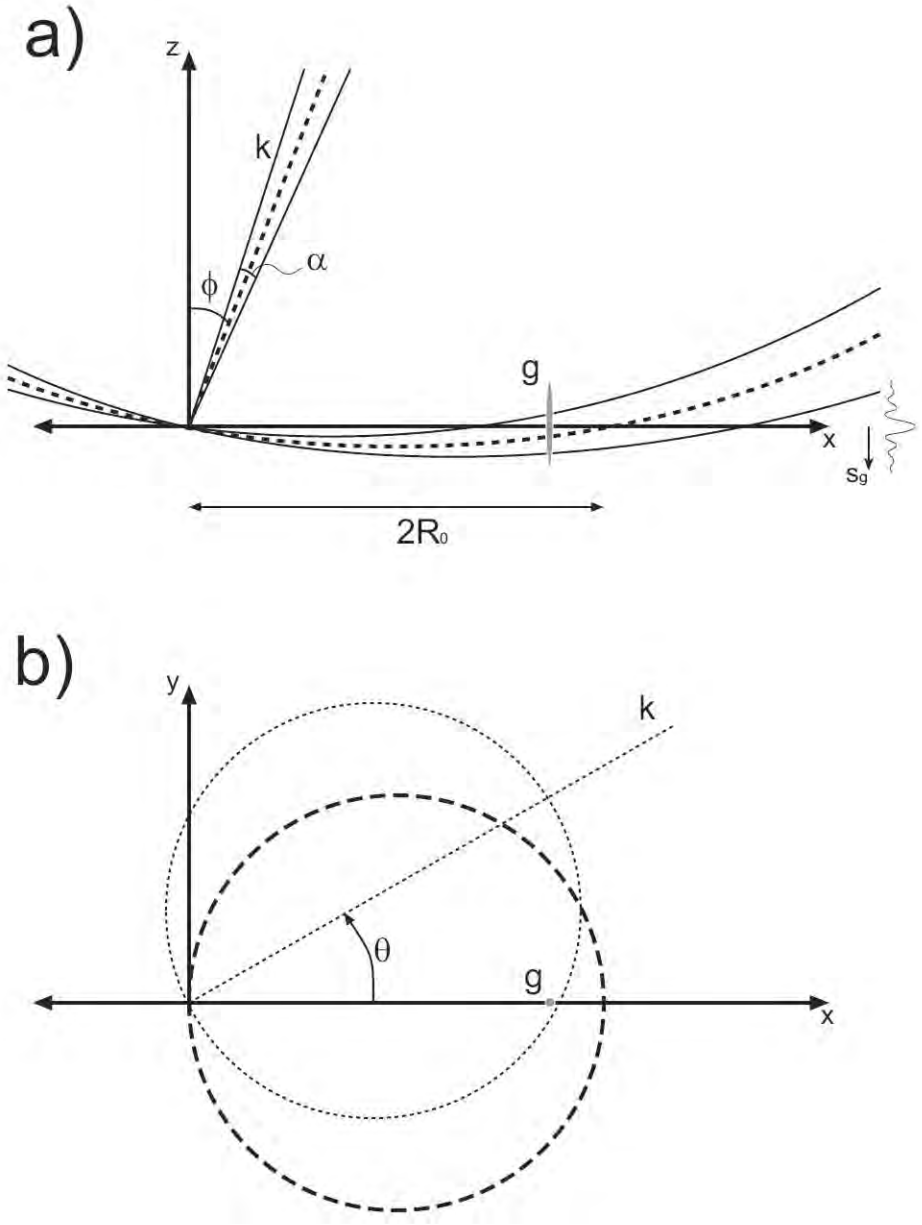

Figure 4.1. Reciprocal space geometry of P.E.D. in (a) $x-y$ plane and (b) $x-z$ plane. The beam precesses about the z-axis maintaining constant ϕ. In (b), the ZOLZ (bold dashed circle) precesses about the z-axis.

$$\mathbf{g}^2 - 2\mathbf{k}_x\mathbf{g}\cos\theta - 2k_z s_{\mathbf{g}} = 0, \tag{4.7}$$

where s^2 is very small and has been eliminated from the previous equation. Since $\mathbf{k}_z \approx \mathbf{k}$, and $\mathbf{k}_x \approx \mathbf{k}\phi$ in the limit of small ϕ, this is rearranged to get excitation error as a function of θ:

$$\mathbf{s_g}(\theta) = \frac{g^2 - 2k\phi g\cos\theta}{2k}. \tag{4.8}$$

In kinematical scattering theory, the relrods representing the scattered intensity are described by the inversion of the top hat function, therefore

$$I(\mathbf{s_g}) = \frac{1}{\xi_\mathbf{g}^2}\frac{\sin^2(\pi t s_\mathbf{g})}{{s_\mathbf{g}}^2}. \tag{4.9}$$

The characteristic length $\xi_\mathbf{g}$ (also called the extinction distance) is a function of the experimental variables structure factor $F_\mathbf{g}$, unit cell volume V_c, electron wavelength λ, and Bragg angle θ_B given by

$$\xi_\mathbf{g} = \frac{\pi V_c\cos\theta_B}{\lambda F_\mathbf{g}}. \tag{4.10}$$

The correction factor follows from equations 4.8 and 4.9, giving

$$\int_0^{2\pi} I(\theta)d\theta = \frac{1}{\xi_\mathbf{g}^2}\int_0^{2\pi}\frac{\sin^2\left\{\pi t\left(\frac{g^2-2k\phi g\cos\theta}{2k}\right)\right\}}{\left(\frac{g^2-2k\phi g\cos\theta}{2k}\right)^2}d\theta \equiv \frac{1}{C_{kin}(g,t,\phi)}. \tag{4.11}$$

In equation 4.11, the function within the integral over θ yields two peaks, illustrated in figures 4.1(b) and 4.2. A relrod with $g < 2R_0$ enters the zeroth Laue 'bowl' once and then exits once as θ traverses 2π. The excitation error, describing the deviation from the Bragg scattering condition, traces a cosine curve shifted in the z-axis due to the curvature of the Ewald sphere and scaled depending upon distance of the reflection from the origin (equation 4.8). During the precession, reflections close to the origin are sampled slowly with smaller excitation error, so the shape of the modulus-squared of the sinc function along the θ-axis is widened and more intensity is sampled per unit time from low-$\mathbf{g}$ reflections than from high-$\mathbf{g}$ reflections. The higher-index reflections are more rapidly sampled, hence the squared sinc functions are narrow in the θ-axis. A large cone semi-angle ϕ increases the range of $\mathbf{s_g}$ over which the integration occurs, and in practice almost all reflections (except for very low indices) are rapidly sampled.

The model in equation 4.11 is useful as a starting correction, especially for thin specimens and large precession angle. However, apart from geometry errors, dynamical effects become prominent with increasing thickness, as evidenced in the lobstertail error plots in figure 3.9. In order to deal with specimens that are thicker, a more sophisticated model is needed to account for these effects.

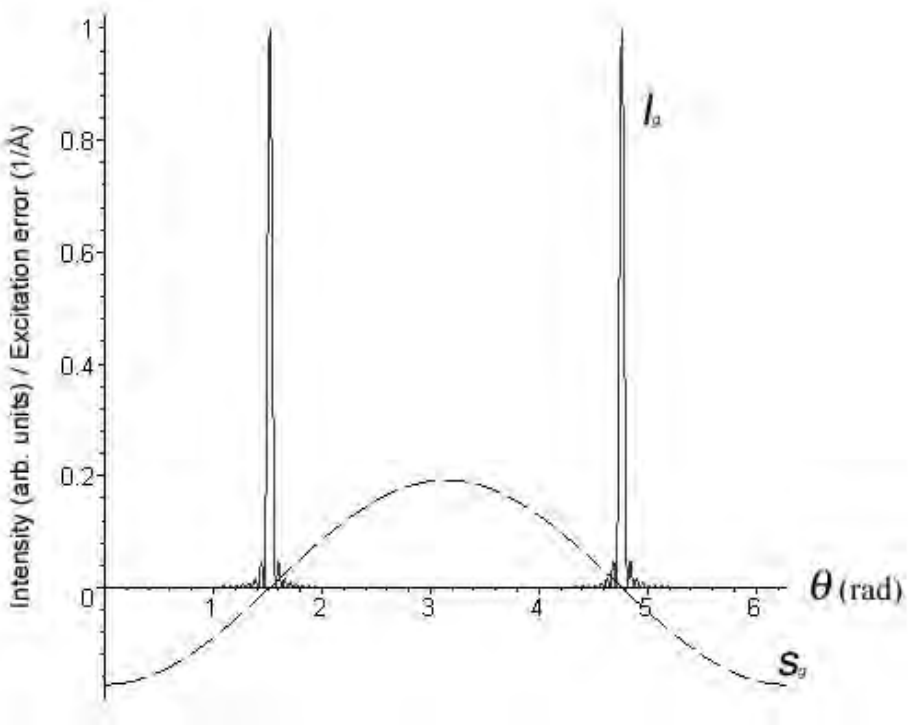

Figure 4.2. Intensity collected ($I_{\mathbf{g}}$) and excitation error ($s_{\mathbf{g}}$) during the integration in the kinematical model, plotted against azimuthal angle for a low-index reflection ($|\mathbf{g}| = 0.1R_0$, where $R_0 \approx \phi k = 0.96$ Å). Parallel illumination, with t = 100 Å, ϕ = 24 mrad, 200 kV.

4.1.2. Introduction of Two-beam Dynamical Excitation

When $\mathbf{s_g}$ = 0, equation 4.9 reduces to $I(s_{\mathbf{g}}) = (\pi t/\xi_{\mathbf{g}})^2$, meaning the diffracted intensity can exceed the incident intensity when $t > \xi_{\mathbf{g}}/\pi$. This is not physical, and a better model is realized by considering the interaction of two beams propagating in a perfect crystal (Hirsch et al. 1965). The solutions to the analytical equations that describe this two-beam interaction are a pair of Bloch waves with relative magnitudes dependent upon the orientation of the crystal (e.g., the linear combination of the two must always meet the boundary condition at the exit surface). The scattered intensity is governed by a new deviation parameter called the effective excitation error, defined as

$$\mathbf{s}_{\mathbf{g}}^{eff} = \sqrt{\mathbf{s}_{\mathbf{g}}^2 - \frac{1}{\xi_{\mathbf{g}}^2}}. \tag{4.12}$$

The effective excitation error modifies equation 4.9 to account for dynamical exchange between the transmitted and diffracted beams, giving

$$I(\mathbf{s_g}) = \frac{1}{\xi_\mathbf{g}^2} \frac{\sin^2(\pi t s_\mathbf{g}^{eff})}{(s_\mathbf{g}^{eff})^2}. \tag{4.13}$$

When $\xi_\mathbf{g} > t$, the scattered intensity behaves like a conventional sinc function (with new scaling and periodicity — see the solid curve in figure 4.3). However, when $\xi_\mathbf{g} < t$, the scattered intensity at zero excitation error begins to fall, creating a minimum between two nodes centered about $s_\mathbf{g} = 0$ for some combinations of t and $\xi_\mathbf{g}$. The most dramatic change occurs when the argument of the sine function in the numerator of equation 4.13 becomes $n\pi$, where n is an integer (e.g., $\frac{t}{\xi_\mathbf{g}} = n$), at which point the scattered intensity at $\mathbf{s_g} = 0$ falls to zero (dashed curve in figure 4.3).

The two-beam correction factor for precession thus comprises the integration along $\mathbf{s_g}$ of intensity profiles that vary with the extinction distance and specimen thickness (extinction distance is in turn inversely proportional to the structure factor). It models the exchange of intensity between the diffracted and transmitted beams and is valid when only one diffracted beam is strongly excited. Substituting 4.12 in 4.11, the exact two-beam correction factor is obtained:

$$\int_0^{2\pi} I(\theta) d\theta = \frac{1}{\xi_\mathbf{g}^2} \int_0^{2\pi} \frac{\sin^2(\pi t s_\mathbf{g}^{eff})}{(s_\mathbf{g}^{eff})^2} d\theta \equiv \frac{1}{C_{2beam}(g, t, \phi)}. \tag{4.14}$$

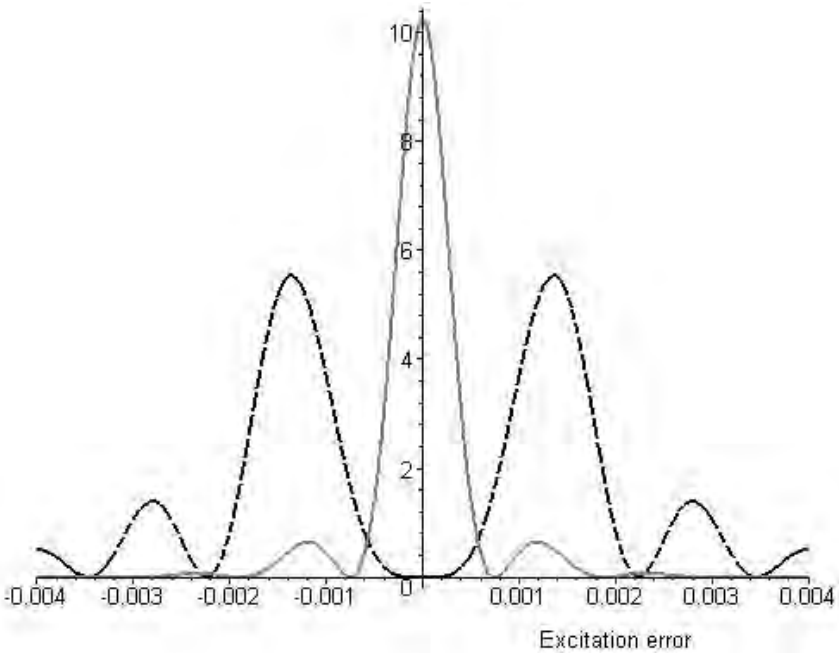

Figure 4.3. Scattered intensity ($I_\mathbf{g}$) v. excitation error ($s_\mathbf{g}$) in the two-beam model. Thickness $t = 500$. For the solid curve $\xi_\mathbf{g}$ = 1500 Å and for the dashed curve $\xi_\mathbf{g}$ = 500 Å (intensities not to scale). The binodal behavior occurs when $t > \xi_\mathbf{g}$.

4.1.3. The Blackman Formula Revisited

In the early paper by Blackman (1939), the intensities of powder rings were elegantly described by two-beam dynamical theory. Using the same approach as presented in the previous section, the Blackman formula arises from a simple identity of the integrated scattered intensity. Equation 4.13 can be rewritten in slightly different form:

$$I_{\mathbf{g}} = I_0 \frac{\sin^2 A_{\mathbf{g}} \sqrt{(W^2+1)}}{W^2+1}. \tag{4.15}$$

Here, I_0 is the incident beam intensity, assumed to be 1 in equation 4.13, $A_{\mathbf{g}} = \frac{\pi t}{\xi_{\mathbf{g}}} \propto F_{\mathbf{g}} t$, and $W = \mathbf{s}_{\mathbf{g}} \xi_{\mathbf{g}}$. In powder and polycrystal diffraction, each constituent crystal is illuminated off of the zone axis by some angle ϕ, causing a corresponding excitation error for a given $\mathbf{g}$. A simple change of variables gives the excitation error as a function of this angle: $\mathbf{s}_{\mathbf{g}} = 2k\theta\phi$. If the crystal is rocked with angular speed $\omega = \frac{d\phi}{dt}$, the total reflected intensity becomes

$$\begin{aligned} I^{tot} &= \frac{I_0}{\omega} \int_{-\infty}^{+\infty} \frac{\sin^2(A_{\mathbf{g}} \sqrt{(W^2+1)})}{W^2+1} d\phi \\ &\propto \frac{I_0}{2k^2\theta\omega} \frac{F_{\mathbf{g}}}{V_c} \int_{-\infty}^{+\infty} \frac{\sin^2(A_{\mathbf{g}} \sqrt{(W^2+1)})}{W^2+1} dW. \end{aligned} \tag{4.16}$$

The integration of the sinc function in equation 4.16 is equivalent to π times the integral from 0 to $A_{\mathbf{g}}$ of the zeroth order Bessel function. This identity gives the basic form of the Blackman formula:

$$\begin{aligned} I^{tot} = I_{\mathbf{g}}^{dyn} &= \frac{\pi I_0}{2k^2\theta\omega} \frac{F_{\mathbf{g}}}{V_c} \int_0^{A_{\mathbf{g}}} J_0(2x) dx \\ &\propto A_{\mathbf{g}} \int_0^{A_{\mathbf{g}}} J_0(2x) dx. \end{aligned} \tag{4.17}$$

It is important to note that the structure factors used to calculate $A_{\mathbf{g}}$ must be known as accurately as possible or the periodicity and amplitude of the integral will be altered. Figure 4.4 shows equation 4.17 plotted for the three strongest reflections in GITO. The strongest reflection has the greatest average intensity, and the average intensities decrease with decreasing structure factor. Note that in some thickness ranges such as 350-500 Å, the intensity of the strongest reflection drops below that of the next-strongest reflections.

The plots in figure 4.4 represent the Bessel integral for exact thickness values, however in real specimens there is usually some thickness variation Δt . The effect of thickness averaging on equation 4.17 in PED has previously been pointed out by Gjønnes et al. (1998b). In this model, Δt will generate a range of oscillation periodicities; superposition of scattered intensity from a range of thicknesses generates an effective curve that has reduced oscillation amplitude and slightly decreased intensity. The behavior at small $A_{\mathbf{g}}$, however, will remain essentially the same. In other words, the integral scales linearly with $A_{\mathbf{g}}$ regardless of thickness variation for small $A_{\mathbf{g}}$, but for large $A_{\mathbf{g}}$ the oscillations are

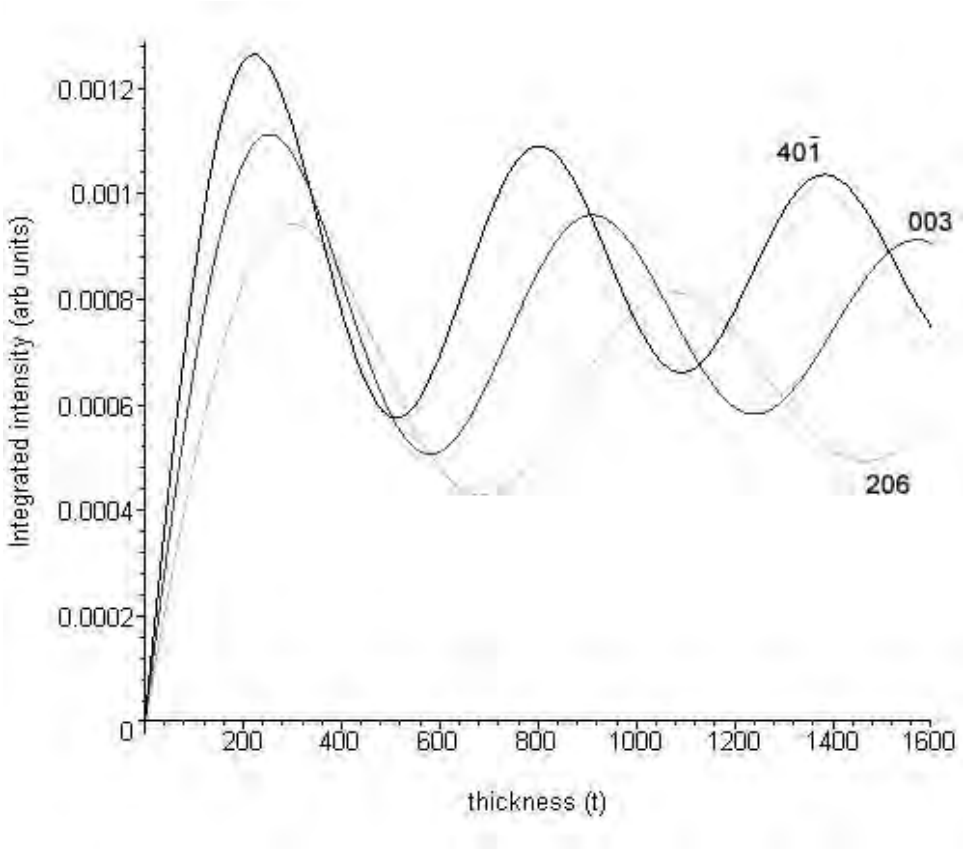

Figure 4.4. Equation 4.17 plotted for the three strongest reflections in GITO. The oscillation periodicities are slightly different because the extinction distance $\xi_{\mathbf{g}}$ varies between reflections. The extinction distances are 580 Å, 660 Å, and 780Åfor the 40$\bar{1}$, 003, and 206 reflections, respectively.

damped and converge more rapidly to their final value when $\Delta t \neq 0$. This is advantageous because strong reflections will more likely maintain kinematical phase relationships between each other when there is some variation in thickness (recall equation 1.27).

4.2. Comparison between models

Five models of precession have now been discussed. To summarize, they are:

- Finite integration limits:
  - (1) Kinematical integral over $\mathbf{s_g}$ (Lorentz portion);
  - (2) Dynamical (two-beam) integral over $\mathbf{s}_{\mathbf{g}}^{eff}$;
- Gjønnes form:
  - (3) Lorentz portion (approximation of (1));

(4) Lorentz and Blackman combined (approximation of (2); the Blackman portion has infinite integration limits);

- (5) Multislice (described in chapter 3).

Table 4.1 shows the different forms of the correction and some nomenclature by which to refer to them in the following sections. The fact that the Blackman formula also represents an integration of the two-beam condition is understood. However, for naming convenience, correction (2) will be denoted C_{2beam} while correction (4) will be denoted $C_{Blackman}$.

The multislice model is exact and effectively describes the physical behavior of PED, as demonstrated in section 3.2. Multislice will serve as the reference for comparing the approximate models listed above. We begin with a general discussion of their relationships, looking at trends from a theoretical standpoint. Later in this section, these relationships will be proven in practice by comparing the effectiveness of the correction factors at linearizing the simulated datasets.

4.2.1. Expected Trends

The integration limits along s_g are an important characteristic within the proposed models. Assuming for the time being that the scattered intensity in precession is always either kinematical or two-beam in nature (not n-beam where $n > 2$), the corrections C_{Gj} and $C_{Blackman}$ approximate the more exact corrections C_{kin} and C_{2beam} only if the precession has integrated nearly all of the scattered intensity. The conditions where this is satisfied are investigated below.

Figure 4.5 shows the behavior of the integral of the squared sinc function as a function of the integration limits. Most of the intensity is contained within the first period of the sinc function, and 98% of the intensity is sampled by integrating 5 periods. Beyond 5 periods, the integral converges toward unity more slowly, and 99% of the intensity is sampled only after integrating 10 oscillation periods. Depending upon the detector sensitivity and the amount of thickness averaging, experimental error is often within 3-5%, hence the integral can be considered complete as long as 5-10 periods are sampled *and* the sampled periods include the region near $\mathbf{s_g} = 0$. The latter constraint arises because the correction factors are inversely related to the integrated intensity; if only a tail of the squared sinc function is sampled, the integrated intensity is very small and both experimental measurement and calculation become unreliable due to, respectively, insufficient signal-to-noise ratio and numerical error.

This behavior is still true when two-beam dynamical effects are introduced. The binodal curve that occurs when $t > \xi_{\mathbf{g}}$ exhibits the same behavior except the intensity within the tails does not damp as rapidly as in the squared sinc function (see the dashed curve in figure 4.3). The consequence is that a larger number of periods must be sampled for complete integration. The Blackman integral is a bipolar integration, therefore in order to apply it to precession data, all correction factors within the dataset must represent relatively complete integrations over both positive and negative excitation error.

To understand where the approximation $C_{Blackman}$ breaks down, it must be noted where the integration does not sufficiently sample the intensity scattered into the reciprocal lattice rods. Figure 4.6(a) shows the limits of the excitation error in the PED experiment. The minimum negative excitation error exceeds the maximum positive excitation error, and their ratio scales roughly with g. For example, the most positive excitation error occurs at the center of the Laue bowl when $g = R_0$ (reflection $\mathbf{g}$ in 4.6(a)),

Table 4.1. Correction factors for correcting PED intensities. Note $C_{Blackman}$ has corrected integrand. The prefactor $\frac{1}{\xi_{\mathbf{g}}^2}$ in corrections 1-2 can be approximated by $F_{\mathbf{g}}^2$ in the case of swift electrons.

	Moniker	Type	Equation no.	Form
1	Finite kin	Goemetry only	4.11	$C_{kin}(g,t,\phi) = \left(\frac{1}{\xi_{\mathbf{g}}^2}\int_0^{2\pi}\frac{\sin^2\pi t(s_{\mathbf{g}})}{(s_{\mathbf{g}})^2}d\theta\right)^{-1}$
2	Finite dyn	Full correction	4.14	$C_{2beam}(g,t,\phi) = \left(\frac{1}{\xi_{\mathbf{g}}^2}\int_0^{2\pi}\frac{\sin^2(\pi t s_{\mathbf{g}}^{eff})}{(s_{\mathbf{g}}^{eff})^2}d\theta\right)^{-1}$
3	Gjønnes	Geometry only	4.1	$C_{Gj}(g,\phi) = \mathbf{g}\sqrt{1-\left(\frac{\mathbf{g}}{2R_0}\right)}$
4	Gjønnes × Blackman	Full correction	4.1	$C_{Blackman}(g,t,\phi) = \mathbf{g}\sqrt{1-\left(\frac{\mathbf{g}}{2R_0}\right)}\frac{A_{\mathbf{g}}}{\int_0^{A_{\mathbf{g}}}J_0(2x)dx}$
5	Multislice	Exact	1.16	none (exact)

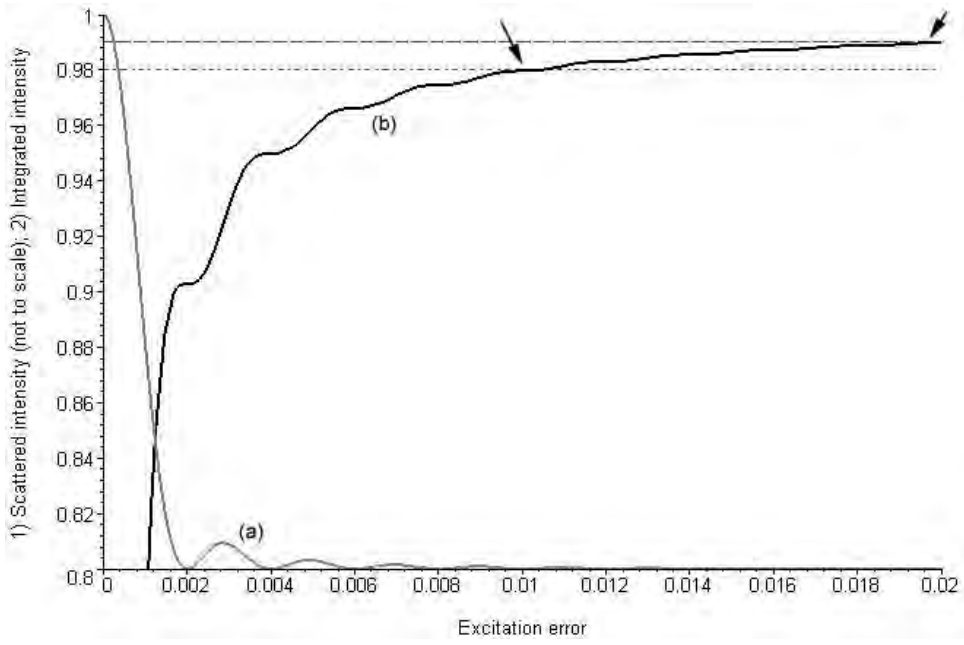

Figure 4.5. The squared sinc function (a) and the integral of the sinc function (b) plotted against excitation error for a crystal thickness of 500 Å. The integral converges rapidly toward unity as indicated by the arrows: 98% of the intensity is sampled when 5 oscillation periods are integrated, and 99% of the intensity is sampled by 10 oscillation periods.

giving $s_{\mathbf{g}} = k(1 - \cos 0.024) \approx 0.012$ Å^{-1} for the experimental conditions of 200 kV and 24 mrad cone semi-angle (k is about 40 Å^{-1}). The most negative excitation error for reflection $\mathbf{g}$ is $s_{\mathbf{g}} \approx 0.035$ Å^{-1}. Typical extinction distances for strong reflections are on the order of a few hundred Ångströms or greater, and crystal thicknesses are normally greater than 50 Å, giving an oscillation periodicity of < 0.005 Å^{-1} for the strongest reflections. Under these conditions, over a dozen periods of the shape function will be integrated as illustrated in figure 4.6(b).

The worst-case scenario occurs when the sinc-like function describing the scattered intensity has a large period in reciprocal space. This will occur when extinction distance (large structure factor) and specimen thickness are small, both on the order of 50 Å. This is very rare because the smallest $\xi_{\mathbf{g}}$ occurs for the strongest reflections, of which there are not many, and specimens are usually more than 200 Å thick. Recall the earlier example where the integration limits were -0.035 Å^{-1} and 0.012 Å^{-1} for a reflection at $g = R_0$. For a material with t = 250 Å and $\xi_{\mathbf{g}} = 60$ Å, only about 7 oscillations will be integrated and the Gjønnes corrections will have greater than 15% error. For GITO, which has a very large unit cell volume, and correspondingly large extinction distance of 580 Å for its strongest reflection (index $40\bar{1}$), the intensity will be sufficiently integrated under most experimental conditions.

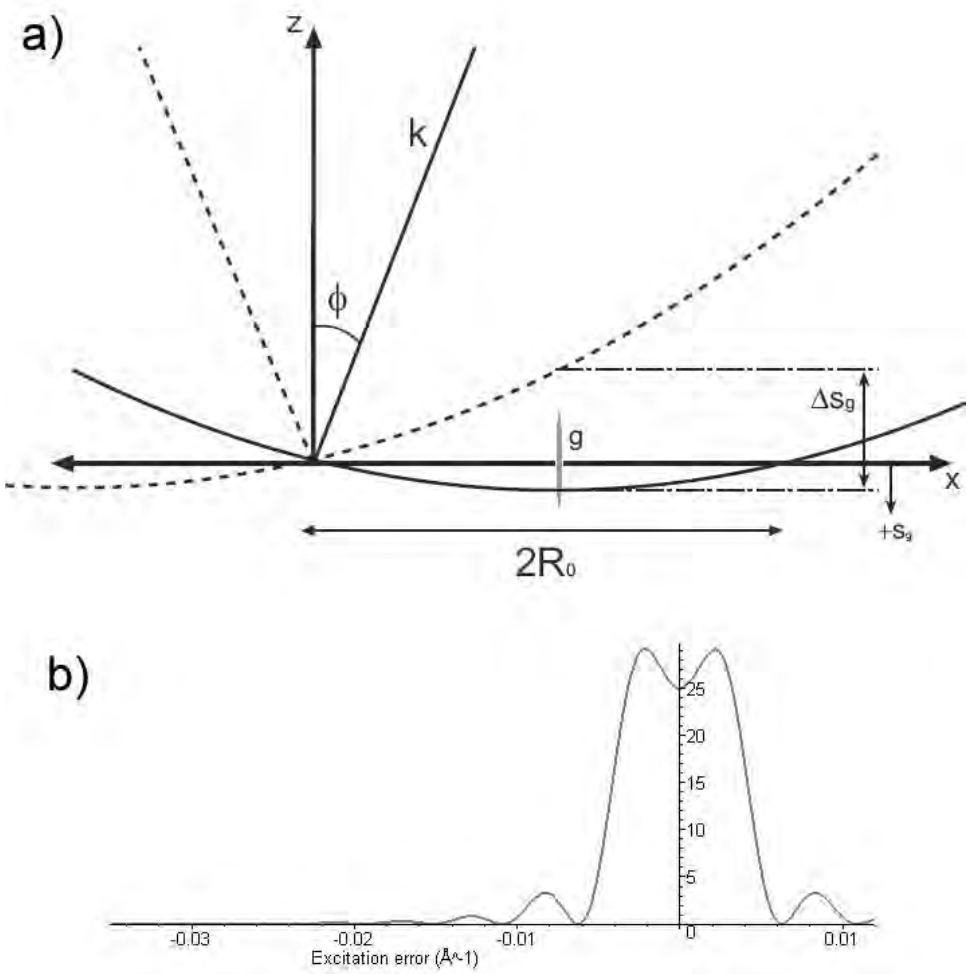

Figure 4.6. (a) The integration range $\Delta \mathbf{s_g}$ for reflection $\mathbf{g}$ located at $x = R_0$. Excitation error is positive in the $-z$ direction. (b) The scattered intensity over the range Δs from (a) for a crystal with $t = 200$ Å and $\xi_{\mathbf{g}} = 250$ Å.

When $g > 2R_0$, positive excitation error does not occur. Corrections C_{Gj} and $C_{Blackman}$ break down beyond this point and are no longer applicable. However, the correction factors with finite integration limits (C_{kin} and C_{2beam}) will still be applicable slightly beyond $2R_0$ because the negative half of the sinc function is still integrable. Nevertheless, the correction factor will soon blow up beyond $2R_0$ and will be much less practical than simply extending the ZOLZ radius by increasing the cone angle ϕ (figure 4.7). In other words, the precession angle should be chosen such that the largest g of interest in the diffraction pattern is smaller than $2R_0$ by at least $0.25R_0$. Reflections with sufficient intensity to be measurable are typically within about 1.5 Å^{-1}, so ϕ = 20-25 mrad (at 200 kV) is the minimum acceptable angle for PED studies where correction factors are applied.

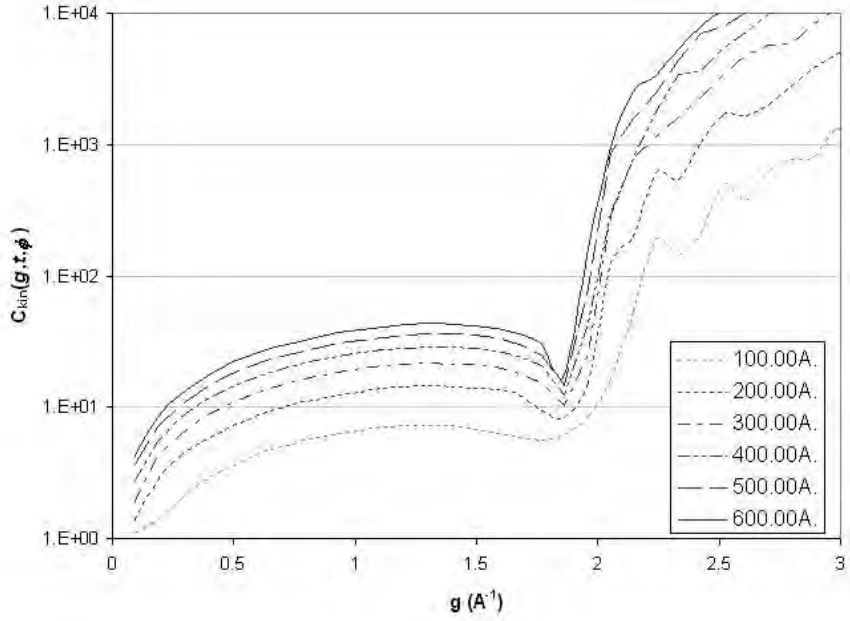

Figure 4.7. The kinematical correction factor C_{kin} for crystal thicknesses between 100 Åand 600Å, for ϕ = 24 mrad. The correction factors behave nearly identically (with scaling) for $g < 1.8$ Å^{-1}, corresponding to about twice the radius of the zeroth order Laue zone ($2R_0$). Beyond $2R_0$, the correction factor is inversely proportional to the area within the tails of the relrod where there is very little scattered intensity, and the correction factor blows up.

Exploring cone angle selection further, recall that the structurally important reflections generally fall within the band g = 0.25-1.5 Å^{-1}, so it is advantageous to have larger cone angle to increase the positive limit of integration within this band (e.g., deepen the Laue bowl). Furthermore, recall from chapter 3 that going off-zone reduces simultaneous excitation of multiple strong reflections, thereby reducing amplitude errors in the PED dataset. Fortuitously, the constraints necessary for good integration coincide with the reduction of dynamical effects: large cone angle improves the correction factors by extending the integration limits along $s_{\mathbf{g}}$, and additionally reduces multiple scattering effects such that two-beam theory is adhered to better.

4.2.2. Comparison of Calculated Corrections Factors

The cases where the Gjønnes forms C_{Gj} and $C_{Blackman}$ deviate from the finite integration corrections C_{kin} and C_{2beam} will be illustrated first. Figure 4.8 shows C_{2beam} and $C_{Blackman}$ calculated for a number of thicknesses and tilt angles. Dynamical effects are reduced in thin crystals, so C_{2beam} and

$C_{Blackman}$ (the full corrections) converge with the geometry-only corrections C_{kin} and C_{Gj}, respectively, in the limit of small t (applicable in figures 4.8(a)-(c)). Figures 4.8(a)-(c) represent small thickness, where the agreement between C_{2beam} and $C_{Blackman}$ models is poorest. A number of conclusions can be drawn from the figures:

- Small thickness produces a large oscillation period in the relrods, meaning that the integration along $s_{\mathbf{g}}$ is incomplete for many reflections. Therefore for small t, C_{Gj} represents a poor approximation to C_{kin}; in other words, $\mathrm{C}_{Blackman}$ does not match C_{Gj} (figures 4.8(a)-(c)).
- Small cone semi-angle ϕ combined with small t results in the worst agreement between C_{2beam} and $\mathrm{C}_{Blackman}$ (figure 4.8(a)).
- Larger cone semi-angle improves the agreement between C_{kin} and C_{Gj} (figure 4.8(b)-(c)) due to larger integration limits along $s_{\mathbf{g}}$.
- The dynamical effects are reduced at small t, therefore Lorentz geometry dominates the correction factor. The tiny peaks on the $C_{Blackman}$ curve in figure 4.8(c) are dynamical corrections.
- $C_{Blackman}$ converges with C_{2beam} for larger thickness because periodicity in the relrod is small. Dynamical effects are accentuated, therefore a large correction is necessary for many reflections 4.8(d). For very large thickness, the dynamical correction is much larger than the geometry background.

As seen in chapter 3, the small thickness regime is where a correction factor is not strictly necessary; it is instead the large thicknesses ($>$ 50 nm) where the correction factors are needed. For crystals with large thickness, the shape function has much smaller periodicity, so the integration within finite limits converges toward the integration over all excitation error and correction $C_{Blackman}$ is a good approximation to C_{2beam}. This agreement is demonstrated in figure 4.8(d): the whale-shaped background curve (Lorentz contribution) is consistent between the two corrections at 634 Å, and the peaks match to within a few percent. Note that the corrections are plotted as curves to accentuate the peaking and the correction factors are not really continuous: each peak represents a correction for a specific reflection.

At large thickness, dynamical effects naturally begin to dominate. This is clearly seen in figure 4.8(d), where many reflections within the structure-defining regime 0.25-0.75 Å^{-1} have large corrections above the background curve. The key observation is that the correction factor *selectively* corrects reflections that have large error due to dynamical scattering. A second major point is that at large thickness, where relrods have small oscillation period, the geometry can indeed be separated from the thickness-dependent dynamical effects and the geometry can be approximated in the limit of moderate-to-large thickness by C_{Gj} which is independent of thickness. The net correction is reduced to the product between the Lorentz and Blackman terms.

Figure 4.9 shows the trends in more detail using plots of C_{2beam} for various thicknesses (increasing horizontally) and cone angles (increasing down each column). The thicknesses are large enough that $C_{Blackman}$ is a good approximation and will yield similar results for all plots except the top left (ϕ = 10 mrad, t = 32 nm). Small cone angles yield incomplete integration of scattered intensity and the errors become substantial beyond $g = 2R_0$. The integration is fairly complete with larger cone angle, evidenced by the decay of dynamical-type corrections (spikes) at higher g within the plots. Large corrections are necessary for the reflections in the structure-defining range of 0.25-1 Å^{-1}. For very

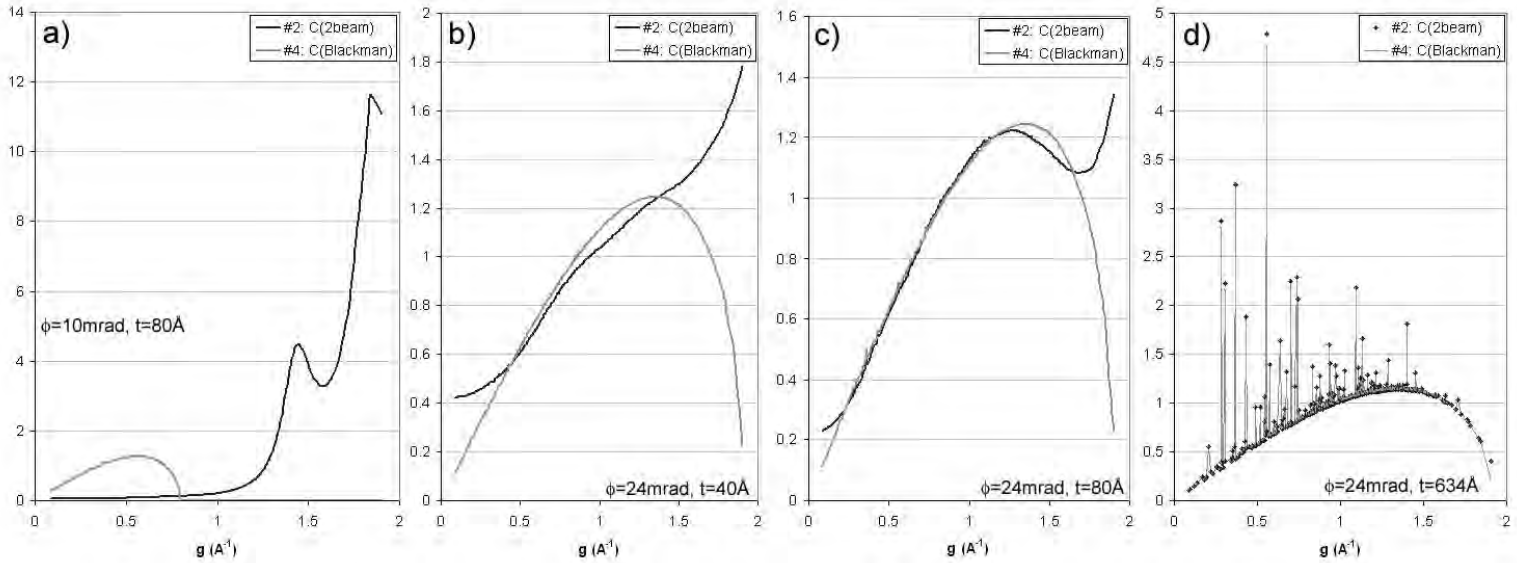

Figure 4.8. Comparison of the full correction factors C_{2beam} and $C_{Blackman}$ from table 4.1 plotted against g. (a)-(c) When t is small, $C_{Blackman}$ does not match C_{2beam} well at small thickness. Recall that dynamical effects are reduced for small t, therefore the full corrections converge with their simpler geometry-only equivalents, C_{kin} and C_{Gj}, respectively. Consequently, C_{kin} is the better correction for small thickness. (c) For larger tilt angle, $C_{Blackman}$ matches C_{2beam} for $g < R_0$. Small peaks begin to appear on top of the geometry term (whale-shaped curve) as thickness increases. (d) $C_{Blackman}$ matches C_{2beam} for large thickness because the periodicity within the relrod is very small. The dynamical corrections (peaks) dominate the correction factor values.

thick crystals (right-most column), dynamical effects extend out to very high spatial frequencies in the diffraction pattern, and their corrections extend to greater g correspondingly.

4.2.3. Application to Multislice Data Sets

The results from the previous analyses showed that $C_{Blackman}$ is a good approximation to the exact two-beam correction factor C_{2beam} in the thickness regime where a correction would be necessary ($>$ 10-20 nm). In *ab initio* structure studies, the structure factors necessary for either correction are not available so the obvious tendency would be to apply a geometry-only correction. This approach requires only two pieces of information — an estimate of thickness and the cone angle — circumventing the need for forward calculation. Unfortunately, this proves to be a rather poor approach at the larger thickness regimes where the correction factors are needed. This seems counterintuitive, but the geometry

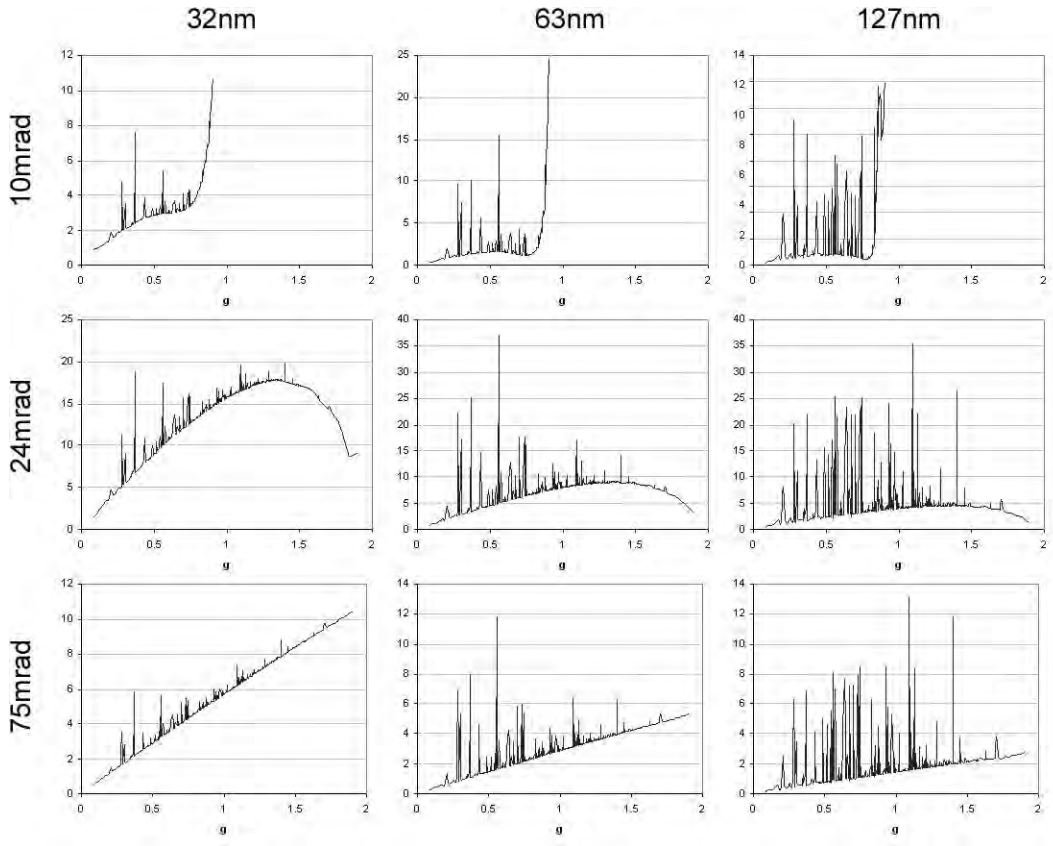

Figure 4.9. Tableau of correction factor plots for the GITO system calculated for various cone semi-angles and specimen thickness. The constituent plots represent C_{2beam} v. g. The plots in the 10 mrad row have a cutoff of g = 0.9 Å^{-1} because for small cone semi-angle the correction factor blows up at high spatial frequencies.

correction is non-selective, so many intensities that need a large correction do not get the boost and weaker reflections can become too strong.

The kinematical Lorentz correction C_{kin} applied to simulated PED amplitudes is shown in figure 4.10 for thickness of 16, 32, and 63 nm. Refer to figure 3.8 for the uncorrected intensities. The amplitudes are slightly improved for 16 nm crystals, however there is no clear improvement for the 32 nm and 63 nm specimens. In thin crystals, almost none of the reflections have two-beam corrections. The weak reflections spread out along the z-axis for thick crystals because the dynamical corrections for the coupled beams have been omitted. Because there is not much correlation between precession geometry and the beam intensity, the strongly coupled beams will receive insufficient correction under most circumstances.

This helps to explain why the R-factors were much worse in the Al_mFe and Ti_2P studies using intensities corrected only for geometry (Gjønnes et al. 1998a; Gemmi et al. 2003) versus the Al_mFe study utilizing the full correction (Gjønnes et al. 1998b). The reported R_1 values for the structures found using C_{Gj}-corrected intensities were 42% and 36%, respectively, versus 32% for the structure found using $C_{Blackman}$. The most uncertain step in the first two studies was the merging of multiple projections. This is to be expected with the crystal thickness on the order of 100 nm. The two-beam dynamical effects would be severe, and the reliability of scaling for common reflections is doubtful. The

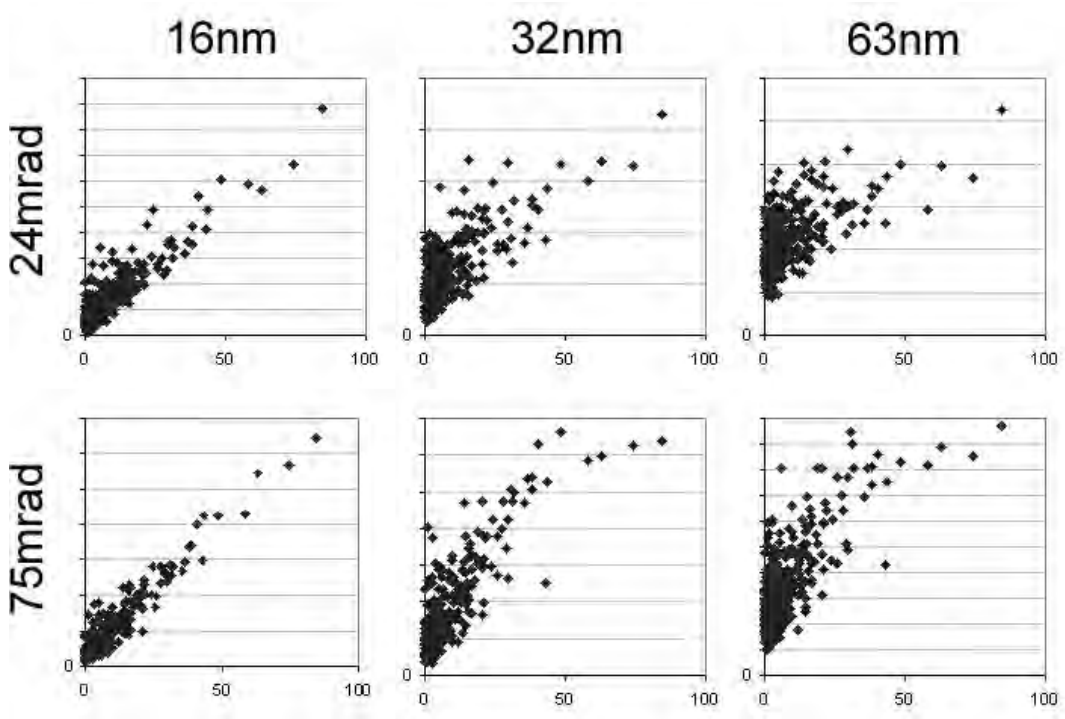

Figure 4.10. Multislice amplitudes with correction factor C_{kin} applied.

preferred solution is to simply use thinner crystals (e.g., fine probe near the specimen edge) and remove the reflections near the transmitted beam instead of treating the intensities for precession geometry.

If structure factors are known, as in the case of partially-solved structures or where some structure factors have been obtained through other means such as CBED, then the C_{2beam} correction may be used. Figure 4.11 shows the application of the full corrections, some of which were shown in figure 4.9, to correct multislice amplitudes from figure 3.8. The top two rows of plots show that there is some divergence between C_{2beam} and $C_{Blackman}$ at small precession cone angle. This is less of a problem at large thickness, but in any case the error is not more than 10%. At larger cone semi-angles of 24 mrad and 75 mrad, C_{2beam} and $C_{Blackman}$ are virtually identical and only C_{2beam}-corrected plots are shown for those cone semi-angles.

The corrections work very well for thicknesses in the regime of 48-100 nm for the GITO structure. In this regime, the weak reflections still exhibit some residual offset, however the intensity ordering is very good. The residual offset occurs because there is always a small amount of multi-beam coupling around the ZOLZ ring and the stronger beams will contribute some intensity to some of the weaker beams through short systematic paths. The strongest beams will be weakened slightly as they couple with the weakest beams surrounding them, giving rise to an apparent curvature in the amplitude reference plots. This effect is most pronounced in the 50-75 nm thicknesses.

At very large thickness ($>$ 90 nm), the corrected intensities exhibit a minor inflection. This is a residual dynamical feature attributed to n-beam intensity exchange. The inflection is less pronounced for ϕ = 75 mrad, but occurs for a similar set of reflections (the strongest ones) regardless of changing experimental conditions. The inflected reflections all have extinction distance less than the specimen thickness and do not appear to lie in a specific band of g in the structure-defining range of 0.25-0.75 Å^{-1}.

The distribution of the reflections is shown expanded in figure 4.12 for the case of t = 127 mm, ϕ = 75 mrad, and the indices of the strong reflections are labeled. The spread at low structure factor amplitude comprises weak reflections from the entire range, and reflections of varying spatial frequency ranges are distributed throughout, clearly indicating that the correction factors are applicable to reflections at all spatial frequencies. The nonlinear behavior evident in the corrected intensity shows that n-beam effects are still present, however the overall behavior of the dataset is linear. The fact that the inflected strong reflections span a range of g and do not seem to preferentially lie in a specific band of spatial frequencies indicates that the primary errors are due to weak dynamical excitations between neighboring beams and are not due to interaction between simultaneously-excited strong beams.

An interesting exercise is to investigate the effect of error in the forward calculation. This is a crude test for determining how well-conditioned the correction factor model is. Noisy structure factors were generated using the algorithm

$$F_{\mathbf{g}}^{noi} = \left(1 + \frac{e}{100} \times (n_{rand} * 2 - 1)\right) F_{\mathbf{g}}^{kin}, \tag{4.18}$$

where e is the percent error and n_{rand} is a random number between 0 and 1. The error introduced is bipolar and independent of the structure factor, so it is not intended to model dynamical effects. The

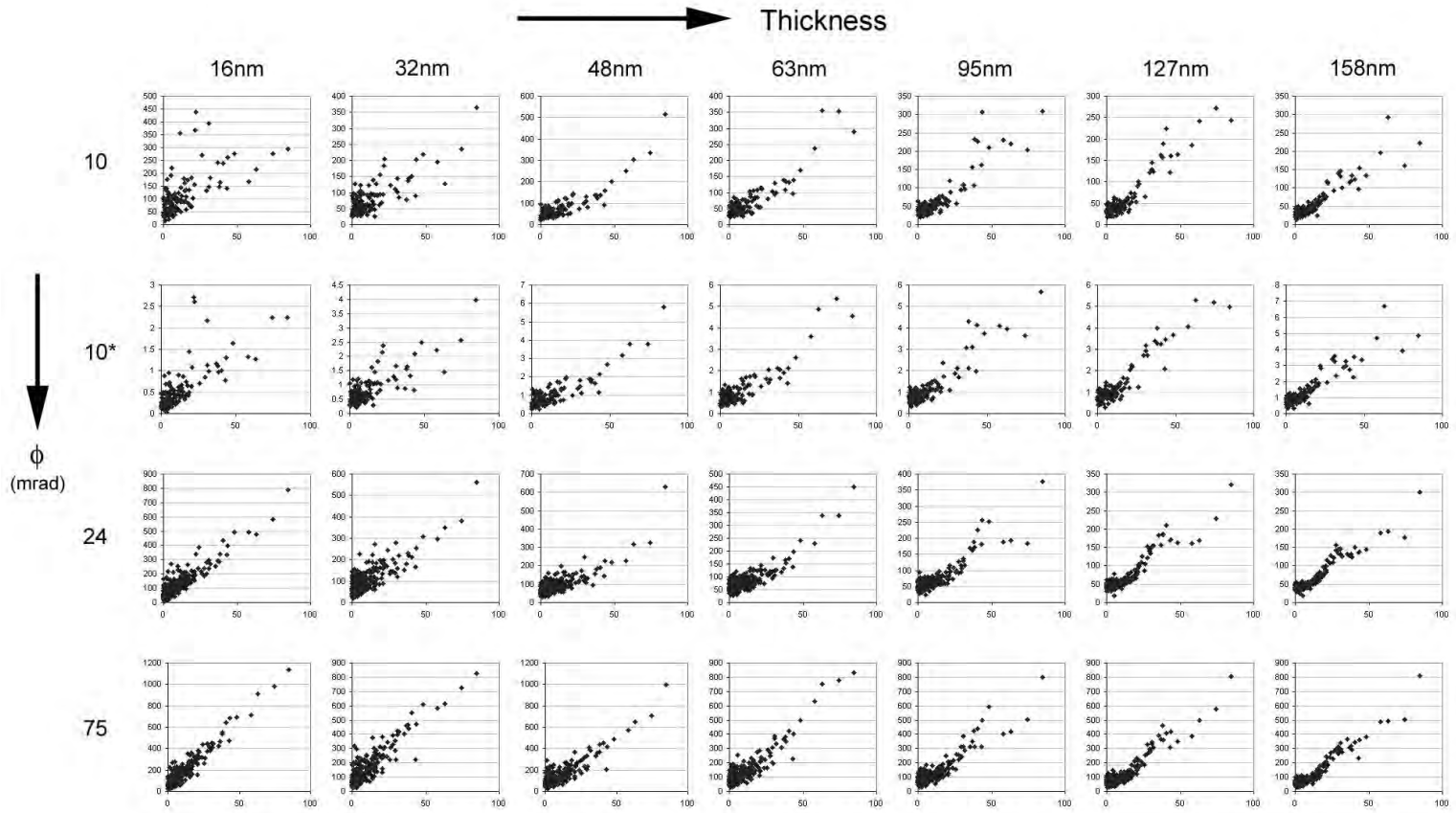

Figure 4.11. Plots of corrected amplitude v. kinematical amplitudes. Correction factors were applied to datasets simulated from multislice (200 kV). All plots use correction factor C_{2beam} except row 10*, which uses $C_{Blackman}$ (refer to table 4.1). 10 mrad corrected datasets include only $g < 0.8$ Å^{-1} due to the ZOLZ limit $2R_0$.

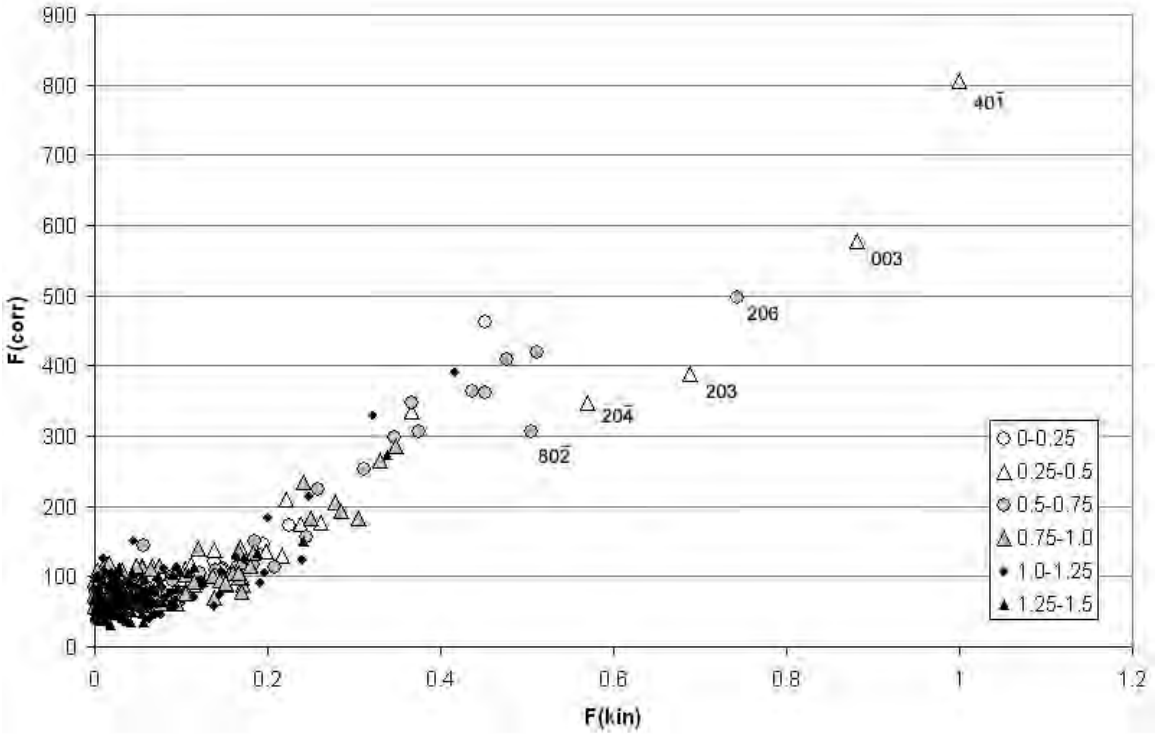

Figure 4.12. Detail plot of simulated intensities for t = 1268 Å corrected using C_{2beam}. The distribution of the intensities with g is indicated by symbol. Weak intensities from the entire range of g contribute to the spread at low amplitude, showing that dynamical effects are not strongly tied to spatial frequency (except in the continually multiply-excited condition near the transmitted beam).

R-factors for the structure factors with noise added are given in table 4.2. Each dataset had a different noise profile to control for any serendipitous correction behavior.

The datasets corrected with a C_{2beam} that has been calculated using the noisy structure factors were then plotted against the true structure factor. Figure 4.13 shows the corrected simulated datasets with

Table 4.2. R_1 for the structure factors with noise added using equation 4.18.

Thickness	10% error	20%error	40%error
		— 24 mrad —	
400	9.734	20.122	41.498
800	9.800	21.315	39.140
		— 75 mrad —	
400	10.492	20.103	40.601
800	10.077	19.266	40.528

largest noise profiles in the correction factors. R_1 values have been calculated for each set and are given in table 4.3. The R-factors of the corrected data shown in that table are much lower than the error contained within the inputted data. The improvement is, however, dependent upon the experimental conditions, which means that the geometry term plays a substantial role here. It is important to note that while the approach yields low R-factors, the plots in figure 4.13 indicate that the correction factors do not strongly preserve intensity relationships. This is to be expected, since there is no way that equation 4.14 can predict the correct structure factor. However, the moderately well-conditioned character of this algorithm does make way for a potential iterative correction factor scheme, wherein a poor starting set of structure factors might be refined into more accurate structure factors by applying *a priori* constraints and then refining based upon a statistical two-beam dynamical model.

We conclude this section by mentioning that the mechanism behind some of the residual dynamical behaviors are not manifestly obvious. For example, the R-factor is lower for larger thickness (also observed qualitatively in figure 4.11). This might be explained by the fact that the integral over excitation error converges to a constant in the limit of large t. Under this condition, the correction factor behavior is dominated by the prefactor $1/\xi_{\mathbf{g}}$. In other words, equation 4.1 (which holds within the very large thickness regime) becomes

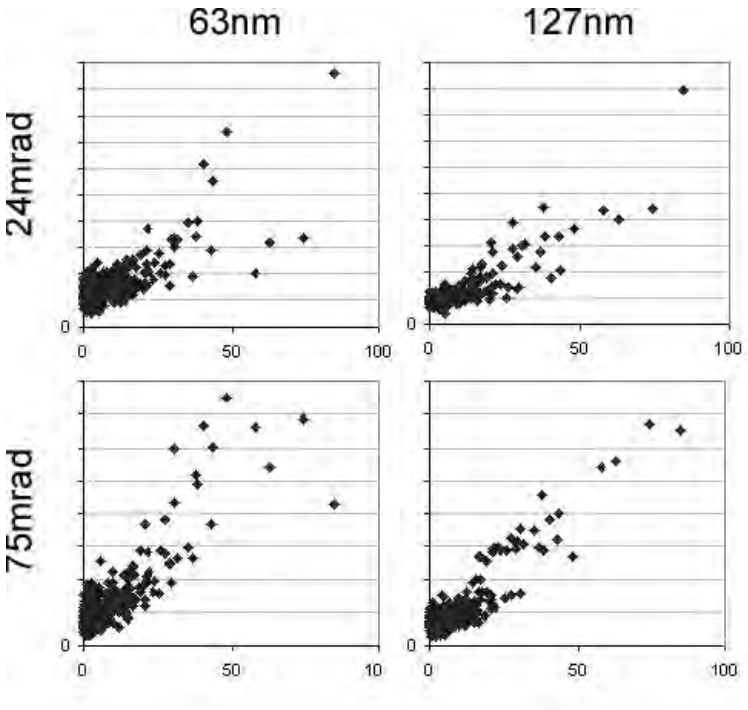

Figure 4.13. Multislice datasets corrected with C_{2beam} using structure factors with 40% noise added. The abscissa within each plot represents the true kinematical structure factor. R-factors for these plots are given in table 4.3.

Table 4.3. R_1 for C_{2beam}-corrected intensities using noisy structure factors. Table values in percent.

Thickness	10% error	20%error	40%error
	— 24 mrad —		
400	9.370	9.398	9.501
800	6.991	6.977	7.019
	— 75 mrad —		
400	15.337	15.480	15.622
800	12.716	12.694	12.807

$$I_{\mathbf{g}} \propto F_{\mathbf{g}} I_{\mathbf{g}}. \tag{4.19}$$

Most intensities, except for the weakest ones, are in the regime of large $A_{\mathbf{g}}$ where the Bessel integral has converged, resulting in a more consistent behavior. Also, surprisingly, the R-factors for ϕ = 75 mrad are worse than for ϕ = 24 mrad. This is counter to the trends seen so far, which almost universally show that large precession cone angle is favorable. The exact mechanism behind this is not clear and requires further analysis in a future study.

4.3. Discussion: Approach for Solving Novel Structures

For precession to become a reliable and widespread technique for generating good starting structure models from electron diffraction data, it must be fast and consistent. Chapter 3 showed that it is natively psuedo-kinematical for small-to-moderate thickness regimes, with primary errors in the range of $g < 0.25$ Å^{-1}. PED offers a new working range of up to 40-50 nm crystal dimension, representing a very favorable regime for dealing with real-world bulk structures. The next step, covered in detail within this chapter, has been to extend the capabilities to even greater thickness by means of correction factors.

It has been shown here that if structure factors are known, the correction generated by a two-beam dynamical model is quite successful up to extraordinary thickness (beyond 160 nm). This result proves that PED adheres very closely to two-beam dynamical scattering, especially at large thickness and large precession angle. It also shows that the data are affected by n-beam effects, as seen in the structure factor plots where there remain some residual nonlinearities that depend upon thickness. The effects, however, vary systematically with increasing experimental thickness and angle, and are slowly varying with changing experimental conditions.

The two-beam dynamical model, while fairly accurate, is unfortunately not immediately practical for generating an *a priori* correction factor for general use. This is because successful correction for large thickness requires a forward calculation: the structure factors must be known before the crystal structrure can be solved. Nevertheless, the analyses do give some new tools for enhancing *ab initio* structure solution using PED and open the way toward less complex iterative structure solution methods than multislice, which requires both structure factors and phases.

The structure solution in chapter 3 on GITO already made use of a crude form of the correction factors that were investigated in this chapter. In section 3.1 a simple modification was made to the experimental precession data from GITO (figure 3.4(a)) that appeared to linearize the measured amplitudes to a kinematical approximation. This simple approach involved using the square of the amplitudes — the intensities — instead of the amplitudes to solve with direct methods. The structure maps that were generated from this procedure had identical atom positions to the solution found using high-pass filtered amplitudes, however it more clearly displayed some of the atom positions (e.g., clearer peaks) that were very close to the noise floor in the amplitude solution. This is an interesting behavior for which an explanation is not manifestly obvious.

The underlying principle can be found by examining the limits of the Blackman formula 1.24. By rearranging the Blackman equation, the measured intensity $I_{\mathbf{g}}^{dyn}$ from a crystal of greater than moderate thickness ($t > 25$ nm) becomes

$$I_{\mathbf{g}}^{dyn} \propto F_{\mathbf{g}}^{kin} \int_0^{A_{\mathbf{g}}} J_0(2x)dx. \tag{4.20}$$

In the limit of large $A_{\mathbf{g}}$, the integral converges to a constant of 0.5. Therefore, when the thickness is very large or if $\mathbf{g}$ is a strong reflection,

$$I_{\mathbf{g}}^{dyn} \propto F_{\mathbf{g}}^{kin}. \tag{4.21}$$

In effect, even though not all reflections necessarily obeyed equation 4.20, the important reflections (the strong ones) did and became more linearized toward pseudo-kinematical values. The fact that weaker reflections might not obey equation 4.20 offers a mechanism as to why the background in figure 3.6 contains noisy oscillations.

In *a priori* investigations of novel structures, a clear path for how to treat the data has now been elucidated. There is overwhelming evidence that large cone semi-angle ϕ is beneficial to the quality of the data. Additionally, thin specimens are advantageous because they decrease error, and the thinnest ones (< 15 nm) are easy to treat via a kinematical correction for geometry. The geometry corrections C_{kin} and C_{gj}, counterintuitively, are not favorable. The low spatial frequency reflections contained in the range $g < 0.25$ Å^{-1}, which are usually weak, exhibit the largest dynamical error because they are near the transmitted beam and are almost always undergoing simultaneous excitation with other beams during the precession experiment. Unless important reflections lie within that range for the structure under investigation, they should be high-pass filtered regardless of whether correction factors are used.

The requirement for forward calculation is an unfavorable one because precession is still not able to solve novel structures from data that is taken from very thick specimens. The effects are slowly varying with thickness if a large hollow-cone angle is used, and complementary methods can indicate the approximate thickness regime. Therefore, the conditions giving rise to large dynamical errors in the data can usually be avoided. The major breakthrough from this chapter is that there is strong evidence showing that the structural electron crystallography problem has been reduced from a many-beam problem

to a largely two-beam one. This is a major simplification and future methods, keeping in mind that $|F_g|$ is all that is required for the forward calculation, will need to take advantage of this new understanding.

The methods presented in chapter 3 should give favorable starting structure solutions for structures that project well, e.g., they exhibit the property that scattered intensities fall within an already pseudo-kinematical approximation (section 1.4). The use of intensities rather than amplitudes is advantageous in the moderate-to-large thickness range (t = 25-75 nm) if used with large cone angle. This method must, however, be used with caution since dynamical behaviors in uncorrected intensities may be substantial at the top of the thickness range for some materials. A classic example is where two neighboring reflections are both strong: a clear path for strong dynamical exchange exists in such a case. Reflections near the transmitted beam predictably contain the largest dynamical errors, and in *a priori* structure studies it is recommended that those reflections be removed using high-pass filtering except in cases where such beams are structurally important, such as for large superstructures. A flowchart describing a suggested solution procedure is given in figure 4.14.

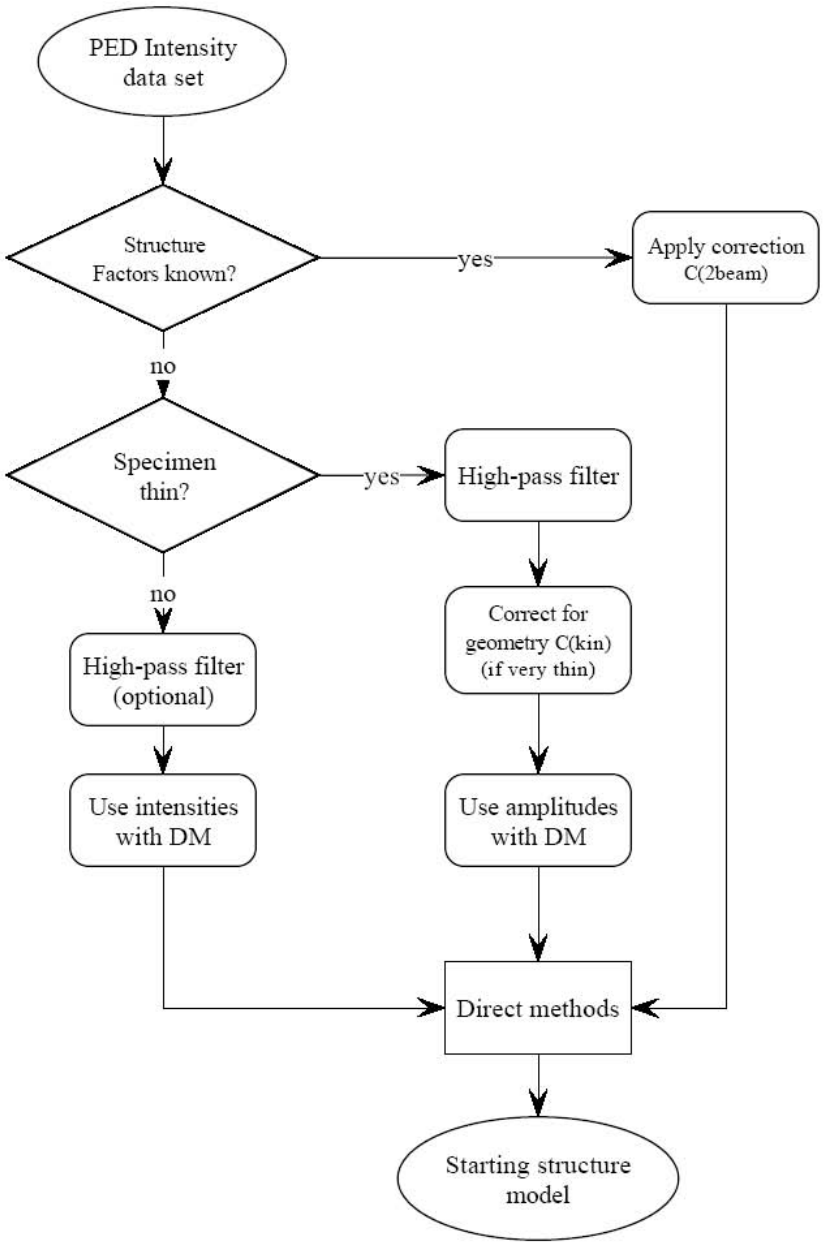

Figure 4.14. Flowchart for generating a starting structure model from a PED data set.

CHAPTER 5

Precession Examples

In chapter two, a high-performance precession system was built and the parameters for its operation were determined. Chapters 3 and 4 provide a theoretical understanding and experimental basis supporting it. Parameters for good precession experiments have been described. This chapter will demonstrate precession experiments on real specimens using the principles described in the previous chapters. Some of the experiments were conducted before a complete understanding of favorable experimental parameters for PED were known. However, it will be seen that the results are consistent with the analyses previously described.

All TEM samples were prepared by crushing larger polycrystals and dispersing them onto a copper grid supporting holey carbon film. Diffraction experiments were conducted on specimen edges that did not overlap carbon film in order to avoid the superposition of scattering from carbon with the crystal diffraction pattern.

5.1. (Ga,In)$_2$SnO$_4$

Here we revisit the GITO model system a final time. In chapter 3, the atom positions in the 010 projection in GITO were found using two processing methods prior to input into direct methods: 1) high-pass filtered experimental amplitudes and 2) intensities. The rationale for using intensities was explained in section 4.3. Here we will solve the structure using corrected intensities using the two-beam dynamical correction factor C_{2beam} (equation 4.14). While this requires a forward calculation based upon known structure factors, this exercise will illustrate the two-beam model's accuracy, demonstrate the validity of using intensities as an approximation to the two-beam correction experimentally, and reaffirm the data quality from the GITO precession experiment.

The true structure factors based upon the atomic positions from Sinkler et al. (1998b) were used to calculate C_{2beam}-type correction factors using equation 4.14. The experimental cone semi-angle of ϕ = 24 mrad, determined by measuring the radius of the beam tilt ring with descan off, and the thickness of 412 Å (determined in section 3.3 using multislice calculations) were used for calculating the correction factor. Figure 5.1(a) shows the correction factor plotted against spatial frequency g. The correction factor was then applied to the experimental intensities from chapter 3 — measured in the PED pattern out to a spatial frequency of 1.4 Å^{-1} — to generate corrected experimental amplitudes (figure 5.1(b)). Recall that the incident radiation energy was 200kV.

At the end of chapter 4, it was shown that in the limit of large structure factor and thickness, the intensities that have been corrected for two-beam dynamical scattering will behave like the square of the structure factor. The caveat was that weaker structure factors might not follow this trend, as will

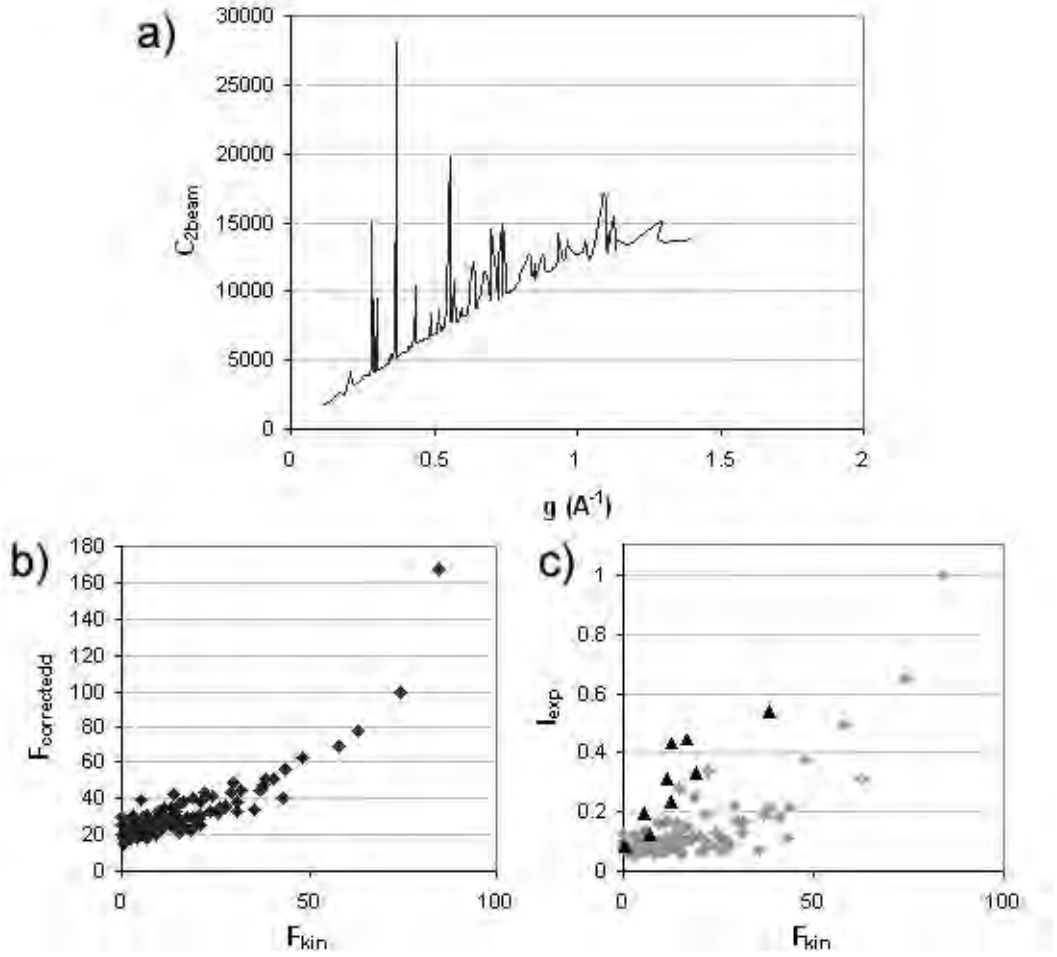

Figure 5.1. (a) C_{2beam} correction factors calculated for GITO using true structure factors and known experimental parameters ϕ =24 mrad and t = 412Å. (b) The experimental amplitudes corrected by C_{2beam} v. true structure factor . (c) Intensities plotted against true structure factor for the GITO system. Black triangles correspond to low-index reflections with $g < 0.25$ Å^{-1}. The grey data points represent reflections in the range from g = 0.25-1.4 Å^{-1}.

demonstrated in this example. For reference, the experimental PED intensities from figure 3.4(b) have been plotted against the true structure factors. The grey data points correspond to reflections in the range of g = 0.25-1.4 Å^{-1}, and the spatial frequencies that were found by multislice to have high error ($g < 0.25$ Å^{-1}, see section 3.2.2) have been plotted separately using black triangles. Excluding these black triangles that result from multi-beam coupling, there is a striking similarity between the C_{2beam}-corrected amplitudes and the rest of the intensity dataset, demonstrating adherence to equation 4.19. Of these, the reflections that demonstrate large error are the reflections near the transmitted beam (low $\mathbf{g}$).

They are amply corrected in figure 5.1(b) showing that they are two-beam in nature — likely the result of systematics — and excluding them would be advantageous in further ensuring dataset linearity.

Referring back to the theoretical result — the plot corresponding to 24 mrad, 48 nm in figure 4.11 — the C_{2beam}-corrected experimental dataset is dissimilar to the theoretical only in that the low-g region should have a larger spread. This can be explained by the fact that missing reflections are likely low-amplitude reflections spread throughout the PED pattern that were below the measurement threshold. The intensities and corrected amplitudes have very similar characteristics in the strong reflections and should generate similar structure maps.

The direct methods solution using the intensities shown in figure 5.1(c) has already been shown in figure 3.6. A new direct methods solution was generated using the corrected amplitudes in figure 5.1(b), and this is shown in figure 5.2. The new solution is essentially identical to the earlier solution using intensities, showing that similar phase relationships were recovered by direct methods for the structural reflections. Some of the structure-defining amplitudes were stronger, giving better-localized peak shapes that are evident in comparing the two maps. The agreement between the datasets in figures 5.1(b) and 5.1(c) and the theoretical reference dataset in 4.11 confirms that the two-beam model is applicable in the thickness regime where a correction factor would be needed. It also demonstrates experimentally that using the intensities is a valid approach as a first (and much-needed) *a priori* approximation to the two-beam correction factor for thick specimens, effectively extending the range of thicknesses that PED can handle.

5.2. $La_4Cu_3MoO_{12}$

The first precession experiment conducted on the 300kV Hitachi UHV H-9000 system was on the $La_4Cu_3MoO_{12}$ materials system (Own et al. 2004). This early experiment showed some promising results even though the experimental conditions were not particularly favorable. To be more specific, the precession cone semi-angle ϕ was only about 20 mrad, the integration was not complete, the specimen was very thick (> 35 nm), and the measurement methods for precession data were not as accurate as in

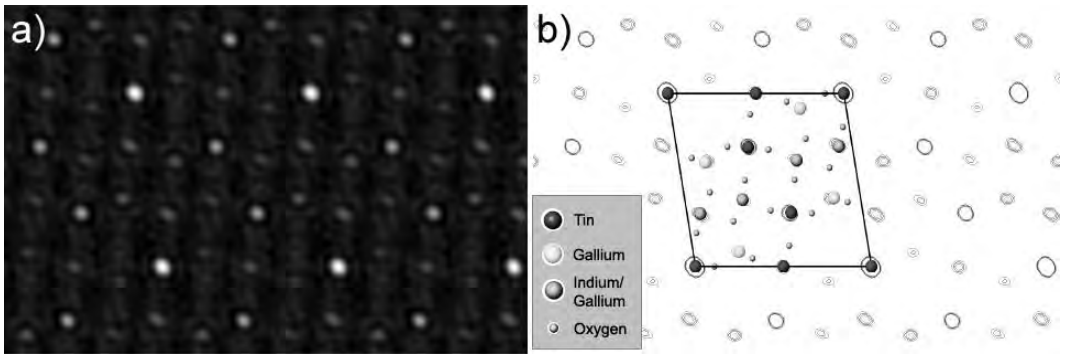

Figure 5.2. (a) Direct methods potential map from amplitudes corrected for 2-beam effects (C_{2beam} correction factors, figure 5.1(b)). (b) Contour map of (a) with the atoms overlaid.

later precession implementations. However, employing the methods developed in this thesis for dealing with thick specimens, useful structural information was extracted from this data.

$La_4Cu_3MoO_{12}$ is a complex oxide exhibiting "frustrated" magnetic behavior. The structure is a homeotype of $YAlO_3$, a rare-earth hexagonal phase. The crystal is very slightly monoclinic but was assumed to have a rectangular cell for the calculations. Unit cell parameters are a = 6.86 Å, b = 10.98 Å, and c = 7.9147 Å, and β = 90.02° (Griend et al. 1999). The structure model in the [001] projection is shown in figure 5.3. Intra-triangle anti-ferromagnetic interactions align two of three spins, yielding trimers with $S_{total} = \frac{1}{2}$. This spin coupling causes an ordering between adjacent cells that doubles the unit cell along the a direction. The space group for this structure is $P112_1/m$, translating into P2gm symmetry in the [001] projection.

During refinement of the X-ray data using ShelX software by Griend et al. (1999), it was found that the structure model derived from X-ray diffraction intensities had much better R-factors (improved by a factor of two, to $\approx 5\%$) if a twinning model was introduced to improve the match with the intensities. Because the data was acquired from a single-crystal X-ray diffraction experiment, the question arises as to what sort of length scale the twinning really occurs at (if it exists at all). Electron microscopy is

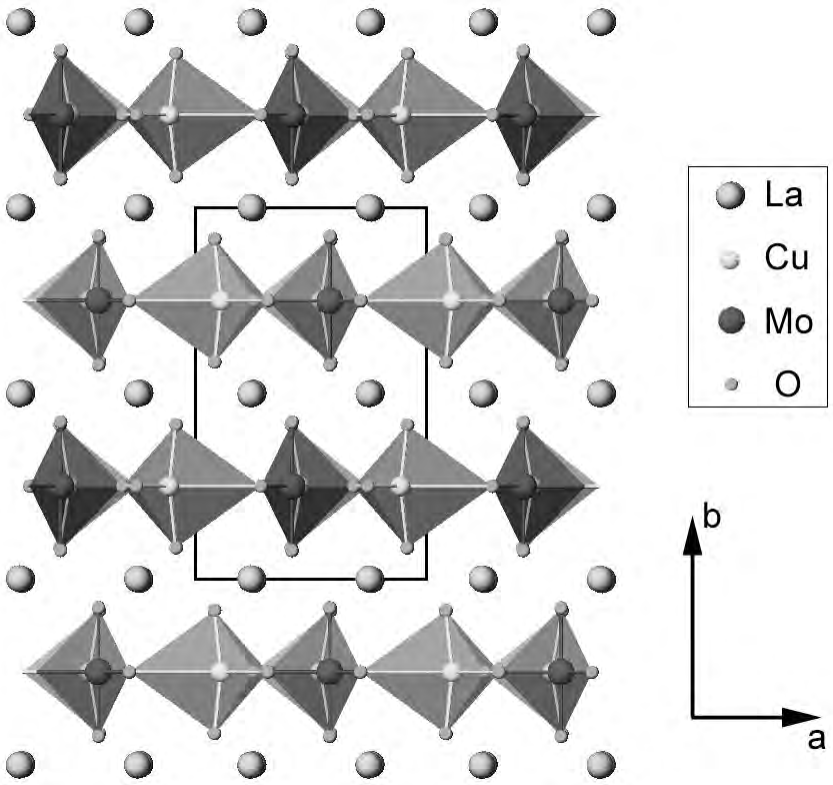

Figure 5.3. [001] projection of the $La_4Cu_3MoO_{12}$ structure model. In this model, the frustrated structure alternates Mo-rich columns along the b-axis to ensure stoichiometry, resulting in a doubling of the unit cell along a.

a suitable tool for studying this due to its ability to probe single-crystal regions of the specimen at very fine length scales.

Diffraction patterns along the [001] zone axis of a $La_4Cu_3MoO_{12}$ crystal were taken in both selected-area and precession modes ($\approx$ 20mrad precession angle) from a crystal edge in a powder specimen (figure 5.4(a)). Nine negatives comprised each exposure series and were digitized using an Optronics microdensitometer at a scale of 25 μm per pixel. SADP intensities were then acquired by first pattern-matching a unitary spot motif to the digitized diffraction spots and then integrating the intensity of the matched pattern. Precession intensities were quantified in a slightly different way by first applying a background subtraction algorithm within a masked area around each spot and then integrating the remaining intensity. The measurement procedures are discussed in more detail in appendix F.

Reduction of nine data sets into a single set was conducted by scaling the data from each negative while minimizing the overall error between data sets. Details of this procedure can also be found in appendix F. Intensities from the precession exposure series matched very well when scaled, resulting in extremely low error between negatives. Compared to the conventional SAD data set, the precession data set had errors at least an order of magnitude better. This is an important practical point; the lower error can be attributed to the fact that the precession technique is much less sensitive to minor variations in the experimental conditions, and is consequently less susceptible to systematic errors than the SAD

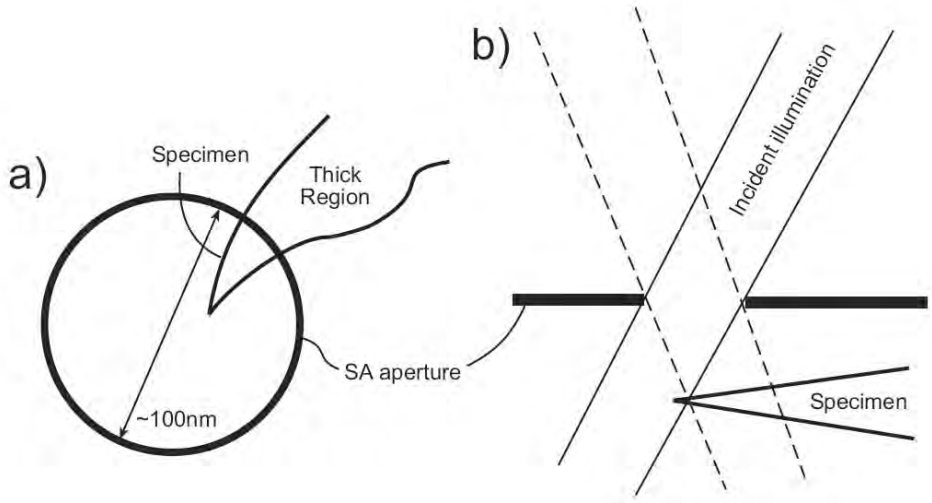

Figure 5.4. Experimental conditions for the $La_4Cu_3MoO_{12}$ precession diffraction experiment. The selected-area image (with precession off) is shown in (a). The specimen morphology was a spike shape with thin region masked using the selected-area aperture. The sample became very thick just outside of the masked region. With precession on, the probe, specimen, and aperture image wander because of optical aberrations and SA errors occurring, for example, if the aperture is not conjugate with the specimen plane. Incomplete integration and/or thickness sampling variation along the circuit may result as shown in (b).

methods. Precession provides nearly the same intensities for symmetry-equivalent reflections and is fairly tolerant of a slightly off-zone diffraction condition.

Figures 5.5(a)-(c) show the kinematical diffraction pattern, the selected-area diffraction pattern (SADP), and PED data set (non-symmetry-averaged). The intensity of each reflection is represented using grayscale as well as spot size to visually demonstrate relative spot intensities. Intensities were collected to ≈ 3 Å^{-1} in the conventional diffraction pattern whereas measureable intensities extended only to about 2.25 Å^{-1} in the precession pattern. This is a common behavior with precession patterns because systematic dynamical scattering is reduced by precession, and in this case the Lorentz geometry decreases sampling limits for the higher-index reflections. Less intensity is scattered out to high-index reflections through dynamical scattering paths, therefore precession patterns will have less intensity at high angle than their conventional diffraction counterparts.

The SADP has the effects of considerable specimen tilt. The precession pattern was acquired from the same illuminated region using the same specimen tilt condition as the SADP, and it is apparent that the Friedel symmetry has been improved considerably. There is a slight emphasis toward one side of the precession pattern (apparent in a slightly larger $(2\bar{1}0)$ spot); this can be attributed to the fact that the pattern was taken from a thick wedge-shaped specimen using low precession angle. Thickness effects are considerable with smaller ϕ, as explained in chapter 3, and because of probe wandering, the precession causes the beam to sample different thickness regimes and areas along the circuit. The intensity integrated can thus vary and violate Friedel symmetry even though precession in theory should not. This is uncharacteristic in a well-aligned precession experiment and can be avoided in most cases by ensuring good real space localization during alignment (see appendix E).

The (040)-type reflections in the kinematical pattern are considerably more intense than other reflections. This high intensity is not apparent in the SADP pattern nor in the precessed pattern. There is enhanced dynamical interaction near the transmitted beam as evidenced by the large error occuring for (200)-type reflections. The fine intensity ordering is rather well-preserved in the precessed DP, especially the alternating spots which show, qualitatively, appropriate ratios. The SAD pattern, in contrast, loses some fine information such as the subtle intensity ordering in the reflections that occur between the (130) and $(1\bar{3}0)$ spots.

The crystal from which the patterns were taken did not exhibit the superstructure reflections that would otherwise occur as weak spots halfway between strong columns of diffracted spots. The missing superstructure can be explained through two possible mechanisms. If the twinning occurs in every other plane along the b-axis, then the superstructure reflections may disappear. The other possibility is disorder. If the structure is disordered, the distribution of Mo and Cu tetrahedra would be random such that the light grey columns in figure 5.3 would become filled with Mo-rich (darker) tetrahedra.

The measured diffraction intensities were processed for use with direct methods to investigate the twinning model. Three approaches were taken:

(1) Dynamical amplitudes used with direct methods;
(2) Precession amplitudes band-pass filtered and used with direct methods;
(3) Precession intensities band-pass filtered and used with direct methods.

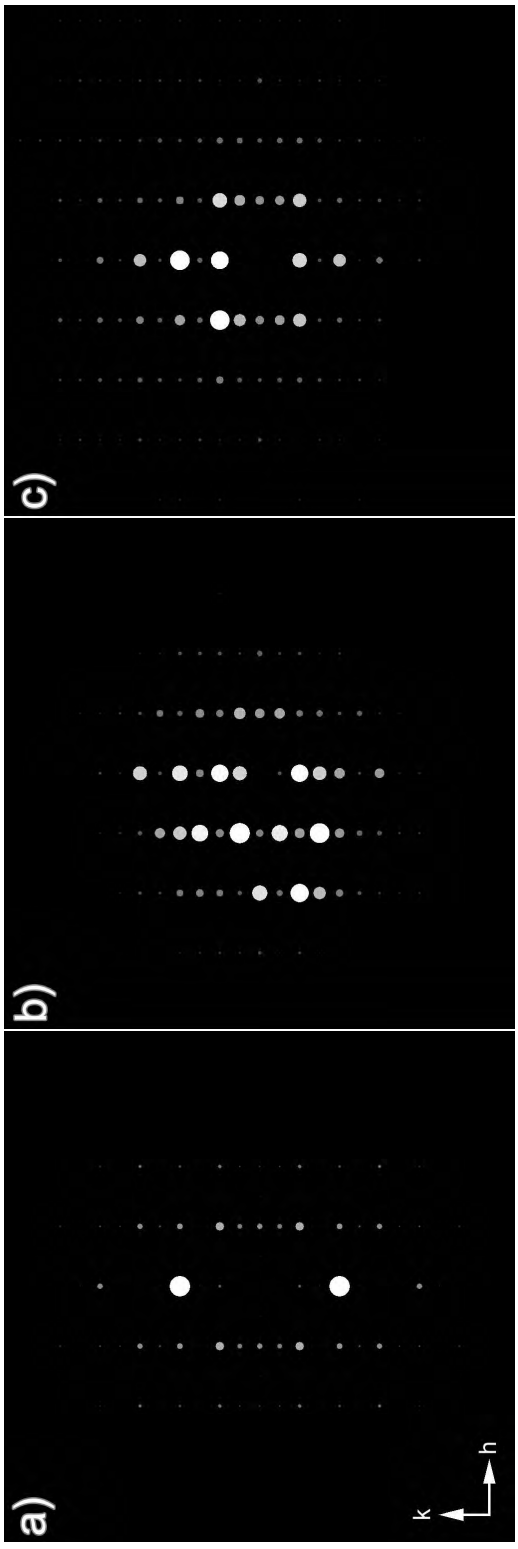

Figure 5.5. $La_4Cu_3MoO_{12}$ intensity diffraction patterns. (a) Kinematical pattern calculated from the structure in figure 5.3. (b) Conventional on-zone zone-axis pattern (dynamical dataset). The dataset had considerable tilt, so intensities are not symmetric. This was exacerbated by large specimen thickness. (c) Precession pattern from the same specimen region as (b) taken under the same specimen tilt conditions. Precession angle was 20 mrad.

Because the precession angle was not large, the intensities needed to be band-pass filtered to avoid the region past $2R_0$ (where R_0 is the radius of the zeroth order Laue zone). For ϕ = 20 mrad and 300 kV radiation, reflections beyond 2 $Å^{-1}$ needed to be rejected. The reflections with g = 0.25-1.5 $Å^{-1}$ were used with direct methods to ensure ample integration of intensity.

The dynamical amplitudes did not generate sensible structure maps, not a surprising result from bulk diffraction data. Precession amplitudes fared better, however in general the maps had low contrast. The intensities were then used with direct methods to generate structure maps. The quality of the intensities was not ideal and many false solutions were generated in the top solutions, but two families of solutions with distinct sparsely-spaced peak-like features emerged. One family had difficulty localizing the La framework atoms, but the other family gave very realistic cation features. The top amplitude and intensity solutions that gave discrete atom-like features (both 6th ranked) are given in figures 5.6(a)-(b).

One of the difficulties of initially interpreting these structure models was that the Cu/Mo rows had smeared features in many structure maps. It is now recognized that this is possible because of disorder: with partial occupancy of both Cu and Mo tetrahedra in the framework, it would be difficult to precisely localize the Cu and Mo cation columns, which project very closely next to each other. In some maps, it appeared that the oxygen atoms that create the wingtips of the tetrahedra (the oxygen rows between Cu/Mo and La rows) were present. The oxygen atoms — whose positions depend upon which cation they are coordinated with — would likely not be seen in maps if the precession data was of sufficient quality, so peaks appearing at shifted locations that would cause bond angles to deviate too much were

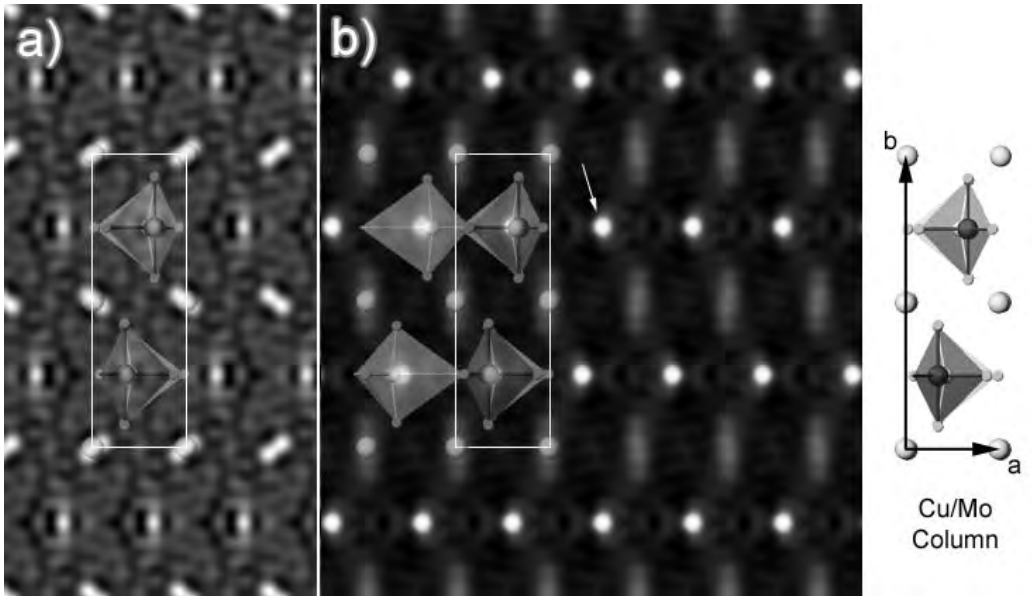

Figure 5.6. Direct methods solutions from PED on $La_4Cu_3MoO_{12}$. The amplitude solution is shown in (a) and the intensity solution is shown in (b). The frustrated structure suggested in Griend et al. (1999) has been replaced with a disordered structure that includes. The cation positions are localized and show that the mixed Cu/Mo tetrahedra.

considered spurious artifacts. This is also supported by the fact that the oxygen atoms in the Cu/Mo rows are never clearly localized either. This consideration allowed several families of solutions to be eliminated by virtue of false peaks. This left the maps that generated clear atom-like features, but that did not localize the La framework. These were easy to identify and remove, leaving the solution family shown in figure 5.6.

In the new disordered model, the tetrahedral motif is still present. However, the Cu tetrahedra cannot exist in the new structure exclusively within their own columns in the projection plane. In the previous model, the Cu tetrahedra (lighter color) are larger in size in the b-axis, whereas mixed Cu/Mo tetrahedra have a more compressed frame along that axis. Additionally, the location of the Cu cation in the Cu-only column is displaced from the peak location in the map whereas Cu/Mo falls right onto it. This indicates that the average structure contains Cu/Mo tetrahedra dispersed throughout the structure rather than the alternating Cu and Cu/Mo columns. In order to maintain stoichiometry, there must be a consistent ratio between Cu and Mo atoms, nevertheless a random disordered model can still satisfy this constraint. Diffraction is an averaging technique, so the structure maps shown here represent hundreds if not thousands of unit cells. There may be short-range order — which might be identified through nanoprobe precession or high-resolution imaging — however, the superstructure intensities were not seen at all in this crystal, indicating that the disorder is dominant and is widespread throughout the crystal on which the diffraction experiments were conducted.

5.3. Al_2SiO_5

Andalusite (Al_2SiO_5) is an aluminosilicate mineral that crystallizes in a dense orthorhombic cell. This system was used to test the latest precession retrofit on the JEOL 3000F, and was chosen to complement density function theory calculations exploring charge density. Andalusite is orthorhombic with four formula units per unit cell, giving 32 atoms per cell. The cell dimensions are a = 7.7942 Å, b = 7.8985 Å, and c = 5.559 Å with space group Pnnm giving P2 symmetry in the plane.

[$1\bar{1}0$] zone axis patterns were taken from an andalusite powder specimen using conventional diffraction and PED at 300kV. The PED cone semi-angle was 36 mrad. The amplitude diffraction patterns for the two experimental datasets are given in figure 5.7. Figure 5.7(a) shows the conventional DP; the precession pattern, 5.7(b), shows better ordering in the spots. More striking is the absence from the precession pattern of the forbidden reflections of type $(00n)$, where n is an odd integer. These reflections — which are quite strong in the conventional pattern — are extinct in the precession pattern, adhering to kinematical behavior.

Amplitudes from both diffraction patterns were each used with direct methods for generating structure maps. All measured reflections were used from the conventional DP while the precessed DP was high-pass filtered to remove $g < 0.25$ Å^{-1}. The top solutions are given in figure 5.8. The structure in this projection has Si and Si/O columns at half the cell distance along each edge flanked by Al columns. The conventional diffraction solution identifies the Si and Si/O positions and the central Al position; it also locates Si/O column positions at the $\frac{1}{2}$-vertical cell location. The conventional diffraction solution does not show all the cation positions but it does hint at the existence of potential around the edges of the unit cell. In contrast, the precession potential map locates all cation positions and also has relatively

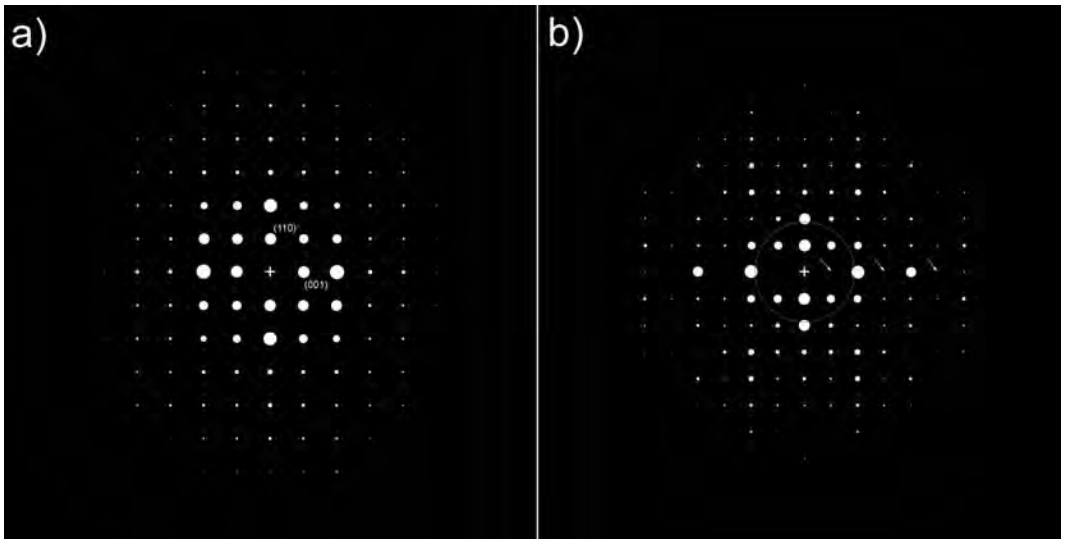

Figure 5.7. Amplitude diffraction patterns from (Al_2SiO_5. (a) Conventional DP and (b) precessed DP (ϕ = 36 mrad). The amplitude ordering in the precession pattern is more distinct. Additionally, the forbidden reflections (odd-order (001)-type reflections), which are very strong in the conventional pattern, are extinct in the precession pattern as indicated by the arrows. The ring overlay describes the spatial frequency g = 0.25 Å^{-1}.

good agreement with expected scattering strength. It also indicates some of the vertical peak-splitting that is due to the oxygen atoms projected near the Al atoms on the cell edge. This precession-based solution would be an outstanding *a priori* starting structure from which to conduct refinement.

5.4. Mordenite

Not all structures are amenable to solution by PED. One case is for materials with very large unit cell structures. In studies of unknown structures, the success of the high-pass filtering approach to avoid the low-index errors hinges upon the fact that most structures do not have strong structure factors in the low-g reflections. For structures that are very large — greater than about 12 Å cell size — the slowest-varying spatial frequency in the structure is less than 0.1 Å^{-1}.

In section 1.2 it was explained that part of the robustness of the direct methods algorithm used is its ability to interpolate missing reflections. In precession, omitted low-index reflections are also interpolated. For cell structures with considerable scattering strength in the low-index reflections, for example, Mordenite, it may be more detrimental to remove the reflections rather than allowing intensities with large error into the data set. Mordenite is a nanoporous zeolite commonly used as a metal catalyst support. It is very similar to the zeolite ZSM-5, constisting of continuous-pore structures along the [001] direction made up of large 12-member oblong pores of 7 Å $\times$ 6.5 Å inner dimension. In addition to being a large cell material, it has a number of characteristics that dramatically reduce its tractability by direct methods:

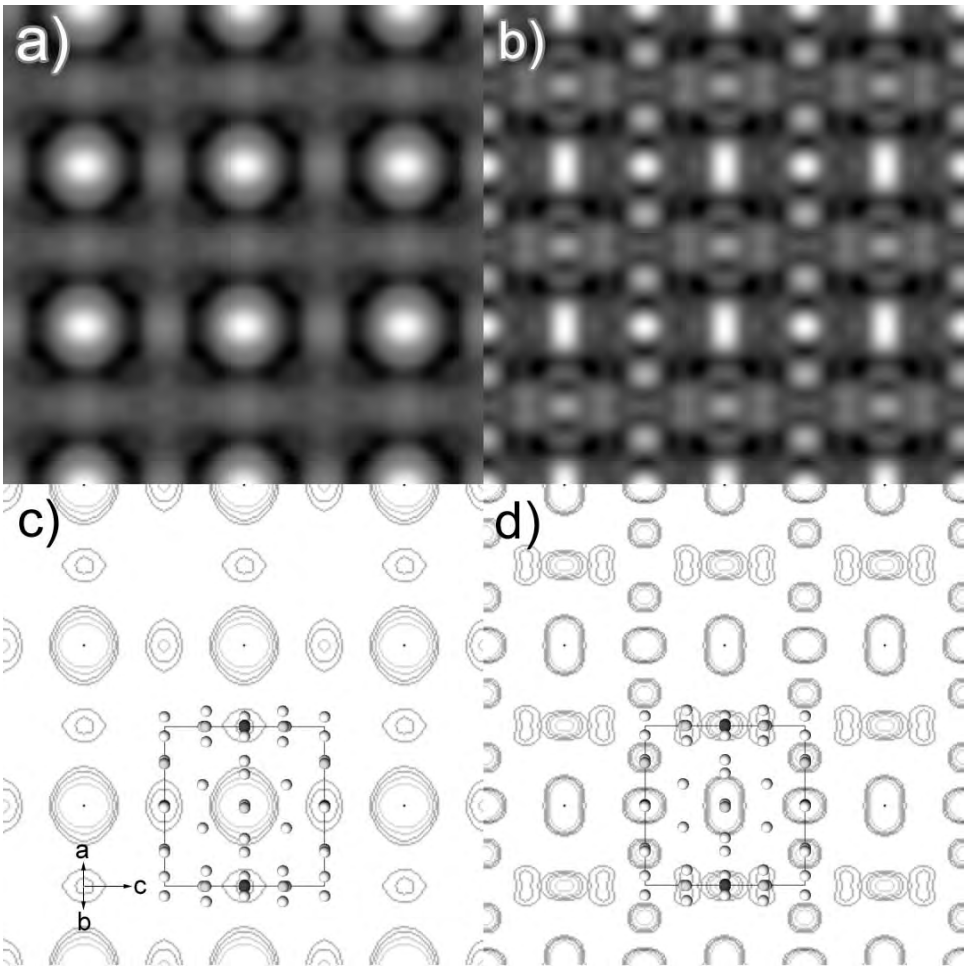

Figure 5.8. Potential maps from direct methods on Andalusite. (a) Map from conventional amplitudes. (b) Map from high-pass filtered PED amplitudes. Contour plots are shown in (c)-(d) and the structure is overlaid for reference. Dark atoms are Si, light atoms are Al, and white atoms are O. The white atoms along at $\frac{1}{2}$ the vertical distance represent mixed Si/O columns.

(1) The structure projects very poorly, so direct methods will be ineffective unless very accurate structure factors are used;
(2) It is an open-framework structure, so the Debye-Waller temperature factors are enormous ($B_{Si} \approx 1.2$ Åand $B_O \approx 3$ Å).
(3) The cations are both light atoms (Z = 13 and 14), which worsens the above two characteristics.

An experimental mordenite PED pattern was taken at 200 kV on the precession-enabled JEOL 2000FX microscope using a 40 mrad cone semi-angle. The crystal has space group Cmcm, yielding cmm plane group symmetry in the [001] zone with unit cell parameters a = 18.3 Å and b = 20.5 Å. 182 symmetry-equivalent reflections were quantified to a spatial frequency of ≈ 1 Å^{-1}. The intensity

dataset that was acquired on this instrument is shown in figure 5.9(b). The kinematical pattern — calculated using the large temperature factors from above — is shown for reference in figure 5.9(a). A circle describing $g < 0.25$ Å^{-1} is overlaid on top of the experimental pattern demonstrating that many very strong reflections are contained within the regime that is subject to large dynamical error. The resemblance of the precession result to the kinematical intensities, especially the rectangular spot ordering near the transmitted beam, is readily seen. However, the over-emphasis of low-g reflections is also apparent and additionally, the specific ordering and strong intensity of the high-index reflections diminished in the precession pattern.

This type of poorly-projecting structure is generally impossible to solve via direct methods unless very high quality intensities (to high spatial frequency) are provided, or unless known phases from high-resolution images are used to help constrain the direct methods. Direct methods on the kinematical intensities alone will yield the true structure (demonstrated in figure 5.10(a)), however, since there are many overlapping atoms, inclusion of high spatial frequencies is required to pinpoint their locations. Practical experiments only allow measurement to limited spatial frequency, depending upon the dynamic range of the measuring medium, so it is unlikely that precession would be able to recover this structure unless high-resolution phases were available.

At the time of the study, it was not know whether the low index spots contributed considerably to the final structure in the context of direct methods. The beams are very strong, so direct methods was initially conducted using the full set of amplitudes. Surprisingly, only one unique solution resulted from this exercise. This initial map was confusing because it placed a large amount of intensity within the pore centers and exhibited spurious oscillations throughout the denser regions of the structure.

The homologue of mordenite investigated here often has relatively thick platelet morphology of $\approx$ 500 Å, so it was decided that intensities could possibly give better results and direct methods was run a second time using high-pass filtered intensities. The standard high-pass filtering cutoff of 0.25 Å^{-1} was applied to this set, removing a large number of strong reflections. A set of four unique solutions was obtained describing two solution families, one of which exhibited slightly smeared strong features, and the other containing more peak-like features. The second solution family is shown in figure 5.11 (contrast is reversed).

One effect that can occur with direct methods is that the algorithm may consistently converge to a particular configuration of phases. The Babinet solution, which is the inverse of the potential map with opposite phases, is also a likely solution. The structure map with contrast reversed shows distinct peak-like features near the cation positions within the framework. The potential near the pore structure exhibits a strong oscillation. This may arise from lack of physical constraint in an open framework structure; anisotropic Debye-Waller factors can be larger than the isotropic factors by a factor of two for the atoms bounding the large pores, therefore loosely-constrained atoms within the pore structure would contribute some scattering from within the pore.

While we have used precession to demonstrate something very close to the true structure of Mordenite, the path to its determination was less straightforward than in the previous examples in this chapter. At this time, one might argue that precession is not accurate enough to ensure reliable determination of

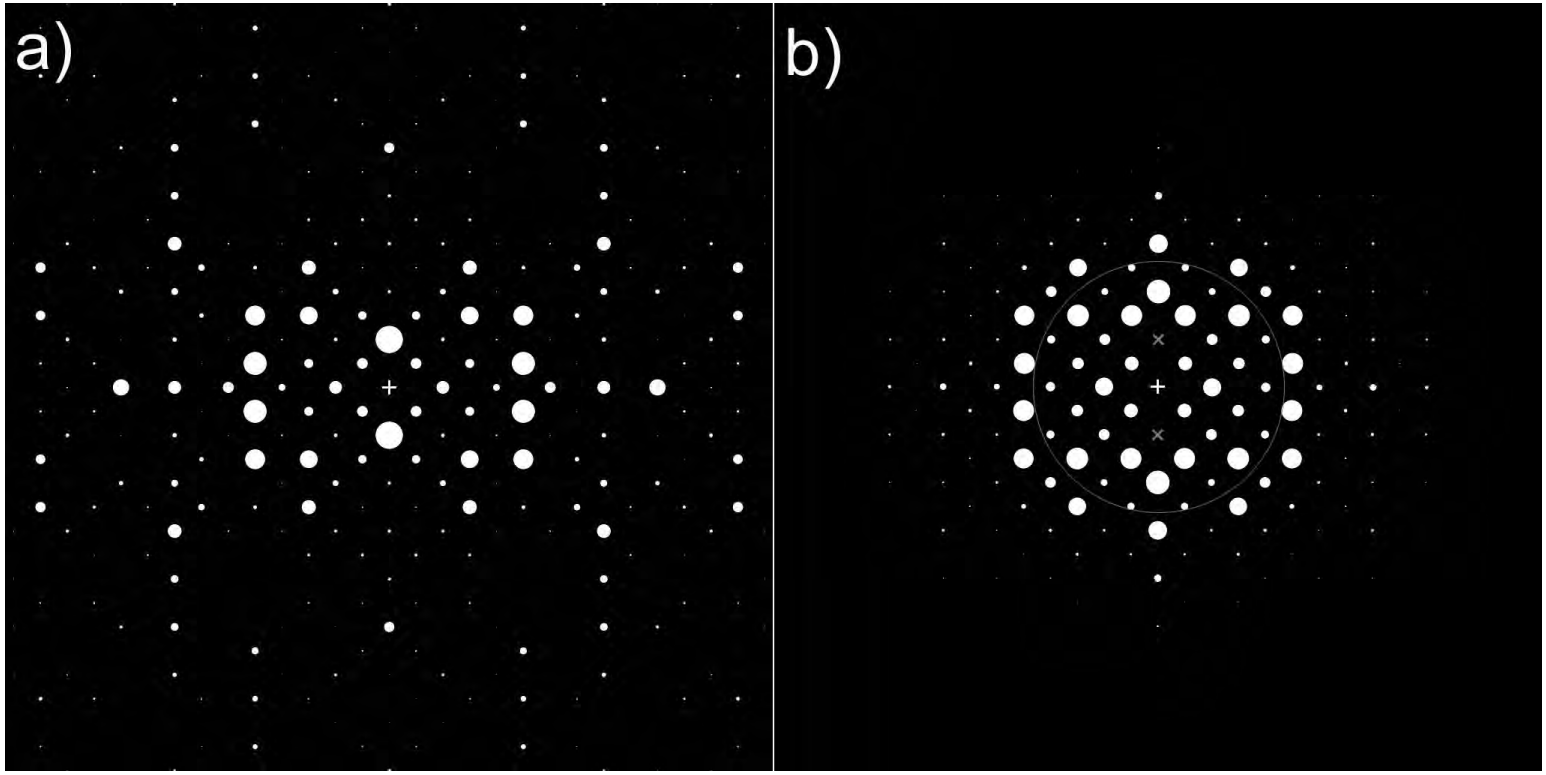

Figure 5.9. (a) Kinematical diffraction pattern for Mordenite [001] zone axis. (b) The precession pattern for the same zone (ϕ = 40 mrad). The spatial frequency g = 0.25 is indicated the ring overlay.

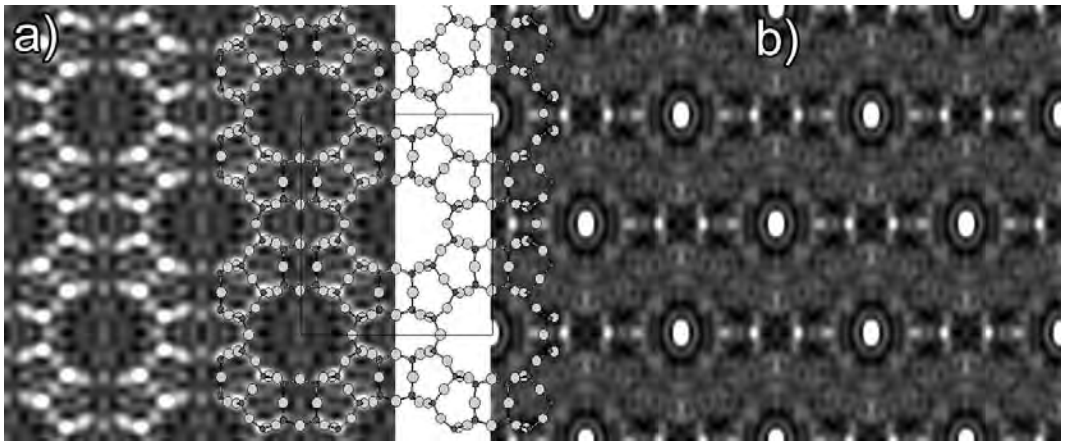

Figure 5.10. (a) Structure map from direct methods on Mordenite using kinematical amplitudes to 1 Å^{-1} with no additional phases. The cation locations are poinpointed but the structure map has many spurious Gibbs oscillations due insufficient sampling of spatial frequencies. (b) Preliminary PED direct methods solution using amplitudes with direct methods (no filtering). Considerable intensity is put into the pore centers where no atoms should exist, and spurious oscillations occur throughout the denser regions of the structure. The true structure is overlaid on top of both solution maps for reference; light atoms represent Al/Si and dark atoms represent O.

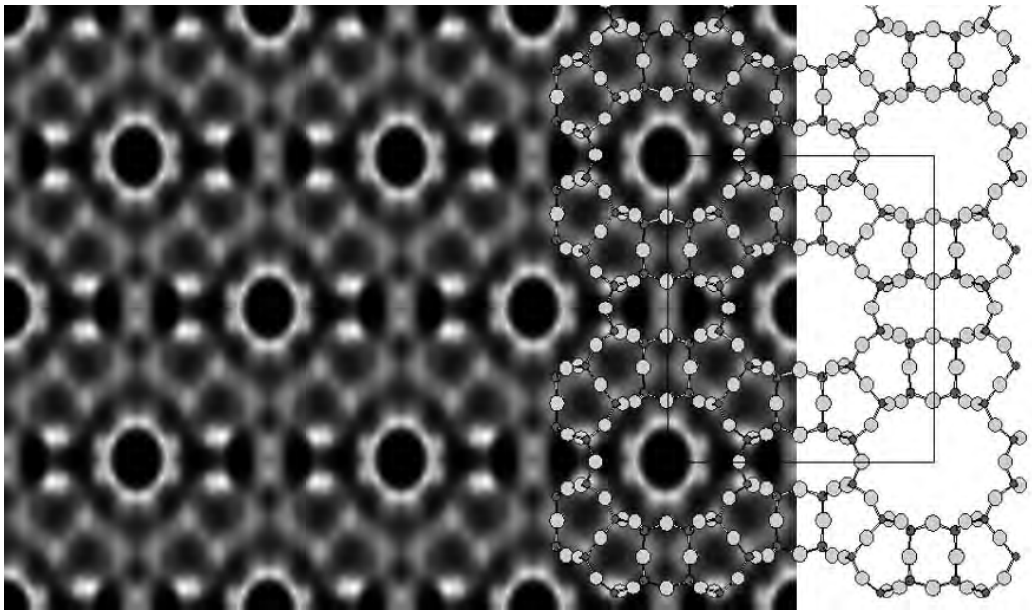

Figure 5.11. Direct methods potential map of Mordenite generated using high-pass filtered intensities. Peaks occur near cation locations within the framework.

weakly scattering loose framework structures from the *ab initio* structure solution standpoint. In a case such as this, high-resolution phases should be used with PED intensities to constrain the solutions.

5.5. Conclusion

This chapter has demonstrated procedures for generating starting structure maps. The materials systems investigated in this chapter possess differing compositions and structures, and have demonstrated some of the advantages as well as disadvantages of precession from a practical standpoint. Generally, the structure maps from direct methods on PED data give realistic positions and features as long as the projection constraint is reasonably satisfied. When precession data is used, the direct methods solutions list always contain maps that are sparsely populated with well-defined discrete peaks. The correct solution can be readily filtered out from these. Perhaps the most remarkable feature is that realistic maps — of which GITO was one example that produced essentially exact atoms positions — were generated without the use of *any* fixed phases.

It is important to note that these are all known structures and some influence on how the studies were carried out was influenced by *a priori* knowledge. Additionally, the types of structures shown here do not represent the huge variety of possible problems. However, the examples do show that the true solution is indeed contained within the list of potential solutions generated by direct methods, and the amount of work necessary to generate a good starting structure for refinement is considerably diminished compared to conventional electron crystallography.

CHAPTER 6

Conclusions and Future Work

The precession technique was first introduced over ten years ago by Vincent and Midgley (1994). It was extremely promising, and over the past decade a small number of groups have attempted to solve difficult problems using the technique. The Al_mFe precipitate system was investigated by precession through the use of multiple 2D projections corrected for precession geometry merged into a 3D data set (Gjønnes et al. 1998a). A second study on the same system explored one zone axis using a very involved correction factor (Gjønnes 1997; Gjønnes et al. 1998b). Midgley et al. (1998) showed that the precession intensities can be used with Wilson plots to determine Debye-Waller factors fairly accurately in simple crystals, and Gemmi et al. (2003) have studied Ti_2P using a similar 3D merged projection method using geometry correction factors. Recently, the Marks research group has published an investigation on $La_4Cu_3MoO_{12}$ with the interest of understanding the scattering physics.

The results have been mixed. Precession electron diffraction technology has been deficient in two areas. Firstly, the early instrumentation was limited: there were few instruments available on which to conduct studies, and the poor probe localization crippled the technique as a true nanoprobe method. The instrumentation limitation caused considerable confusion in the results by confounding the effects of thickness averaging with the other linearizing (toward kinematical) effects of precession, such as the resistance to systematic diffraction paths. The second problem was that experimental parameters were not well-understood. The latter was badly needed to understand in more detail what the ideal conditions for the experiment were. With a better understanding of the experimental parameters, one can start to build robustness into the method. For example, the mediocre R-factors obtained in Gjønnes et al. (1998b) and Gjønnes et al. (1998a) — 32% (unrefined) and 42% (refined), respectively — were due to too large thickness and variability in the first study, and too low precession angle combined with thickness in the second study. These could be avoided relatively easily by the researcher at the microscope; in the first, a thinner specimen would have been preferred, and in the second, the 3D merge might have been better if no corrections were applied and larger angles were used.

There is frequently a large gap between the introduction of a technique and its successful widespread application. This thesis endeavors to take a large step toward the realization of precession electron diffraction as a useful and reliable crystallography technique. The two issues mentioned above have been treated here, first through a development phase where new precession instrumentation based upon the early concept was designed and refined from an applications engineering standpoint. The design stressed versatility and user-friendliness, so it is easily re-configurable for functionality, yet always ensures usability by the end user. The versatile instrument design aided the successful acquisition of high quality PED patterns for comparison with theoretical models. The second phase involved development

of the technique from a standpoint of basic scattering theory. Multislice simulation allowed control of variables and a thorough investigation of experiment space. The correction factors in the literature were investigated in detail through comparison with the multislice and exact two-beam models, and from these a new set of guidelines for PED experiments have been formulated.

Through thorough investigation of experimental parameter space, it has been found that the variables cone angle ϕ and specimen thickness determine the majority of the data set behavior. Their interaction, along with the specimen's extinction characteristics, causes modification of the intensities to a pseudo-kinematical model for specimens of small-to-moderate thickness, given that large ϕ is used. In the limit of large thickness, the intensities converge to a two-beam model. This is because the only major dynamical effect occurs when the systematic row condition is satisfied, which behaves superficially like the two-beam condition so it does not cause large deviation. This happens twice during the precession, and with large cone angle the duration is short. Very little n-beam interaction occurs otherwise in the PED experiment.

In more specific practical terms, a large cone angle of ϕ = 50-75 mrad is best used under all conditions. The probe localization is linked to the precession angle, so it may be compromised if very high angle is desired. Provided that large ϕ is used, the amplitudes can be interpreted as pseudo-kinematical amplitudes up to thicknesses about 35-50 nm, depending upon the distribution of strong reflections with g and projection characteristics of the material. The correction factor that acts only on geometry (C_{kin}) is useful for very thin specimens (under 20 nm) but is ill-advised for thick specimens. The geometry correction C_{Gj} proposed by Gjønnes (1997) is invalid except for large thickness, where it must be used in conjunction with the dynamical correction factor (the full correction factor $C_{Blackman}$ or C_{2beam}). This is because the geometry term is independent of dynamical effects, hence applying only C_{Gj} will result in incomplete scaling and force weak beams above beams that have been damped by dynamical exchange.

For thicker specimen ranges, correction factors are necessary to correct for two-beam dynamical effects that cause the data to deviate from psuedo-kinematical. For *a priori* investigations where structure factors are not known, thicker specimens may be linearized by squaring the structure factors in the limit of large thickness; if the structure is known to be thick, it will likely fall under the limit of the Blackman equation. This will not, however work for exceptionally large thicknesses ($>$ 60 nm, to be conservative) because it only works to correct strong intensities that have deviated from their values due to two-beam dynamical exchange. At such large thickness, multi-beam mixing is so strong that many weak reflections may become as intense as the strong reflections, so phase relationships are not preserved.

Not all types of structures will be amenable to precession. PED will work best on structures that better obey the statistics that preserve phase relationships between scattered intensities. In the best case, the intensities will behave within a completely pseudo-kinematical interpretation. In the worst case where the structures do not project well or become extremely dynamical at small thickness, statistical dynamical direct methods will hopefully still apply. With pseudo-kinematical data, the intensity relationships will largely be preserved, hence the phase relationships will more likely match the true phase relationships rather than approximate them. Therefore, structures that project well are most suitable. Structures

with poor projection (such as Mordenite) have intensity ordering at high spatial frequency, representing an ill-conditioned problem for DM (e.g., small changes in intensity easily corrupt the recovered phase relationships). Fortunately, the imaging capabilities of the electron microscope can be used in tandem to acquire phases in these cases: specimens that are suitable for high-resolution imaging are usually thin, so if HREM is employed the precession pattern is simultaneously available. Additionally, the phases of low-index reflections — for which intensities may unavailable in precession due to large error — are the easiest to acquire in HREM.

The major problem we set out to solve was whether precession electron diffraction could be the universal bulk electron crystallography tool. It is difficult to definitively state that PED will or will not work in a general sense because its operation is inherently statistical in nature; it depends strongly on specimen type and morphology. The results here show that thus far it is not the final solution for bulk electron diffraction ultimately because of thickness limitation, but it does provide the crystallographer with a new tool for solving many structure problems that would ordinarily be very difficult, very time-consuming, or simply impossible. Elucidation of a standard procedure with which to employ PED represents a significant step toward routine bulk structural crystallography via electron direct methods.

6.1. Future Work

While the results in this thesis show that the technique is ready to be used in the field, this work can be extended in a number of areas. The foremost extension is application to more structures to build a repertoire of structures solved by PED. We have looked at known structures in order to build and confirm an accurate model of the physics of precession. Unknown structures need to be solved to garner more attention for the technique.

In the discussion on instrumentation (chapter 2), the topic of aberration correction was introduced as a way to extend cone semi-angle. Originally developed for direct imaging, it has now found use in diffraction as well. It would be interesting to see the limits of the technique in terms of ultra-high-angle precession instrumentation. Methods for data collection from individual Laue zones would need to be developed to avoid Laue zone overlap, but an inherent advantage of large cone angle is that reliable 3-D precession may be possible. Advanced instrumentation will enable fancy scanning configurations allowing, for example, circumvention of multi-beam excitation conditions that cause deviation from two-beam excitation.

Ab initio recovery of the structure from very thick specimens is still out of reach. One suggestion that may allow thick specimen investigation by PED is to develop an iterative dynamical Lorentz correction that could start from a set of rough structure factors and refine them to the true structure factor (suggested at the end of chapter 4). This will require a detailed analysis of how the conditioning of the two-beam model behaves. A more complex analytical model would be ideal for developing this correction. Work in the Marks group on developing a reduced analytical form is already underway.

A final idea that has garnered great interest lately is using diffraction to probe the charge density of structures. The atom positions are useful as a starting point for describing the materials, but it is the electronic structure that determines the properties of the material. Beam electrons scatter from the electron charge, therefore they are inherently more sensitive to the charge in the structure than X-rays.

It would be advantageous if, instead of locating atoms, the charge density can be determined directly from the diffraction experiment. It has been seen that the reflections most sensitive to charge density are the low-index reflections (Deng and Marks 2005), but unfortunately the reflections with the most error in PED are the same ones. A robust correction factor applied to these reflections may restore their usefulness in revealing the charge density within the structure.

References

Avilov, A.S., A.K. Kuligin, U. Pietsch, J.C.H. Spence, V.G. Tsirelson, and J.M. Zuo. 1999. Scanning system for high-energy electron diffractometry. *J. Appl. Cryst.* 32:1033–1038.

Bagdik'ianc, G.O., and A.G. Alexeev. 1959. *Izv. Akad. Nauk SSSR Ser. Fiz.* 23:773–779.

Batson, P.E., N. Dellby, and O.L. Krivanek. 2002. Sub-ångstroøm resolution using aberration corrected electron optics. *Nature* 418:617–620.

Berg, B.S., V. Hansen, P.A. Midgley, and J. Gjønnes. 1998. Measurement of three-dimensional intensity data in electron diffraction by the precession technique. *Ultramic.* 74:147–157.

Bethe, H.A. 1928. Theorie der beugung von elektronen an kristallen. *Ann. Phys. (Leipzig)* 87:55–129.

Blackman, M. 1939. On the intensities of electron diffraction rings. *Proc. Roy. Soc.* 173:68–82.

Cheng, Y.F., W. Nuchter, J. Mayer, A. Weickenmeier, and J. Gjønnes. 1996. Low-order structure-factor amplitude and sign determination of an unknown structure al_mfe by quantitative convergent-beam electron diffraction. *Acta Cryst. A* 52:923–36.

Chukhovskii, F.N., J.J. Hu, and L.D. Marks. 2001. Statistical dynamical direct methods ii: The three-phase structure invariant. *Acta Cryst. A* 57:231–239.

Cochran, W. 1955. Relations between the phases of structure factors. *Acta Cryst.* 8:473–478.

Combettes, P.L. 1996. Method of successive projections for finding a common point of sets in metric spaces. *Adv. Imag. Elec. Phys.* 95:155–261.

Cowley, J.M., and A.F. Moodie. 1957. The scattering of electrons by atoms and crystals. i. a new theoretical approach. *Acta Cryst.* 10:609–619.

Deng, B., and L.D. Marks. 2005 in preparation.

Dorset, D.L. 1995. *Structural electron crystallography*. New York:Plenum Publishing Co.

Dorset, D.L., S. Hovmoller, and X. Zou, eds. 1997. *Electron crystallography*. Dordrecht:Kluwer Academic.

Edwards, D.D., T.O. Mason, W. Sinkler, L.D. Marks, K.R. Poeppelmeier, Z. Hu, and J.D. Jorgensen. 2000. Tunneled intergrowth structures in the ga_20_3-in_2o_3-sno_2 system. *Journal of Solid State Chemistry* 150:294–304.

Egerton, R.F. 1989. *Electron*. New York:Plenum Press.

Franco, S. 2002. *Design with operational amplifiers and analog integrated circuits*. New York:McGraw-Hill.

Gemmi, M. 2001. Precession technique. In *Electron crystallography and cryo-electron microscopy on inorganic materials and organic and biological molecules*, ed. J. Puiggali, A. Rodriquez-Galan, L. Franco, and M.T. Casas, L91–L97. Barcelona:Universitat Politecnica De Catalunya.

Gemmi, M., X.D. Zou, S. Hovmoller, A. Migliori, M. Vennstrom, and Y. Andersson. 2003. Structure of ti_2p solved by three-dimensional electron diffraction data collected with the precession technique and high-resolution electron microscopy. *Acta Cryst. A* 59:117–126.

Gjønnes, J., V. Hansen, B.S. Berg, P. Runde, Y.F. Cheng, K. Gjnnes, D.L. Dorset, and C.J. Gilmore. 1998a. Structure model for the phase al_mfe derived from three-dimensional electron diffraction intensity data collected by a precession technique. comparison with convergent-beam diffraction. *Acta Cryst. A* 54:306–319.

Gjønnes, J., and A.F. Moodie. 1965. Extinction conditions in dynamic theory of electron diffraction. *Acta Cryst.* 19:65–&.

Gjønnes, K. 1997. On the integration of electron diffraction intensities in the vincent-midgley precession technique. *Ultramicroscopy* 69:1–11.

Gjønnes, K., Y.F. Cheng, B.S. Berg, and V. Hansen. 1998b. Corrections for multiple scattering in integrated electron diffraction intensities. application to determination of structure factors in the 001 projection of al_mfe. *Acta Cryst. A* 54:102–119.

Griend, D.A. Vander, S. Boudin, V. Caignaert, K.R. Poeppelmeier, Y.G. Wang, V.P. Dravid, M. Azuma, M. Takano, Z.B. Hu, and J.D. Jorgensen. 1999. $La_4cu_3moo_{12}$: A novel cuprate with unusual magnetism. *J. Am. Chem. Soc.* 121:4787.

Haider, M., S. Uhlemann, and B. Kabius. 1999. Towards sub-ångstrøm resolution by correction of spherical aberration. *Scanning* 21:89–90.

Haider, M., S. Uhlemann, E. Schwan, H. Rose, B. Kabius, and K. Urban. 1998. Electron microscopy image enhanced. *Nature* 392:768–769.

Harker, D., and J.S. Kasper. 1948. Phases of fourier coefficients directly from cyrstal diffraction data. *Acta Cryst.* 1:70–75.

Hauptman, H.A. 1991. The phase problem of x-ray crystallography. *Rep. Prog. Phys.* 54:1427–1454.

Hirsch, P.B., A. Howie, R.B. Nicholson, and D.W. Pashley, eds. 1965. *Electron microscopy of thin crystals*. London:Spottiswoode, Ballantyne, & Co. Ltd.

Horowitz, P., and W. Hill. 1989. *The art of electronics*. New York:Cambridge University Press.

Hu, J.J., F.N. Chukhovskii, and L.D. Marks. 2000. Statistical dynamical direct methods. i. the effective kinematical approximation. *Acta Cryst. A* 56:458–469.

Hwang, J.H., D.D. Edwards, D.R. Kammler, and T.O. Mason. 2000. Point defects and electrical properties of sn-doped in-based transparent conducting oxides. *Solid State Ionics* 129:135–144.

Jansen, J., D. Tang, H.W. Zandbergen, and H. Schenk. 1998. Msls and a least-squares procedure for accurate crystal structure refinement from dynamical electron diffraction patterns. *Acta Cryst. A* 54: 91–101.

Khattak, C.P., D.E. Cox, and F.F.Y. Wang. 1975. Magnetic ordering in ba_2mnreo_6. *J. Solid State Chem.* 13:77–83.

Kilaas, R., L.D. Marks, and C.S. Own. 2005. Edm 1.0: Electron direct methods. *Ultramic.* 102:233–237.

Krivanek, O.L., N. Dellby, and A.R. Lupini. 1999. Towards sub-å electron beams. *Ultramic.* 78:1–11.

Krivanek, O.L., and P.A. Stadelmann. 1995. Effect of three-fold astigmatism on high resolution electron micrographs. *Ultramic.* 60:103.

Landree, E., C. Callazo-Davila, and L.D. Marks. 1997. Multi-solution genetic algorithm approach to surface structure determination using direct methods. *Acta Cryst. B* 53:916–922.

Levi, A., and H. Stark. 1984. Image restoration by the method of generalized projections with application to restoration form magnitude. *J. Opt. Soc. Am. A* 1:932–943.

Mancini, R. 2002. *Op amps for everyone*. Dallas:Texas Instruments, Inc.

Marks, L.D., E. Bengu, C. Callazo-Davila, D. Grozea, E. Landree, C. Leslie, and W. Sinkler. 1998. Direct methods for surfaces. *Surf. Rev. Let.* 5:1087–1106.

Marks, L.D., and W. Sinkler. 2003. Sufficient conditions for direct methods with swift electrons. *Micros. and Microanal.* 9:399–410.

Midgley, P.A., M.E. Sleight, M. Saunders, and R. Vincent. 1998. Measurement of debye-waller factors by electron precession. *Ultramic.* 75:61–67.

Nellist, P.D., M.F. Chisholm, N. Dellby, O.L. Krivanek, M.F. Murfitt, Z.S. Szilagyi, A.R. Lupini, A. Borisevich, W.H. Sides, and S.J. Pennycook. 2004. Direct sub-ångstrøm imaging of a crystal lattice. *Science* 205:1741–1741.

Newsam, J.M. 1988. Synthesis and structural characterization of a lithium gallosilicate with the zeolite abw framework. *J. Phys. Chem* 92:445–452.

Nicolopoulos, S., J.M. Gonzalezcalbet, M. Valletregi, A. Corma, C. Corell, J.M. Guil, and J. Perezpariente. 1995. Direct phasing in electron crystallography — *ab-initio* determination of a new mcm-22 zeolite structure. *J. Am. Chem. Soc.* 117:8947–8956.

O'Keefe, M.A., and R. Kilaas. 1988. Advances in high-resolution image simulation in image and signal processing in electron microscopy. In *Scanning microscopy supplement 2*, ed. P.W. Hawkes, F.P. Ottensmeyer, W.O. Saxton, and A. Rosenfeld, 225. AMF O'Hare, IL:SEM, Inc.

Own, C.S., and L.D. Marks. 2004. Hollow-cone electron diffraction system. US Patent application no: 60/531,641.

———. 2005a. Prospects for aberration-corrected precession. *Micros. and Microanal.* submitted.

———. 2005b. Rapid structure determination of a metal oxide from pseudo-kinematical electron diffraction data. *Ulramic.* in press.

Own, C.S., L.D. Marks, and W. Sinkler. 2005a. Electron precession: A guide for implementation. *Rev. Sci. Instr.* 76:Art. no. 033703.

Own, C.S., W. Sinkler, and L.D. Marks. 2005b in preparation.

Own, C.S., A.K. Subramanian, and L.D. Marks. 2004. Quantitative analyses of precession diffraction data for large cell oxides. *Micros. and Microanal.* 10:96–104.

Sayre, D. 1952. The squaring method: a new method for phase determination. *Acta Cryst.* 5:60–65.

Scherzer, O. 1936. Uber einige fehler von elektronenlinsen. *Zeit. Phys.* 101:593.

Sinkler, W., W. Bengu, and L.D. Marks. 1998a. Application of direct methods to dynamical electron diffraction data solving bulk crystal structures. *Acta Cryst. A* 54:591–605.

Sinkler, W., and L.D. Marks. 1999a. Dynamical direct methods for everyone. *Ultramic.* 75:251–268.

———. 1999b. A simple channelling model for hrem contrast transfer under dynamical conditions. *J. Microscopy* 194:112–123.

Sinkler, W., L.D. Marks, D.D. Edwards, T.O. Mason, K.R. Poeppelmeier, Z. Hu, and J.D. Jorgensen. 1998b. Determination of oxygen atomic positions in a ga-in-sn-o ceramic using direct methods and electron diffraction. *Journal of Solid State Chemistry* 136:145–149.

Spence, J.C.H. 2003. *High-resolution electron microscopy*. Oxford:Oxford Univ. Press.

Spence, J.C.H, and J.M. Zuo. 1992. *Electron microdiffraction*. New York:Plenum Press.

Suzuki, Y., A. Takeuchi, H. Takano, and H. Takenaka. 2005. Performance test of fresnel zone plate with 50 nm outermost zone width in hard x-ray region. *Jap. J. Appl. Phys. 1* 44:1996–2000.

Vainshtein, B.K. 1964. New York:Pergamon Press.

Vainshtein, B.K., B.B. Zvyagin, and A.S. Avilov. 1992. Electron diffraction structure analysis. In *Electron diffraction techniques, vol.2*, ed. J.M. Cowley, 216–312. Oxford:Oxford University Press.

Vincent, R., and D.M. Bird. 1986. Measurement of kinematic intensities from large-angle electron-diffraction patterns. *Phil. Mag. A* 53:L35–L40.

Vincent, R., D.M. Bird, and J.W. Steeds. 1984. Structure of augeas determined by convergent-beam electron diffraction: 1. derivation of basic structure. *Phil. Mag. A* 50:745–763.

Vincent, R., and P. Midgley. 1994. Double conical beam-rocking system for measurement of integrated electron-diffraction intensities. *Ultramic.* 53:271–282.

Weirich, T.E. 2004. The crystal structure of zr_2se reinvestigated by electron crystallography and x-ray powder diffraction. *Cryst. Rep.* 49:379–389.

Xu, P., G. Jayaram, and L.D. Marks. 1994. Cross-correlation method for intensity measurement of transmission electron diffraction patterns. *Ultramic.* 53:15–18.

Youla, D.C. 1987. Mathematical theory of image restoration by the method of convex projections. In *Image recovery: theory and applications*, ed. H. Stark, L91–L97. Orlando:Academic press, Inc.

Yu, B.Y., A. Abramov, V.G. Tsirelson, V.E. Zavodnik, S.A. Ivanov, and I.D. Brown. 1995. The chemical bond and atomic displacements in $srtio_3$ from x-ray diffraction analysis. *Acta Cryst. B* 51:942–951.

Zukhlistov, A.P., M.S. Nickolsk, B.B. Zvyagin, A.S. Avilov, A.K. Kulygin, S. Nicolopoulos, and R. Ochs. 2004. Imaging plates - a new life for electron diffraction structure analysis. *Zeit. Krist.* 219:2004.

Appendices

APPENDIX A

Electronics Background

This section contains a review of some basic electronics that may be helpful for interpreting the circuit schematics in the PED implementations and understanding alignment procedures in later appendices. Discussion is limited based upon relevance to physical precession systems.

A.1. Limited-bandwidth systems

In feedback control theory, a *system* represents an entity to be controlled. It is treated as a black box with inputs and outputs, and the outputs exhibit a specific behavior for a given input. Such a system can be described by a transfer function (TF), a function of the frequency variable s, that describes its behavior. Here we will be concerned only with linear time invariant systems, which exhibit proportionality between cause and effect, and demonstrate additivity of effects (e.g., they obey the principle of superposition).

Beam deflector coils in the microscope are simple inductors that generate a response — a magnetic field, which deflects a beam of electrons — when current within the coil changes with time (e.g., response scales with dI/dt). They behave as low-pass filters when configured in series within a circuit, and can be modeled in feedback theory as a single-pole system P_{coil} in the series configuration, for example:

$$P_{coil} = \frac{1}{s+5}. \tag{A.1}$$

A pole is a factor of s contained within the denominator of the TF.

This transfer function describes a coil with rather poor bandwidth and the output of the coil is much lower than the input, indicating losses within the coil. The attenuation requires an input that is 5 times larger in order to generate the desired response: if a response of 2 is desired, an input command of 10 must be provided. In this discussion, the units are simply "response units" as pertains to the desired output of system. It may be current, magnetic field, or deflection amplitude.

Bode diagrams describe the frequency-amplitude behavior of a system such as the one in equation A.1. It represents the amplitude response (frequency response) and the phase response of the system to a unity input over a range of frequencies. A sample Bode plot is shown in figure A.1(b) for the TF described in equation A.1 (its block diagram is given in figure A.1(a)). The figure shows that the system's amplitude reponse is about 15 dB down at DC (0 Hz) and decays at 20 dB per decade. The system phase responds quite favorably with increasing frequency, never exceeding 90° phase delay behind the input.

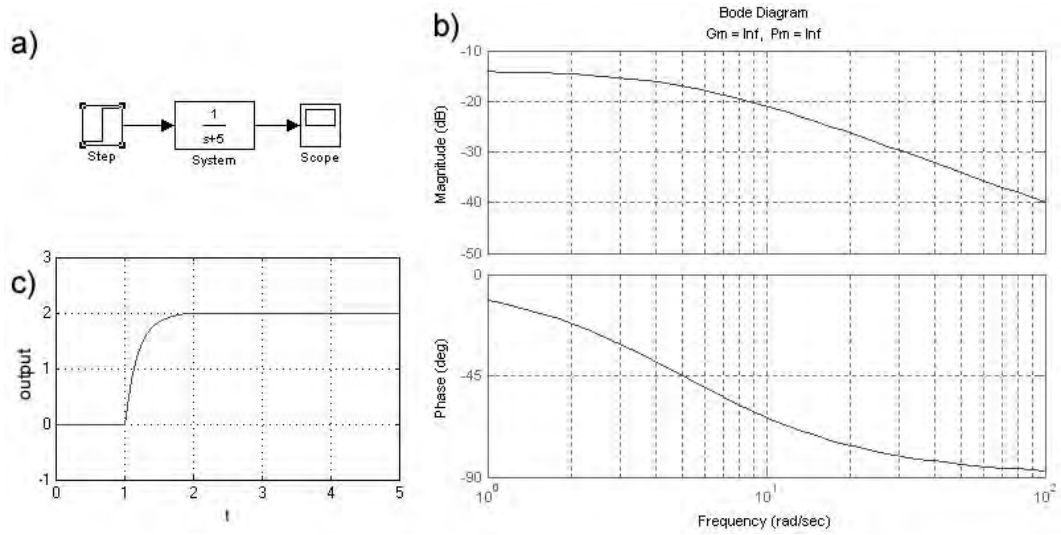

Figure A.1. (a) The block diagram for the system described by equation A.1. The Bode plot for this system is shown in (b), and the scope output showing the response to a step input of 10 units is displayed in (c).

The system is operated in single-ended mode, meaning that the system is given an input and is responsible for meeting the input with the appropriate output response; the system in this case does not monitor whether or not it has actually met the targeted output. The rise time at the output with response to a step input (infinitely steep) is relatively slow (about 1.7s, see figure A.1(c)), scaling with the time constant of the coil. Because the system is configured to be single-ended, it is susceptible to external factors such as oscillating magnetic fields that might alter the current in the coil at any given time.

This situation is not ideal for precise control of the system. Feedback is a solution: addition of feedback will give considerable improvements because it allows control of the current within the coil with the ability to correct for external disturbances, and it can be tailored to improve response. The system depicted in the block diagram in figure A.2(a) shows such a feedback network. In this case, some integrating electronics with effective transfer function $\frac{300}{s}$ are inserted in series, and a feedback loop with gain of 0.5 is installed around the two systems in series to provide the desired whole-system gain of 2. The effective transfer function of multiple systems in series is the product of their TF's, hence the TF of this feedback system can be calculated by taking the effective TF of the single-ended system divided by the sum, 1 + the TF around the feedback loop, giving:

$$G_{fb} = \frac{300}{s^2 + 5s + 150}. \tag{A.2}$$

The Bode plot in figure A.2(b) shows that the system response has been improved. A resonant peak occurs at about 5 rad/sec, and the step response (figure A.2(c)) shows a more rapid rise in output accompanied by some overshoot and then settling behavior to the steady state value. This system is optimized for rapid rise time, however such a coil control system would be deficient in many applications

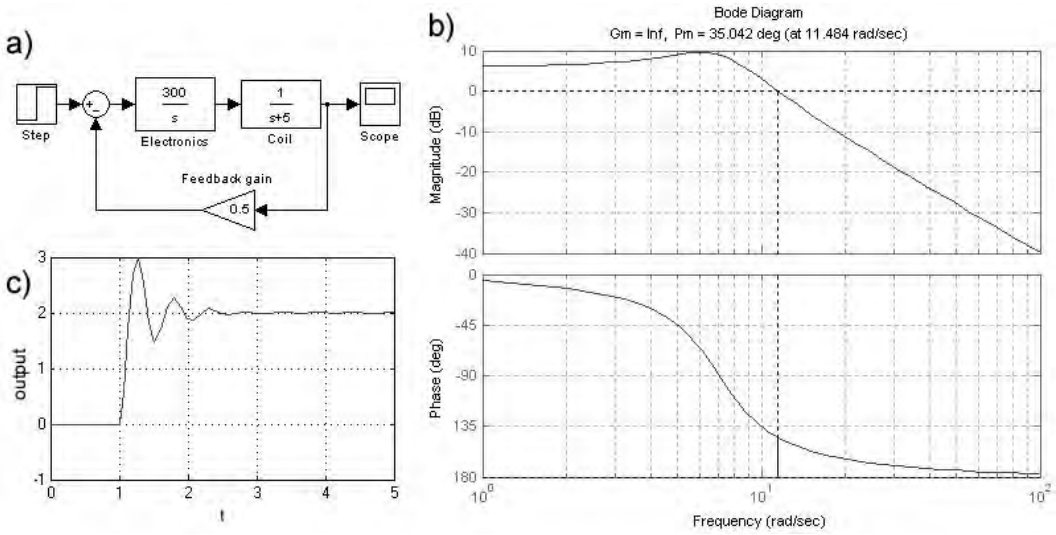

Figure A.2. (a) The block diagram for the system described by equation A.2. The Bode plot for this system is shown in (b), and the scope output showing the step response (1 unit) is displayed in (c).

because it is underdamped and does not settle rapidly. Further modification of the electronics transfer function with a different pole (e.g., changing the location of zeros in the denominator), or introducing higher order filtering (adding more poles to get higher powers of s in the denominator) can damp the overshoot and quell the ringing faster while not compromising rise time.

The bandlimiting occurs after the resonant peak with increasing frequency. The frequency response is 3 dB down by about 10 rad/sec and decreases in amplitude at a rate of 20 dB per decade. A second characteristic is that the phase of the oscillating signal varies between a few degrees to about -145° over its frequency bandwidth (180° phase lag corresponds to an unstable system). This is an important point because both BT and DS amplifiers will exhibit decreased output amplitude and increased phase lag as frequency increases. The result will be a change in the phase shift between the two coil sets when scanning frequency changes unless the coils and coil drivers are of the same type, the scanning frequency is low, or the system bandwidth is very high.

A.2. Amplifier design

The electronics used in the precession implementations of appendices B-D are based upon operational amplifiers (op-amps). Op-amps are complex feedback systems that are very versatile and easy to use for a variety of analog control and filtering applications. A short guide on how to implement basic op-amp circuits is given in this section. For advanced op-amp usage details, the reader is referred to an analog circuits textbook or IC application notes (Horowitz and Hill 1989; Franco 2002; Mancini 2002).

An ideal op-amp is shown in figure A.3. It exhibits very specific characteristics:

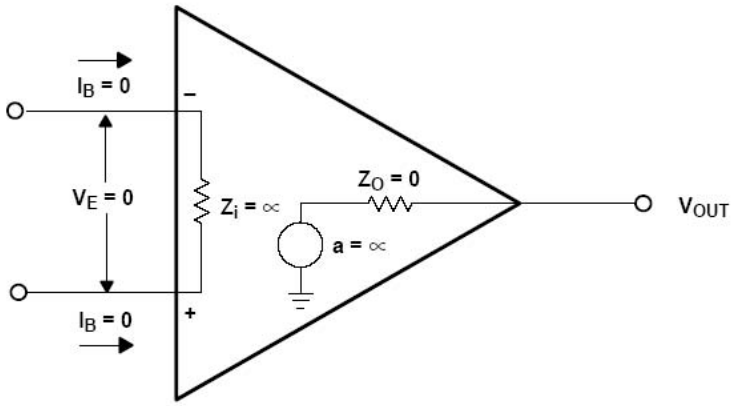

Figure A.3. The ideal op-amp (from Mancini (2002)).

- The two inputs ($+$ and $-$) have infinite input impedance: $z_{in} = \infty$. Thus, the inputs demand zero input current and do not load down the source. [1]
- The op-amp has infinite gain on either input: $a = \infty$. When the op-amp is in single-ended configuration, a small voltage applied on either input will force the output to $\pm\infty$.
- The output impedance is zero: $z_{out} = 0$. The op-amp will therefore supply sufficient current to whatever load it is called upon to drive.
- The op-amp will do whatever it can to force the voltage difference between the inputs to zero: $V_e = 0$. This usually means that the output of the op-amp will change to meet this condition.

The application of feedback to the op-amp is what makes it a very powerful electronic component. A diagram of a common operational amplifier, the LM741 (in DIP8 package) is depicted in figure A.4. It possesses two signal inputs (inverting and non-inverting), one output, power supply inputs, and pins for offset nulling. Figures A.4(b)-(d) show the most basic configurations for amplification using this type of device. The non-inverting amplifier outputs a signal with the same polarity as the input waveform whereas the inverting amp naturally inverts polarity of the input. The gain of each configuration, shown to the right of each circuit in figure A.4, is set by a combination of the feedback resistor R_f and a second resistor R_i.

In circuit analysis terms, R_f and R_i represent a voltage divider (figure A.5(a)). The op-amp ensures that the two input terminals stay at the same voltage at equilibrium, thus the output terminal is forced to a voltage dependent upon the values of R_f and R_i. This can be determined by the voltage divider equation:

$$V_2 = \frac{R_i}{R_i + R_f} V_1 \tag{A.3}$$

[1] Impedance is the resistance to current flow dependent upon frequency in an AC system. Source impedance usually arises due to inductive effects.

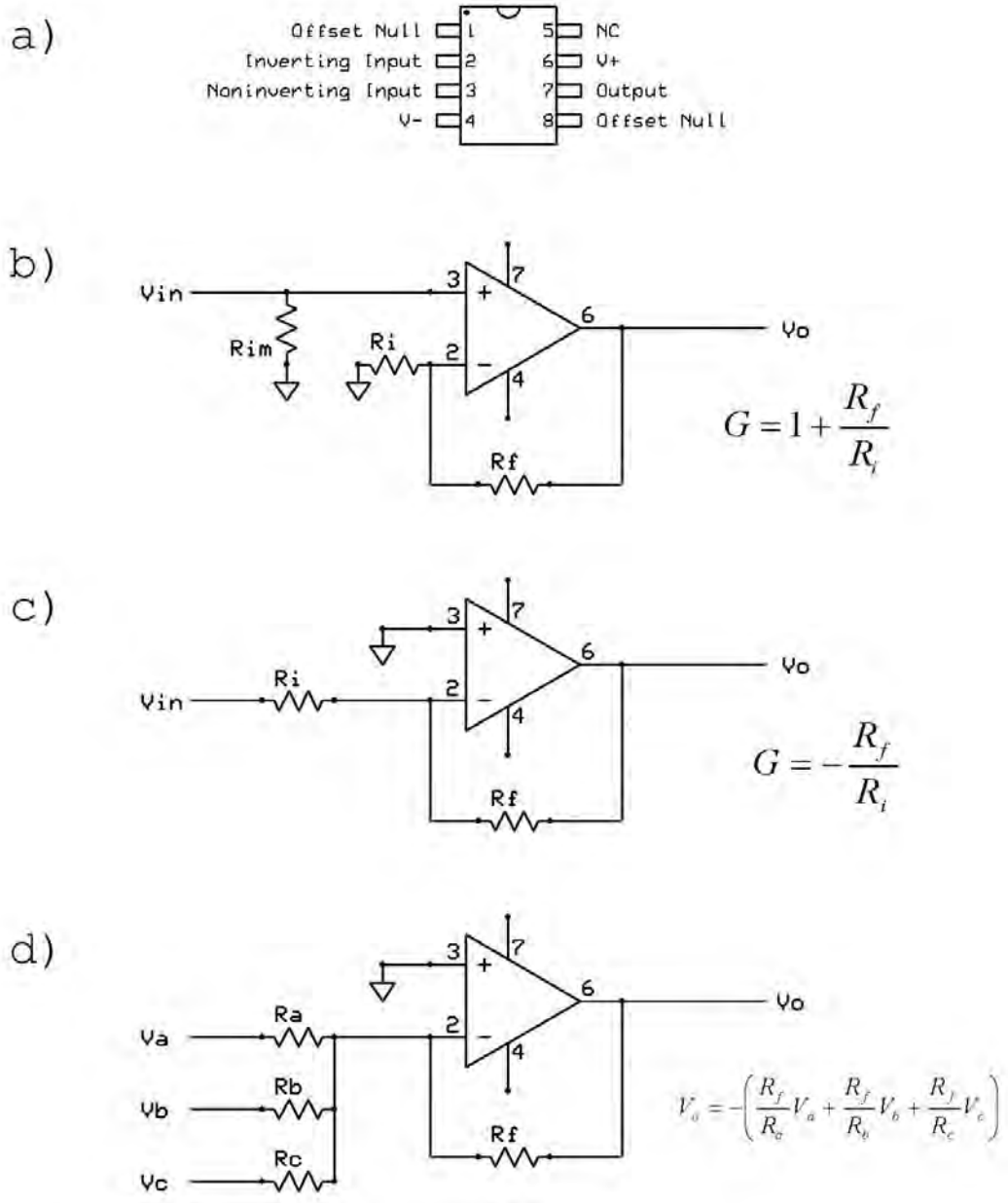

Figure A.4. (a) LM741 op-amp, DIP8 package. (b) Noninverting, (c) inverting, and (d) mixer (inverting) operational amplifier circuit configurations.

The output of the op-amp decreases the impedance at its connection to the voltage divider such that that terminal can drive (ideally) any downstream component. This is the reasoning behind a unity gain buffer stage, which does nothing other than convert impedances (and inverts the signal if configured to be inverting). In the mixer configuration, multiple input resistors are used which isolate the inputs from

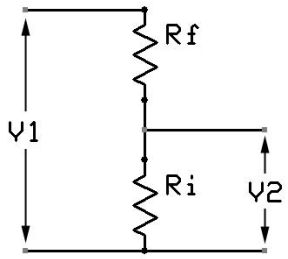

Figure A.5. Voltage divider.

each other. A relatively high value resistor (typically > 1 kΩ) is necessary to ensure that the inputs do not drive the others.

For precession, at least two inputs are necessary, one for steady-state control from the microscope console and the other for the oscillatory scan signal from the precession scan generator. In certain cases where the zero-point is significant (e.g., an "inputs-are-zeroed" indicator trigger), the amplifier may require offset trimming to remove voltage offset at the output. Some devices available on the market feature low intrinsic offset voltage to address this without user intervention.

Active filtering can be accomplished by adding capacitors or inductors to the feedback network. A simple low-pass filter was shown in 2.12(a), which results in a -3 dB point at a frequency of $\frac{1}{2\pi R_f C_f}$, where R_f and C_f are paralleled in the feedback loop. In feedback control theory, this represents an integrator, which produces a stronger negative feedback signal if the output does not respond as time passes. The capacitor time constant determines the bandwidth of the filter. Other configurations are available that provide high pass, band pass, or notch filtering behavior, the latter two generated by cascading different filter configurations in series. The reader is referred to reference texts for examples.

Real-world op-amps are naturally imperfect and are designed with compromises to meet specific application needs. Some basic constraints for selecting an amplifier device off the shelf for small signal buffering in precession are: high input impedance, moderate bandwidth, high power supply rejection ratio, and unity gain stability for the output buffer (second gain stage). FET-input (field-effect transistor) operational amplifiers that operate at unity gain in a moderate frequency range of DC to a few hundred kHz are quite suitable.

While operational amplifiers in general have excellent supply noise rejection, a well-designed power supply is nevertheless critical for performance. The supply should be able to deliver the current demanded by the amplifier rapidly (low supply impedance) and should have low noise to avoid poisoning the output signal with supply noise. Further, a split voltage supply is required for amplifying bipolar signals. The supply voltage rails should exceed the maximum signal amplitude by a fair margin to account for dropout voltage in the active devices, additionally it should be noted that many small-signal op-amps perform best when powered near their maximum rated supply voltage. Supplies of ± 15 V are common in TEMs and it is often sufficient to use the on-board supply (commonly accessible from test points on the signal board) to power the precession electronics. Alternatively, an external supply can be

used so that the precession power supply is immune to fluctuations caused by circuits elsewhere in the microscope and vice versa.

Low supply impedance — already mentioned — is important for satisfying current demands. It is also crucial for amplifier stability and performance. The supply inductance can be decreased by decoupling the supply, synonymous with power supply bypassing. This is generally accomplished by providing a low impedance path to the amplifying device by placing extra capacitance near the device power supply leads. It is generally good practice to tier this: a high capacity electrolytic capacitor should be used, followed by a smaller low-ESR (equivalent series resistance) tantalum capacitor, and finally a low-loss, low-impedance film or ceramic capacitor of small capacity near the leads. The electrolytic capacitor is lossy and has high impedance compared to the others but it decreases power supply ripple by providing additional capacitance. Combination with smaller, faster, and low loss capacitors provides an extremely low impedance path to current reserves. A properly-bypassed op-amp will have better frequency response (closer to rated slew rate), and have less supply-related distortion at its output.

A.3. Simple Linear Power Supply Design

The type of power supply used in the later precession implementations is a simple regulated linear supply using off-the-shelf active regulator components. Linear power supplies are less efficient than switching power supplies commonly found in electronics, however, they exhibit much lower noise so are preferred in this application. A conventional linear supply comprises three main stages, a transformer to convert the AC mains voltage into an AC voltage with amplitude suitable for the electronics being supplied, a rectification stage to rectify the waveform polarity, and filtering (including regulation) to store the charge and/or reduce the ripple to form a stable supply voltage. Figure A.6(a) shows a simple LC supply that incorporates a full-wave bridge rectifier.

In this supply, a transformer with internal resistance of 31 Ω supplies a 48 VRMS AC waveform to the bridge rectifier. Specifically, the primary winding of the transformer accepts 120VAC and the secondary winding outputs 48VAC, meaning the turns ratio between primary and secondary is about 2.5. The bridge is designed such that the top legs only conduct positive current and the bottom legs conduct only negative current, rectifying the voltage. The rectifier bridge is a full wave rectifier, so charge is being conducted during all parts of the AC waveform. The bottom legs may be fixed to a reference such as ground, forcing the top of the bridge to be positive with respect to that reference. An LC filter follows. The 1 H inductor acts as a current choke, limiting large current flow except when demand is very high. Referring to figure A.6(b), the steady state behavior of the inductor is a mild oscillation of about 25 mA peak-to-peak that charges the capacitor C1 between AC waveform rectification cycles. The time constant of the 220 μF capacitor is on the order of 700 s, therefore the capacitor does not discharge much into the 5 kΩ load R1 during each AC cycle. The inductor, L1, whose time constant is much lower, is able to effectively replenish the charge being drawn from C1 by the load.

The start-up behavior is the most stressful part of operation and components must be chosen to endure the turn-on conditions. During a period of about 50 ms, the capacitor acts as a short circuit, demanding as much instantaneous charge as can be supplied through the inductor. The current through the inductor peaks at about 410 mA and then declines to steady state behavior as the capacitor nears

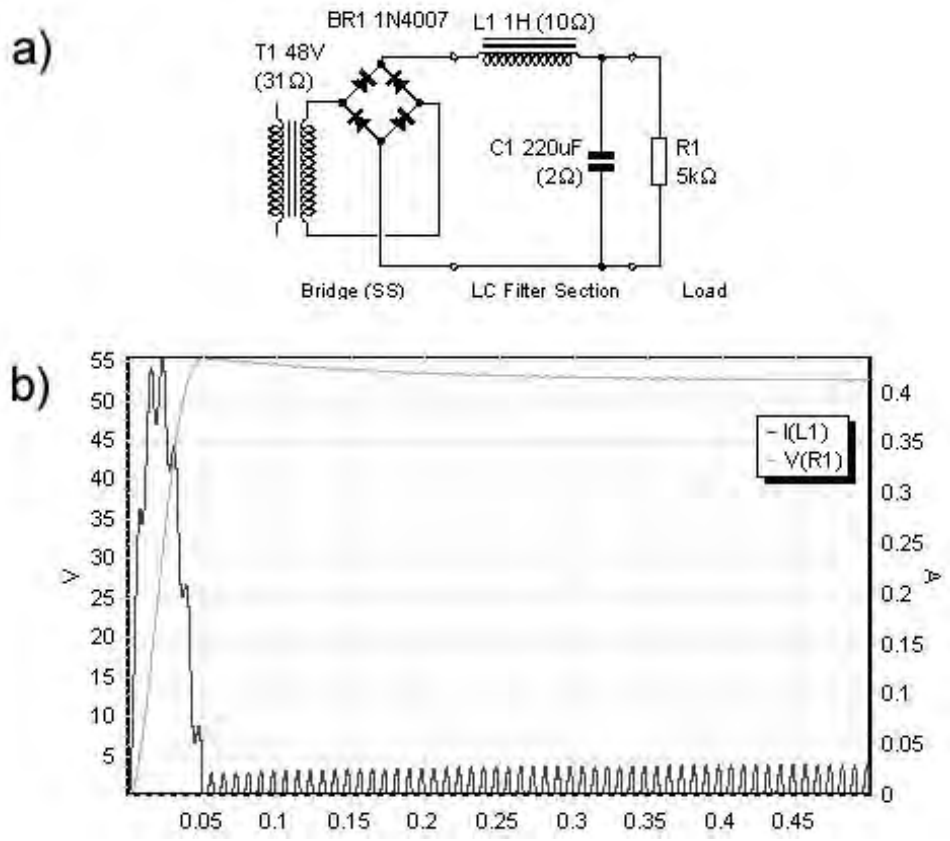

Figure A.6. (a) Full-wave 48V LC unregulated supply. (b) The current and through the inductor L1 and the voltage supplied to the load V(R1). The turn-on behavior results in a spike in current and a slow build-up of supply voltage with stabilization by about 300ms.

full charge. C1 experiences a slight overshoot before settling to the steady state loaded voltage of ≈ 52 V. The rectifier must have sufficient headroom (typically a factor of two or three) to handle the large instantaneous current demanded by the supply at turn-on. In this case, rectifier diodes rated at 1-1.5 A would be desired.

Split supplies simply fix a reference voltage in between the two voltage rails. Since the secondary windings and rectifier are floating (they do not reside at an absolute voltage), it will graciously supply the full voltage across the secondaries and the downstream electronics divide this as necessary to provide positive and negative voltages.

If the supply is more heavily loaded, this voltage may sag. Regulation is the solution to this problem. The raw DC voltage provided by the supply in figure A.6 can be fed into a regulation stage, a feedback system itself, which monitors the output voltage and keeps it at the same value regardless of load (lowers

supply impedance). Regulators are often made from discrete components, however monolithic three-terminal fixed-voltage regulators are quite straightforward to use — they are simply placed in series with the supply leads and a reference pin is tied to an appropriate voltage reference. Usage details can easily be found in datasheets for off-the-shelf components.

APPENDIX B

Implementation 1

B.1. Hitachi H-9000 retrofit

The Hitachi UHV H-9000 is a 300 kV instrument designed for high resolution imaging and diffraction. The instrument incorporates a special SA imaging mode for selected area diffraction experiments intended to minimize SA errors. Because the system has a small objective polepiece gap, the stage allows only about $\pm 10^{\circ}$ tilt and the UHV side insertion system has been designed without z-height adjustment for mechanical simplicity.

A stacked pair of coils (a dipole and quadrupole deflector) located several centimeters above the objective polepiece gap provides BT deflections. DS deflections are provided by a dipole deflector nested inside the projector lens. Upper column electronics can be found on the board BD STB under the left console, and image shift is controlled from a small potentiometer box that controls an amplifier board mounted the left console side, called Image S. The relevant section of the BD STB schematic is shown in figure B.1 Each beam tilt axis is set using a digital encoder that controls a DAC (not shown) followed by a small unity gain buffer. This signal is in the range of ± 5 V and supplies the BTX and BTY inputs on connector CN3503. Section I in the figure is part of an analog hollow cone driver called STIG MON for monitoring astigmatism in the objective lens (not active during normal operation). Following is the tilt amplifier (II) comprising an op-amp in summing mode driving a FET-output voltage-to-current amplifier. There is some biasing circuitry in this stage that ensures sufficient bandwidth for the tilt wobbler adjustment, favorable for precession because it offers operation up to about 1 KHz. Section III is a voltage divider and switching array used to split the current between the three coil windings for each tilt axis. Four user-accessible potentiometers in this stage control the division of current to each winding: these are the X_{main}, X_{vert}, Y_{main}, and Y_{vert} controls used during shift-tilt purity alignment.

The custom modules described in section 2.5 (figure 2.12) were retrofitted at points a and b in series with the input CN3503. The modules were built around an LM324 integrated circuit in DIP14 package (a quad 741 IC with class AB biasing). The BT mixer module was mounted onto a short length of 34-conductor ribbon cable that also serves as a quick-release pass-through extender for connector CN3503. Conductors 3 and 5 on the cable, corresponding to pins 2 and 3 of CN3503, were used to insert X and Y signals, respectively, and conductor 1 was used for the ground reference. Power was supplied to the add-on boards via the $\pm$15V supply pins on the BD STB and Image S. boards.

The image shift circuit is intended for steady state operation and is correspondingly quite different from BD STB (figure B.2). The signal originates from a 10 V precision reference (I.), converted into ± 4 V reference legs (II.) by an op-amp stage. These are divided into control voltages by linear potentiometers (III.) followed by a differential op-amp buffer stage (IV.) that feeds the coil amplifier

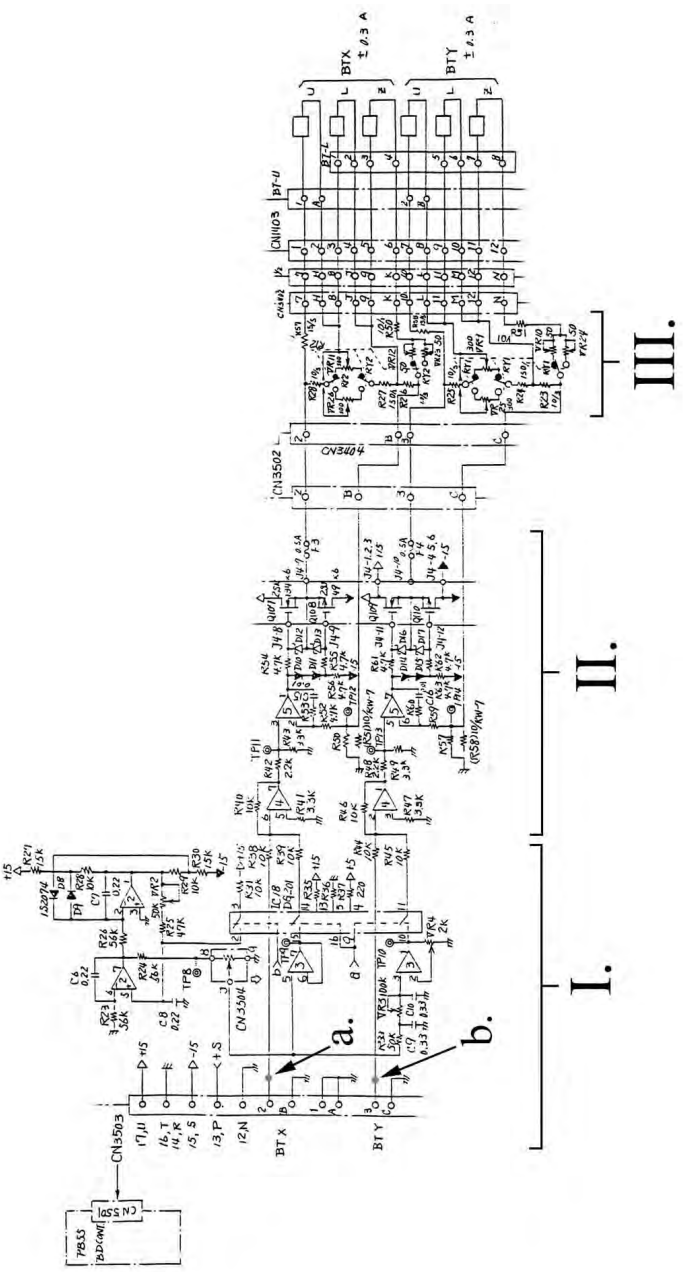

Figure B.1. BD STB circuit, Hitachi H-9000. Courtesy of Hitachi High Technologies.

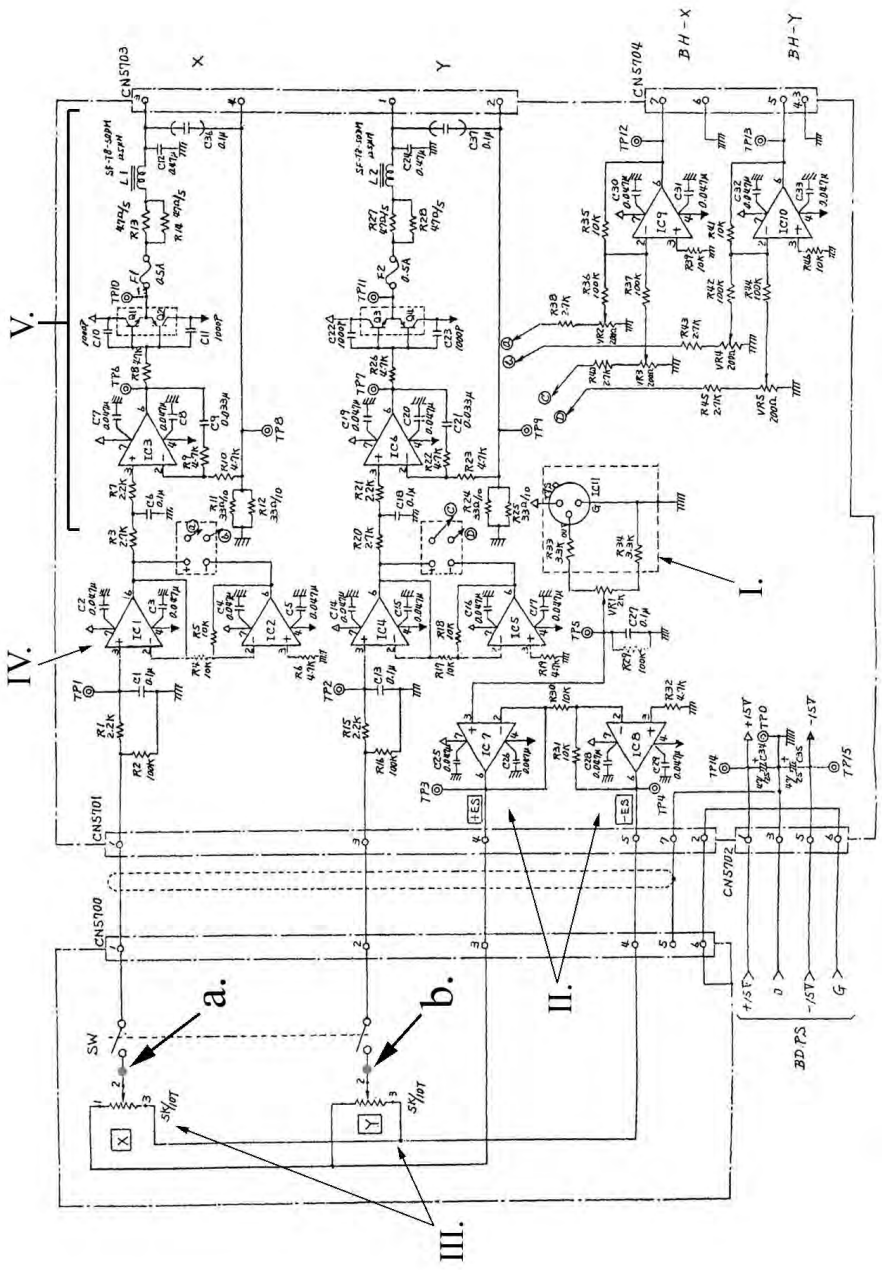

Figure B.2. Image S. circuit, Hitachi H-9000. Courtesy of Hitachi High Technologies.

(V.). The inverted leg of the differential buffer (not connected in this instrument) provides an optional compensation signal for an extra dipole deflector (BH-X,Y) earlier along the optic path. The DS current amplifier terminates in a bipolar push-pull output stage that delivers larger currents than the BT (around several hundred milliamps) to achieve appreciable deflections of the image on the viewing screen. The circuit is precise and has low noise for image stability.

While excellent for DC signals, the stock image shift circuit was found to be unsuitable for precession due to the class B problem (see section 2.5.1 for details). Push-pull amplification stages, if not properly biased, can cause distortion at the zero-crossing point of rapidly varying signals because each device in the complementary pair has a finite switching time. A possible solution was to bias the output stage into class A to remove the distortion, however working around the design proved difficult and the final solution took the form of a completely redesigned board based on power op-amps shown in figure B.3. This preserves the service warranty for the instrument and provides extra performance headroom. The Image S. circuit is broken at R3/R20 and the output of the preceding driver stage is routed directly to the custom DS amplifier board, bypassing the stock amplifier. The replacement amplifier consists of an OPA544T power operational amplifier in a current-sense feedback loop similar to that used in the stock circuit. Power and ground are supplied from Image S. and additional supply filtering is employed. The replacement unit extends usable bandwidth beyond 2KHz.

Figure B.4 contains photographs of the completed UHV H-9000 precession implementation demonstrating the installation locations.

B.2. Performance and limitations

The precession mode is typically operated at about 60 Hz to ensure ample intensity averaging for short exposures. During operation, an artifact often appears in the scan due to power supply ripple identified by a "snail" (a small kink in the circle pattern) that travels slowly around the BT circle. Its speed depends on the relation between the scan and mains frequencies. The artifact can be removed by precisely matching the scan rate with the oscillation frequency of the mains. This can vary throughout the day, depending on the mood at the power company. On-site, the mains frequency typically varies between about 59.25 Hz to 60.25 Hz and can change during a microscopy session.

The H-9000-based precession instrument is limited by its lack of eucentric height adjustment and small tilt range ($\pm 10^{\circ}$). Depending upon insertion conditions, the specimen height may deviate from optimum crossover by over 100 μm, limiting the spatial resolution of the precession probe. The shift-tilt purity correction range is insufficient to localize the probe. To circumvent this problem, precession is typically operated with selected-area mode using parallel illumination: the SA aperture limits probe wandering by ensuring even illumination of the specimen. However, the smallest probe size becomes limited by aperture size, and SA errors give rise to excess delocalization of illumination that cannot avoided because optimum lens excitation and specimen height are unavailable (Hirsch et al. 1965).

Poor probe localization is the ultimate limitation of this system, making nanocrystal precession diffraction studies difficult. The instrument nevertheless acquired patterns from large regions and isolated small particles rather well, giving good averaged patterns from sample regions about 200 nm in

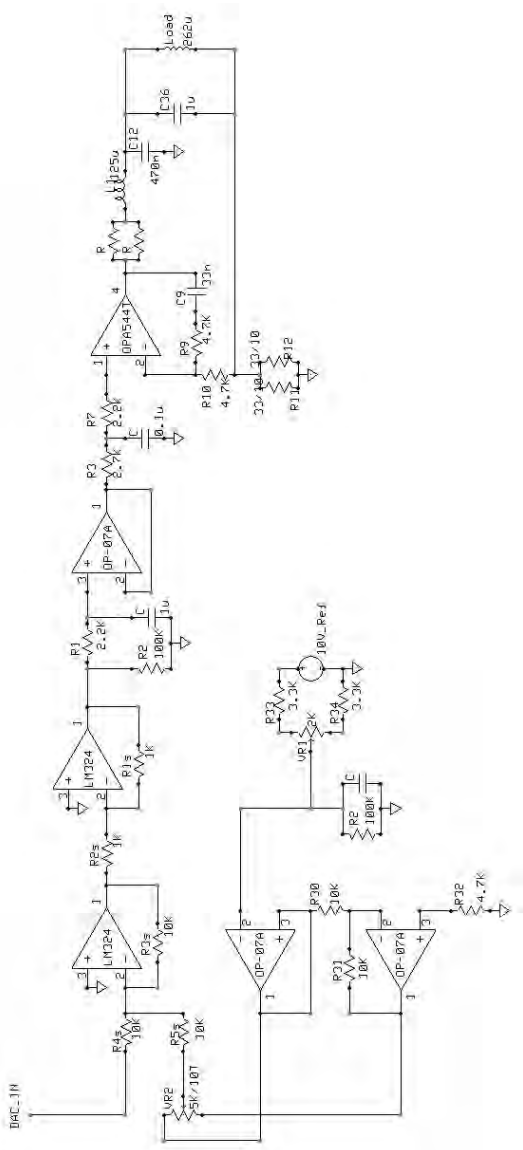

Figure B.3. Revised coil driver circuit, based around the OPA544T power operational amplifier.

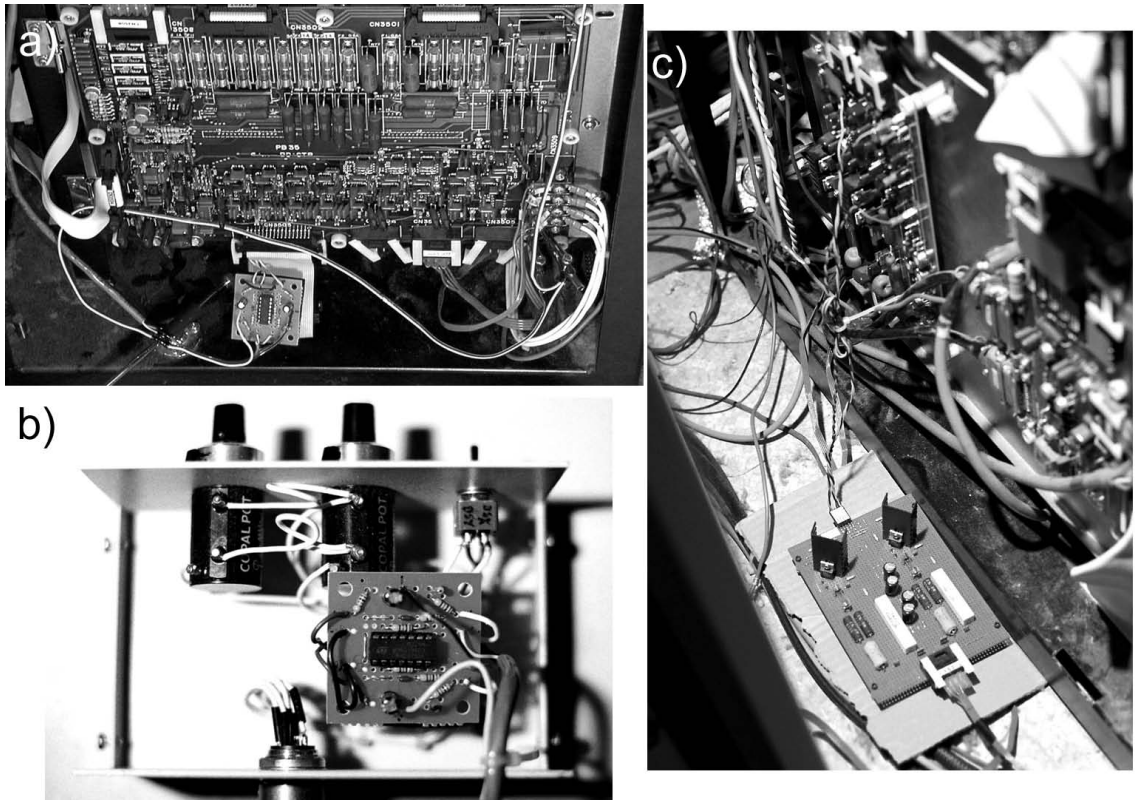

Figure B.4. The hardware for the first-generation precession instrument installed on the Hitachi UHV H-9000. (a)-(b) BT and DS signal insertion modules. (c) Replacement DS coil driver of figure B.3.

diameter. Measurable patterns have been acquired from $Mg_3V_2O_8$ and $La_4Cu_3MoO_{12}$ with this machine (Own et al. 2004). For the $La_4Cu_3MoO_{12}$ experiments, the cone angle of 25 mrad was large for this instrument and the spots became ill-defined and difficult to measure. Rather than employing the more accurate method of cross-correlation using average unitary spot motif (requiring similarly-shaped spots), the intensities from this pattern were integrated after background subtraction from small masked regions around each spot. This quantitation method is described in appendix F.

APPENDIX C

Implementation 2

C.1. JEOL 2000FX Retrofit

A second-generation precession instrument was constructed based on the JEOL 2000FX microscope chassis located at UOP, LLC in Des Plaines, Illinois. The 2000FX is an analytical instrument well suited for precession since the polepiece supports high tilts by virtue of a well-developed convergent beam mode. The instrument included a $\pm 45^{\circ}$ side-entry double-tilt holder and a model US1000 2K $\times$ 2K CCD camera from Gatan, Inc. This implementation drew upon the knowledge gained from the previous precession implementation and integrated some refinements that improved performance dramatically:

(1) Specimen holder z-height adjustment;
(2) The polepiece supports large tilts;
(3) A large CCD streamlines dataset acquisition;
(4) Beam blanking above specimen decreases radiation damage;
(5) Miniaturized plug-in modules using surface mount devices;
(6) Independent power supply (external);
(7) Improved grounding scheme;
(8) Updated software.

Photographs of this implementation are shown in figure C.1.

The 2000FX deflector electronics are located on a single board DEF UNIT, which controls all deflector coils in the column (accessible below the right-hand console behind an acrylic cover). The current values for each coil set, controlled by a pair of digital encoders, is stored in memory and held constant by the microscope computer, changing only when console control is passed to that coil set. The power amplifier design is common to most of the deflectors in the instrument and is simply replicated in each coil driver circuit down the column. The 2000FX has provisions for a hollow-cone illumination option, thus its deflectors can process fast scan signals without modification.

Block diagrams for the BT and DS amplifiers are displayed in figure C.2. Coils COND1,2X,Y provide BT deflections, and PROJX,Y denote the DS deflectors. For precession, the location at which the digital stage feeds the analog stage is an ideal location to insert the scan signal. The mixer modules can simply be inserted in series before resistors R63, R70, R103, and R106, corresponding to BTX, BTY, DSX, and DSY.

The plug-in modules (figure C.3(a)) were based on Burr-Brown OPA2604 dual operational amplifiers in SOIC8 package — low noise amplifiers designed for audio. Most of the electronics were

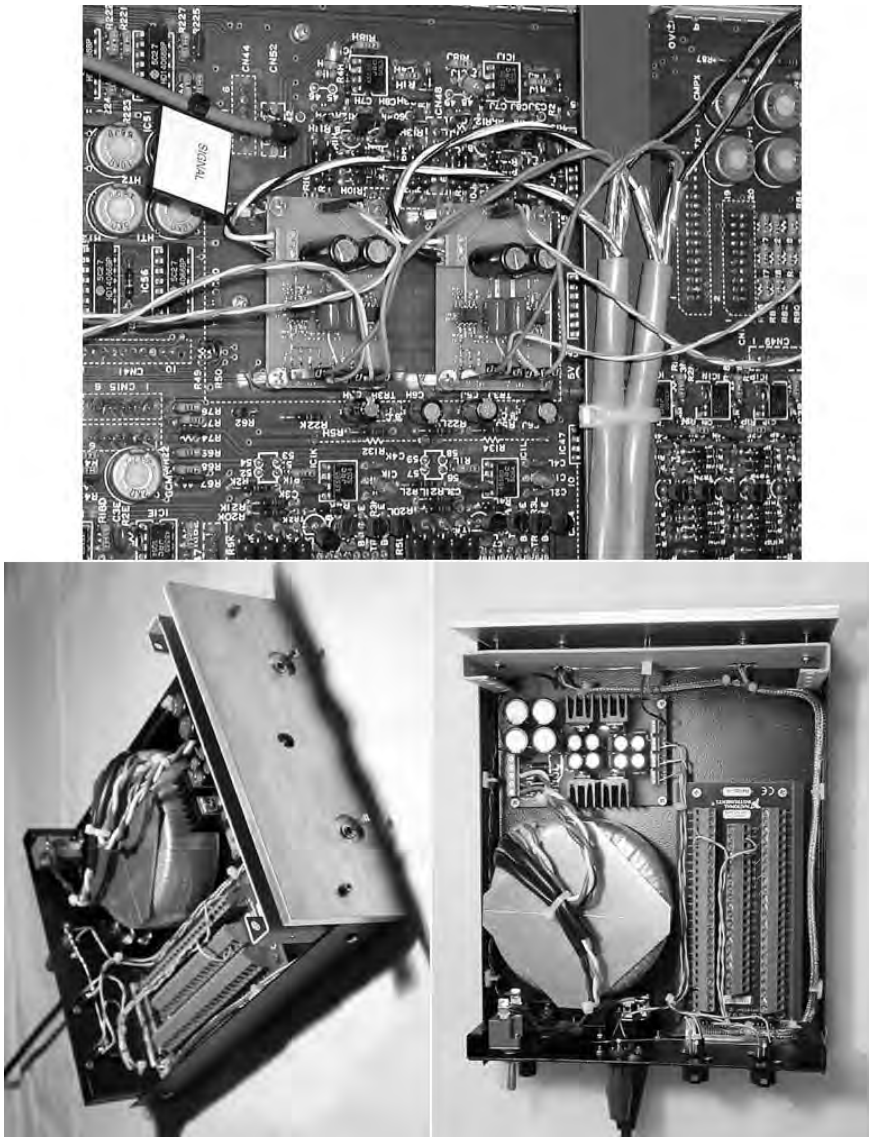

Figure C.1. The hardware for the second-generation precession instrument. Left: outboard power supply and signal distribution box. Right: Plug-in signal insertion modules.

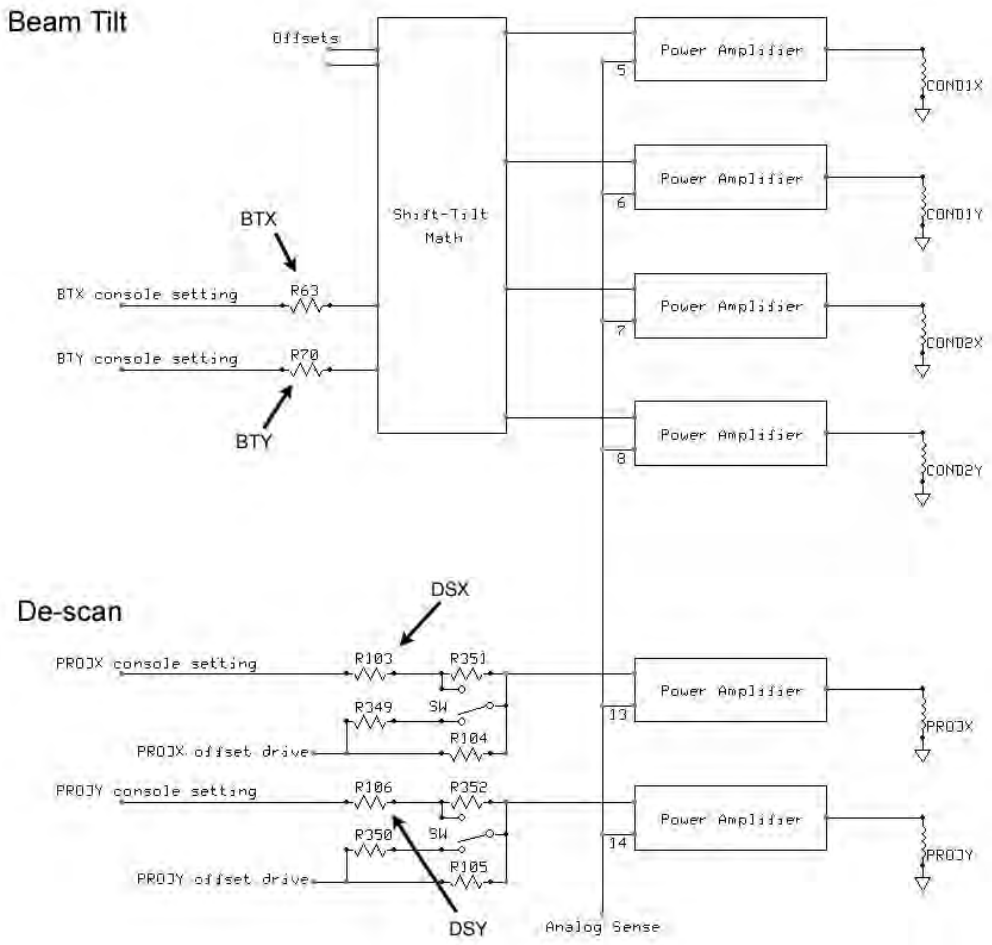

Figure C.2. DEF UNIT block diagram for the JEOL 2000FX. BTX, BTY, DSX, and DSY indicate the locations where the plug-in module should be inserted.

migrated to surface mount technology, easing installation by virtue of miniaturization. A simple dedicated linear regulated supply, comprising capacitive decoupling between two regulation stages, was built for the plug-in modules (figure C.3(b)). JEOL specifies < 10 mV ripple for the DEF UNIT, which the custom supply meets. The power supply and a National Instruments signal distribution board were incorporated into a project box that included BT and DS on/off toggle switches on the front panel for manual control independent of software. The PC DAC board interfaces with the project box via a 68-pin high-density cable, upper and lower coil outputs on the rear panel incorporate power leads and signal lines (isolated from each other via foil shields) into a single cable bundle for each module, and an additional terminal for the microscope ground is also provided. The ground connection from the microscope is shorted to the PC ground and can be broken with a toggle switch when precession is not in use.

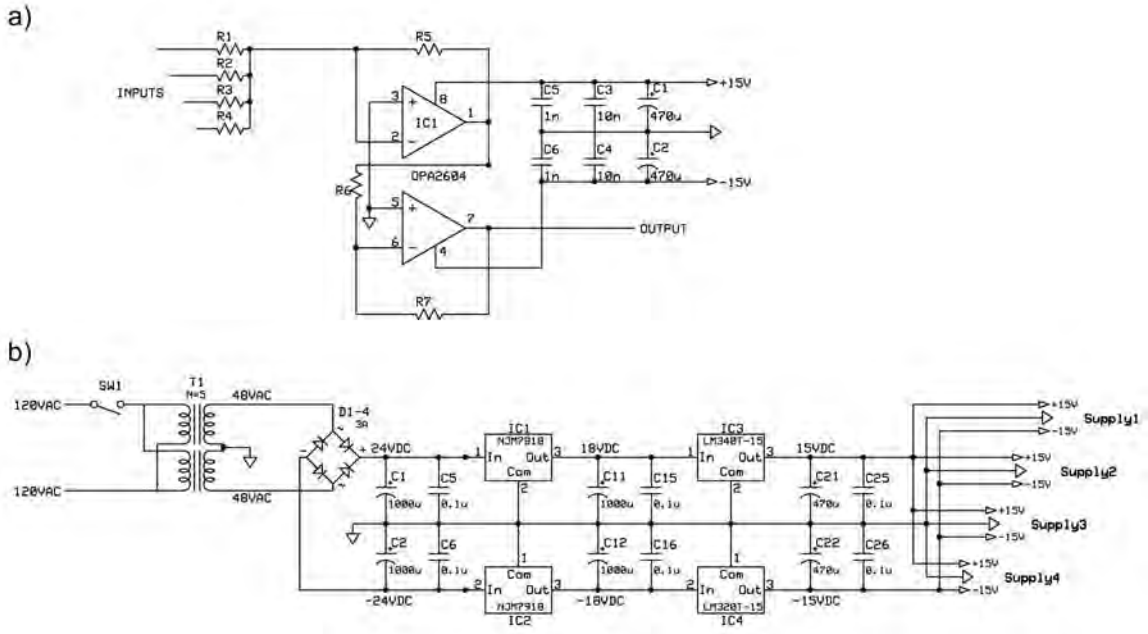

Figure C.3. Schematics for the second generation precession system. The plug-in modules are shown in (a) and the outboard power supply, capable of powering up to four modules, is shown in (b).

C.2. Performance and limitations

The instrument is operated in Koehler mode (see section 2.3) with smallest condenser aperture and spot size for small probe, coherence, and low dose to protect the CCD. BT on the 2000FX can be operated in either a bright mode or dark mode. In the latter, the control input is multiplied by a factor of 10 to increase the tilt control sensitivity. It is advantageous to operate in the bright mode to make best use of the scan generator's dynamic range. A scan amplitude of 3.5 V yields about 40 mrad in this mode.

Careful alignment of the precession device yields very high quality patterns (the procedure is given in appendix E). Figure C.4(a) is a montage of probe images at several points along the precession route for a near-aligned condition. The probe has been spread to about 50nm to clearly show the crystal edge. Each tile in the montage contains a different image of the specimen representing a specific tilt condition, and for each scan step the beam becomes slightly displaced from the centered beam in the image plane (not apparent in the figure). This probe wandering causes delocalization when the beam is precessed at full speed. The center image is the composite of the full precession; the specimen image becomes blurred and the probe becomes delocalized if alignment is poor. Moving the specimen closer to eucentric height and optimizing the lens settings and aberration compensations improves both localization of the probe and sharpness of the specimen features (figureC.4(b)).

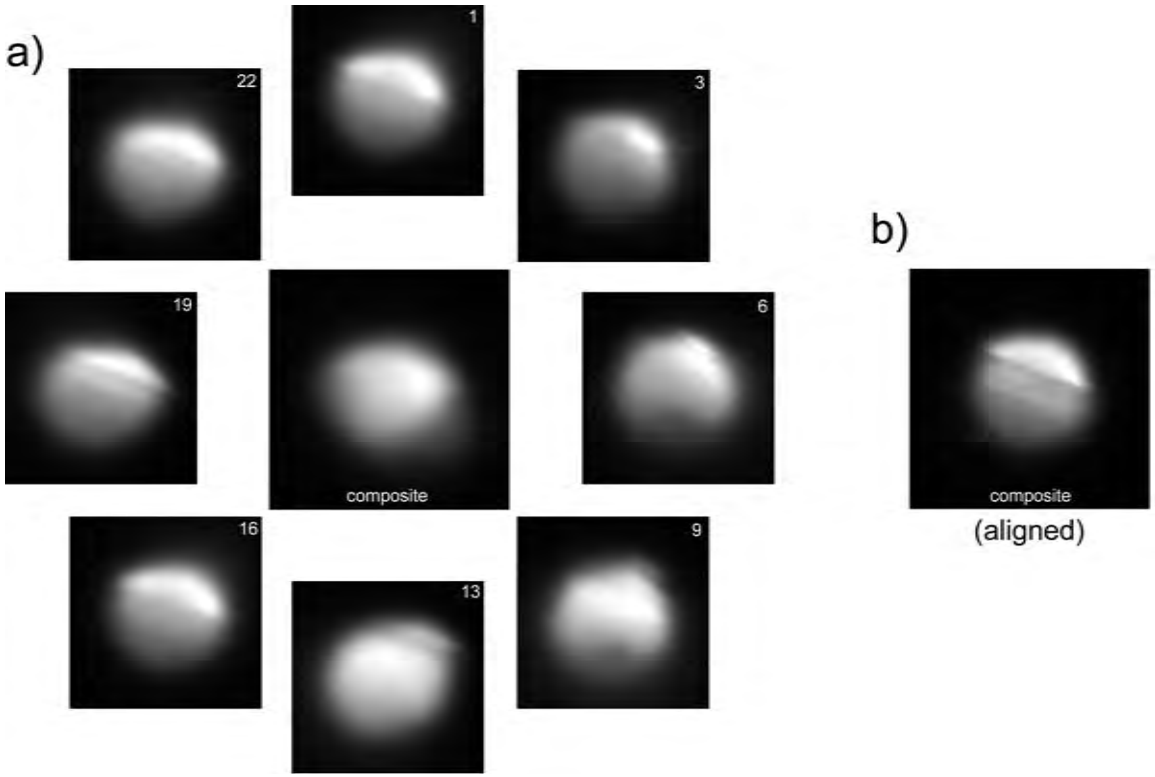

Figure C.4. (a) Montage of probe images during a precession revolution (close to aligned). 24 frames denote a full revolution; 8 of 24 are shown here. The center image shows the composite of all tilts. Both probe and specimen image wander for in the unaligned condition, contributing to a blurry composite image. The right image (b) shows a well-defined specimen image and excellent alignment of the cone pivot point after alignment. Probe size is $\approx$ 50 nm.

The 2000FX implementation can generate usable patterns using cone semi-angles of up to about 50 mRad. Appreciable projector distortions result beyond this point, as seen in figure 2.14(a), but patterns may still be measurable if integration methods less sophisticated than auto-correlation are used. The highest quality patterns are obtainable using cone semiangle between 0 and 40 mrad (see for example figure 2.14(b)); probe localization is excellent up to about 35 mrad, yielding approximate probe size of 25 nm for a very well-aligned experiment. A larger 50 nm probe is readily achievable with about 15 minutes of alignment time. The 2000FX instrument has been used to obtain high-quality precession patterns for particle regions as small as 30 nm.

APPENDIX D

Implementation 3

D.1. JEOL 2100F

At the time of this writing, a new precession implementation has been designed for installation on a JEOL 2100 analytical microscope. The design principle is similar to the previous PED systems described in these appendices. The new system is designed for more portability and should be more easily retrofittable to most microscopes. The power supply in the signal distribution box has been improved and the unit uses differential drivers to send the signals to the microscope. Differential receivers at the microscope receive the signals and apply them to the appropriate summing junctions in the deflector electronics.

The receivers can be powered by the microscope circuit or by the onboard supply. Ground is not shared between the control box and the microscope, thus avoiding common mode noise and preventing noise from filtering into the microscope circuits from the control computer. Some additional functionality has been designed in, such as receiver circuit disable (allowing precession to be switched out of the microscope system completely by the control computer) and some health status monitoring. Up to 8 channels are available in the case that double-deflectors are used for both scan and descan. The signals are provided by a NI PCI-6733 16-bit DAQ board.

Schematics for a version of the new system that use single-ended signaling are given on the following pages.

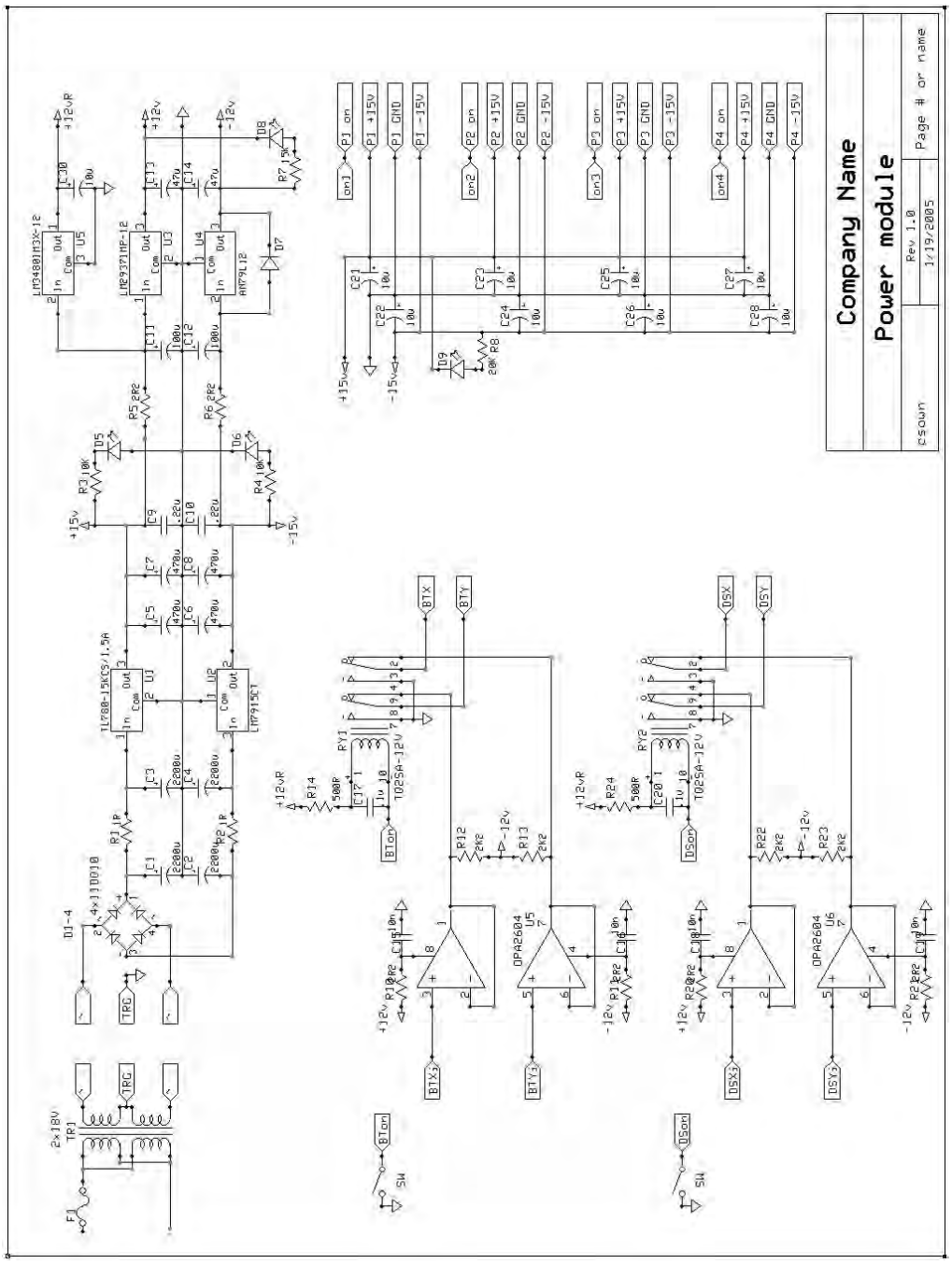

Figure D.1. Power supply schematics for the new PED system.

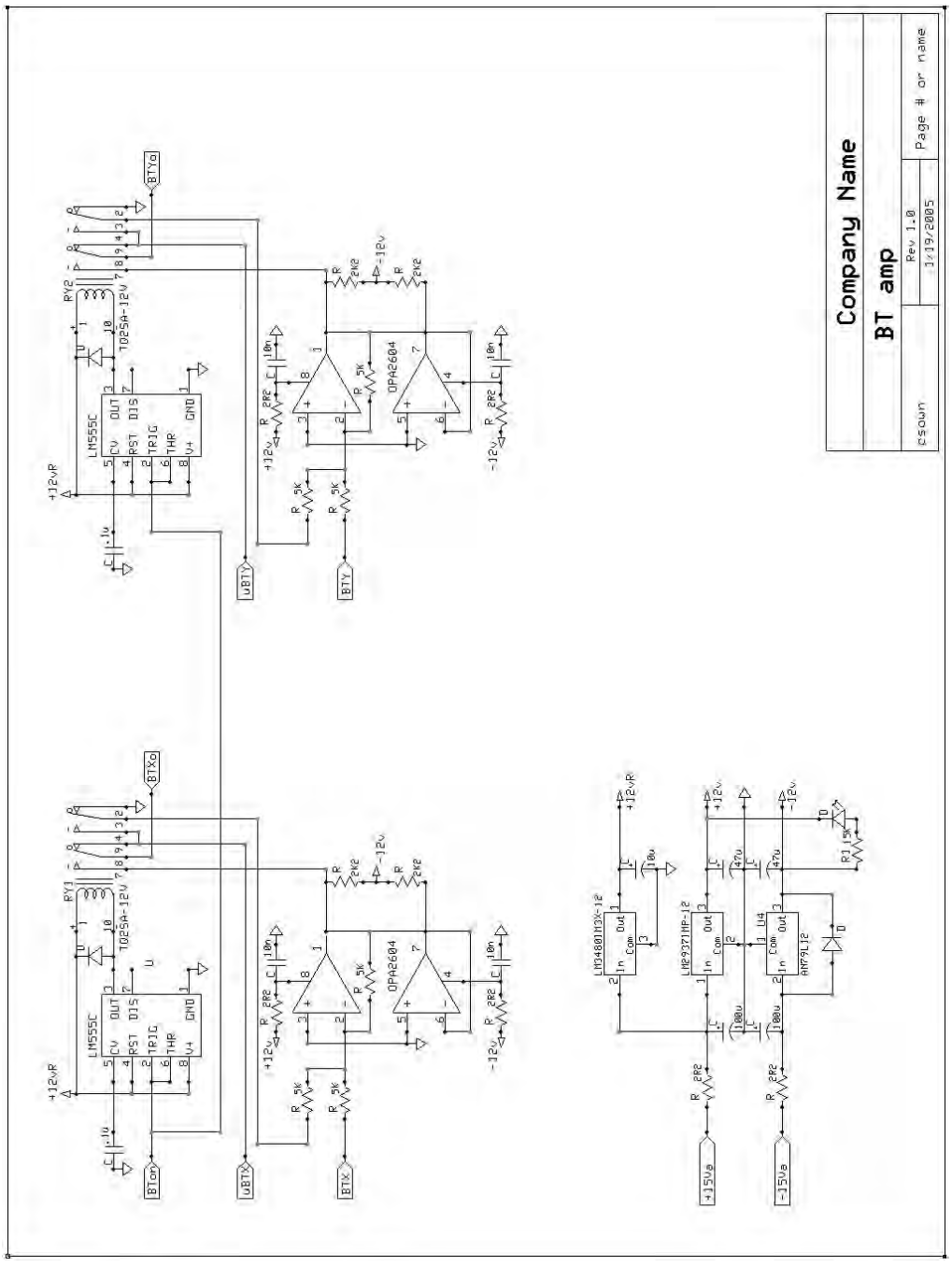

Figure D.2. BT signal board schematics for the new PED system.

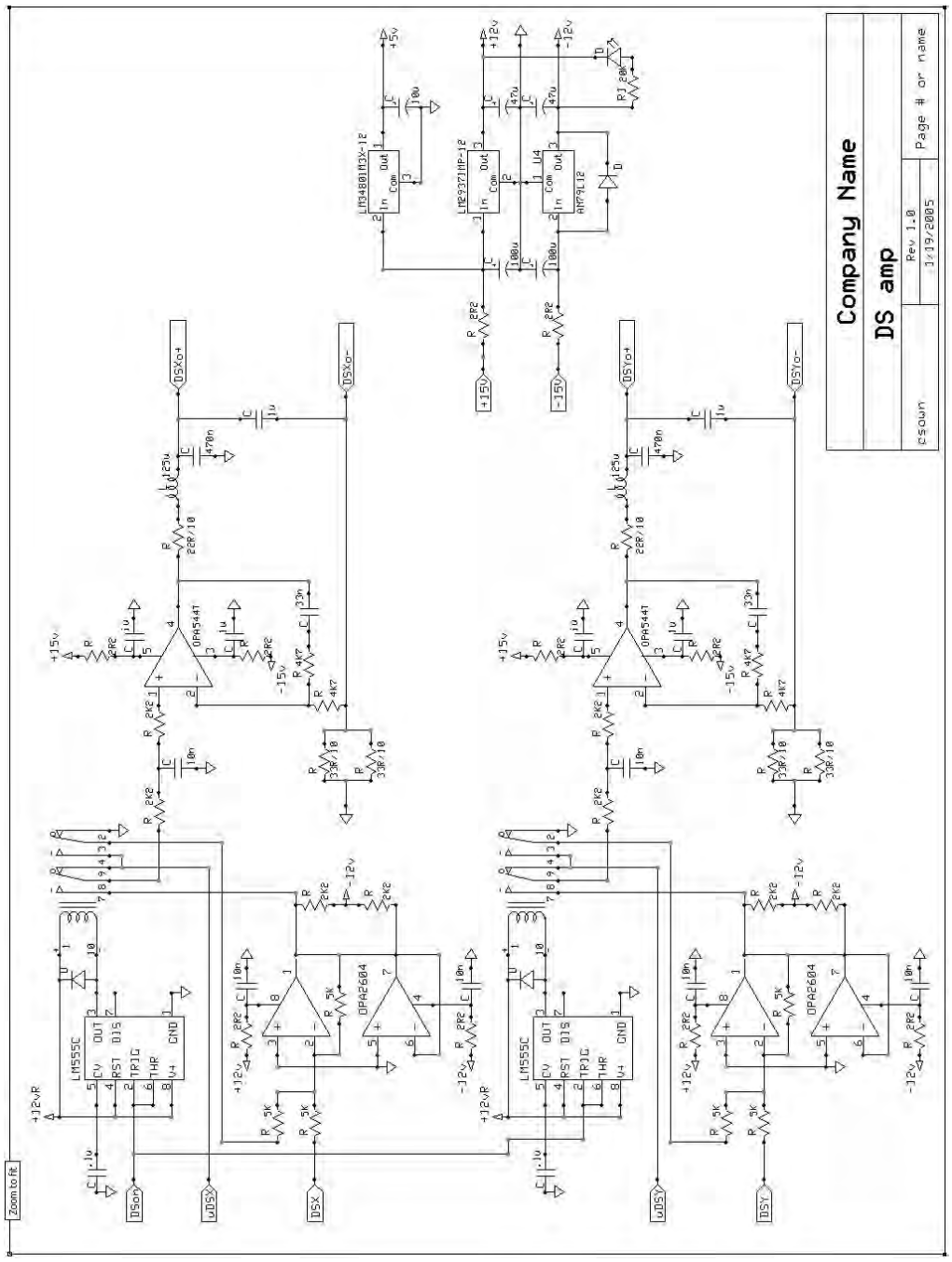

Figure D.3. DS signal board schematics for the new PED system.

APPENDIX E

Alignment Procedure

Alignment of the precession system is similar to conventional column alignment, e.g., from the gun toward the detector. With the column previously aligned for imaging, the precession alignment described here is straightforward and can typically be completed within about 15 minutes.

The following conditions are required for a high-quality precession experiment:

(1) Specimen on-zone to within ± 1 mrad. Precession patterns are quite tolerant of a slightly off-zone condition, but a better on-zone condition will yield better accuracy in the intensity integration;
(2) Specimen located close to or at eucentric height in the z-direction;
(3) Beam well-aligned with the optic axis (HV centering);
(4) Diffraction spot carefully focused and intermediate lens stigmation corrected;
(5) De-scan coils roughly zeroed to minimize deflector nonlinearity and avoid parallax distortions;
(6) If a CCD camera is used, spot size and convergence set so as to not over-expose the camera.

Highest tilt is achievable when the objective lens system is excited to its optimal current setting: this is the point where lens aberrations are lowest and smallest probe size is possible. Optimal objective excitation is factory-specified and can be obtained from the microscope manufacturer. Objective excitation is the most important parameter in the precession experiment, and the alignment of the system derives from this starting point.

The procedure for alignment is detailed pictorially in the flow diagram in figure E.1. The objective should be optimally excited and the region of interest (ROI) located at optimum focus. After conventional alignment of the imaging system, precession alignment begins by exciting the scan in the upper tilt coils (BT) to the desired cone angle in diffraction mode. One can determine cone angle by referencing the scan against diffraction spots or a calibration pattern. With scan on, switching to image mode will yield a circle that shows the intersection of the hollow cone with the specimen. The circle may be distorted due to objective aberrations. If the scan rate is lowered to below 1 Hz, one can easily see the beam tracing a path in real space through the aberrations in the lens field.

Shift-tilt purity correction (sometimes also called tilt wobbler alignment) should be adjusted next to obtain the smallest and least distorted ring pattern possible. This adjustment aligns the stacked BT deflector coils, compensating for rotations and minor dipole non-uniformities. Since the beam is swept around a perimeter inside the tilt coil, the adjustment may not result in the same shift-tilt purity settings as the conventional two-axis tilt purity adjustment, which sweeps only along the two major axes.

Continuing in real space, beam convergence should be re-adjusted if necessary to obtain minimum probe size. This will generate a fine ring pattern (though possibly distorted). If the tilt purity correction

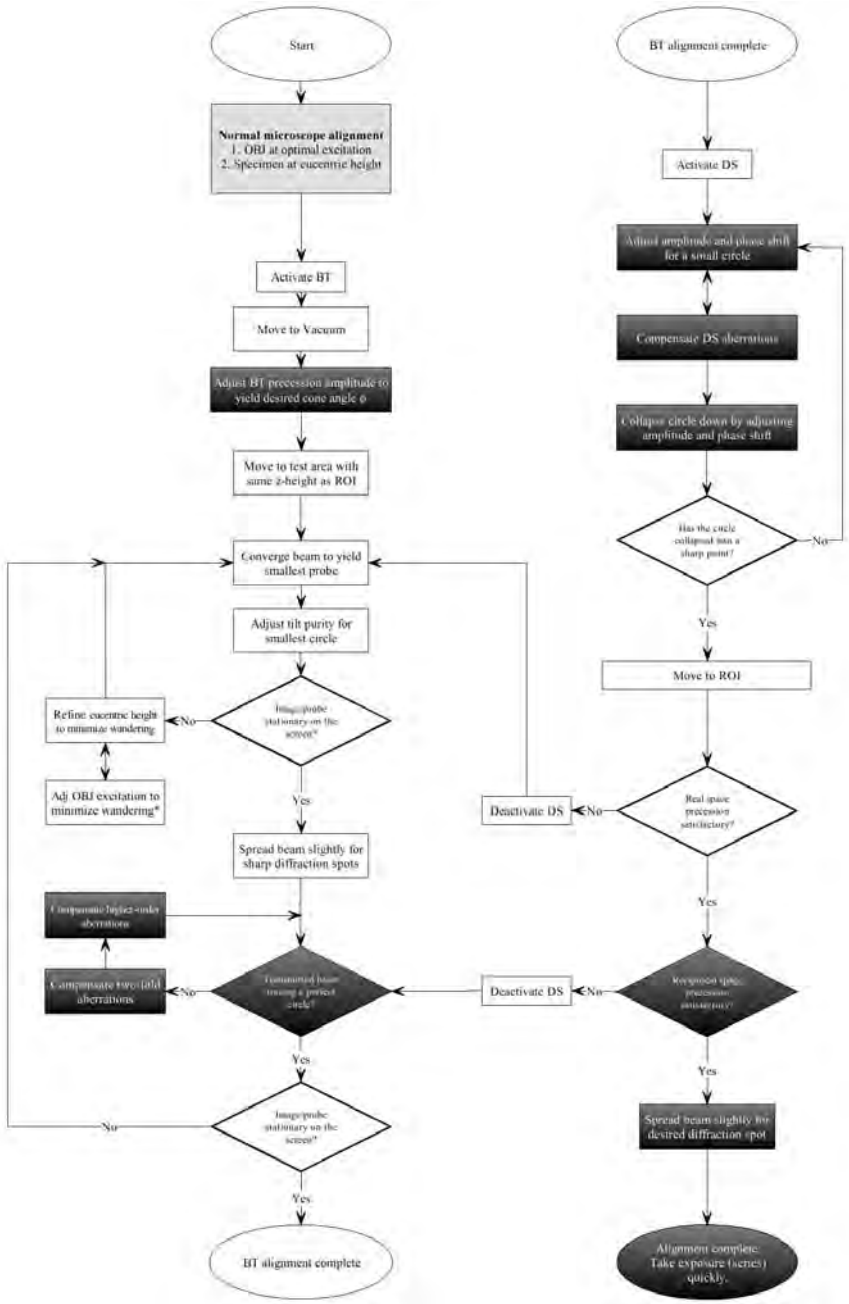

Figure E.1. Alignment procedure for the PED systems described in appendices B-C.

forms a fine spot and the specimen image moves minimally with BT scan active, the real space tilt alignment is complete. If not, specimen height must be adjusted to better intersect the convergence point of the cone and subsequent refinement must be carried out. The three variables — objective

excitation, sample height, and tilt purity — can be iteratively refined in this way until a reasonably stationary hollow cone probe and sample image are achieved in real space.

The next step is to refine the reciprocal space behavior of the BT precession. This is demonstrated in figure E.2. It is usually convenient to do this alignment off the specimen in vacuum to make use of a sharp and bright transmitted beam. In diffraction mode, the scan parameters on the precession control panel can be used to compensate for the aberrations and make the ring round. If digital capture is available, one can use a circle overlay as a reference for applying the compensations until the pattern is incident to or concentric with the reference circle (figure E.2(a)). If the real space alignments were done well, these compensations should have little or no effect on the real space behavior of the beam. Otherwise, refinement of real space alignment may be necessary after BT alignment in reciprocal space. If the scanned circle in diffraction space is concentric and the real space image and probe are stationary, BT alignment is complete.

Once beam tilt alignment is complete, de-scan can be activated (figure E.2(b)). The procedure for DS alignment is easier and less sensitive than the BT. The software implementation has real-time updates, so one can simply "wobble" the slider bars for DS amplitude and phase shift to perturb the de-scanned pattern, revealing the direction in which the alignment should progress in order to collapse the BT circle down to a sharp spot. Elliptical compensations for two-fold distortions can be applied concurrently to form a sharp point. Moving the specimen into the path of the beam allows the user to check the quality of the alignment for higher angle reflections.

Once the alignment of the transmitted beam is complete and a high quality zone axis pattern is obtainable, it is advantageous to double-check real-space alignment before switching to precession mode

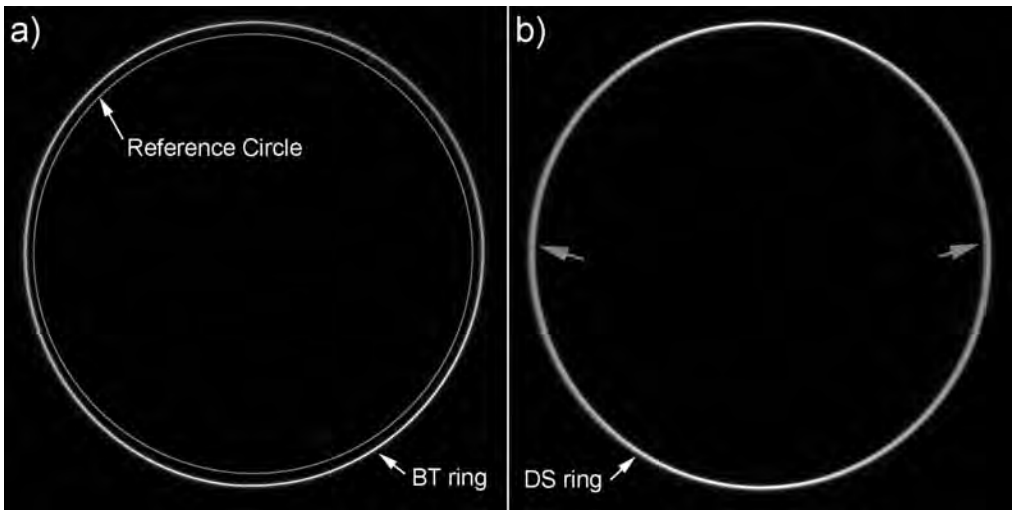

Figure E.2. Reciprocal space alignment on the JEOL 3000F systems described in appendix C. (a) shows the BT ring alignment and (b) shows the complementary descan alignment. The x and y descan coils do not have the same number of windings on this instrument. Consequently, the precision of the DACs is more limited in one axis, leading to a slight broadening of the ring indicated by the grey arrows.

to take exposures. The conditions in the microscope are dynamic (specimen drift, lens instability) making it important to take exposures quickly before alignment conditions require readjustment. Along with diffraction pattern exposures, it is useful to record the precession amplitudes in the form of voltages and record an image of the BT circle (DS disabled) to document the cone semi-angle.

APPENDIX F

Intensity Measurement

Several methods for accurate intensity measurement are available for quantifying intensities gathered during the experiment. Serial detection using a Faraday cup sensitive single electrons has been discussed in section 2.2 (Bagdik'ianc and Alexeev 1959; Avilov et al. 1999). Parallel detection methods include film, image plates (Zukhlistov et al. 2004), and charge-coupled devices (CCDs). In this appendix, quantification of the data recorded using the parallel detection methods listed will be discussed in more detail.

The data on the recording medium is transferred into grey levels in the digital domain by means of an optical scanner. Patterns from the Al_mFe studies were measured by digitizing the negative on a light box using a CCD, obtaining 512 $\times$ 512 pixel images of each pattern with 8-bit precision (Berg et al. 1998). In the acquisition of intensities from $La_4Cu_3MoO_{12}$, the negatives were scanned using an Optronics P-1000 microdensitometer at 25 μm per pixel, resulting in 8-bit images approximately 2000 $\times$ 3000 pixels in size (Own et al. 2004).

The most basic quantification method is background subtraction followed by intensity integration, as shown in figure F.1. The background is typically approximated by a linear interpolation between points tangent to the peak tails. Often the curve can be interpolated by a polynomial spline, making analytical quantification possible. The drawback to this method is that the background is often curved,

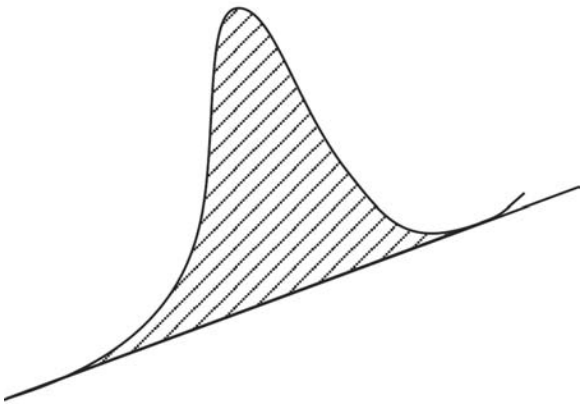

Figure F.1. Demonstration of the background subtraction technique for measuring peak intensity. The background is approximated by a line connecting points tangent to the probe tails. The background is subtracted and the area under the curve (shaded region) is integrated, or calculated from a spline approximation.

or neighboring peaks may overlap with the peak being quantified causing an overestimation of the background level.

In the the Al_mFe study, line profiles through each spot were made after background removal. Line profiling assumes each reflection exhibits perfectly circular symmetry, which is acceptable for the convergent beam case since spatial resolution constraints are more relaxed; however, with (near-) parallel illumination, the constraints are much tighter because peaks are sharper. Convergent mode precession limits measurable patterns to sparse diffraction patterns, making surfaces and superstructures more difficult to study.

Background subtraction followed by integration in two dimensions is necessary when precession patterns are not well-aligned. Patterns from the UHV H-9000 instrument demonstrated this problem often, where peak shapes were irregular and did not follow a common motif. Figure F.2(a) shows a typical diffraction spot from this system. Multiple peaks appear during different points along the precession cycle where strong excitation occurred. The optical system was not able to bring the intensity to a single point for easy measurement, so a manual routine was implemented in Synoptics Semper VI software to first identify and subtract a background level (linear), then apply a mask around the spot, and finally integrate the levels within the masked region. This method was very time-consuming but proved fairly accurate and the datasets demonstrated excellent statistics when the intensities were merged from multiple datasets (Own et al. 2004).

A resolution of 8-10 bits (2-3 orders of magnitude) — the resolution of the measurements described above — is very limited; what is desired is a large dynamic range spanning at least 3-4 orders of magnitude. The dynamic range as well as the statistical strength of the data can be improved by taking multiple measurements. In this scheme, several negatives are taken with differing exposure times in order to faithfully measure very strong beams without saturation and give weak beams a chance to be detected with suitable resolution. Negatives are individually quantified, forming separate datasets. The saturated peaks and peaks below a noise threshold within each set are discarded. The remaining peaks that are common to multiple datasets are used to scale the negatives for merging, with the intent to decrease the overall error of the merge. The scaling results in effective peaks, many of which span several measurements. A measure of their statistical error is intrinsically available and the dynamic range can readily be expanded to 4 or 5 orders of magnitude by this method.

A more sophisticated method of quantification utilizes cross-correlation, which is very accurate because of subpixel interpolation (oversampling) (Xu et al. 1994). This scheme is robust against streaking and diffuse scattering and can extract intensity from very weak spots. Additionally, it can be completely automated. In this process, a lattice is initially defined, which identifies lattice vectors $\mathbf{u}$ and $\mathbf{v}$ that describe spot positions to reasonable accuracy. A peak-finding algorithm samples several reflections — ideally of strong intensity with low background — and averages these after scaling to generate a cross-correlation kernel (unitary spot motif) that has a profile that models the majority of the diffraction spots in the data set. The cross-correlation algorithm then traverses all integer multiples of $\mathbf{u}$ and $\mathbf{v}$, masking off a region and using the spot motif to quantify the spot intensity in a consistent fashion.

The cross-correlation method works best in conventional diffraction patterns where the spot profile is representative of the image of the electron probe — itself an image of the source — convolved with

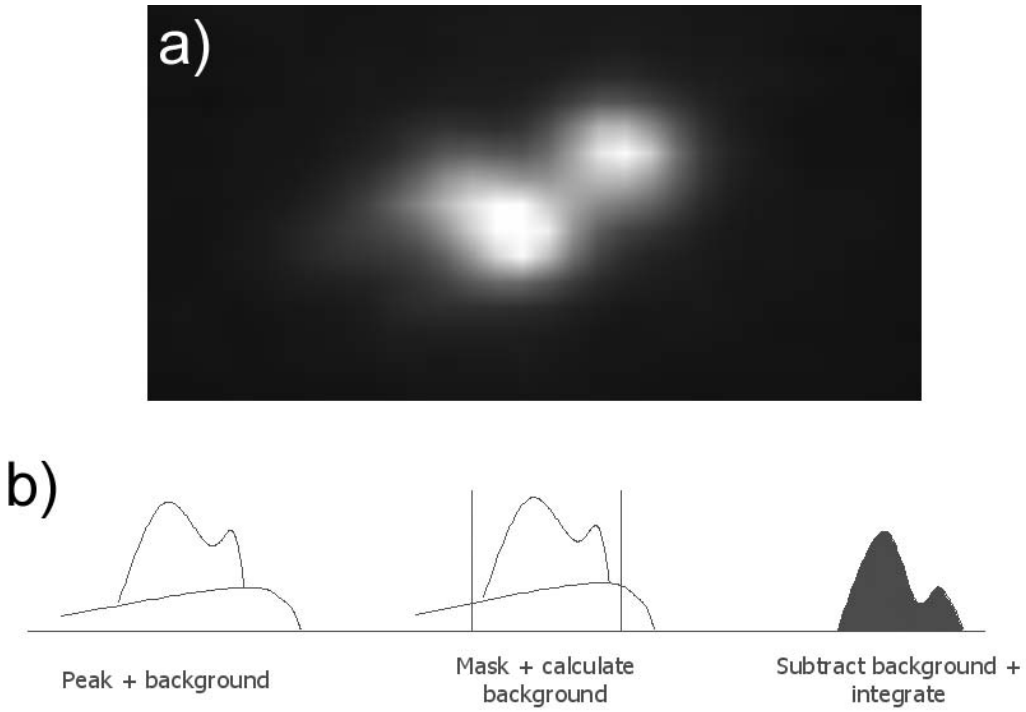

Figure F.2. Measurement of an irregular peak shape. An irregular precession spot is shown in (a). The quantification procedure is demonstrated in (b): the spot is masked, the background is subtracted, and the remaining intensity integrated.

the specimen. This is the case in selected-area and conventional electron diffraction. In precession, the peak shapes may vary because of optical aberrations and the measurement algorithm will fail if the profiles vary anisotropically in different parts of the diffraction pattern because an accurate common motif cannot be found. However, it will be successful if a common peak shape can be generated in some way. This can be accomplished by converging the illumination slightly, or ensuring very good alignment.

A cross-correlation method has been implemented by the Marks research group in the Semper software and has been reliably used to quantify many surface diffraction data sets over the past decade. The patterns taken on the newer instrument have been measured using the new EDM software (Kilaas et al. 2005), which integrates image processing, intensity measurement, and direct methods into a single software package. A comparison between the two implementations was made in order to benchmark EDM's cross-correlation implementation. An 8-bit test image was created in Semper using randomly-placed Gaussian-shaped peaks with intensities spanning over 10 orders of magnitude. A Gaussian background centered over the transmitted beam was added to simulate the decrease in scattering strength with angle. The pattern was measured by both Semper and EDM; the results are shown in figure F.3. In comparison, Semper was slightly more sensitive, being able to extract almost three orders of magnitude

from the 8-bit image whereas EDM reliably extracted intensities over 2.5 orders of magnitude. EDM's measurements coincided with the Semper results almost exactly over the measured range.

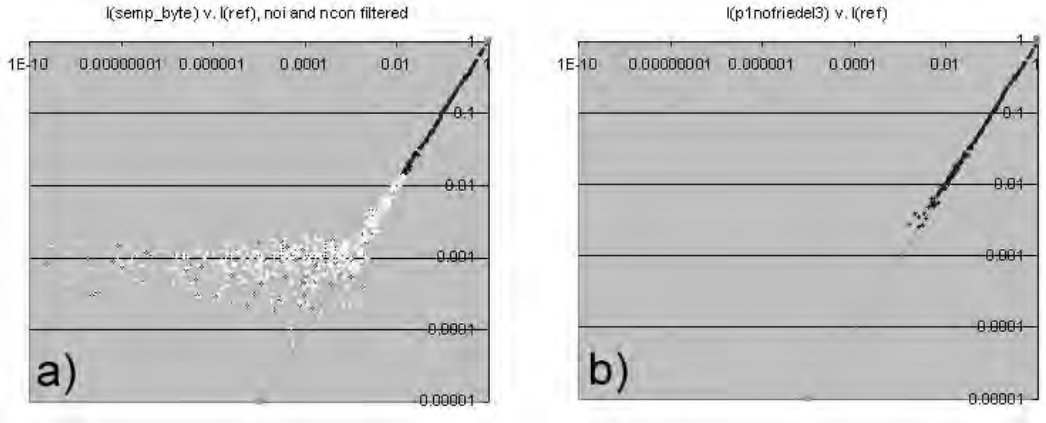

Figure F.3. (a) Semper-measured Gaussian intensity profiles. The straight line corresponds to the true spot intensities. Lighter data points correspond to low-intensity spots and spots below the noise floor (the flattened region). (b) EDM-measured intensity profiles. The cutoff is just above the noise floor measured by Semper, with very good correspondence to the true intensity over 2.5 orders of magnitude.

APPENDIX G

$(Ga,In)_2SnO_4$ Dataset

Table G.1: Kinematical amplitudes and experimental amplitudes for the GITO precession experiment (normalized to strongest reflection). See figure 3.2 for experimental errors. Reflections excluded in direct methods are starred (*).

h	**k**	**g**	F_{kin}	F_{prec}
1	1	0.1162	1.47E-01	6.13E-01*
-1	1	0.136	1.38E-01	5.21E-01*
2	0	0.1711	2.25E-01	5.46E-01*
2	1	0.1816	3.98E-03	2.75E-01*
0	2	0.1864	8.14E-02	3.41E-01*
1	2	0.1925	1.49E-01	4.50E-01*
-2	1	0.2072	4.52E-01	7.09E-01*
-1	2	0.2169	1.94E-01	6.43E-01*
2	2	0.2325	6.26E-02	4.15E-01*
3	0	0.2566	1.99E-01	3.54E-01
3	1	0.259	1.69E-01	5.04E-01
-2	2	0.272	4.92E-03	2.69E-01
1	3	0.2793	2.16E-01	3.19E-01
0	3	0.2796	8.81E-01	7.65E-01
-3	1	0.2864	1.80E-01	3.03E-01
3	2	0.2926	4.21E-04	2.95E-01
2	3	0.3041	6.88E-01	6.61E-01
-1	3	0.3049	1.64E-01	3.51E-01
-3	2	0.34	1.04E-01	3.84E-01
4	1	0.3403	7.82E-02	2.82E-01
4	0	0.3422	4.63E-02	2.54E-01
3	3	0.3487	2.38E-01	3.17E-01
-2	3	0.3499	1.39E-01	3.95E-01
4	2	0.3631	2.61E-01	5.38E-01
-4	1	0.3684	1.00E+00	1.00E+00
1	4	0.3692	4.51E-03	3.29E-01
0	4	0.3728	3.59E-02	3.30E-01
2	4	0.3851	3.31E-02	2.26E-01

continued on next page...

...continued

h	**k**	**g**	F_{kin}	F_{prec}
-1	4	0.3953	9.80E-02	3.07E-01
4	3	0.4066	9.76E-02	2.70E-01
-3	3	0.408	1.69E-01	3.78E-01
-4	2	0.4145	6.71E-02	2.99E-01
3	4	0.4182	1.22E-01	3.70E-01
5	1	0.4233	1.21E-01	2.64E-01
5	0	0.4277	2.22E-01	4.67E-01
-2	4	0.4338	5.70E-01	5.83E-01
5	2	0.439	1.15E-01	2.89E-01
-5	1	0.4518	1.11E-01	2.32E-01
1	5	0.4604	7.16E-02	2.81E-01
0	5	0.466	2.62E-02	2.53E-01
2	5	0.4706	8.39E-02	2.87E-01
5	3	0.473	4.74E-02	2.61E-01
-4	3	0.4745	6.15E-02	2.36E-01
-3	4	0.4845	6.91E-02	2.52E-01
-1	5	0.4868	3.66E-01	3.36E-01
-5	2	0.4926	1.37E-02	2.71E-01
6	1	0.5071	2.49E-02	2.60E-01
6	2	0.5179	3.47E-01	4.36E-01
5	4	0.5216	1.52E-02	2.38E-01
4	5	0.5332	6.38E-02	3.06E-01
-6	1	0.5358	3.08E-02	2.39E-01
-4	4	0.544	3.66E-01	3.82E-01
-5	3	0.5464	2.58E-01	4.11E-01
2	6	0.5586	7.44E-01	5.24E-01
0	6	0.5592	1.65E-01	3.27E-01
-3	5	0.5661	6.60E-02	2.48E-01
-6	2	0.5728	4.36E-01	4.18E-01
3	6	0.5776	6.87E-02	2.31E-01
-1	6	0.5788	1.37E-02	2.39E-01
6	4	0.5853	6.19E-02	2.36E-01
7	2	0.5987	2.08E-01	2.87E-01
7	0	0.5988	5.03E-02	2.94E-01
4	6	0.6082	4.42E-02	2.73E-01
-5	4	0.6098	1.60E-01	2.42E-01
-4	5	0.6198	3.29E-02	2.59E-01
7	3	0.62	1.45E-02	2.45E-01
6	5	0.637	4.51E-01	4.14E-01
1	7	0.6446	1.39E-01	2.56E-01
5	6	0.6487	9.06E-02	2.43E-01

continued on next page...

...continued

h	**k**	**g**	F_{kin}	F_{prec}
-3	6	0.6507	3.08E-02	2.58E-01
0	7	0.6524	1.85E-01	3.54E-01
3	7	0.6626	2.44E-01	2.42E-01
8	1	0.6761	3.75E-01	3.70E-01
-6	4	0.6799	5.63E-02	2.39E-01
7	5	0.6989	1.04E-01	2.38E-01
-7	3	0.6994	3.44E-02	2.69E-01
-2	7	0.6998	5.12E-01	4.44E-01
5	7	0.722	8.62E-05	2.51E-01
8	4	0.7263	3.11E-01	2.86E-01
-8	2	0.7369	5.04E-01	3.31E-01
1	8	0.737	1.99E-02	2.64E-01
-6	5	0.7453	4.77E-01	4.18E-01
7	6	0.7527	1.72E-01	2.32E-01
-7	4	0.7532	7.52E-02	3.02E-01
-5	6	0.7553	1.23E-02	2.44E-01
9	2	0.7633	7.26E-02	2.70E-01
-1	8	0.7636	3.23E-02	2.38E-01
-9	1	0.7899	1.37E-01	3.46E-01
2	9	0.8294	3.29E-01	2.90E-01
6	8	0.8364	1.66E-01	3.66E-01
10	1	0.8459	1.52E-01	2.61E-01
4	9	0.8549	2.41E-01	2.45E-01
10	0	0.8554	4.02E-03	2.76E-01
-4	8	0.8676	1.70E-01	2.33E-01
10	4	0.878	2.78E-01	2.84E-01
-8	5	0.8861	1.76E-01	2.45E-01
-9	4	0.9064	6.00E-02	3.77E-01
-3	9	0.9147	1.20E-01	2.54E-01
1	10	0.9225	1.14E-01	2.52E-01
11	1	0.931	1.67E-01	2.38E-01
0	10	0.932	3.48E-01	3.69E-01
-10	3	0.9406	3.05E-01	2.66E-01
-7	7	0.952	1.67E-01	2.94E-01
-6	8	0.969	2.84E-01	3.52E-01
-2	10	0.9735	2.50E-01	2.70E-01
10	7	0.9913	1.80E-01	2.44E-01
12	3	1.0208	1.64E-01	2.73E-01
12	0	1.0265	2.49E-01	2.91E-01
-12	1	1.0452	2.28E-02	2.31E-01
-10	6	1.0928	4.17E-01	2.63E-01

continued on next page...

...continued

h	**k**	**g**	F_{kin}	F_{prec}
13	1	1.1013	1.23E-01	2.44E-01
-12	3	1.1053	2.41E-01	2.63E-01
11	8	1.1054	4.00E-02	2.35E-01
4	12	1.1172	1.92E-01	2.74E-01
-4	11	1.1304	3.22E-01	2.60E-01
-1	12	1.1349	3.66E-02	2.56E-01
8	11	1.1401	1.74E-01	2.25E-01
-10	9	1.2883	2.42E-01	2.43E-01
-11	8	1.2887	2.80E-02	2.35E-01
-14	4	1.3088	8.89E-02	2.27E-01
-4	14	1.3997	1.15E-01	2.61E-01

table end.